



The  
University  
Of  
Sheffield.

# Multi-dimensional Structuring of Native Silk

Anastasia Brif

*A thesis submitted in partial fulfilment of the requirements for the degree of*

*Doctor of Philosophy*

*The University of Sheffield*

*Faculty of Engineering*

*Department of Materials Science and Engineering*

**October 2018**



## Thesis Dedication

*“This thesis is dedicated to my husband Yevgeni who encouraged me to try and to our daughter Kira who showed me why I am trying”*





## Acknowledgements

The research benefited from many helpful discussions, advice and collaborations. First, I would like to express my deepest appreciation to my main supervisor, Dr Fred Claeysens, for giving me the opportunity to undertake this exciting and stimulating journey and for his support and encouragement along the way. I would like to extend my deepest gratitude to my second supervisor, Dr Chris Holland, who introduced me to silk research and provided me with inspiration, strength and motivation to overcome any obstacle along the way. Special thanks to Dr Pete Laity, for his guidance and valuable ideas and for his help with rheology. His willingness to give his time so generously has been very much appreciated.

My special thanks to the members of the natural materials group specifically Andreas Köppel, Jamie Sparkes, Nicola Stehling, Edgar Barajas and Frankie Atkinson for their advice and teamwork, Dr Hyo Won Kwak for his help with preparation of reconstituted silk samples as well as Ash Khayatpoor and Jack Rutter for the contribution to this research during their projects. Thanks also to the members of the tissue engineering group, Dr Colin Sherborne for his useful advice on stereolithography and emulsion templating, Dr Shweta Mittar and James Clarke for the cell work and Marwah Alsharif for the pleasant work environment. I would like to acknowledge the assistance of my examiners during the annual review Dr Gwen Reilly and Dr Nicola Green for the helpful tips and research directions and confocal microscopy imaging. Finally, I would like to express my deepest appreciation to my examiners, Dr Philipp Seib and Dr Xiubo (Jon) Zhao who helped improve the quality of this thesis and the depth of my understanding during the course of a very enjoyable viva.

I gratefully acknowledge the funding provided by the University of Sheffield and B'nai B'rith UK organisation.

On a personal note, I would like to thank my husband, daughter, parents and friends for their patience, love and support.

## Thesis Abstract

The development of silk processing techniques has enabled us to benefit from this superior natural material, not only in its spun form as a fibre but also as a rehydrated protein solution which can then be converted into countless shapes, structures and designs.

To date, all non-textile silk-based structuring techniques use rehydrated silk proteins, yet, it is well known that the process of regeneration/reconstitution results in materials that lack the mechanical integrity present in its native silk source. This highlights a key gap in current silk fabrication research, leaving native silk unexplored. In this thesis, I explore the suitability of native *Bombyx mori* silk for the fabrication of 1D lines, 2D patterns and 3D scaffolds using three novel structuring pathways namely photocuring (1D, 2D) and emulsification (3D).

This thesis demonstrates that native silk is a suitable material for successful fabrication of highly detailed 1D and 2D hydrogel patterns which have the potential for a broad range of applications. Moreover, native silk is found to be superior to the current state of the art reconstituted silk. Despite this, native silk was found to be not suitable for 3D fabrication, being outperformed by high-quality reconstituted silk when making 3D structures due to the high sensitivity of native silk to the shear applied during the fabrication process.

By exploring the rheological behaviour of native and reconstituted silks, it was found that avoiding silk degumming, can significantly improve the pattern quality making it comparable to the native protein allowing scaling up of the process for industrial use.

Finally, I believe that the insight into the differences between native and reconstituted proteins together with the exploration of structure formation mechanism and properties can inspire future silk fabrication.



## List of abbreviations

AA	Amino acid	SEM	Scanning electron microscopy
ATR	Attenuated total reflection		
BB	Brilliant blue	TCP	Tissue culture plastic
DI water	Deionised water	TLD	Immersion-through-the-lens detector
DLW	Direct laser writing	UV	Ultra-violet
DMD	Digital micro-mirror device		
DSA	Dynamic shear analysis		
DR	Direct red		
EDT	Everhart-Thornley below-the-lens detector		
FFT	Fast Fourier Transform		
FTIR	Fourier Transform Infrared		
HAZ	Heat affected zone		
LED	Light-emitting diode		
MB	Methylene blue		
MeOH	Methanol		
NS	Native silk		
PA	Polyacrylamide		
PDMS	Polydimethylsiloxane		
PEG	Polyethylene glycol		
PI	Isoelectric point		
P $\mu$ SL	Projection micro stereolithography		
QR code	Quick Response Code		
RB	Rose Bengal		
RF	Riboflavin		
RS	Reconstitutes silk		
SDS	Sodium dodecyl sulphate		



## Table of Contents

Thesis Abstract.....	i
List of abbreviations.....	iii
Table of Figures.....	xi
List of Tables.....	xvii
Chapter 1 Introduction.....	1
Summary.....	2
1. Introduction to silk.....	3
2. <i>Bombyx mori</i> silk.....	5
2.1. <i>B. mori</i> silkworm anatomy.....	5
2.2. The composition of <i>B. mori</i> silk fibroin.....	6
2.3. The structure of <i>B. mori</i> silk fibre.....	9
2.4. The native process of silk fibre spinning.....	10
2.4.1. Criteria for fibre formation.....	12
3. The process of sol-gel transition (gelation).....	14
3.1. Sol-gel transition in silk fibroin solution.....	14
3.2. Evaluation of silk gelation.....	14
3.3. Silk gelation dependence on concentration and temperature.....	15
3.3.1. The secondary structure of fibroin during gelation.....	16
3.3.2. The effect of pH on fibroin gelation time and secondary structure.....	16
3.3.3. The effect of solvents and salts on <i>B. mori</i> silk.....	18
3.4. The rheological behaviour of <i>B. mori</i> silk.....	19
3.4.1. Shear viscosity of native silk.....	20
3.4.2. Viscoelastic behaviour of native silk.....	21
4. Applications of silk.....	23
4.1. Fabrication of silk structures.....	23
4.1.1. Films.....	25
4.1.2. Gels and hydrogels.....	25
4.1.3. Foams and scaffolds.....	26
4.1.4. Fibres.....	26
4.2. Current limitations in silk processing.....	27
4.3. Biocompatibility of <i>B. mori</i> silk.....	28
4.3.1. Bio-degradation.....	29
4.3.2. Immunological responses.....	30
4.3.3. Suitability for sterilisation.....	31
4.4. Silk-based structures for tissue engineering applications.....	31
5. Introducing surface patterns to proteins.....	34
5.1. Soft-lithography of proteins.....	34
5.1.1. Soft-lithography of silk.....	34

5.2.	Electron-beam lithography of proteins.....	35
5.2.1.	E-beam lithography of silk .....	36
5.3.	Inkjet printing of proteins .....	37
5.3.1.	Inkjet printing of silk .....	38
6.	Photo-polymerisation .....	39
6.1.	Photopolymerisable polymers .....	43
6.1.1.	Synthetic polymers.....	43
6.1.2.	Natural polymers .....	44
6.2.	Photo-lithography of proteins .....	47
6.3.	Photo-curing of silk .....	47
7.	Moving into 3D fabrication .....	50
7.1.	Poly-HIPes .....	51
8.	Thesis goals .....	53
8.1.	Chapter introduction.....	53
Chapter 2 Methodology.....		55
Summary .....		56
1.	Native silk extraction and solution preparation .....	57
1.1.	Selection of the silkworm.....	57
1.2.	Silkworm sacrifice .....	57
1.3.	Dissection environment .....	58
1.4.	Gland peeling process.....	58
1.5.	Sericin removal.....	58
1.6.	Silk solution storage .....	59
1.7.	Concentration calculation .....	59
2.	Reconstituted silk solution preparation.....	60
2.1.	Silk degumming.....	60
2.2.	Silk dissolution .....	61
2.3.	Solution dialysis.....	61
2.4.	Solution filtration .....	61
2.5.	Solution concentrating.....	62
3.	Rheological measurements.....	63
3.1.	Viscosity measurements .....	64
3.2.	Oscillation measurements .....	65
4.	Infrared spectroscopy .....	67
4.1.	Silk structure characterisation by FTIR spectroscopy .....	69
5.	Imaging.....	70
5.1.	Optical and confocal microscopy .....	70
5.2.	Scanning Electron Microscopy (SEM).....	71
6.	Summary .....	71
Chapter 3 1D direct laser writing of silk patterns .....		73
Summary .....		73
1.	Introduction to Direct laser writing (DLW) .....	75
1.1.	Theory and Mechanism .....	75



1.2.	DLW experimental set-up .....	78
1.2.1.	Motion system .....	79
1.2.2.	Laser sources in protein DLW .....	79
1.3.	DLW of Silk .....	81
1.4.	Photo-dye selection in protein DLW .....	83
2.	Materials and Methods.....	84
2.1.	DLW set-up.....	84
2.2.	Photoinitiator preparation.....	84
2.3.	Photo-curable silk fabrication for DLW.....	85
2.4.	Optical and confocal microscopy .....	85
2.5.	Characterisation of DLW patterns .....	86
2.6.	Cell culture .....	86
2.6.1.	Cell seeding .....	86
2.6.2.	Alamar Blue and MTT assays .....	87
2.6.3.	Cell fluorescent staining.....	88
3.	Results and Discussion .....	90
3.1.	Optimisation of the writing process .....	90
3.1.1.	Photoinitiator selection .....	90
3.1.2.	Optimisation of Rose Bengal concentration .....	93
3.1.3.	The concentration of native silk solution.....	93
3.1.4.	Sample Z position.....	94
3.1.5.	Laser parameter optimisation.....	95
3.1.5.1.	Writing speed.....	96
3.1.5.2.	Laser output .....	96
3.1.5.3.	Sample alignment .....	97
3.1.6.	The effect of over-heating by the laser.....	99
3.2.	Laser beam effects.....	100
3.2.1.	Speckle patterns.....	101
3.2.2.	Heat affected zone.....	103
3.2.3.	Investigation of the surface topography.....	104
3.3.	SEM analysis of silk DLW patterns .....	106
3.4.	Spectroscopic characterisation of the silk patterns.....	108
3.5.	Pattern transferability.....	110
3.6.	The mechanism of silk crosslinking with rose-bengal.....	112
3.7.	Cell culture on silk patterns .....	114
3.7.1.	Photo-bleaching process of the RB photoinitiator .....	116
3.7.2.	RN-22 Schwann cells .....	118
3.7.3.	Human dermal fibroblasts .....	119

4. Conclusions .....	123
Chapter 4 Fabrication of 2D Silk Structures by Projection Stereolithography.....	127
Summary .....	128
1. Introduction .....	129
1.1. Projection micro stereolithography (P $\mu$ SL).....	129
1.2. Protein stereolithography .....	131
1.2.1. Native silk as a candidate for P $\mu$ SL.....	132
1.2.2. Photoinitiators for protein stereolithography .....	133
2. Methodology.....	135
2.1. Protein solution fabrication .....	135
2.1.1. Photo-curable solution fabrication .....	135
2.2. Silk P $\mu$ SL patterning .....	135
2.2.1. Optimisation of the fabrication parameters.....	136
2.3. Post-fabrication treatment .....	138
2.4. Imaging of the fabricated patterns .....	138
2.5. Spectroscopic characterization of the crosslinked patterns.....	138
2.6. Similarity analysis of the patterns.....	139
2.7. Image analysis of the QR code patterns .....	140
2.8. Rheological measurements.....	141
2.9. Protein analysis by gel electrophoresis.....	142
3. Results and discussion .....	143
3.1. Sub-patterns and biocompatible diffraction grids.....	145
3.2. Silk-based photonic components for labelling and data storage .....	147
3.3. Mechanism.....	149
3.4. Mechanical characteristics.....	152
3.5. Silk vs. PEG in P $\mu$ SL patterning.....	155
3.6. Protein quality in silk P $\mu$ SL patterning .....	156
3.6.1. The effect of RS quality on P $\mu$ SL silk patterning .....	158
3.6.2. Enzymatic degradation of silk patterns.....	163
4. Conclusions .....	167
Chapter 5 3D fabrication of silk structures .....	169
Summary .....	170
1. Introduction .....	171
1.1. Emulsion.....	172
1.1.1. The mechanism of emulsion formation.....	173
1.1.2. Emulsification methods .....	176
1.2. High Internal Phase Emulsion (HIPE).....	178
1.3. Poly-HIPEs .....	179
1.3.1. Poly-HIPEs from natural materials .....	180
2. Methodology.....	182
2.1. Materials .....	182

2.1.1.	Reconstitutes silk solution fabrication.....	182
2.1.2.	Photo-curable silk solution .....	182
2.1.3.	Oil phase.....	182
2.1.3.1.	Oil selection.....	183
2.2.	Direct methods for the fabrication of porous silk scaffolds .....	183
2.2.1.	Pure silk freeze drying.....	183
2.2.2.	Air foaming.....	184
2.3.	Silk HIPEs fabrication.....	184
2.4.	Poly-HIPEs fabrication.....	185
2.4.1.	HIPEs stabilisation by natural gelation.....	185
2.4.2.	HIPEs stabilisation by freeze drying .....	186
2.4.3.	HIPEs solidification by freeze drying in water.....	187
2.5.	Mechanical characterisation.....	187
2.5.1.	Compression test .....	187
2.5.2.	Rheological measurements.....	187
3.	Results and discussions.....	189
3.1.	Selection of silk solution .....	189
3.2.	Preliminary stages of process development.....	189
3.2.1.	Direct methods for the fabrication of porous silk scaffolds .....	190
3.2.1.1.	Freeze drying.....	190
3.2.1.2.	Air foaming.....	192
3.2.2.	Indirect method for scaffold fabrication – two-phase emulsion.....	194
3.2.2.1.	Oil spraying.....	195
3.2.2.2.	Fast stirring.....	196
3.2.2.3.	Centrifugation .....	197
3.2.2.4.	Drop-by-drop oil injection.....	198
3.2.3.	The conclusion from preliminary experiments.....	199
3.3.	The fabrication and study of Oil-in-silk (O/S) emulsions .....	200
3.4.	Silk HIPEs .....	202
3.5.	The effect of vibration speed on the stability of O/S emulsions .....	204
3.6.	The effect of viscosity on the thickness of the voids’ walls .....	208
3.6.1.	Sample viscosity values as a function of container fixation.....	210
3.7.	The fabrication of silk Poly-HIPEs.....	212
3.8.	The effect of stirring on the stability of silk HIPEs and Poly-HIPEs .....	216
3.9.	Optimisation of the HIPE solidification procedure .....	221
3.10.	The effect of silk concentration .....	224
3.11.	The effect of silk degumming method on the poly-HIPE structure .....	226
3.12.	The effect of silk pH on the structure of poly-HIPEs.....	229

3.13. Photo-curing of HIPEs .....	232
3.14. Porosity and interconnectivity of the fabricated silk scaffolds.....	234
3.15. Applications of porous scaffolds .....	235
3.15.1. Application of silk poly-HIPEs with open porosity .....	236
3.15.2. Application of silk foams with closed porosity .....	236
3.15.3. Applications of typical silk foams.....	237
4. Conclusions .....	240
Appendix A - An optimised protocol for the fabrication of silk poly-HIPEs. ....	244
Appendix B.....	245
1. Estimations for the Peclet number in silk/oil emulsions .....	245
1.1. Air velocity .....	245
1.2. Comparison between air-drying and freeze drying .....	246
Chapter 6 Conclusions & Author’s Remarks .....	249
Thesis summary .....	251
1. Intellectual journey and challenges.....	252
1.1. The initial approach to silk photo-gelation, 1D writing .....	252
1.2. Progress in silk photo-gelation, the introduction of 2D fabrication .....	255
1.3. The limits of photo-gelation in 3D fabrication.....	259
1.4. An alternative route for 3D structuring of silk – emulsion templating.....	260
References .....	265

## Table of Figures

Figure 1: Comparison between the stiffness, strength, extensibility and toughness of silkworm and spider silk, wool and man-made materials .....	4
Figure 2: The life cycle of silkworm, a photo of <i>B. mori</i> silkworm and the major sections of the silk gland .....	6
Figure 3: (a). A segment of <i>B. mori</i> silk amino acid (AA) sequence building the H-fibroin chain (b) Amino acid distribution by % in H-fibroin out of the total sequence .....	8
Figure 4: Hierarchical structure of <i>B. mori</i> silk and the cross-section of the fibre.....	10
Figure 5: Schematic overview of the parameters critical for the natural spinning process of silk .....	11
Figure 6: (a) Concentration-dependent fibroin gelation time at room temperature and 37 °C. (b) Relationships between initial solution pH and gelation time at room temperature.....	17
Figure 7: (a) Schematic illustration of pre-gelation and early and late stages of fibroin gelation, a three-stage model. (b) Schematic illustration of pH-dependent fibroin interchain interactions at the early stage of gelation .....	18
Figure 8: (a) Plot of shear viscosity at $\dot{\gamma} = 1 \text{ s}^{-1}$ against silk protein concentration (% w/w dry residue). (b) Plots of elastic and viscous moduli vs. angular frequency, for native silk protein solution at 25 °C.....	22
Figure 9: Key literature examples of patterns made from reconstituted silk by various fabrication methods including: soft lithography, E-beam lithography, photolithography and inkjet printing.....	24
Figure 10: Variable silk structures that were fabricated from native and reconstituted silk solutions: Gels and hydrogels, foams and scaffolds, patterned films and fibres.....	28
Figure 11: (a) Published papers using silk-based scaffolds for tissue engineering applications by discipline. (b) Distribution, in percentage, of the silk-based tissue engineering papers across different disciplines. Data collected from Scopus, Feb 2018. ....	33
Figure 12: Schematic of light-induced polymerisation and crosslinking .....	40
Figure 13: The mechanisms of photopolymerisation (a) Radical photopolymerisation by photocleavage. (b) Radical photopolymerisation by hydrogen abstraction. (c) Mechanism of direct activation of onium salts with light. ....	41
Figure 14: Reaction mechanism for photoinitiated polymerisations. ....	42

Figure 15: Chemical structures of materials that can be photopolymerised to create crosslinked hydrogel networks: (a) PEG diacrylate, methacrylate, and propylene fumarate derivatives, (b) Crosslinkable PVA derivatives, (c) Hyaluronic acid derivatives, (d) Dextranmethacrylate .....	44
Figure 16: Examples of various photopolymerisable natural polymers including (A) collagen, (B) hyaluronic acid, (C) chitosan, (D) dextran, and (E) chondroitin sulfate. ....	46
Figure 17: A porous poly-HIPE structure (SEM) fabricated from native silk solution and rapeseed oil.....	52
Figure 18: (a–d) arbitrary stages of cocoon construction (from anchor threads to full cocoon). (e) photograph of dissected silk gland (unpeeled) (f) Diagram showing parts of a silk gland and origins of the samples used .....	59
Figure 19: The process of silk reconstitution .....	63
Figure 20: Diagram showing the mode of sample deformation under the plates of the rheometer, the evaluated terms for shear rate and viscosity and the figure to be obtained from viscosity experiments in a shear rheometer.....	65
Figure 21: Diagram showing oscillatory test for viscoelastic behaviour, presented as a sinusoidal function versus time, and the calculations that can be derived from the diagram. ....	66
Figure 22: Infrared beam path of Thermo Nicolet 6700 Fourier transform infrared spectrometer .....	68
Figure 23: Schematic diagram of the components of silk fibroin Amide I peak.....	70
Figure 24: The main equipment used in the experimental procedures of this thesis .....	72
Figure 25: Diagram of energy transition in single-photon and 2-photon absorption.....	77
Figure 26: Typical components of a DLW set-up consist of laser source, focusing optics, photo-curable resin and motorised stage. ....	78
Figure 27: (a) Absorption spectra of Rose Bengal, direct red and brilliant blue. (b) Absorption spectra of pure native silk, riboflavin and methylene blue. ....	92
Figure 28: (a) Variation in Rose Bengal concentration, (b) Variation in native silk solution concentration, (c) Variation in sample Z position from the focal point of the laser. ....	95
Figure 29: optimisation WLD parameters for (a) writing speed (b) laser output and (c) sample position and the written line pattern using each parameter .....	98

Figure 30: (a) Silk pattern as fabricated by DLW using optimised parameters. (b) Random elongated pattern of the silk along the writing direction. (c) Radial pattern as generated when the laser was kept in a static position for 5 sec. ....	101
Figure 31: (a) Schematic illustration of speckle pattern formation. (b) a typical speckle pattern received on NS/RB after DLW. ....	103
Figure 32: (a) HAZ calculation (b) Aligned and non-aligned regions (c) 3-layer pattern with a groove like surface. ....	106
Figure 33: SEM images of DLW silk structure. (a) EDT detector and (b) TLD detector of FEI Nova NanoSEM 450. ....	108
Figure 34: FTIR Spectrum of unexposed silk film, silk pattern- fricated by DLW, silk pattern after immersing in water and drying and silk pattern after methanol treatment. ....	110
Figure 35: Transformation of the fabricated. (a) As fabricated. (b) After a wash with water (c) after transferring to a different surface. ....	111
Figure 36: Optical microscope images of NG-108 cell seeded on: silk patterns ....	115
Figure 37: (a) Laser bleached pattern on silk/RB dry film. (b) FTIR spectra of silk/RB film, silk/RB film after the laser bleaching, RB. ....	117
Figure 38: NG-108 cells seeded on: silk patterns ....	118
Figure 39: Optical and confocal images of RN-22 cell seeded on: silk pattern fabricated by DLW; RB control and TCP control ....	119
Figure 40: (a) Cell activity of human fibroblast as measured by Alamar blue and MTT assays, 24h after cell seeding. ....	122
Figure 41: Schematic illustration of a typical projection stereolithography set-up as used in this work for multi-layer and single structure fabrication. ....	131
Figure 42: (a) the chemical structure of riboflavin (b) absorption spectra of riboflavin. ....	134
Figure 43: Native silk patterns of the 'University of Sheffield' logo as received during the optimisation of the image projection time, silk solution concentration and the laser output power. ....	137
Figure 44: The process of Image similarity evaluation ....	140
Figure 45: Native silk QR codes fabricated by P $\mu$ SL. ....	141
Figure 46: (a) Native silk patterns as fabricated by P $\mu$ SL in the presence of riboflavin. (b) silk patterned hydrogels, swelling when immersed in water. (c) The pattern is transparent with light diffraction properties. ....	143

Figure 47: (a) Diffraction pattern generated by projection of laser light on the fabricated pattern. (b) stereolithographic set-up used to generate patterns.....	146
Figure 48: Optical microscopy images of native silk photonic patterns and the light scattering received with the change of illumination angle. ....	148
Figure 49: Native silk QR codes.....	149
Figure 50: (a) UV-VIS spectra of native silk, riboflavin dye and photocured native silk washed with water. (b) Peak fitting of the photocured sample (c) Silk pattern after washing with LiBr solution. ....	152
Figure 51: (a) Elastic modulus ( $G'$ ) values over time as a function of the light intensity. (b) $G'$ value as a function of energy dose projected during pattern fabrication. (c) $G'$ value as a function of MeOH concentration.....	154
Figure 52: 'University of Sheffield' logo pattern fabricated by P $\mu$ SL from PEG and native silk solutions.....	156
Figure 53: Comparison between feature size grid and logo patterns as received for (a) native silk, (b) reconstituted silk (RS), (c) Poly (Glu-co-Tyr) protein. (d) Minimum feature size measured for each sample as a function of optimal solution concentration. (e) Similarity values .....	158
Figure 54: (a) Gel electrophoresis results for RS solutions degummed (b) Patterns fabricated by P $\mu$ SL from the same solutions (c) Change in $G'$ values of native silk and RS with and without illumination. (d) $G'$ values of RS patterns fabricated from solutions that were degummed at various Na <sub>2</sub> CO <sub>3</sub> concentrations.....	162
Figure 55: Enzymatic degradation of silk solutions and patterns by protease XIV. (a) The effect of enzyme concentration (b) The patterns as produced immediately, 10 min and 15 min after the addition of enzyme (c) Gel electrophoresis results of silk solutions (d) Enzymatic degradation over time of silk pattern post-fabrication.....	166
Figure 56: A diagram of emulsion formation and break down process .....	173
Figure 57: Schematic illustration of the radii of curvature in a perfectly spherical droplet and a droplet deformed to ellipsoid shape .....	175
Figure 58: Schematic illustration of laminar flow and turbulent flow .....	177
Figure 59: Schematic illustration of droplet shape transformation during the process of HIPE formation. ....	179
Figure 60: Schematic illustration of the oil-in-silk HIPEs fabrication method, and an optical image of the fabricated HIPE structure. ....	185



Figure 61: The fabrication of silk poly-HIPEs by natural gelation solidification process. ....	186
Figure 62: Reconstituted silk scaffold fabricated by freeze drying process. ....	192
Figure 63: Reconstituted silk scaffold fabricated by air foaming process. ....	194
Figure 64: SEM image of the cross-sections of the silk scaffold as fabricated by oil spraying, stirring and centrifugation .....	198
Figure 65: SEM image of silk scaffold fabricated by drop-by-drop oil injection method. The scaffold has uniform pore size distribution with interconnectivity. ....	199
Figure 66: (a) Viscosity values for pure rapeseed oil, reconstituted silk solution, oil/water mixture and oil/silk emulsion. (b) Viscosity over time of oil/silk emulsion immediately after fabrication and after 25, 50, 160 minutes storage at room temperature. (c) Viscosity vales of oil/silk emulsion measured during first 5 hours after fabrication.....	202
Figure 67: Schematics of Poly-HIPE fabrication .....	204
Figure 68: (a) The optimisation routes of silk solution vibrational speed during the oil addition process. (b) viscosity values of the samples fabricated by slow vibration and medium vibration with and without post stirring. (c) The elastic and storage moduli of the scaffolds fabricated at medium vibration speed, with and without post stirring. (d) A photo of the emulsions directly after fabrication and after 1 week of gelation in a petri-dish. ....	206
Figure 69: SEM images of the structure of the silk fibroin network received by slow vibration of the solution during the oil addition process followed by high-speed stirring or fast vibration .....	207
Figure 70: Scaffold porosity as a function of emulsion viscosity.....	210
Figure 71: A schematic illustration of the (a) top and (b) central fixation modes and sample bottle movement range during the vibration. (c) The variation in O/S emulsion viscosity and the average viscosity measured for each fixation method. ....	212
Figure 72: Silk scaffolds fabricated by drop-by-drop oil injection methods and solidified by natural gelation. (a) Silk HIPE after 1 week of gelation (b) SEM image of the top layer (c) SEM image of the internal area (d) FTIR spectra of the oil, dry internal phase and dry top layer	213
Figure 73: (a) SEM image of silk scaffolds fabricated by air-drying in a petri-dish. (b) Top layer porosity as generated from a sample with low Peclet number and high Peclet number (c) Cross-section of a silk scaffold fabricated by freeze drying .....	216
Figure 74: Schematics of the shear distribution in an orbital shaker and magnetic stirrer ..	217
Figure 75: (a) Viscosity values of oil-in-silk emulsion fabricated by vibration-only and by vibration + stirring methods. (b) 2.5D writing and poly-HIPE fibres fabricated by HIPE	

extrusion from syringe needle. (c) Comparison between vibration only and vibration + stirring samples. (d) Samples construction during post-processing. (e) FTIR spectra of the mixed sample indicating full conversion of the structure. ....220

Figure 76: Silk poly-HIPE fabricated by drop-by-drop injection method followed by high-speed stirring. ....221

Figure 77: SEM images of the top layer and internal structure of silk scaffolds fabricated by air drying, direct freeze drying and water-based freeze drying methods. ....223

Figure 78: A photo of oil-in-silk emulsions after 1 week of gelation and the solid scaffolds fabricated from silk solution with various protein content. ....225

Figure 79: Silk poly-HIPEs fabricated at different silk protein content .....226

Figure 80: Top: SEM images of silk poly-HIPEs fabricated from non-degummed, chemically degummed and mechanically degummed silk solutions. Bottom left: The dry scaffolds used for the SEM analysis. Bottom right: Stress values for solid scaffolds fabricated from non-degummed, chemically degummed and mechanically degummed silk solution. ....229

Figure 81: FTIR spectra of silk films cast from reconstituted silk solution collected after 24h and 48h of filtration. ....230

Figure 82: Comparison between photo-exposed and unexposed silk HIPEs fabricated in the presence of riboflavin .....234

Figure 83: Interconnectivity levels of silk scaffold as received in this work by process optimisation methods. ....235

Figure 84: Schematic illustration of the degradation regime for open porosity and close porosity scaffolds. ....237

Figure 85: Selected structures of porous silk including open-porosity scaffolds, closed porosity scaffolds and typical foams fabricated by emulsion templating and direct freeze drying methods and the list of possible applications for each foam. ....239

## List of Tables

Table 1: Amino acids composition in <i>B. mori</i> H-fibroin protein <sup>42,43</sup> .....	8
Table 2: Weight Loss of Silk Fibroin Films. Enzyme-to-substrate ratio: (a) 1:20; (b) 1:8. (reproduced with permission from <sup>144</sup> ).....	30
Table 3: Current literature describing photo-curing of silk fibroin. Bulk PL described full photocuring of the region without specific pattern fabrication. ....	49
Table 4: Comparison of the laser parameters used for multi-photon excitations in protein materials as used appears in DLW literature.....	81
Table 5: Comparison of multi-photon direct laser writing publications of silk protein. ....	82
Table 6: Photoinitiator dilutions required to the collection of UV-VIS absorption spectra ....	85
Table 7: The optimised parameters as evaluated for NS/RB DLW writing.....	98
Table 8: Optimised experimental parameters for the fabrication of native silk patters by P $\mu$ SL .....	137
Table 9: The summary of the experimental conditions and the pattern characteristic as evaluated in this chapter .....	167
Table 10: The comparison of pore diameter and mechanical properties of silk poly-HIPE scaffolds fabricated from the same silk solution after different filtration times.....	231
Table 11: The optimal experimental parameters for the fabrication of silk poly-HIPEs.....	240
Table 12: Summary of the methods and result discussed in this thesis .....	264



# Chapter 1

---

## Introduction

## Summary

This chapter introduces the reader to the scientific background for the work presented in this thesis. The qualities and benefits of silk, an exceptional natural material used by humans since ancient times, is presented followed by its formation, structure and properties alongside modern silk production methods and applications. An overview follows where current structuring routes are explored with the aim to set the scene for new possibilities in silk-based engineering. Finally, for this thesis, directly relevant techniques for silk structuring, including photo-lithography and emulsion templating are presented as pioneering approaches to silk-based fabrication.

## 1. Introduction to silk

The term silk refers to a fibre spun by animals out of proteins, mostly fibroins <sup>1</sup>. Silk has evolved independently several times over hundreds of millions of years and many animals including insects, arachnids and myriapods have been seen to produce a diverse range of silk structures and architectures <sup>2</sup>. This diversity is observed in the extreme in spiders, where it is not rare to find various silk compositions produced by the same individual, used for different purposes such as mobility, prey-catching, protection, reproduction and sensing <sup>3,4</sup>. Even though such animals may use silks for a variety of functions and possess fundamentally different protein structures, there are some commonalities as it appears silks tend to share similar hierarchical structures <sup>5,6</sup>.

Silk fibres have been used for millennia in both textile and medical applications <sup>7-9</sup> with a great focus on spider silk (especially dragline silk) and *Bombyx mori* (*B. mori*) cocoon silk. Millions of years of natural selection (and in the case of *B. mori* thousands of years of further artificial selection), have resulted in fibres with outstanding mechanical properties including stiffness (resistance to deformation), strength (withstanding force or pressure), toughness (absorbing energy without fracturing) and extensibility, which are superior to most of the man-made materials <sup>10-12</sup> (Figure 1). Spider dragline silk, for example, is remarkably strong and extensible, resulting in a very tough fibre, while silk from the cocoon of *B. mori* is relatively stiff and brittle. However, by force reeling the silk from the silkworm, it is possible to improve the mechanical properties of the fibres by controlling the spinning speed, the environmental parameters (such as humidity and pH) and by post-processing <sup>13,14</sup>. When compared to other types of fibres, the reported strength of the spider dragline silk (1.1 GPa) is in the scale of high-tech materials such as high-tensile steel (1.5 GPa) and carbon fibre (4 GPa) while its

toughness ( $180 \text{ MJ/m}^3$ ) is significantly higher than man-made Kevlar 49 ( $50 \text{ MJ/m}^3$ ) and Nylon ( $80 \text{ MJ/m}^3$ )<sup>12</sup>. Furthermore, these impressive mechanical properties are manufactured under ambient conditions such as room temperature, low pressure and aqueous environment, resulting in an environmentally friendly process with recyclable outcome<sup>4,15</sup>.

At the molecular level, silk fibres consist of crystalline fibroin units which are evenly distributed in amorphous matrix occupying about half of the fibre volume<sup>6,16</sup>. The ratio between the crystalline and the amorphous regions largely defines the mechanical properties of the macroscale fibre<sup>6</sup>. Overall, this can be generalised to say silk elasticity is dependent on the amorphous regions in the material, which allow large extensibility during stretching, while the crystalline regions contribute to the strength and stiffness of the fibre<sup>6</sup>.

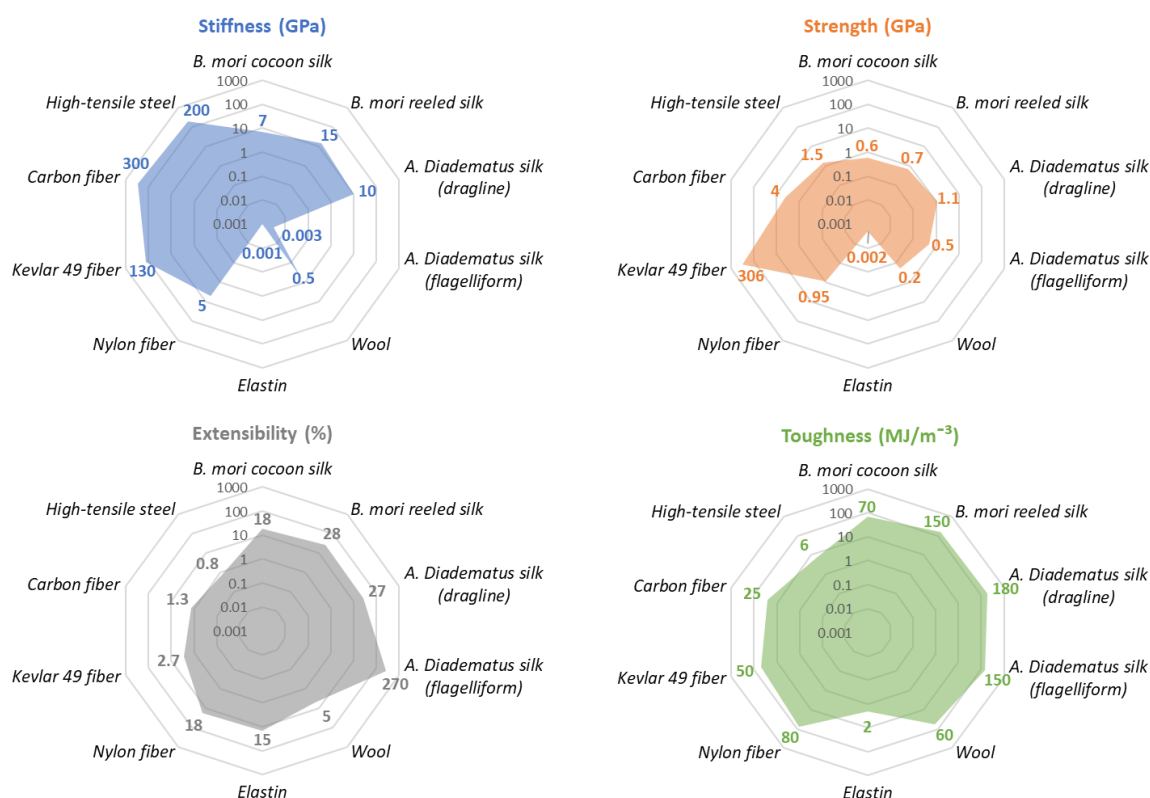


Figure 1: Comparison between the stiffness (blue), strength (orange), extensibility (grey) and toughness (green) of silkworm and spider silk, wool (at 100% relative humidity) and man-made materials (data reproduced from<sup>12</sup>).



## 2. *Bombyx mori* silk

The *Bombyx mori* silkworm, which is, in fact, a caterpillar, is a domesticated insect originating from the wild silkworm *Bombyx Mandarina* about 5000 years ago and is probably the most studied animal among the silk-producing insects<sup>17-20</sup>. Due to the widespread use of its silk by the textile industry, *B. mori* has undergone intensive selective breeding to produce a specific set of fibre properties, resulting in a white, high yield, easy to unravel, triangular cross-sectioned fibre, with up to a 1 km of continuous filament being obtained from a single silkworm cocoon. This is in stark contrast to a complete spider web which will provide only up to 12 m of silk<sup>6</sup>. Therefore this combination of commercial interest and practical sample availability has led *B. mori* to be commonly used as a model organism in silk research<sup>18,21-24</sup>.

### 2.1. *B. mori* silkworm anatomy

In its juvenile form, *B. mori* larvae have a cylindrical body, 10 pairs of legs<sup>25</sup> and a small head equipped with two jaws that move laterally. Inside the animal, alongside the expected digestive tract and breathing spiracles, two silk-secreting and spinning apparatuses (silk glands) can be found on both sides of the silkworm<sup>26,27</sup>. These organs, accountable for 20% to 40% of the total animal weight, are filled with a highly concentrated, water-based, protein solution (spinning dope) which as it passes through the attached spinning duct will form the silk fibre<sup>28,29</sup>.

The silk gland can be divided into three major sections: posterior (where the silk proteins are synthesised), middle area (a reservoir for the silk dope and sericin secretion region), and the anterior region which connected to the spinning duct (where the silk fibres are spun from). The middle section is divided into 3 main divisions based on the natural curvature of the gland

and their functions: Anterior division (secretion of sericin 2 and sericin 3 proteins), middle division (secretion of sericin 1), posterior division (no sericin secretion)<sup>29–31</sup>. The life cycle of the silkworm and the elements of the silk gland are presented in Figure 2.

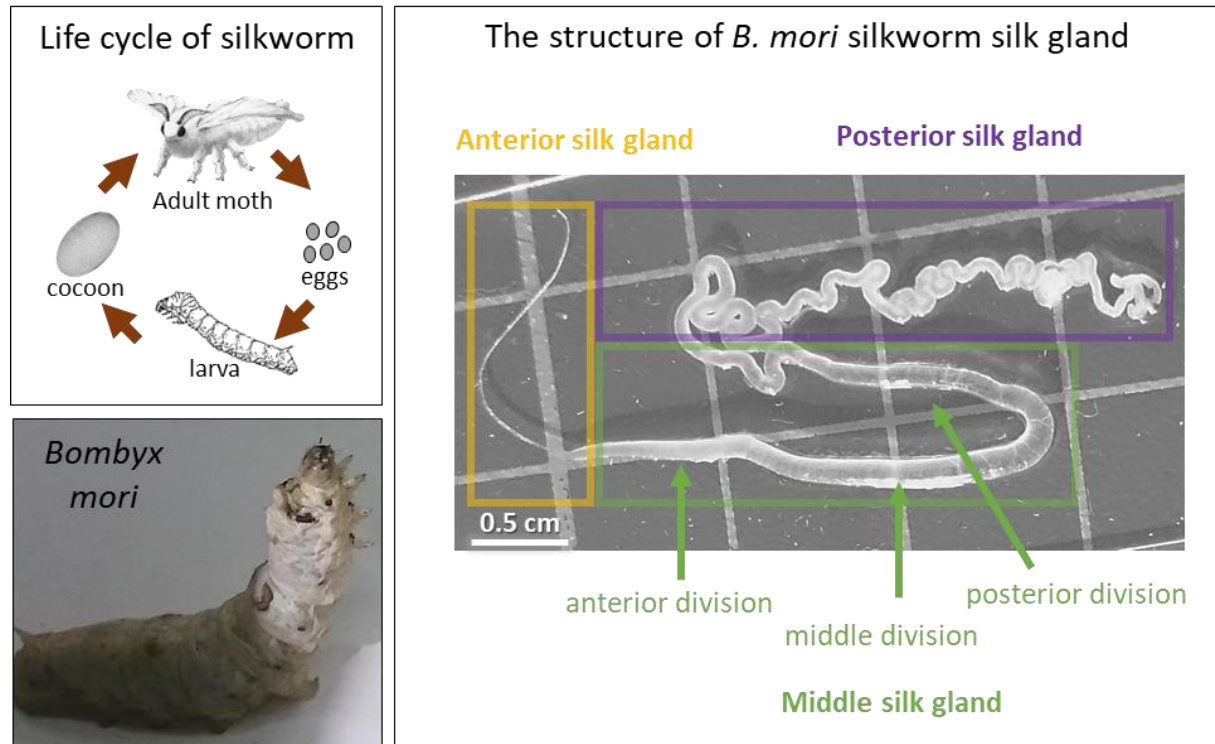


Figure 2: The life cycle of silkworm (top left), a photo of *B. mori* silkworm (bottom left) and the major sections of the silk gland (right): The silk proteins are synthesised in the posterior section (purple), the proteins are stored and sericin is secreted in the 3 sub-divisions of the middle area (green), and the silk fibres are spun in the anterior region (orange) of the gland.

## 2.2. The composition of *B. mori* silk fibroin

The remarkable mechanical properties of silk can be attributed to its primary and secondary protein structure defined by amino acid composition, sequence and architecture together with its folding patterns.

Silk's core protein, fibroin, is built out of two protein chains: heavy chain (H-fibroin,  $M_w = 390$  kDa) and light chain (L-fibroin,  $M_w = 26$  kDa)<sup>32</sup>, which are covalently linked via a disulphide bond between the carboxyl ends of the chains, and an accessory protein, P25<sup>32</sup>.

The H-fibroin contains a highly repetitive central region rich with glycine (46%) and alanine (30%) amino acids and tyrosine domains (5%) making the central region mostly hydrophobic<sup>32</sup> (Figure 3). Those amino acids are unlikely to spontaneously fold into  $\beta$ -sheet rich structures in the dope<sup>33</sup>. The protein's terminal regions are nonrepetitive amine and carboxyl domains which are mostly hydrophilic and considered to have a fundamental role during the fibre formation process<sup>32</sup>. The end domains are highly sensitive to variation in salt content, pH and flow, allowing the production of stable and tough fibres under mild conditions<sup>34</sup>. This fibroin structure, with hydrophobic sequences located in between hydrophilic blocks, increases the solubility of the protein and prevents premature  $\beta$ -sheet formation<sup>35</sup>. The H-fibroin has mainly random coil conformation (> 85%) with minor  $\beta$ -sheet and  $\alpha$ -helix components<sup>5</sup>.

The correlation between specific amino-acid sequences and the properties of the silk fibre has been extensively studied in the literature, mostly by analysing the behaviour of silk inspired poly-peptide chains<sup>36-39</sup>. Using molecular dynamic simulations, it was shown that poly-alanine segments can contribute to the formation of ordered  $\beta$ -sheet structures<sup>39</sup>. This is due to the anti-parallel orientation of the hydrogen bonds and the parallel direction of the side chains leading to stabilisation of the  $\beta$ -sheet conformation. However, glycine-rich domains present less-ordered structures, such as helical structures and  $\beta$ -turns, which form silk's amorphous regions<sup>40</sup>. The density of hydrogen bonds has a strong effect on the crystallinity of the silk domain with higher bond density in the crystalline region<sup>41</sup>. Yet, the molecular structure alone is not sufficient to explain the mechanical properties of silk fibres since recombinant and synthetically spun silk does not present comparable values<sup>14</sup>.

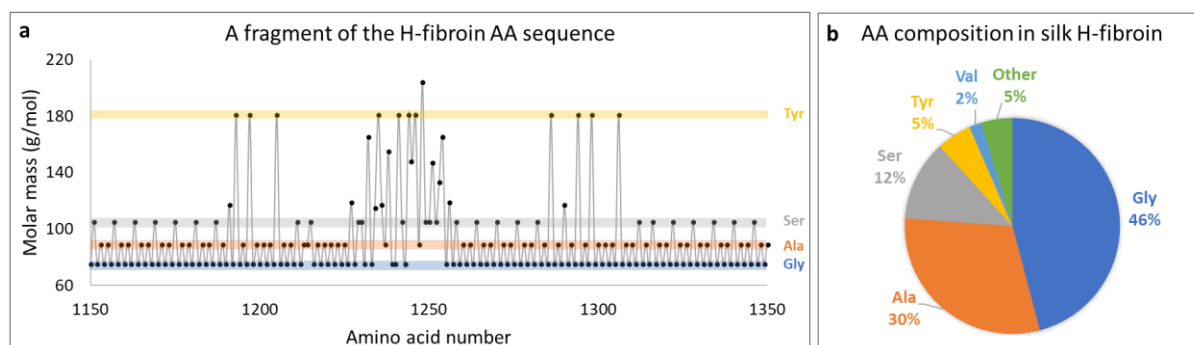


Figure 3: (a). A segment of *B. mori* silk amino acid (AA) sequence building the H-fibroin chain showing the repetitive  $(\text{Gly-Ala})_n$  motif and the Ser and Tyr rich domains. (b) Amino acid distribution by % in H-fibroin out of the total sequence<sup>42,43</sup>.

Table 1: Amino acids composition in *B. mori* H-fibroin protein<sup>42,43</sup>.

Amino acid	Total amount	Percentage	Mw (g/mol) (bound)
Ala	1593	30.27%	71.09
Cys	5	0.10%	103.16
Asp	25	0.48%	115.11
Glu	30	0.57%	129.13
Phe	29	0.55%	147.19
Gly	2415	45.89%	57.07
His	5	0.10%	137.15
Ile	13	0.25%	113.17
Lys	12	0.23%	128.19
Leu	7	0.13%	113.17
Met	4	0.08%	131.21
Asn	20	0.38%	114.12
Pro	14	0.27%	97.13
Gln	10	0.19%	128.14
Arg	14	0.27%	156.20
Ser	635	12.07%	87.09
Thr	47	0.89%	101.12
Val	97	1.84%	99.15
Trp	11	0.21%	186.23
Tyr	277	5.26%	163.19
<b>Total</b>	<b>5263</b>	<b>100%</b>	<b>391.65 (KDa)</b>

### 2.3. The structure of *B. mori* silk fibre

To create the non-woven composite cocoon that is required for protection and environmental control during the silkworm's metamorphosis into an adult moth, the *B. mori* larvae spins a continuous single thread of silk with a diameter of about 20  $\mu\text{m}$ <sup>44</sup>. This fibre possesses a core-shell structure with two fibroin cores (brins) surrounded by sericin protein coating, which accounts for 25-30 wt.% of the fibres mass<sup>12</sup>. This sericin coating acts as a glue for the cores and enables the fibre to be bound together into a layered composite, however recent insights suggest sericin might also have a role as a lubrication agent together with presenting antibacterial and antifungal properties<sup>18,31</sup>.

The fibre is a protein consisting of highly repetitive (Gly-Ala)<sub>n</sub> sequence with crystalline and non-crystalline (amorphous) regions<sup>45</sup>. The crystalline and amorphous regions are equally and evenly distributed along the fibre and organised in 3 major conformations: random coil,  $\alpha$ -helix and  $\beta$ -sheet. Random coil and  $\alpha$ -helix are present in the non-oriented amorphous region which can also contain structures such as  $\beta$ -turns<sup>34,45</sup>.

In solid silk fibre the crystalline units well organise in anti-parallel  $\beta$ -sheet conformation, forming silk II structure, while in the structure in the silk dope in known as silk I. When several  $\beta$ -sheet units are crosslinked together, a  $\beta$ -sheet crystallite with monoclinic unit cell ( $a=0.938$  nm,  $b=0.949$  nm and  $c=0.698$  nm) is formed<sup>45</sup>. The crystallites are uniformly distributed along the fibre, parallel to the fibre axis, with an average crystallite size of 20-170 nm (axial) and 1-20 nm (lateral)<sup>12</sup>. Various parameters of the  $\beta$ -sheet crystallite such as crystallinity level, lattice parameters, crystallite size, location and orientation can highly affect the mechanical properties of the silk<sup>5</sup>. The schematics of fibre structure and cross-section is presented in Figure 4.

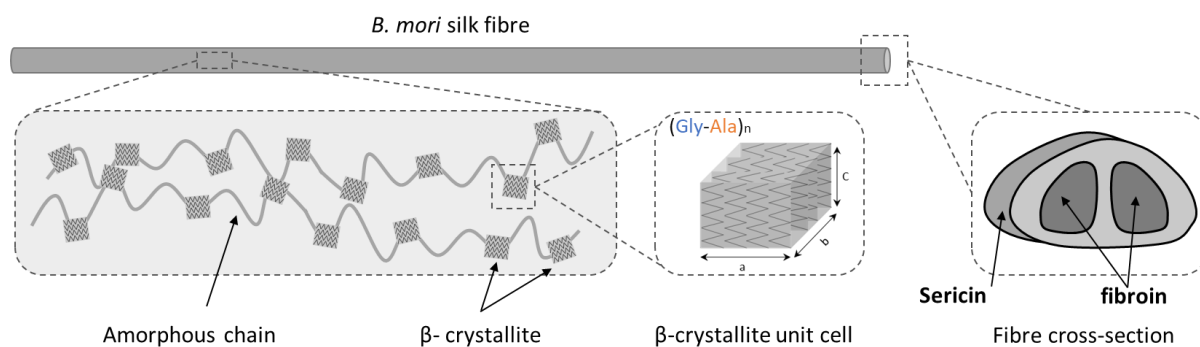


Figure 4: Hierarchical structure of *B. mori* silk and the cross-section of the fibre.

## 2.4. The native process of silk fibre spinning

The native process of silk spinning is rapid since the animal is often required to adapt to changing environmental conditions<sup>28</sup>. The natural spinning rate can vary between 10-20  $\text{mm}\cdot\text{s}^{-1}$  for spider silk and slightly lower for *B. mori* silk<sup>10</sup>. Since the spinning process requires the transition of the unspun silk gel structure into a solid fibre, the energy required for this phase transition needs to be introduced rapidly, allowing for fast formation of the oriented hierarchical structure.

This stress-induced transition is probably a result of mechanical deformation of the gel as a result of the wall shear along the duct and extensional flow<sup>46</sup>. The spinning duct of the *B. mori* is progressively narrowing with a sharper reduction in diameter toward the end of the duct<sup>28,47</sup>. The orientation of the proteins can be maintained, avoiding premature gelation by maintaining a constant elongational flow along the duct<sup>48</sup>. The membrane of the duct allows for the controlled exchange of cations and water into/out of the dope. By controlling the ionic composition in the dope, it can be possible to control the proteins' sensitivity to shear and to initiate a stress-induced phase transition<sup>49,50</sup>.

The mechanism of silk spinning was explained by Asakura *et al.*<sup>51</sup> and is summarised in a simplified scheme adapted from Wohlrab *et al.*<sup>52</sup> (Figure 5). In the process, a highly viscous fibroin solution enters the duct at the anterior part of the silk gland. The solution flows along the duct until its linear velocity reaches a critical value, at which shear at the interface between the fibroin and the sericin overcomes the fibroin molecules attachment to the sericin. The proton pump located in the cells lining the duct allows the secretion of hydrogen ions (together with phosphate and potassium) into the spinning duct which results in a pH gradient in the duct. Following the reduction in pH, the negatively charged groups of the fibroin (Asp and Glu amino acids) are suppressed, which initiates the gelation process and a weak gel is formed. This gel formation increases the viscosity of the solution leading to rapid extensional flow in the duct which orients the fibroin molecules bringing them closer to each other. The hydrophobic interaction between the fibroin molecules contributes to the removal of the water shell around the protein, and initiation of the  $\beta$ -sheet structure formation. The fibroin fibres are transferred to a stiffer region at the end of the duct (silk press) which increases the extensional flow, contributing to the formation of oriented silk fibre.

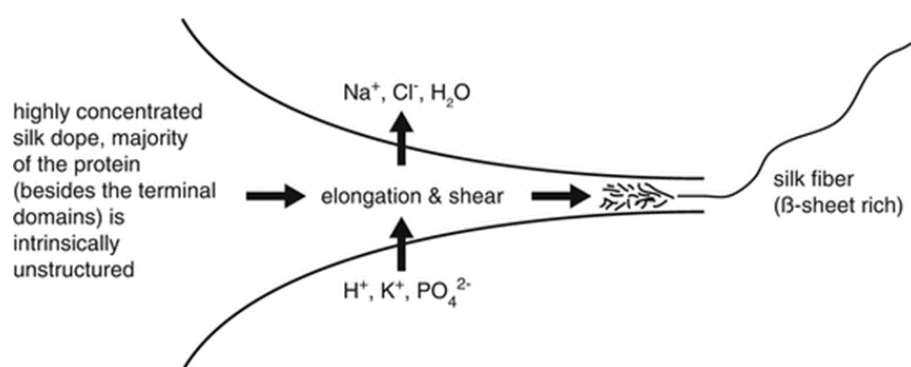


Figure 5: Schematic overview of the parameters critical for the natural spinning process of silk. During this process, the pH is reduced, phosphate and potassium ions are pumped into the silk dope, while water and chloride are extracted from the dope. Mechanical stress induces the formation of a silk fibre with high  $\beta$ -sheet content. (Reproduced with permission from<sup>52</sup>)

#### 2.4.1. Criteria for fibre formation

To facilitate the silk I to silk II transition in ambient conditions, during the evolution of silk spinning, natural selection has overcome several challenges through remarkable adaptation of the protein's solution chemistry, viscosity and the silk duct anatomy to allow optimal spinning conditions <sup>12,53</sup>.

During the final stage of silk spinning, the silk is pulled from the spinneret into the air to allow cocoon formation <sup>53</sup>. The viscosity of the silk solution is an important parameter, which contributes to the formation of a continuing fibre. In a low viscosity stream, the surface tension of the water and the air may result in capillary breakup meaning that the solution breaks into droplets instead of forming a fibre <sup>12</sup>. Due to the fact that in biological systems a rapid fibre formation is required <sup>46</sup>, the viscosity of the silk solution is usually high (in the kPa range for silkworm <sup>54</sup>). This allows to avoid capillary breakup and to spin a whole cocoon from a single fibre of silk.

The fibroin solution in the duct can have a concentration of up to 40 wt.% <sup>55</sup>. Due to this high concentration and viscosity, an extremely high force is required to allow flow along the duct and to produce fibres with a micro-scale diameter <sup>53</sup>. To overcome this limitation and reduce the force required to initiate flow, the silk duct has been suggested to be in the form of liquid crystals (mesogens) <sup>51,56,57</sup>. Asakura *et al.* <sup>51</sup> observed by polarised light that silk is organised in a liquid crystal nematic phase. When organised in this phase, the fibroin molecules (which have a rod-like shape), self-assemble across their long axis in parallel to each other, forming complex aligned patterns <sup>56</sup>. This structure of the fibroin forms highly-concentrated ordered solution at liquid crystalline state (mesophase) while maintaining its liquid-like properties. As a result, the friction between the molecules in the solution is reduced, and a lower energy



threshold is required to induce flow <sup>57</sup>. Those properties, together with precise control over the pH, ionic competition and water content in the dope, allows to maintain solubility and prevent premature solidification of the silk in the spinning dope <sup>58</sup>. In addition, the silk molecular arrangement, along the long axis of the silk gland, prevents the formation of dislocations in the silk, contributing to the tensile strength of the fibre <sup>59,60</sup>.

As described above, silk fibres are produced in a biological system under ambient conditions, from a concentrated protein solution. Many applications utilise the naturally produced silk and reprocess it back into protein solution, to allow a broader range of applications <sup>22</sup>. To gain control over the quality and structure of the native silk, it is important to first understand the process of transition from liquid solution (in the silk gland) to solid fibre structure (in the cocoon). This process is called gelation and will be further explained below.

### 3. The process of sol-gel transition (gelation)

The process of gelation is defined as the transition from a solution containing a soluble polymer (sol) to cross-linked polymer network (gel). The critical point of transition, 'gel-point' is defined as the point where the gel structure appears<sup>61</sup>. The gel can be either chemically or physically cross-linked. Chemical gelation can be achieved by the addition of precipitating agents such as salts and organic solvents to the sol, by modification of the sol's pH, or by the addition of crosslinking agents. During the chemical gelation process, covalent bonds are formed between the chains resulting in a strong irreversible gel. Physical gelation is usually achieved by applying mechanical shear, temperature alteration, sonication or with electrical fields. Physical gels can have strong physical bonds (strong gel) or temporary reversible links between the chains (weak gel)<sup>62</sup>.

#### 3.1. Sol-gel transition in silk fibroin solution

Silk fibroin can undergo liquid-to-solid transition following shear, exposure to solvents, water evaporation and temperature variation<sup>12</sup>. The stability of the gel is achieved due to a physical crosslinking in the gel as a result of irreversible  $\beta$ -sheet structure formation<sup>63-65</sup>. The process of sol-gel transition in silk fibroin was studied in details by Matsumoto *et al.*<sup>66</sup> in diluted fibroin solutions, evaluating the secondary structural (by FTIR) and measuring the turbidity of the solution (by circular dichroism), following variations in concentration, temperature and pH.

#### 3.2. Evaluation of silk gelation

When gelled, silk fibroin exhibits a white opaque colour when compared to the transparent silk solution. This change in solution transparency is a result of light scattering from the

heterogeneous structure of the fibroin gel and can be used to track the gelation process by recording the circular dichroism spectra of the sample <sup>67</sup> and by UV-vis spectroscopy <sup>64</sup>.

The first stage in silk gelation involves the formation of small protein precipitates which gradually increase in size when the gelation process progress. When the aggregates are large and immobile enough, they can interact to form a stable fibroin network. During this process, a variation in the optical density can be recorded providing information about the gelation rate <sup>66</sup>. The variation is attributed to the formation of  $\beta$ -sheet structures in the gel <sup>68</sup>. When the gelation is completed, the optical density of the sample remains stable, and its value depends on the initial fibroin concentration and solution temperature.

### 3.3. Silk gelation dependence on concentration and temperature

It was repeatedly shown in the literature that temperature increase from room temperature to 37°C is leading to higher gelation rates while a decrease in gelation rates can be related to an increase in the fibroin solution concentration <sup>28,66,69</sup> (Figure 6a, adapted from Ref. <sup>66</sup>).

One possible explanation can be associated to the dynamic hydrophobic hydration mechanism <sup>64</sup>. Similar phenomena can be seen in other polymers, in which the balance between the hydrophobic and the hydrophilic groups can be adjusted, such as elastin-like peptides <sup>70</sup> and silk-elastin-like polymers <sup>71</sup>. In those polymers, reversible phase separation with temperature variation was recorded, resulting in higher polymer solubility at low temperatures. When the temperature is low, the hydrophobic groups of the polymer are surrounded by ordered water molecules which are arranged in ice-like crystal structure <sup>72</sup>. When the temperature increases, phase separation occurs leading to protein folding <sup>73</sup>. This process is usually reversible in synthetic polymers <sup>70,74</sup>. However, in silk, this dehydration process is leading to irreversible thermodynamically stable secondary structure <sup>75</sup>.

### 3.3.1. The secondary structure of fibroin during gelation.

When the silk is at a sol-state (as stored in the silk gland), the  $\beta$ -sheet content is about 20% <sup>66</sup>. At the first stage of gelation, there is no variation in the  $\beta$ -sheet content until the gelation level reaches 15-20% gel. With the progression of the gelation process, a gradual increase in  $\beta$ -sheet content occurs, reaching a value of 50% in a fully gelled sample <sup>66</sup>. This delayed structural conversion is a result of the initial gelation stages. During these stages initial inter and intra-molecular hydrophobic interactions are formed. These hydrophobic interactions allow the re-organisation of closely packed molecules in relation to each other, leading to the formation of  $\beta$ -sheet structure at a later stage. Hydrogen bonds and electrostatic interaction can also be present during the gelation but have a smaller influence on secondary structure formation.

### 3.3.2. The effect of pH on fibroin gelation time and secondary structure.

In *B. mori* fibroin, the N-terminus of the heavy chain consists of large, negatively charged hydrophilic domains with acidic amino acids, having a predicted isoelectric point (PI) of 4.59 <sup>66</sup>. In contrast, the C-terminus is positively charged with hydrophilic domains and a predicted PI of 10.53 <sup>66</sup>. Therefore, the process of silk gelation is strongly dependent on the pH of the solution. Matsumoto *et al.* <sup>66</sup> determined that the strongest effect on the gelation rate of the fibroin solution was when the pH was at the range between 4 - 6 and between 9 - 10.5.

When the pH is reduced below 6, the carboxylic groups including glutamic and aspartic acids, are neutralised, reducing hydrophilicity and charge repulsion. Therefore, hydrophobic interactions are promoted, leading to a physical cross-link of the fibroin molecules. Even though at this pH range, the basic groups are fully charged and available for electrostatic interactions with the carboxylic group, the process is dominated by the hydrophobic

interactions due to their larger domain size<sup>45</sup>. Increasing the pH above 9 will result in neutralisation of the basic side groups (while the acidic side groups are charged), leading to a decrease in electrostatic interactions and increase in gelation time. At the neutral pH range, between 6 and 9, both side groups are charged. The electrostatic interaction between the side groups stabilise the structure and increase the probability for fibroin chain interactions, decreasing the gelation time. The effect of the pH on gelation time of diluted reconstituted silk solution can be seen in Figure 6b (adapted from<sup>66</sup>). Schematic illustrations of the gelation model (Figure 7a) and the pH-dependent fibroin interchain interactions (Figure 7b) are adapted from Matsumoto *et al.*<sup>66</sup> and presented below.

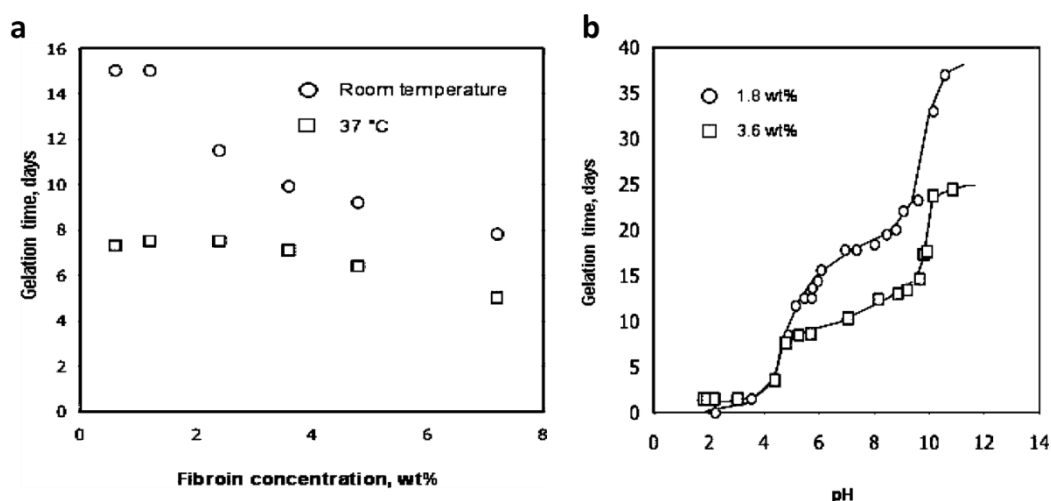


Figure 6: (a) Concentration-dependent fibroin gelation time at (○) room temperature and (□) 37 °C. (b) Relationships between initial solution pH and gelation time at room temperature for (○) 1.8 and (□) 3.6 wt. % (adapted with permission from<sup>66</sup>).

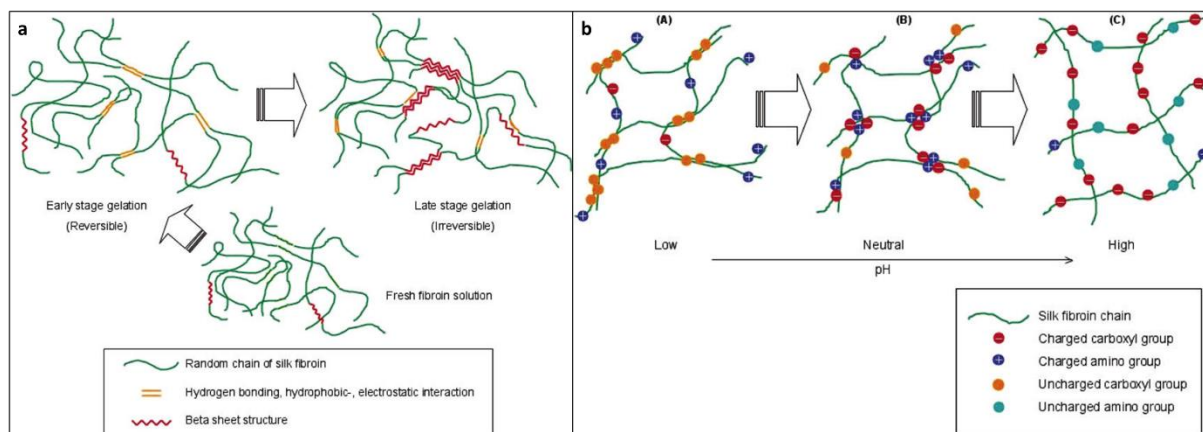


Figure 7: (a) Schematic illustration of pre-gelation and early and late stages of fibroin gelation, a three-stage model. A fresh solution (pre-gelation) has about 20% content of  $\beta$ -sheet structures with negligible intermolecular bindings. Gelation is initially induced by weaker interchain interactions (no  $\beta$ -sheet forming) such as hydrogen bonding, hydrophobic interactions, and electrostatic interactions; and stable  $\beta$ -sheet structures cure in the third phase resulting in stable and essentially irreversible intermolecular structures. (b) Schematic illustration of pH-dependent fibroin interchain interactions at the early stage of gelation. For simplification, the number ratio of (positive and negative) charges does not represent the actual sequence. At low pH (A), strong interchain aggregation is induced due to increasing hydrophobicity of the uncharged carboxyl group (rapid gelation). At neutral pH (B), there is an increasing effect of electrostatic interactions due to the increased number of counterions (relatively rapid gelation). At high pH (C), the interaction is weaker due to increased hydrophilicity of the charged carboxyl group as well as reduced electrostatic interactions (slow gelation) (adapted with permission from <sup>66</sup>).

### 3.3.3. The effect of solvents and salts on *B. mori* silk

Silk properties can be modified by a broad range of solvents dependent on solvents' polarity <sup>22,66,76,77</sup>. This is due to conformational sensitive regions in the silk microstructure <sup>6,78</sup>. One of the main solvents used in silk research and processing is water <sup>79</sup>. In fact, when exposed to water, spider dragline silk can undergo supercontraction <sup>76,80</sup>, resulting in fibre shrinkage of up to 50% of its original length. The rate of contraction can be related to the amorphous molecular structure of the silk which undergoes reversible disruption in the presence of water <sup>81,82</sup>. When a higher proportion of amorphous structure is present in the silk (e.g. fibres that were artificially reeled at high speed), a higher level of contraction occurs <sup>83,84</sup>.

In contrary to spider silk, silkworm silk does not supercontract. However, it is still affected by water. Water immersion can weaken the silk fibre and therefore can be used as an alternative approach for silk degumming, reducing protein degradation caused by chemical degumming<sup>85,86</sup>. Dehydrating solvent such as acetone and methanol increase *B. mori* silk stiffness by increasing its crystallinity<sup>87,88</sup>.

Im *et al.*<sup>64</sup> discovered that silk gelation is induced by the presence of nitrate salts. The salt can stimulate the formation of tyrosine radicals and generate nitro-tyrosine and di-tyrosine bonds, leading to silk-gelation. Boiling of the silk in salt solutions can damage the fibre when highly chaotropic agents are used such as concentrated solutions of metal salts<sup>49</sup>, halogenated alcohols<sup>89</sup> or strong acids<sup>90</sup>. These solvents can interact with the crystalline domain breaking the amide-amide hydrogen bonds which results in partial or full fibre degradation. This silk breakdown is used in the process of silk reconstitution, to produce silk solution by converting the silk proteins to their unspun state<sup>86,91</sup>.

### 3.4. The rheological behaviour of *B. mori* silk

Rheology measurements are used to evaluate sample deformation during flow<sup>92,93</sup>. The physical principles of this technique will be described in the methodology chapter of this thesis. When dealing with silk rheology, most of the current literature is focused on reconstituted silks due to the broad industrial and scientific interest in this material<sup>22,94,95</sup>. However, there are fundamental differences in the rheological properties between the reconstituted and native materials. While reconstituted silk appearing to be a Newtonian fluid, the diluted native silk shows a Non-Newtonian behaviour<sup>96,97</sup>.

The rheological properties of *B. mori* native silks<sup>54,55,69,98</sup>, as well as reconstituted silk<sup>94,99,100</sup>, have been investigated in the literature. *B. mori* silks present significant viscoelasticity. This is

seen by the fact that the values of the elastic or storage modulus ( $G'$ ) exceed the viscous or loss modulus ( $G''$ ) at high frequency and cross-over to viscous behaviour ( $G' < G''$ ) at low frequency<sup>55,69</sup>. This rheological characteristic can be seen in other concentrated polymer solutions in which interchain entanglements are dominating the rheology of the sample<sup>93,101,102</sup>. Recently, Laity and Holland<sup>55</sup> provided detailed rheological characteristics of the native *B. mori* silk protein by investigating a statistically meaningful population of 124 silkworms exploring the combinations of shear and oscillatory measurements to gain information about the molecular relaxation behaviour and chain entanglements of the silk.

#### 3.4.1. Shear viscosity of native silk

The apparent viscosity of the native silk dope can vary between 50 - 6000 Pa·s<sup>98</sup>. This viscosity variation has no obvious correlations between the physical condition of the silkworm or storage times. As previously reported by Holland *et al.*<sup>103</sup>, the viscosity ( $\eta$ ) of native *B. mori* silk protein, as expected for a polymer solution in the 'semi-dilute' concentration range<sup>93</sup>, is dependent on the concentration ( $c$ ) as follow:

$$\eta \propto C^2$$

However, this correlation was not confirmed when a large population was analysed (Figure 8, adapted from Ref.<sup>55</sup>), suggesting that other factors can affect the viscosity of the silk protein apart from the concentration.

Additional parameters that should be considered is the molecular weight of the polymer. When the concentration of the polymer solution is above the entanglement threshold, the viscosity dependence on molecular weight ( $M_w$ ) is given by<sup>93,101,102</sup>:

$$\eta \propto M_w^{3.4}$$

It was observed by Manning and Gage<sup>104</sup> that due to polymorphism in the silk fibroin genes in different inbred stocks of *B. mori*, a range of fibroin proteins was produced with molecular



variations between 410 kDa (longest) and 350 kDa (shortest). However, in a recent paper by Laity *et al.*  $M_w$  variation was discredited as a significant influence of native silk rheology<sup>105</sup>. Additional variation in the  $M_w$  of the silk solution, resulting in viscosity variations, can be related to the presence of supplementary species in addition to the fibroin, which are present in the silk gland and affect the  $M_w$  distribution of the dope<sup>106–108</sup>. It was also reported, by Laity *et al.*, that silk solution viscosity is also related of interchain interactions which can be affected by pH and variations in the ion content of the solution (e.g. calcium and potassium concentration)<sup>105</sup>.

### 3.4.2. Viscoelastic behaviour of native silk

In the same work of Laity and Holland<sup>55</sup>, oscillatory sweeps measurement, performed at room temperature, indicated that *B. mori* native silk had similar rheological behaviour to that of a concentrated polymeric solution, in which entanglements constrain the rate of molecular relaxations in response to the applied oscillating strain<sup>102</sup>. In general, when the elastic and viscous moduli plotted against angular frequency ( $\omega$ ) two distinct regions can be observed<sup>54,55,69,98</sup>:

At higher frequencies:  $G' > G''$ , meaning that the applied oscillations were faster than the dominant molecular relaxation process.

At low frequencies:  $G' < G''$ , meaning that the applied oscillations were slower than the dominant molecular relaxation process.

A typical oscillatory sweep figure of native silk dope is presented in Figure 8b (reproduced from<sup>55</sup>) The cross-over frequency indicates the separation between solid-like and liquid-like behaviour and provides an indication of the overall relaxation rate of the specimen. The main values for the frequency ( $5.6 \pm 2.5 \text{ Rad}\cdot\text{s}^{-1}$ ) and the modulus ( $3338 \pm 66 \text{ Pa}$ ) at the cross-over

point found by Laity *et al.* were in agreement with those previously reported by Terry *et al.*<sup>97</sup> and Holland *et al.*<sup>47,54,103</sup>.

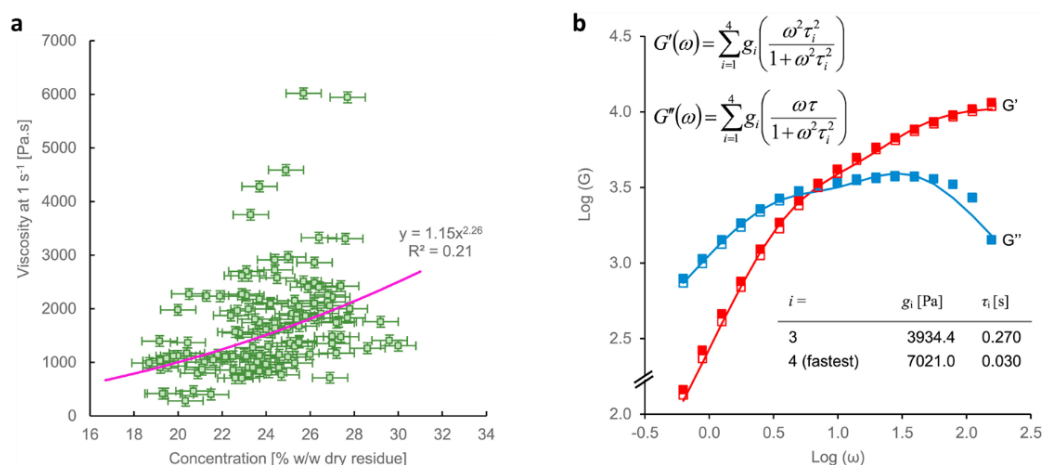


Figure 8: (a) Plot of shear viscosity at  $\dot{\gamma} = 1 \text{ s}^{-1}$  against silk protein concentration (% w/w dry residue); the continuous line represents the best fit power-law relationship. The horizontal error bars represent  $\pm 1\%$  w/w, the vertical error bars ( $\pm 100 \text{ Pa}\cdot\text{s}$ ) are expected to be considerably larger than the actual uncertainty in viscosity measurements. (b) Plots of elastic and viscous moduli vs. angular frequency, for native silk protein solution at 25 °C; the filled and open symbols represent duplicate measurements on the same specimen, before and after the stress relaxation measurements. The continuous lines represent the best fits to  $G'$  and  $G''$  data using the binary model described by the equations, using the parameters shown (reproduced with permission from<sup>55</sup>).

## 4. Applications of silk

Silks have been used for millennia in textile and medicine, mostly in the form of fibres obtained by unreeling *B. mori* cocoons<sup>23</sup>. Despite the impressive mechanical properties and appealing appearance of the fibres, silk's application range was mostly limited to threads and woven mats<sup>24</sup>. Manipulations before or during the spinning process can highly affect the final fibre properties and help to match them to the desired application<sup>14</sup>. Such manipulations might include control over silkworm nutrition<sup>109,110</sup>, climate<sup>111</sup> or via genetic engineering<sup>112-114</sup> which will result in modified protein solution in the silk dope leading to adjusted fibre quality. An alternative method to modify fibre properties has been to manipulate the spinning process. This can be achieved by forced reeling of the silkworm using a spinning apparatus in a controlled environment and subsequent post-processing of the fibres<sup>14</sup>. However, the use of fibres is limited and do not allow sufficient customisation of the structure and geometry to adapt to the constantly growing demand for natural materials based applications<sup>22</sup>.

### 4.1. Fabrication of silk structures

Due to the broad use of silk over many centuries, the production of silkworm cocoons, known as sericulture, produces larvae with proportionally larger glands in comparison to their wild silkworm relatives leading to high yields of silk fibres. In fact, 400,000 tons of dry silkworm cocoons are available annually worldwide for textile and other industries<sup>115</sup>. The last century of silk research introduced the process of silk reconstitution which allows the dissolution of the solid silk into the "unspun" fibroin solution state<sup>22</sup>. The dissolved fibre can be reprocessed and solidify, *ex vivo*, into desired material formats and structures. This process allows extensive control over the properties of the fabricated structures which can be achieved by denaturation and dehydration of the silk proteins under pre-designed and controlled

experimental conditions. Those processes allow replicating, in part, some of the hierarchical structuring of the original fibre mentioned in previous sections. This process has opened the door to an almost unlimited range of processing possibilities and utilisation of various fabrication techniques to generate many structures and geometries in 2D and 3D<sup>22,23</sup> for a broad range of applications.

Figure 9 summarises selected key publications presenting reconstituted silk patterns as received by various fabrication techniques described above.

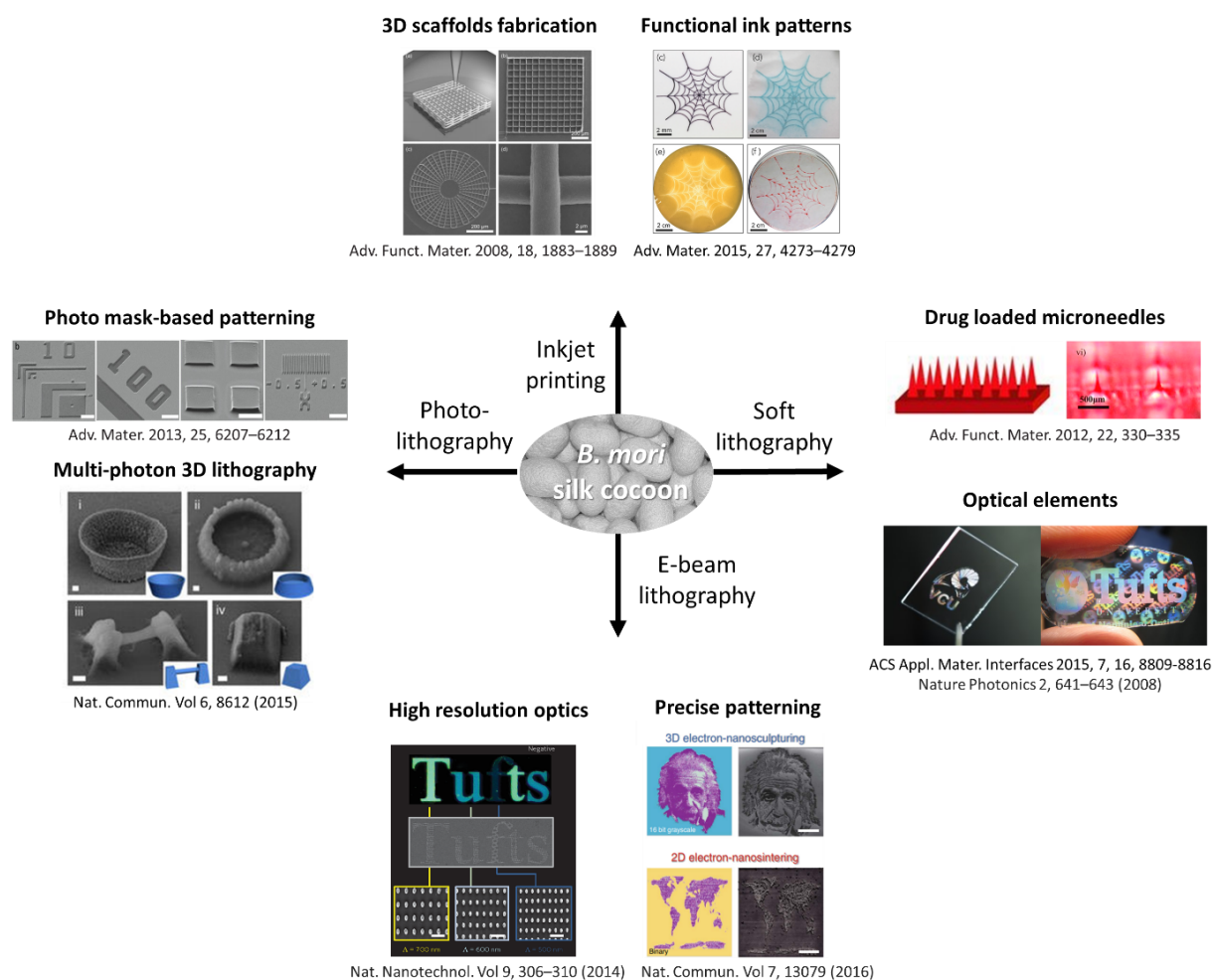


Figure 9: Key literature examples of patterns made from reconstituted silk by various fabrication methods including: soft lithography (right), E-beam lithography (bottom), photolithography (left) and inkjet printing (top) (all images reproduced with permission, sources indicated below the images).

#### 4.1.1. Films

Silk films can be used in a broad range of applications since they can be produced easily by casting them on the desired surface and drying <sup>116</sup>. Applications of polymeric films include coatings <sup>117</sup>, membranes <sup>118</sup>, lenses <sup>119</sup> and tissue replacement such as skin grafts <sup>120</sup> and cornea <sup>121</sup>. When compared to the solid crystalline silk fibre, silk fibroin solution is mostly amorphous <sup>29</sup>. The amorphous nature of the protein is maintained during some solidifying processes such as drying and photo-curing resulting in transparent films <sup>121,122</sup>. In fact, the fibroin possesses near-perfect transparency in the visible light spectrum <sup>123</sup>. Casting the fibroin solution onto smooth or rough surfaces allows the fabrication of patterned transparent silk films ideal for optical applications such as lenses <sup>119</sup>, fibre optics <sup>124</sup>, and substrates for electro-optical devices <sup>125,126</sup>. This transparency is also beneficial for applications such as coatings for food and drugs <sup>117</sup>.

In the last decade, a pioneering approach of light-based fabrication was introduced to fabricated complex transparent patterns on films such as holograms and barcodes (chapter 4 in this thesis).

#### 4.1.2. Gels and hydrogels

Gels are a substantially diluted three-dimensional cross-linked systems composed of liquid particles which are dispersed in a solid medium <sup>127</sup>. The rate of the crosslinking, the rheological properties, and the hydrogel water content can be controlled mainly by the pH level, protein concentration, temperature and the number of calcium ions in the solution <sup>55</sup>. Gels present solid like behaviour and do not flow in an equilibrium state. Hydrogels comprise of a hydrophilic crosslinked polymer chains with sufficient structural integrity to prevent dissolution in water <sup>128</sup>. The hydrophilic nature of the hydrogels makes them highly water

absorbing, with a water content of up to 90% <sup>129</sup>, which makes them suitable for the fabrication of hydrogels for medical (*e.g.* cornea, cartilage) <sup>121,130</sup> or sensing (*e.g.* humidity, temperature sensors) applications <sup>131</sup>.

#### 4.1.3. Foams and scaffolds

Foams are solid materials with a substantial amount of gas (most often) pockets embedded into liquid or solid matrix <sup>132</sup>. They are extensively used in many engineering applications due to their significantly lower weight than the bulk material (without major compromising on the mechanical properties) and their large internal surface area <sup>133,134</sup>.

Silk foams, sponges and scaffolds with various porosity and geometries on the micro and macro scale can be formed using porogens (salt or sugar), gas foaming and lyophilisation <sup>135</sup>. The porosity of the silk scaffolds can be controlled by choosing the porogen size or combining different porogens in the process <sup>136</sup>. When used for biomaterials applications, by controlling the porosity, it is possible to control cell attachment, mechanical properties and the overall scaffold degradation rate <sup>134,135</sup>. A novel method for foam fabrication using emulsion templating technique will be discussed in chapter 5 of this thesis.

#### 4.1.4. Fibres

As discussed previously, due to the rheological properties of the silk solution including high viscosity and the ability to gel when shear is applied <sup>55,69</sup>, silk fibres can be artificially drawn from concentrated silk solution by applying suitable shear force using various methods including wet/dry spinning techniques (hand/machine drawing or filament stretching), extrusion and electrospinning <sup>14</sup>.

## 4.2. Current limitations in silk processing

Despite the fact that the reconstituted silk solution has exceptionally broad processing potential, it has limitations in some applications resulting from the production process of the solution <sup>22</sup>. In order to transform the solid silk cocoon into a liquid solution, two major processing stages are currently used: Firstly, the cocoon is boiled in a nitrate salt solution to remove the sericin coating in a process known as silk degumming <sup>86</sup>. The presence of sericin might reduce the biocompatibility of the silk <sup>115,137</sup> and therefore only the fibroin component of silk is usually used for medical applications. Secondly, the solid degummed silk is dissolved in lithium bromide solution, in a process known as silk dissolution <sup>138,139</sup>. Finally, a purified reconstituted silk fibroin solution is created after filtration and dialysis. Due to the fact that nitrate salts are used in the process, and the cocoons are boiled at high temperature, it results in significant degradation of the fibroin's molecular weight when compared to the native dope solution in the spinning dope <sup>103</sup>. This directly affects the properties of the fabricated structures and limits the current application range <sup>91</sup>.

An alternative approach, as presented in this work, utilises native silk fibroin, extracted directly from the spinning dope for the fabrication of silk structures. By using the gold standard, native silk <sup>98</sup>, it is hoped that any protein degradation is avoided, improving structural properties and broadening the potential range of applications.

Figure 10 presents the different structures fabricated in this work from native and reconstituted silk solutions. The fabrication methods are discussed in next chapters as follows: Gels and hydrogels (chapter 4,5), foams and scaffolds (chapter 5), films (chapter 4), fibres (chapter 3,5).

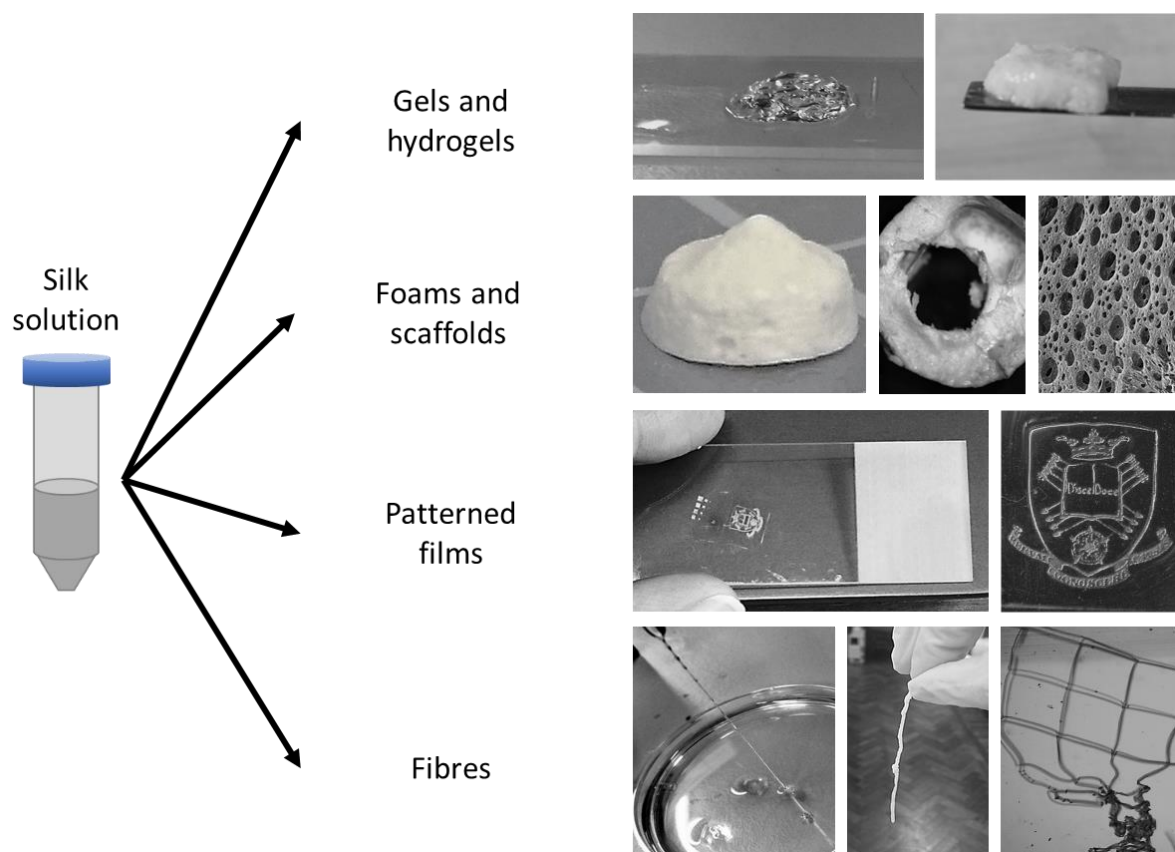


Figure 10: Variable silk structures that were fabricated from native and reconstituted silk solutions: Gels and hydrogels, foams and scaffolds, patterned films and fibres.

#### 4.3. Biocompatibility of *B. mori* silk

The biocompatibility of the silk fibroin protein has been extensively evaluated<sup>140–142</sup>. Many tissue engineering approaches, such as corneal tissue regeneration, using acellular allograft tissues from an animal source, which establishes potential bioburden formation<sup>143</sup>. Reconstituted silk fibroin has been shown to have reduced bioburden content<sup>24</sup>, however still offering the potential of acellular implantation for native tissue regeneration<sup>24</sup>. Due to the presence of  $\beta$ -sheet structure, silks have relatively slow degradation rate *in vitro* and *in vivo*, when compared to collagens and other biopolymers<sup>144,145</sup>. This makes the use of silk, advantageous in compared to most natural or synthetic polymers.



#### 4.3.1. Bio-degradation

Biodegradable material is defined by the US Pharmacopeia <sup>146</sup> as a material that loses the most of its tensile strength within 60 days *in vivo*. According to that definition, silk is classified as non-biodegradable. However, silk literature shows that silk undergoes long-term degradation *in vivo* following foreign body response <sup>147,148</sup>. Long-term degradation *in vivo* indicates that silk implants lost most of their tensile strength after 1 year *in vivo*, were unrecognisable after 2 years in the implantation site <sup>149–151</sup>. The degradation rate of synthetic polymers such as poly (lactic acid) (PLA), poly (glycolic acid) (PGA), and PLGA is based on the polyester composition, purity, and processing conditions and is usually controlled by adjusting the polymer composition by choosing polymers with different degradation rates or by modifying the molecular weight of the polymer <sup>152</sup>. Some disadvantages of synthetic polymers are that they might decrease local pH and induce inflammation, during the degradation process <sup>153</sup>.

The degradation process of natural polymers is largely driven by proteases <sup>145</sup>. Usually, the rate of the degradation is altered by the degree of the crosslinking in the polymer. In collagen, crosslinking can also reduce immunogenicity <sup>154</sup>. The rate is also depending on the structure, morphology, and the mechanical and biological conditions at the implantation site. The bio-products of such degradation are peptides and amino acids. The degradation process of silk scaffolds, films and fibres is usually explored by several types of proteases, including  $\alpha$ -chymotrypsin and collagenases <sup>144,145,155</sup>.

The degradation rate of silk fibroin films was extensively explored by Arai *et al.* <sup>144</sup> The weight loss of the films after enzymatic degradation is summarised in Table 2. In addition to the

weight loss, reduction in the average molecular weight, increase in the crystallinity level and a decrease of tensile properties of silk were observed following the degradation.

*Table 2: Weight loss of silk fibroin films. Enzyme-to-substrate ratio: (a) 1:20; (b) 1:8. (reproduced with permission from <sup>144</sup>)*

Degradation time (days)	Weight loss (%)					
	Collagenase		α-Chymotrypsin		Protease	
	(a)	(b)	(a)	(b)	(a)	(b)
<b>1</b>	2.6	3.8	6.0	9.0	18.2	35.0
<b>3</b>	4.1	5.5	9.2	11.8	27.4	45.5
<b>10</b>	7.4	8.9	13.0	14.9	35.7	55.6
<b>17</b>	9.4	10.7	14.7	16.5	45.5	64.3

The degradation rate of reconstituted silk porous sponges fabricated from depends upon the processing conditions <sup>136</sup>. When exposed to protease, silk sponges fabricated in wet environment from high-concentration silk solutions, degraded slowly that the ones fabricated from solutions with lower concentration. However solvent-processed scaffolds degraded slower than the aqueous-processed scaffolds with similar porosity. Those scaffolds kept 65% of their mass after 21 days, in compared to aqueous-based sponges, which fully degraded after 4 days. This difference can be attributed to the difference in silk crystallinity between the samples.

#### 4.3.2. Immunological responses

When investigating a material's biocompatibility, the immunological reaction should be explored. Virgin silk sutures showed the difference in hypersensitivity (undesirable reactions produced by the normal immune system) when compared to sutures made from degummed silk <sup>23</sup>. When the inflammatory response was compared *in vitro* between degummed silk and polystyrene and poly(2-hydroxyethyl methacrylate), less adhesion of immuno-competent cells was recorded on the silk <sup>156</sup>. In fact, silk films had a lower inflammatory response than

collagen and PLA films<sup>157</sup> Non-woven silk fibroin mats induced a weak foreign body response and no fibrosis when implanted subcutaneously in rats<sup>158</sup>. It was suggested in the literature that sericin can cause hypersensitivity<sup>23</sup> however, sericin has been used to increase cell proliferation and attachment of skin fibroblasts, T-lymphocytes and hybridomas<sup>159,160</sup>.

#### 4.3.3. Suitability for sterilisation

There are versatile options for silk sterilisation including autoclaving, ethylene oxide<sup>23</sup>,  $\gamma$ -radiation, 70% ethanol<sup>161,162</sup>, or UV light (used in this work). When sterilised by autoclaving, no change in morphology or  $\beta$ -sheet structure was observed at 120°C<sup>163,164</sup>. This makes silk more stable than collagen, which denatures at these temperatures<sup>165</sup>.

The silk patterns produced in this work were non-converted. Therefore, most of the common sterilisation methods are unsuitable for silk pattern sterilisation and can induce structural conversion influencing silk properties, failing to represent the real hydrogel structure. Therefore, UV illumination was selected for sterilisation<sup>166</sup> prior to cell seeding experiments.

#### 4.4. Silk-based structures for tissue engineering applications

The broad processing options for the silk fibroin together with its biocompatibility<sup>140</sup>, biodegradability<sup>145</sup> and the ability to support cell attachment and to encourage cell proliferation<sup>120</sup> makes silk a suitable candidate for tissue engineering and implants. In the last decade, silk has been used in most fields of tissue engineering utilising various fabrication methods and structural designs<sup>120</sup>. Silk fibres can be used as sutures or as a replacement for ligaments<sup>167</sup>. Non-woven silk mats produced by electrospinning have shown to guide the formation of vascularised reticular connective tissue<sup>158</sup>. In addition, the mats have shown to induce attachment and proliferation of endothelial cells<sup>168</sup>. Silk films designed to replace skin

and tissues <sup>169</sup> can be used as wound dressings <sup>170</sup> and can also improve bone formation <sup>171</sup>, especially when coupled with growth factors <sup>162,172</sup>, and they also have potential as artificial corneal implants <sup>121,122</sup>. Hydrogels are often used for bone and cartilage repair <sup>173</sup>. When injected into a defect in the femoral bone in rabbits, silk hydrogels have been shown to encourage a high rate of bone formation <sup>174</sup>. Porous scaffolds, broadly used in tissue engineering, can encourage cell attachment, migration, proliferation and promote nutrient and waste transport <sup>120</sup>. Silk foams are used to replace bone defects and were shown to induce bone tissue formation <sup>175</sup> as well as being effective in cartilage engineering, inducing chondrocytes proliferation <sup>176</sup>. Silk tubes can act as a platform for nerve restoration <sup>177,178</sup> blood vessels replacement <sup>169</sup>, engineering of tracheal scaffolds <sup>179,180</sup> and more <sup>142</sup>. The number of silk-based tissue engineering publications annually is constantly increasing and has doubled in the past 5 years with the introduction of new fabrication techniques such as photolithography and 3D printing (Figure 11a).

Among all the silk-based tissue scaffolds currently under testing, bone is the most heavily researched application for clinical use, occupying 40% of the total publications in the field (Figure 11b). This can be attributed to the large market share of bone implants and driven by the osteoconductive properties of the silk which encourage osteoblasts proliferation and the formation of new bone tissue when bone regeneration is required such as areas with bone defects or fractures <sup>181</sup>. This is possible due to the mechanical properties of silk-based scaffolds (which are similar that of cancellous bone <sup>181</sup>), the ability to produce scaffolds with high porosity and interconnectivity (to allow cell penetration into the scaffold <sup>182</sup>) and the biodegradation rate (which can be adjusted to fit the bone regeneration rate) <sup>183</sup>. This can also be a result of the large market potential of bone-based biomaterials and the relative simplicity of their structure.

However, the mechanical properties of all current silk scaffolds are still inferior to that of a cortical bone and are not sufficient to act as a load bearing bone substitute <sup>181</sup>.

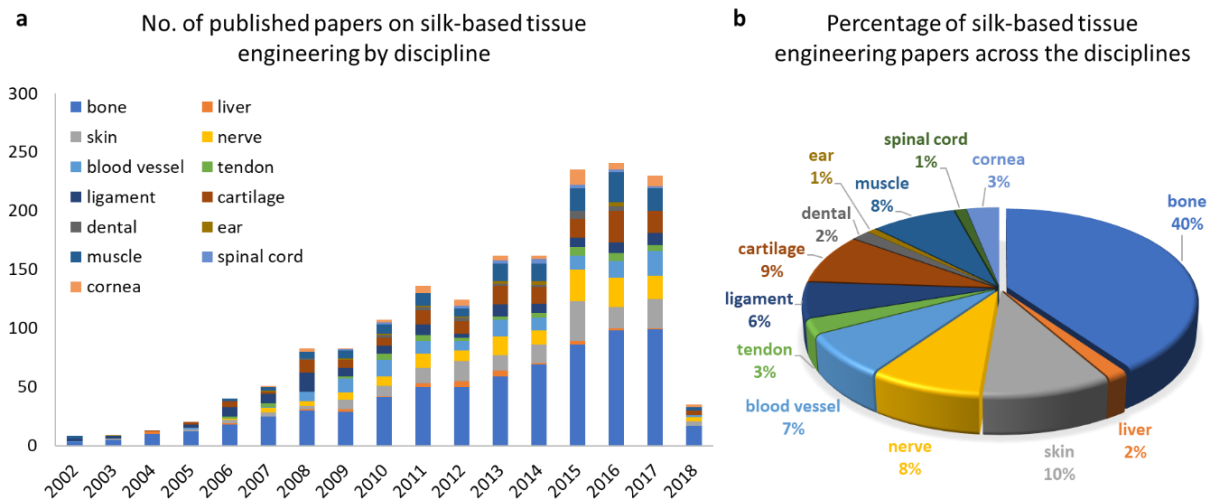


Figure 11: (a) Published papers using silk-based scaffolds for tissue engineering applications by discipline. (b) Distribution, in percentage, of the silk-based tissue engineering papers across different disciplines. Data collected from Scopus, Feb 2018.

## 5. Introducing surface patterns to proteins

Soft matter such as proteins can gain increased functionality and broader application ranges by introducing surface topographies in a controlled and precise manner <sup>184</sup>. It is especially beneficial when designing bio-sensors, applications in cell biology and tissue engineering <sup>185</sup>. Protein solutions can be patterned using several fabrication techniques.

### 5.1. Soft-lithography of proteins

Soft-lithography, one of the most common processes to generate polymer surface topography, is a technique based on structure replication, from a pre-fabricated elastomeric stamp or mould, most commonly made from polydimethylsiloxane (PDMS) <sup>186</sup>. A wide range of pattern designs and geometries can be fabricated by casting a liquid polymeric solution on the mould and removing it after solidification. Some benefits of soft-lithography include its low cost since no specialised equipment is required. This room temperature process is suitable for patterning of biological and heat sensitive materials and allows the incorporation of drugs and living cells <sup>123,187</sup>. No chemical modifications and photo-reactive dyes are required however in some cases photo-sensitive dyes are added to the polymer to allow rapid solidification in the mould <sup>188</sup>. Key applications of soft-lithography include the fabrication of optical patterns on protein surfaces <sup>123</sup>, introducing channels in micro-fluidics devices <sup>189</sup>, creating desired architectures for cells guidance and alignment <sup>190</sup>, generating surface functionality to control chemical reactions, guiding crystallisation <sup>191</sup> and many more.

#### 5.1.1. Soft-lithography of silk

Silk is a suitable candidate for soft-lithography processing due to its mechanical properties and various solidification methods available to produce patterning in ambient conditions <sup>55</sup>.

In addition, silk can be chemically modified or mixed with photo-responsive dyes to allow accelerated photo-curing in the mould <sup>192</sup>. This technique allows researchers to fabricate silk films with complex topographies and designs such as drug-loaded micro-needles patches (for control drug release) <sup>187</sup> and optical films with light diffraction properties generated by the fine patterns on the film <sup>193,194</sup>. The addition of various polymers (*e.g.* Polydiacetylene (PDA)<sup>195</sup>, poly(vinyl alcohol) (PVA)<sup>196</sup>, Polyethylene glycol (PEG)<sup>197</sup>) allows the tuning of the mechanical properties of the silk complexes and the fabrication of 3D functional structures <sup>195</sup>.

Despite the broad variety of publications on silk-based soft-lithography, this method requires pre-preparation of the mould, which strongly limits the design flexibility and does not allow in-situ modifications. The process is time consuming and usually require hours to allow full crosslinking or even days when freeze drying is used for the solidification <sup>119,121,187</sup>.

## 5.2. Electron-beam lithography of proteins

A common technique for ultrahigh-resolution patterning is electron-beam (e-beam) lithography often used for complex pattern writing for many scientific and industrial applications <sup>198</sup>. E-beam systems can be integrated into a scanning electron-microscope (SEM) which allow the fabrication of pattern at a resolution lower than 10 nm. The maximum obtained resolution is dependent on the beam current, which defines the number of electrons impinging on the sample each second. High current beam is usually physically larger than a small current electron beam. Typically, the current range for high-resolution patterning is 0.05 to 0.5 pA <sup>199</sup>.

In e-beam patterning, a focused electron beam is scanning a surface, covered with a resist. Many materials were found to be suitable for e-beam writing including polymers, proteins

and silk<sup>200–202</sup>. When interacting with polymers, the beam can cause chemical changes in the material, depending on the polymer competition, which will result in a variation in the solubility level of the exposed and non-exposed regions. Then, the soluble residues of the resist can be washed out to reveal the fabricated pattern.

### 5.2.1. E-beam lithography of silk

E-beam has shown to be a suitable technique for fabrication of fine and complex patterns on silk fibroin films<sup>202,203</sup>. When patterning amorphous silk solution, the interaction with the e-beam results in intermolecular crosslinking and the formation of new  $\beta$ -sheet regions, leading to water-insoluble patterns. In contrast, when the e-beam interact with solid crystalline silk it outcomes in degradation of the protein, breaking it to short water-soluble peptides.

By using e-beam lithography Kim *et al.*<sup>203</sup> were able to fabricate coloured photonic crystals from reconstituted silk protein by producing highly repetitive patterns with controlled spacings between of 500 - 700 nm. The same method was used by Qin *et al.*, for 2D and 3D nano-sculpturing of silk<sup>202</sup>.

The main limitation of e-beam lithography is the significantly longer fabrication time in compared to optical and soft lithography. The fabrication time might vary between hours and days for a patterning of mm<sup>2</sup> area, depending on the resolution and the total image size with beam speed limited to 10 mm/s<sup>204</sup>. This strongly limits the total area that can be patterned ( $\mu\text{m}^2$ -mm<sup>2</sup>) and makes it challenging for up-scaling to an industrial level. In addition, e-beam systems are high-cost and have limited availability for most research groups, let alone companies, worldwide.



### 5.3. Inkjet printing of proteins

Inkjet printing is a common direct write technique used for rapid fabrication of structures in 2 and 3 dimensions <sup>205,206</sup>. It is applicable to diverse fields of material fabrication such as organic electronics, chemistry, sensors, optics and biology <sup>205,207</sup>. The technique is highly suitable for protein and biomaterials structuring <sup>208,209</sup> because the writing is usually performed under mild conditions which allows printing of heat sensitive biomaterials and cells. The system can be adapted to provide sterile printing conditions necessary for clinical applications <sup>210</sup>. In addition, the sample quantities required for printing are accurate with minimal material wastage which is crucial when dealing with autologous cell lines or samples with restricted availability. The material (or materials in multi-channel printing) is usually added to a syringe which located above the substrate surface and connected to a motorised stage. By applying impulses (piezoelectric, thermal or electrostatic) a liquid droplet with picolitre volume is accurately ejected onto a substrate from a micron-size nozzle <sup>211</sup>. Then, the syringe is moved to the next location and the structure is produced. Photo-responsive materials are often used in inkjet printing when multiple layer structure is required. The exposure of such materials to UV light after the deposition allows rapid solidification of the structure before the second layer is added and increase structural stability <sup>212</sup>. The printability of materials (ink) is determined by their key physical properties including texture, competition, viscosity, density and surface tension. The optimisation of the process requires accurate selection of nozzle geometry and diameter, extrusion pressure and rate, sample and surface temperature and nozzle motion speed (writing speed) <sup>205</sup>.

### 5.3.1. Inkjet printing of silk

Following the success of native protein patterning, silk was a natural choice for printing applications due to its high solubility in water, biocompatibility and polymorphic features. In addition, the amphiphilic nature of silk protein chains<sup>112</sup> allows to generate drops of silk solution in the volume of pico- to nano- litre without any modification<sup>213</sup>, making it a suitable material for printing technologies. The rheological properties of silk ink can be tuned by adjusting the molecular weight of the fibroin (during the degumming process) and silk concentration<sup>99</sup>. Silk inks can be doped with additives such as nanoparticles, enzymes, antibiotics, growth factors, and antibodies to introduce functionality to the printed pattern<sup>214</sup>.

However, when multi-layered silk structures are required, inkjet printing technology is facing a few challenges which yet to be resolved. Due to the fact that silk is highly shear sensitive and the ink extrusion process involves shear force, it is difficult to define suitable fabrication parameters to allow extrusion without crystallisation, especially when high molecular silk is used (*e.g.* native silk). In addition, due to the spontaneous silk gelation process, especially after applying initial shear, the solution is not stable over time requiring constant adaptation of the printing parameters during the fabrication process<sup>69</sup>. When printing pure silk solution, the structural stability is not sufficient to support the second layer, restricting the process to 2-dimensional structures. This can be improved by post-processing with solvents like methanol which increase the crystallinity level of the silk<sup>215</sup> or by using silk/polymer composites to alter final material properties and functionality<sup>216</sup>. A possible route for multi-layer silk printing might be combining of inkjet extrusion with photo-curing to stabilise the fabricated structure.

## 6. Photo-polymerisation

The process of photopolymerisation occurs in the presence of light and light-sensitive compounds known as photoinitiators. The reaction between the light and the photoinitiator generates free radicals that can initiate polymerisation reaction, resulting in a cross-linked polymer structure. This method has been used for processing of electronic materials, printing materials, optical materials, membranes, polymeric materials, and coatings and surface modifications<sup>217</sup>. It is commonly used in the lithography industry<sup>218–221</sup>.

Some of the advantages of photopolymerisation, when compared to conventional chemical or physical polymerisation, include the spatial and temporal control over the process (allows local polymerisation), fast curing rates (second to minutes), the ability to polymerise at room or physiological temperatures, and minimal heat production<sup>222</sup>. This method also allows *in situ* polymerisation, making it a suitable technique for polymerisation during medical procedures, such as transdermal photopolymerisation during implantation<sup>223</sup>, thrombosis Inhibition<sup>224</sup>, cornea crosslinking<sup>225,226</sup> and adhesions of tissues after surgery<sup>197,227</sup>.

Photocuring can be achieved by both, ultra-violet (UV) and visible light irradiation. The UV photons carry higher energy than visible-light photons and can affect more chemical bonds, making UV- irradiation more attractive for industrial applications. However, UV radiation can burn tissue and damage DNA, potentially leading to cancer<sup>228,229</sup>. Such risks can limit the range of biomedical applications, however, can be reduced by using visible light polymerisation<sup>230</sup>. The polymerisation process can be categorised into two groups (Figure 12 reproduced from<sup>230</sup>):

1. light-induced polymerisation – light exposure induces monomer polymerisation in the presence of a photoinitiator and a crosslinker.

2. light-induced crosslinking – A photoreactive group of the polymer (usually pre-added to the polymer) is crosslinked under irradiation, with or without a photoinitiator.

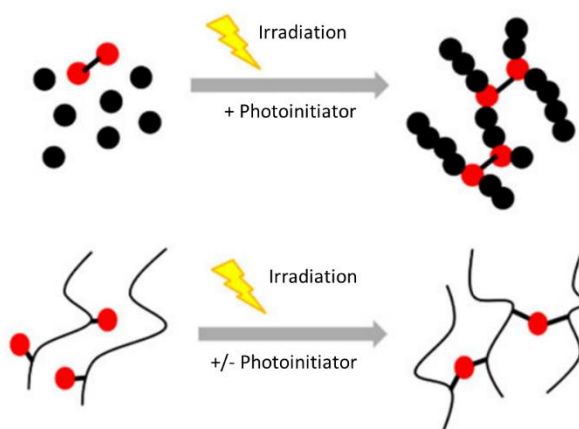


Figure 12: Schematic of light-induced polymerisation and crosslinking (reproduced with permission from <sup>230</sup>).

In light induced polymerisation, the photoinitiator absorbs the light energy and transfers it to radicals or ions that can induce chemical reactions <sup>231,232</sup>. It usually has high absorption at a specific wavelength and should be carefully selected to maximise efficiency for each illumination source. In addition, it is also important to account for the biocompatibility, solubility in water, stability, and cytotoxicity of the photoinitiator <sup>217,233</sup>.

The photoinitiator can be divided into 3 major groups according to the mechanism involved in the photolysis process <sup>217,222,233</sup>.

1. Radical photopolymerisation by photocleavage – following light exposure, radicals are generated by cleavage at C–C, C–Cl, C–O, or C–S bonds. Those photoinitiators have aromatic carbonyl compounds such as benzoin derivatives, benziketals, acetophenone derivatives, and hydroxyalkylphenones.
2. Hydrogen abstraction- following light exposure, the photoinitiator generates a ketyl radical and a donor radical following hydrogen abstraction from an H-donor molecule.

The polymerisation is usually initiated through the H-donor radical while the ketyl radical undergoes radical coupling with the growing macromolecular chains.

3. cationic photopolymerisation – Those photoinitiators undergo either homo or heterolytic cleavage, thus generating a radical cation/aryl radical pair or an aryl cation, respectively. Since they generate protonic acids (oxonium ions) they are not used in tissue engineering applications.

The mechanisms are summarised in Figure 13, which is reproduced with minor modification from <sup>234,235</sup>.

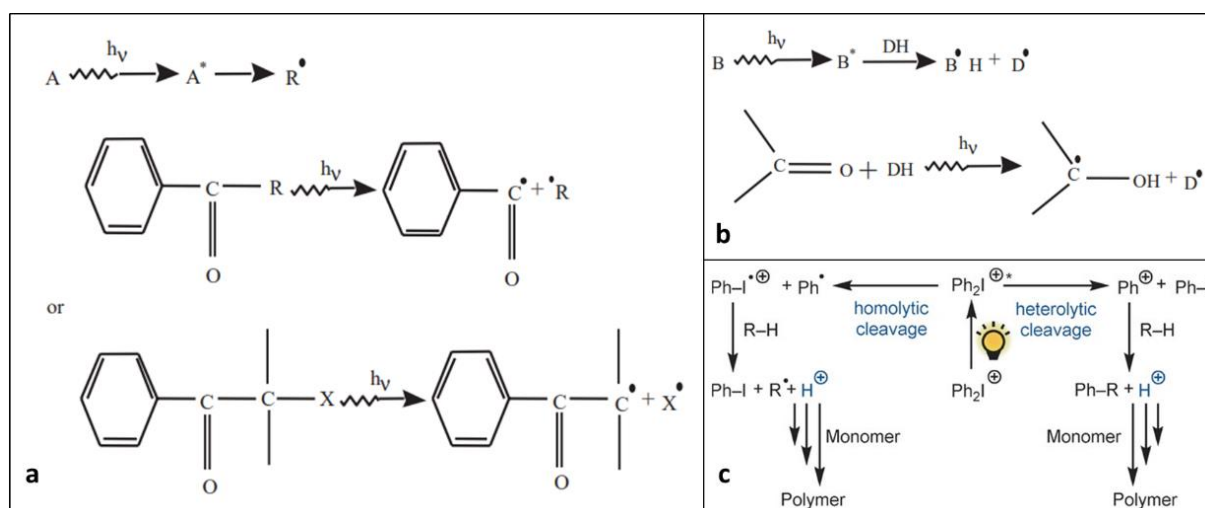


Figure 13: The mechanisms of photopolymerisation (a) Radical photopolymerisation by photocleavage. Upon exposure to light, these photoinitiators undergo cleavage to form radicals that promote the photopolymerisation reaction. (b) Radical photopolymerisation by hydrogen abstraction. Upon UV irradiation, these photoinitiators undergo hydrogen abstraction from the H-donor (DH) to generate radicals. (c) Mechanism of direct activation of onium salts with light. (reproduced with permission from <sup>234,235</sup>)

In radical photopolymerisation, the reaction mechanism is a multi-step process composed of initiation, propagation, and termination stages (Figure 14, reproduced from <sup>236</sup>). The initiation rate ( $R_i$ ) can be dependent on parameters such as the efficiency and concentration of the initiator and the intensity of the irradiated light.

During the process, the formed radicals can migrate through unreacted double bonds to form long monomer chains. When no radicals are left in the system or the chains are transferred, the growth of the chain is terminated. The termination rate ( $R_t$ ) depends on radical concentration. The rate of polymerisation ( $R_p$ ) indicates the rate of double bond consumption and can be approximated as a second-order reaction depending on the double bond and radical concentrations.

If the radical concentration is assumed to be at a pseudo steady-state ( $R_i=R_t$ ), the propagation rate can be described as a function of the monomer concentration ( $M$ ) and the kinetic constants of the propagation ( $k_p$ ) and the termination ( $k_t$ ) stages. Those kinetic constants are highly dependent on the conversion and evolving network structure, which makes the mechanism of polymerisation a complex process.

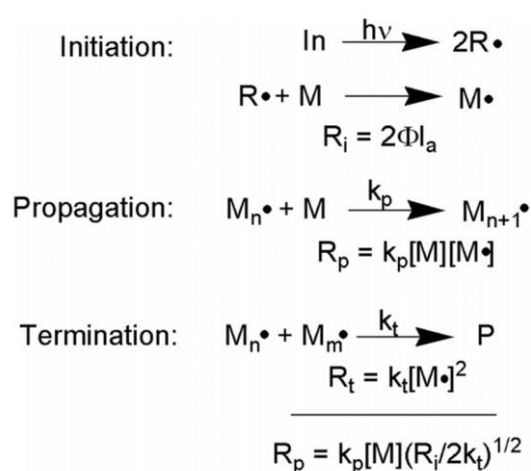


Figure 14: Reaction mechanism for photoinitiated polymerisations.  $I_a$  is a function of the initiating light intensity, initiator concentration, and molar absorptivity coefficient. The polymerisation rate equation shown assumes pseudo steady-state conditions (adapted with permission from <sup>236</sup>).

## 6.1. Photopolymerisable polymers

In many applications, especially in medicine and tissue engineering, hydrogel materials are required <sup>128,235</sup>. Therefore, the following section will focus on materials suitable for the fabrication of hydrogels by photopolymerisation.

### 6.1.1. Synthetic polymers

Generally, hydrogels for tissue engineering are formed from macromolecular hydrogel precursors <sup>235</sup>. Those are usually water-soluble polymers with two or more reactive groups and include polymers such as poly-ethylene-glycol (PEG) acrylate derivatives <sup>237</sup>, PEG methacrylate derivatives <sup>238,239</sup>, polyvinyl alcohol (PVA) derivatives <sup>240,241</sup>. In addition, modified polysaccharides such as hyaluronic acid derivatives <sup>242,243</sup> and dextran methacrylate <sup>244,245</sup> were found to be suitable for the polymerisation of hydrogels. The structure of those polymers is presented in Figure 15 (reproduced from <sup>235</sup>).

Some of the benefits of PEG is its extreme hydrophilicity (which can be used to alter the interaction between materials and tissues and cells) and the fact that the end groups are easily modified and allow the addition of photoreactive groups. It can also be used to produce block copolymers which allow control over the biodegradation rate by controlling the length and the composition of the copolymer segments <sup>237</sup>.

Poly(vinyl alcohol) (PVA) Hydrogels have high water content, tissue-like elasticity, and are not-challenging for fabrication and sterilisation <sup>246</sup>. Their most attractive feature is the presence of hydroxy groups along the backbone allowing chemical modifications such as the introduction of methacrylate groups or biological molecules like fibronectin <sup>246–248</sup>.

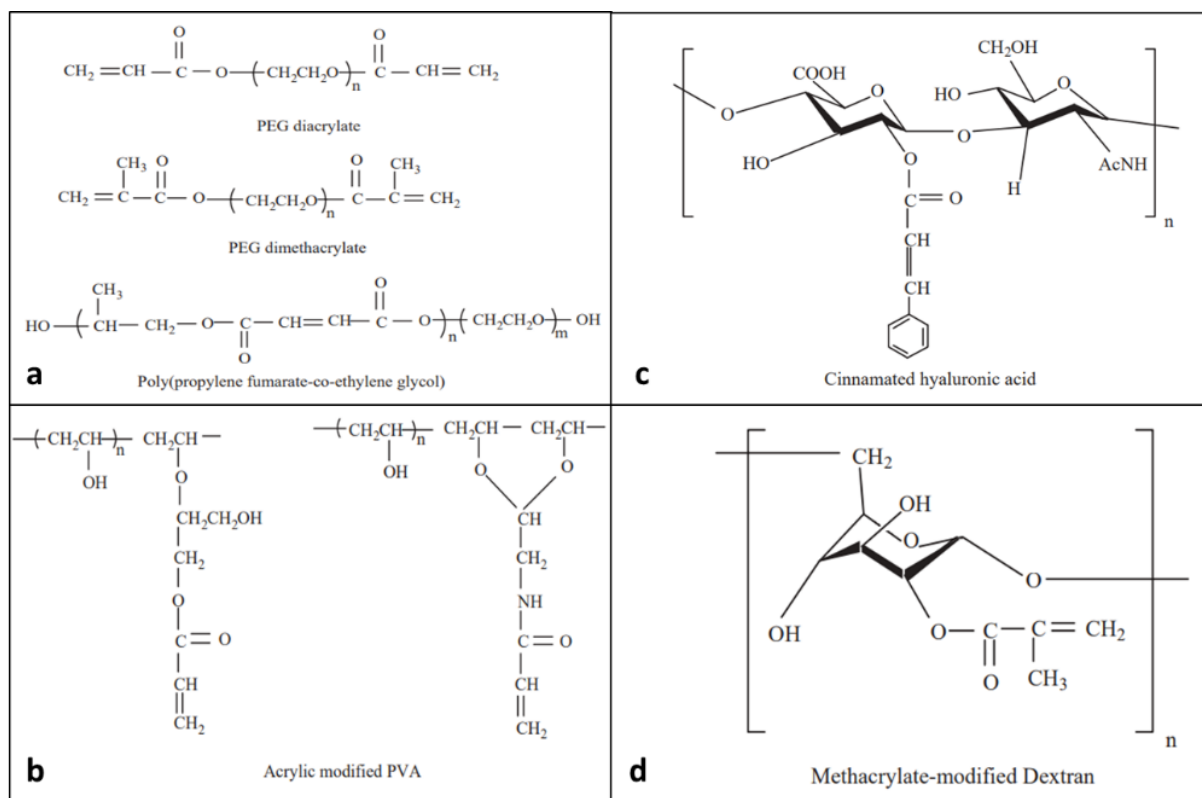


Figure 15: Chemical structures of materials that can be photopolymerised to create crosslinked hydrogel networks: (a) PEG diacrylate, methacrylate, and propylene fumarate derivatives, (b) Crosslinkable PVA derivatives, (c) Hyaluronic acid derivatives, (d) Dextranmethacrylate. (Reproduced with permission from <sup>235</sup>).

### 6.1.2. Natural polymers

The most common natural materials suitable for photopolymerisation are collagen <sup>143,154,249,250</sup> and gelatin <sup>251–253</sup>. Photocurable gelatin was produced by Van Den Bulcke *et al.* <sup>254</sup> in the presence of methacrylic anhydride. The overall strength of the gel was controlled by the degree of substitution and the storage conditions of the gelatin. Collagen photocuring was also achieved by methacrylic anhydride incorporation. It was found that photocuring led to improved mechanical integrity without compromising the triple helical conformation of the collagen <sup>255</sup>.

Another natural polymer of interest for biomedical application is hyaluronic acid (HA) which is found in many connective tissues and plays roles in the promotion of cell motility and



proliferation, wound healing, angiogenesis and reduce inflammation<sup>256</sup>. Photopolymerisation of the HA can be achieved with the addition of a methacrylate group resulting in hydrogels that are capable of swelling up to 14 times their dry weight with increased strength and resilience than corresponding alginate gels<sup>257,258</sup>.

Dextran, a bacterial polysaccharide, has previously been studied for delivery of pharmaceutical drugs, peptides, and proteins<sup>244,245,259,260</sup>. There are 3 free hydroxy groups in its repeat units which allow functionalisation and covalent crosslinking<sup>259</sup>. It was suitable for photopolymerisation when an acrylate functional group was incorporated onto one of the hydroxy groups of dextran, producing hydrogels with a wide range of swelling properties.

Chitosan exhibit hemostatic and immunological activity with the ability to accelerate wound healing<sup>261</sup>. Chitosan photopolymerisation was achieved by reaction with N,N,N',N'-tetramethylethylenediamine, EDC, and 4-O-b-D-galactopyranosyl-(1,4)-D-gluconic acid to introduce azide and lactose moieties. After photocuring, it demonstrated a higher binding strength than fibrin glue and was effective sealant for punctures in thoracic aorta and lungs in rabbit models<sup>262</sup>. The structure of polymerisable natural polymers is presented in Figure 16 (reproduced from<sup>236</sup>)

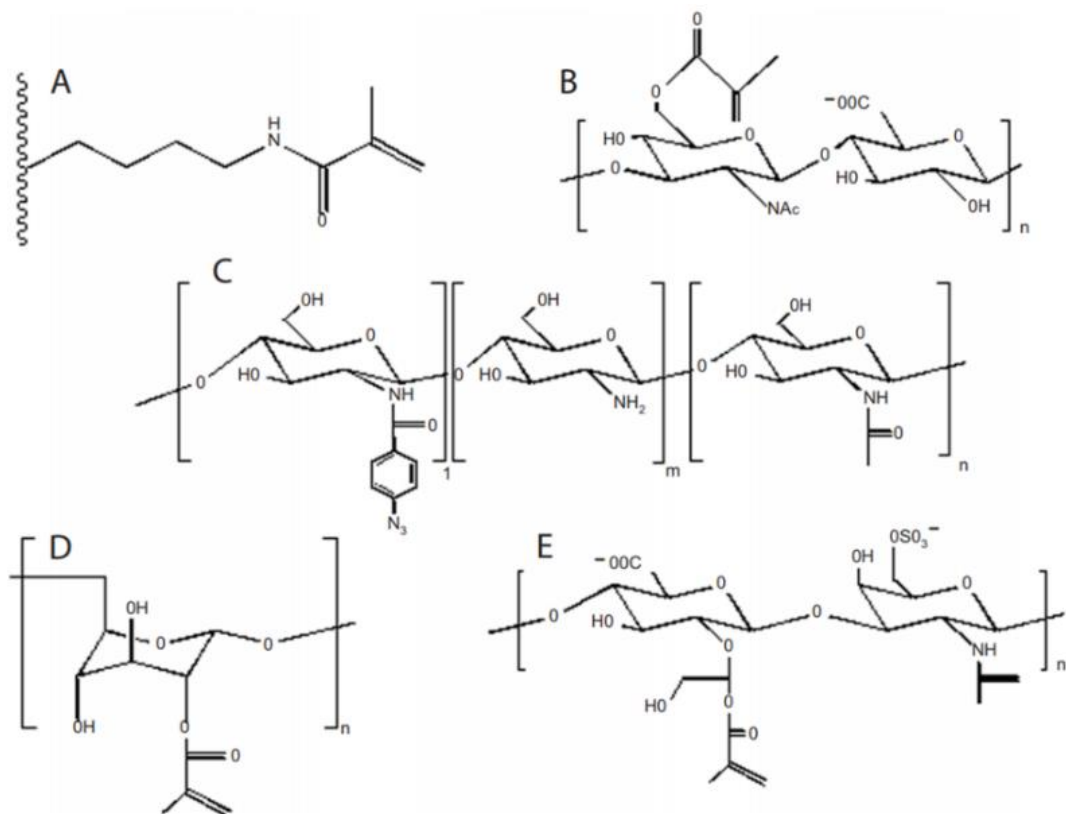


Figure 16: Examples of various photopolymerisable natural polymers including (A) collagen, (B) hyaluronic acid, (C) chitosan, (D) dextran, and (E) chondroitin sulfate. (reproduced with permission from Ref. <sup>236</sup>)

## 6.2. Photo-lithography of proteins

Photo-lithography (PL) is a micro-patterning technique where a photo-curable resin undergoes photochemical reaction under laser light to generate desired patterns <sup>219</sup>. PL allows producing cross-linked complex patterns, in a controlled and fast manner, over large areas ( $\text{mm}^2\text{-cm}^2$ ). The process is usually fast (seconds to few minutes) with resolution limitation varying from  $<10\ \mu\text{m}$  for projection photo-lithography (PPL) <sup>263</sup> and  $<100\ \text{nm}$  for multi-photon direct laser writing (DLW) <sup>264</sup>. Those techniques are broadly explained in chapters 3 and 4 of this work, accordingly.

PL is extensively studied for many proteins such as collagen <sup>265</sup> and albumin <sup>266</sup> and in the last few years is expanded to reconstituted silk (Table 3). Generally, when the photo-reactive protein is exposed to UV or visible light, an excitation of a photo dye results in protein photo-crosslinking <sup>267</sup>. This process usually occurs through free radical or singlet oxygen mechanisms and is dependent on the excitation wavelength, selected photo dye, and accessible protein surface residues <sup>266</sup>.

## 6.3. Photo-curing of silk

For the past 5 years, several research groups have investigated the suitability of reconstituted silk fibroin (RSF) for various PL techniques with a goal to fabricate patterns and geometries generating new material properties and application range (Table 3). Many tactics were used to tailor the silk for PL fabrication by introducing photoresponsive properties into the silk. Some papers suggested a chemical modification of the silk by the addition of reactive groups to the protein which in turn can cross-link in the presence of the dye (Irgacure 2959) during light exposure <sup>193,268,269</sup>. It is possible because the fibroin chain is composed of a number of specific amino acids allowing chemical modification without substantial alteration of the

protein structure and properties <sup>45</sup>. Another approach to silk photo-curing is the addition of photo-sensitive dye to the fibroin (*e.g.* riboflavin, rose bengal and methylene blue) which can generate crosslinking under light exposure <sup>122,270,271</sup>. The crosslinking can be direct, between the side groups of the fibroin (usually tyrosine) or through silk/dye complexes formed between the side groups of the fibroin (usually arginine, lysine and histidine) and the dye <sup>249,272</sup>.

To date, reconstituted fibroin was used as silk standard in all PL literature as summarised in Table 3. However, as will be discussed in this work, the reconstitution processes can strongly affect the production, properties and the resolution of the fabricated patterns. Therefore, there is an urgent need to standardise silk fibroin quality and to characterise the silk used in any future publications.

Chapters 3 and 4 of this work introduce native silk as a gold standard source of un-modified fibroin and explore its suitability and performance in DLW and mask-less PPL systems. The photo-curing reaction mechanism is explained, pattern quality is investigated, and the importance of fibroin quality is emphasised especially when precise patterning is required. The results provide a comprehensive understanding of the process allowing to broaden the application range of silk PL techniques in many fields of bioengineering.

*Table 3: Current literature describing photo-curing of silk fibroin. Bulk PL described full photocuring of the region without specific pattern fabrication.*

Ref	Technique	Light source	Silk type	fibroin concentration (wt/wt)	Photo-initiator	Pattern Resolution
Kurland <i>et al.</i> 2013 <sup>268</sup>	Mask PPL	UV light	Modified RSF	2 %	Irgacure 2959	1 μm
Whittaker <i>et al.</i> 2014 <sup>273</sup>	Bulk PL	250 W light source	RSF	14 %	Ru(bpy) <sub>3</sub> <sup>2+</sup>	N/A
Sun <i>et al.</i> 2015 <sup>270</sup>	DLW	Ti:Sapphire laser (800 nm)	RSF	2.5 %	methylene Blue	< 1 μm
Pal <i>et al.</i> 2015 <sup>193</sup>	PL	UV light	Modified RSF	3.75 %	Irgacure 2959	2 μm
Park <i>et al.</i> 2016 <sup>274</sup>	Mask PPL	ArF laser (193 nm)	RSF	7 %	-	1 μm
Wang <i>et al.</i> 2016 <sup>275</sup>	Bulk PL	UV light (365 nm)	RSF/PVA composite	13 %	Irgacure (I-2959)	N/A
Applegate <i>et al.</i> 2016 <sup>122</sup>	Mask PPL	LED (450 nm)	RSF	6 %	riboflavin	50 μm
Pal <i>et al.</i> 2016 <sup>220</sup>	Mask PPL	UV light (365 nm)	RSF, RSS	2 %	Irgacure 2959	5 - 100 μm
Maximova <i>et al.</i> 2016 <sup>276</sup>	DLW	Yb:KGW Laser (1030 nm)	RSF	10 %	-	3 μm
Liu <i>et al.</i> 2017 <sup>269</sup>	Mask PPL	UV light	Modified L-chain RSF	2 %	Irgacure 2959	1.5 μm
Dickerson <i>et al.</i> 2017 <sup>271</sup>	DLW	Nano-scribe commercial system	RSF	15 %	rose bengal, Ru(bpy) <sub>3</sub> <sup>2+</sup>	< 5 μm
Zhou <i>et al.</i> 2018 <sup>277</sup>	Bulk PL	UV light	RSF/chitosan composite	3 %	Darocur (2959)	N/A
This work (chapter 3)	DLW	Nd:YAG Laser (532 nm)	native silk	1 %	Rose bengal	20 μm
This work (chapter 4)	Mask-less PPL	violet diode laser	native silk	1 %	riboflavin	40 μm
		(405 nm)	RSF	2 %		70 μm

## 7. Moving into 3D fabrication

Most patterning techniques are suitable for fabrication of 2-dimensional structures with surface topographies up to a few hundreds of microns. Although multi-photon PL has proven to produce self-supporting true 3D structures<sup>270,271</sup>, those structures are very small (microns) and are not feasible for real-life applications such as tissue engineering, which require larger scaffolds, typically a few centimetres in size<sup>120</sup>. Due to the high cost of PL, slow fabrication time and silk instability over several days of fabrication (required for large sample size), it is unlikely that PL alone will become an industrial scale technique for 3D silk structuring.

When designing scaffolds for applications such as tissue regeneration, it is important to meet several criteria such as high level of porosity (to allow a significant surface for cell attachment), pore size above 100  $\mu\text{m}$  (to allow cell penetration), open porosity (for cell migration) and physiological biodegradation rate<sup>142</sup>. Currently, three main fabrication techniques are used for the production of porous 3D silk scaffold including porogen leaching, freeze drying and gas foaming<sup>22,135,136,142</sup>.

In porogen leaching, salt or sugar granules with specific dimensions are added to the polymer solution and the solution allow to solidify in the desired geometry to form a polymer/porogen composite. When the scaffold is formed the porogen is dissolved, leaving behind a porous structure while the size of the granules reflects the size of the final pores<sup>278</sup>. Porogens with multiple granule sizes can be used to create a gradient in scaffold porosity<sup>136</sup>.

Freeze drying (lyophilisation) is one of the most commonly used methods in the silk literature for fibroin scaffold fabrication<sup>22,135,142,279,280</sup>. In this dehydration procedure, the pre-structured material is frozen and then placed under vacuum to remove the access water by sublimation (solid to gas transfer). Most of the fibroin scaffolds solely made by freeze drying

have insufficient porosity and pore size for tissue engineering applications<sup>135,279</sup>. This can be overcome by combining freeze drying with additional fabrication techniques (e.g. gas foaming)<sup>280</sup>, by controlling the freezing rate<sup>155</sup> and by using silk-based composites<sup>155</sup>.

Scaffold fabrication by gas foaming method utilises gas pressure to generate internal porosity. In short, the samples are compressed to produce bulk disks. The disks are then placed in a chamber with high gas pressure (usually CO<sub>2</sub>) for several days. Then, the chamber pressure is restored gradually forcing the gas molecules to abandon the sample leaving a porous structure behind<sup>278</sup>.

To select the optimal scaffold fabrication method for silk, Nazarov *et al.*<sup>135</sup> compared the porosity and mechanical properties of silk fibroin scaffold producing by salt leaching, gas foaming and freeze drying processes. This study indicated that for application in cortical bone engineering, gas leaching method produced the most suitable scaffolds. This is because these scaffolds had the highest compressive modulus and compressive stress with highly interconnected and porous structure (pore size ~ 150 μm), which maintained high strength when placed under compression.

Additional processes were suggested for the fabrication of porous silk scaffold including the addition of organic solvent prior to sample freezing<sup>281</sup>, 3D silk printing in the presence of sacrificial particles<sup>278</sup> and by emulsion-templated synthesis (chapter 5 of this thesis).

## 7.1. Poly-HIPes

Poly-HIPE is a unique structure of a polymeric foam which consists of continuous internal interconnected network between larger main pores. The pores are often called voids while the interconnected holes are known as windows<sup>282-284</sup>.

Poly-HIPEs are fabricated through an emulsion templating polymer synthesized within high internal phase emulsions (HIPEs). HIPE structure can be formed when the major component (internal phase) which occupies more than 74% of the total volume, is dispersed within the minor phase (external phase). Due to the immiscible nature of the two phases, a stable emulsion is generated. When the external phase is polymerised (*e.g* by photopolymerisations), a continuous poly-HIPE structure is generated around the dispersed droplets of the internal phase. During the polymerisation, ruptures (windows) can develop at the thinnest point of contact between the internal phase droplets transforming the discrete droplets in the HIPE into a continuous interconnected phase in the poly-HIPE. When the internal phase is removed voids are created in the place of the droplets and as a result, a highly interconnected structure is formed. An example of poly-HIPE structure voids and interconnecting windows can be seen in Figure 17.

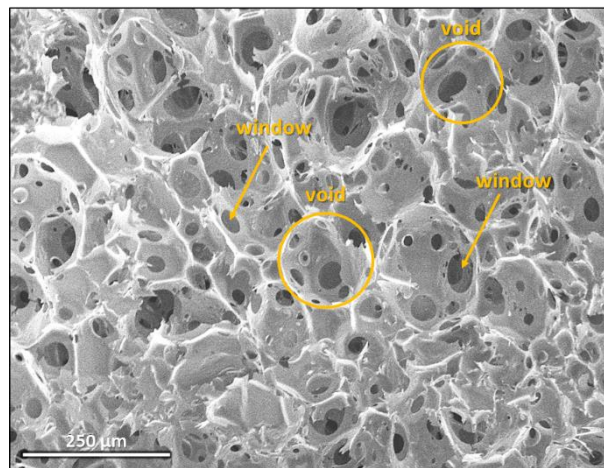


*Figure 17: A porous poly-HIPE structure (SEM) fabricated from native silk solution and rapeseed oil as discussed in chapter 5 of this thesis.*



## 8. Thesis goals

The guiding hypothesis of this work was that silk can be structured by light illumination. This aims to introduce a new processing approach in addition to the current mechanical and chemical routes for the structuring of silk. In addition, the author of this thesis hypothesised that the use of native silk, instead of its reconstituted substitute, can significantly improve the current field of silk processing, leading to higher quality patterning.

This thesis explores several low-cost and environmentally friendly routes for the fabrication of 1D, 2D and 3D structures from native and reconstituted silk solutions. The thesis is split into 6 chapters which explore the process of structure fabrication from simple 1D writing through 2D patterning and eventually generation of 3D silk scaffolds. Each chapter presents a novel approach for silk structuring utilising either new material (such as native silk), a new technique (such as P $\mu$ SL and emulsion-templated synthesis) or new structure (such as poly-HIPE) which were never introduced before in the published silk literature. Each chapter includes an introduction section to the relevant fabrication techniques, results and discussion section followed by the conclusion section. The range of potential applications for each technique is explored and discussed at the end of each chapter. A brief summary of the chapters is presented below.

### 8.1. Chapter introduction

#### Chapter 2 - Methodology

This chapter introduces all the general fabrication and characterisation techniques used in this thesis. Specialised techniques are introduced in the methodology sections of each relevant chapter. This chapter includes a detailed explanation of native and reconstituted silk fabrication, basic principles of rheology and short descriptions of characterisation techniques.

### Chapter 3 - 1D direct laser writing of silk patterns

This chapter introduces and explores, for the first time, direct writing of native silk proteins. The chapter will discuss the optimisation of the process, characterisation of the structures and the mechanism of photo-gelation of the silk. It will also discuss the limitations of this process in the fabrication of multi-dimensional structures.

### Chapter 4 - Fabrication of 2D silk structures by projection stereolithography

This chapter explores a novel low-cost approach to silk patterning and presents the benefits of projection stereolithography compared to other fabrication methods currently used for silk patterning. The process is optimised, the pattern is characterised, and the mechanism is evaluated. In addition, this chapter investigates the effect of the molecular weight of the protein on the patterning process and introduce the benefit of native silk in this area.

### Chapter 5 - 3D - Silk structures fabrication by emulsion templating method

This chapter develops and explores emulsion templating route to fabricate silk poly-HIPES. This structure, although very desirable in many applications, is not yet been presented for silk in the literature. The chapter explores all the parameters that affect structure porosity and explores the scaffold characteristics and application range.

### Chapter 6 - Conclusions

This chapter discusses all the results and the conclusions of the research performed in this thesis. It will present the limitations of each technique and the novelty achieved by each fabrication route. It will also raise all the research questions following this research as well as discuss future experimental directions and the contribution this thesis represents in the broader context of silk research.

# Chapter 2

---

## Methodology

## Summary

This chapter introduces the main experimental methods used in this thesis. Starting with silk protein solutions, both silkworm dissection is explained as a means to extract native silk as well as the reconstitution process to fabricate reconstituted silk. Furthermore, the underpinning theories behind the characterisation techniques applied to the silk structures are discussed.

## 1. Native silk extraction and solution preparation

All silk processing routes described in this thesis require silk protein in the unspun (aqueous) form. The only way to obtain unprocessed native silk is directly from the silk dope through careful silkworm dissection and extraction of the silk glands. All dissections were performed using an Olympus SZ40 dissection microscope (Olympus, UK) and Leica MZ12 dissection microscope (Leica, Germany) with fibre optic light source, fine forceps and dissection scissors. The dissection method used in this thesis is following the method previously described by Holland <sup>285</sup>.

The following principles were used through all the dissection processes:

### 1.1. Selection of the silkworm

*B. mori* silkworms yield silk at only one point in their life cycle and the accumulation of silk occurs only a few days before this event <sup>25</sup>. In addition, silk dope undergoes a maturation just before spinning, altering the composition and viscosity of the solution <sup>105</sup>. Therefore, all silkworm dissections were performed on individuals who were at the early stage of cocoon construction (stage 2) as seen in Figure 18b (reproduced from Reference <sup>105</sup>).

### 1.2. Silkworm sacrifice

All silkworms were sacrificed without anaesthetic to avoid any possible changes to the pH of the hemolymph, previously seen in anaesthetised spiders <sup>286,287</sup>. The silkworms were stored in the fridge (9°C) and transferred to room temperature 10 minutes prior to the dissection. Animals were slain by separating the head from the body using a pair of heavy scissors and cutting along the ventral surface between the legs in an anterior to posterior direction.

### 1.3. Dissection environment

Ideally, the dissected gland should be placed in a buffered Ringers solution at room temperature to maintain an appropriate ionic balance in the silk solution <sup>288</sup>. However, due to a lack of a suitable Ringers solution recipe for silkworm haemolymph and the likelihood that this would not represent the ionic and pH conditions in the dope <sup>63,289</sup> gland was placed directly in chilled distilled water to enable rapid preparation with the minimum of effects on the dope.

### 1.4. Gland peeling process

After 6-10 minutes of whole gland immersion in chilled water, the epithelial layer of cells covering the entire gland detached sufficiently to allow easy peeling, exposing the native silk dope without damaging the gland. To remove the gland epithelium a small tear was made in the epithelial layer with two pairs of forceps. One pair of forceps was used to hold the tear and the second pair was used to gently separate the epithelial coat minimising contact with the sensitive gland contents.

### 1.5. Sericin removal

As discussed in the introduction chapter of this thesis, the sericin is present mostly in the middle and anterior divisions of the middle gland section. The posterior section of the gland is extremely narrow and difficult to peel. Therefore all silk samples were extracted from the posterior division of the middle section of the gland (Figure 18e,f). Other sections of the gland were discarded. The gland was washed twice after the peeling process to remove sericin and haemolymph remains.

## 1.6. Silk solution storage

After the washing procedure, the gland section was placed into 2 ml Eppendorf tube and covered fully with chilled distilled water. The tube was sealed and stored in the fridge overnight to relax and homogenise the solution prior to experimentation. If the dissection and peeling performed carefully without damaging the dope, the solution can be stored for up to 1 week.

## 1.7. Concentration calculation

Concentrations or the percentage of dry weight (% DW) of the final diluted silk solution was determined by taking a small part of the solution from the Eppendorf tubes, 24 hours after fabrication, and drying to a constant weight using vacuum oven or A&D MX-50 moisture analyser (A&D company, Japan). This method provides the total organic and ionic content minus water and any volatiles.

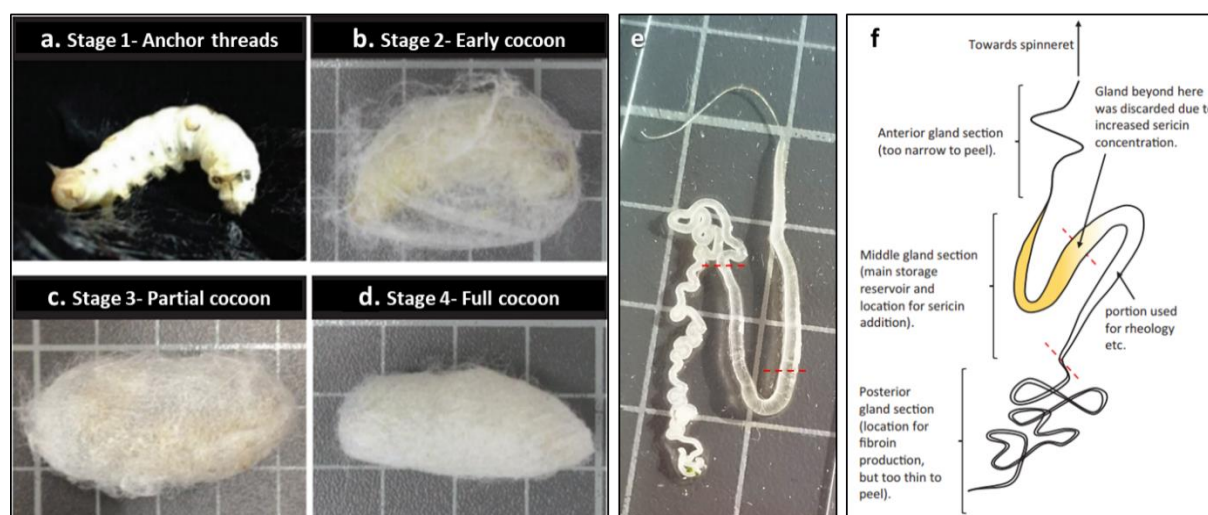


Figure 18: (a–d) arbitrary stages of cocoon construction (from anchor threads to full cocoon). (e) photograph of dissected silk gland (unpeeled). Red lines indicated the regions of the gland that were used for all the experimental work in this thesis. (f) Diagram showing parts of a silk gland and origins of the samples used (dashed lines demark where the gland was cut). (reproduced with permission from<sup>3</sup>)

## 2. Reconstituted silk solution preparation

Reconstituted silk (RS) solution was prepared in accordance with the protocol described by Rockwood *et al.* <sup>22</sup>.

The aim of this protocol is to convert solid silk cocoons into liquid silk solution, which can be reprocessed into various shapes and structures. To achieve this, several intermediate steps should be performed, following the protocol, including degumming, dissolution and dialysis of the silk. At first, the cocoons are collected and cut with scissors into small pieces. The silkworm from the cocoon is removed and placed in the freezer (-18°C) for several days before disposal.

### 2.1. Silk degumming

The cut cocoons are placed in a boiling beaker filled with Na<sub>2</sub>CO<sub>3</sub> solution. The concentration of the salt will affect the final molecular weight of the fibroin in the solution (see chapter 4). In this thesis, concentration ranges between 0.003 to 0.3 M were used. Standard degummed silk was prepared at 0.02 M. The cocoons were boiled for 30 minutes and stirred occasionally to improve dispersion of the fibroin. It is important to note, that longer boiling times can result in additional degradation of the protein <sup>22</sup> and therefore were avoided in this work.

After 30 minutes of boiling, the degummed cocoons were washed with tap water (room temperature) and transferred to a beaker filled with distilled water and stirred for 20 minutes. The process was repeated 3 times until all salt residues were removed. The silk was then squeezed, spread on an oven tray and was left to dry in a fume hood overnight. The dry silk was sealed in a plastic bag, labelled and stored at room temperature until needed.



## 2.2. Silk dissolution

LiBr solution (9.3 M) was prepared by the addition of 86.85 gr of LiBr to 100 ml of distilled water. It is important to highlight that the process of LiBr dissolution in water is a highly exothermic reaction which results in significant heating of the container. Therefore, the beaker was placed in an additional larger beaker filled with cooled water and the LiBr powder was added slowly, few grams at a time to allow heat diffusion and avoid sample overheating. After all the LiBr was added, the solution was placed on a hot plate and kept at 60°C. Then, the solution was distributed into 50 ml tubes and 1 gram of degummed cocoons was added to every 10 ml of solution. The cocoons were gently packed at the bottom of the container, using a glass rod, to reassure full coverage of the cocoons by the solution to allow full dissolution. The containers were kept at 60°C for 4h.

In most cases, full dissolution was not achieved after 4 h and small remains of non-dissolved silk were present. Those remains were removed during the filtration stage.

## 2.3. Solution dialysis

After the dissolution, the solution was cooled down to room temperature and transferred into a dialysis membrane (MWCO 12-14 kDa, Spectra/por®). The membrane was sealed and immersed in a container filled with 1 litre of distilled water. This is to allow removal of LiBr ions and small proteins (< 12 kDa) from the protein solution. The water in the container was changed frequently to reach a total of 5 water exchanges over 24 h. During the dialysis process the container was stored in the fridge (4°C).

## 2.4. Solution filtration

After the dialysis, the membrane was gently opened, and the solution was filtered using Whatman® qualitative filter paper, Grade 1 (pore size 11 µm, Sigma Aldrich, UK) to remove

undissolved silk and any other contamination. The filtered solution was transparent with a slightly yellow colour. The concentration of the solution was measured gravimetrically by oven drying a small quantity of the sample to evaluate the dry weight of the protein. The solution was then gently transferred to a plastic beaker and stored in the fridge until needed. It should be noted that under these conditions a reconstituted solution can be stored for a longer period (about 1 month) than the native one (about 1 week). In the experimental work when both solutions were compared, fresh reconstituted silk was used (less than 1 week old).

## 2.5. Solution concentrating

The average concentration of the reconstituted silk solution was between 3 – 5 wt%. Some of the experimental work performed in this thesis, especially in chapter 5, required a higher concentration of 6 wt%. To increase the concentration, the solution was transferred into a dialysis membrane (same as used for the dialysis stage), the membrane was sealed and immersed in a container filled 30% (wt/vol) PEG solution (35000 g/mol). The PEG has hydrophilic properties<sup>290</sup>, and due to the higher concentration, it can draw the water from the silk solution across the membrane via osmosis, increasing the concentration of the solution. After few hours of immersion in PEG, the membrane was removed from the PEG and wiped with tissue paper. The concentration was measured, and the solution was stored in the fridge until needed. Dilution of silk solutions was always done by the addition of the desired amount of distilled water. In this instance, to avoid premature gelation, the solution was not mixed but left in the fridge for 24 h to achieve uniform distribution of the protein in the vial.

The process of silk reconstitution is summarised in Figure 19 below:

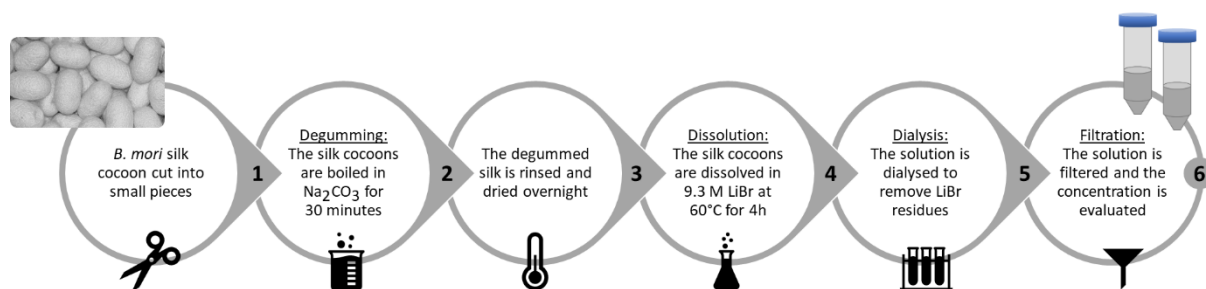


Figure 19: The process of silk reconstitution. (1) The cocoons are cut into small pieces. (2) Silk degumming: the cocoons are boiled in  $\text{Na}_2\text{CO}_3$  solution for 30 min. (3) The degummed silk cocoons are rinsed and dried overnight. (4) Silk dissolution: The cocoons are dissolved in 9.3 M LiBr solution at 60°C for 4h. (5) The dissolved silk is dialysed in semi-permeable membrane against distilled water to remove LiBr residue. (6) The final solution is filtered to remove undissolved silk and any other contaminants; the concentration is measured, and the sample stored at 4°C until required.

### 3. Rheological measurements

Rheology, or the measurement of deformation under flow, is often used for the characterisation of materials which are neither completely liquids or solids such as polymers, physiological fluids and gels <sup>291</sup>. The deformation used in rheology is usually applied as dynamic or static shear or as extensional flow. Those modes of deformation allow, when combined, to characterise the macroscopic flow behaviour of a material. Samples can respond to deformation elastically (stress proportional to strain) or viscously (strain is independent of stress but proportional to the rate of strain). Most of the biological materials, including all silk solutions in this thesis, present a non-linear behaviour known as viscoelasticity (i.e. are Non-Newtonian).

The rheological measurements that were used in this thesis can be divided into constant shear (viscosity) and dynamic shear (oscillation). Viscosity measurements were mostly used in chapter 5 to characterise the viscosity of the fabricated emulsions while oscillation

measurements were mostly used in chapter 4 to evaluate the mechanical properties of the hydrogels during the photo-curing process.

### 3.1. Viscosity measurements

In constant shear viscosity measurements, the material is placed between two horizontal plates and a force is applied to the sample by moving the plates relative to the other. For practical reasons, usually the top plate (a.k.a the tool or measuring geometry) is mobile while the bottom plate remains in a constant position. The stress ( $\sigma$ ) required to move the upper plate primarily depends on the rheological properties of the sample that is located in-between.

If a low viscosity material (*e.g.* oil, water) is placed between the plates, it will present low resistivity to flow and requires very little stress to move the plates. In fact, the viscosities of water and very diluted silk solutions (< 1 wt.%) were below the minimal threshold of the rheometers used in this thesis, and therefore those values are not presented. However, if those materials are replaced by a viscous material (*e.g.* honey or gelatine) a larger stress will be required to move the plates due to the higher resistivity of those materials to flow.

The resistance to flow, or internal friction, can be calculated from the value of the stress input ( $\sigma$ ) relative to strain and known as viscosity ( $\eta$ ). In non-Newtonian fluids (*e.g.* silk solutions and most of biological fluids<sup>292</sup>) the viscosity is dependent on the rate of deformation known as shear rate ( $\dot{\gamma}$ ). While in Newtonian fluids (*e.g.* water) the viscosity is constant regardless of the shear rate (Figure 20).

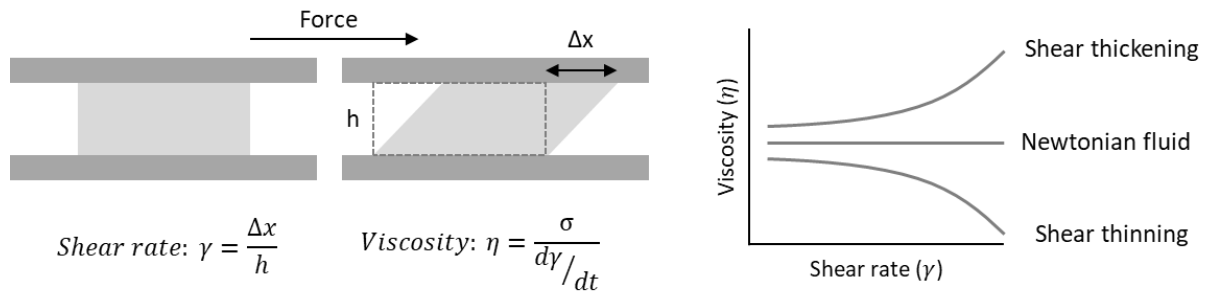


Figure 20: Diagram showing the mode of sample deformation under the plates of the rheometer, the evaluated terms for shear rate and viscosity and the figure to be obtained from viscosity experiments in a shear rheometer.

### 3.2. Oscillation measurements

Dynamic shear tests are performed in an oscillatory mode in which a sinusoidal strain with amplitude  $\gamma_0$  is applied to the system at a frequency  $\omega$  and the resulting stress  $\sigma$  is measured. The time shift  $\Delta t$  in the sine waves of the strain and the stress defines the phase angle shift  $\delta$  ( $\delta = \Delta t \cdot \omega$ ). The values for the storage modulus ( $G'$ ), the loss modulus ( $G''$ ) and the complex modulus ( $G^*$ ) can be obtained as described in Figure 21.  $G'$  represents the elastic component and the  $G''$  is the viscous component of the material. Those components can be measured as a function of strain amplitude or as a function of frequency. When oscillatory shear measurements are performed in the linear viscoelastic regime,  $G'$   $G''$  are independent of the strain amplitude.

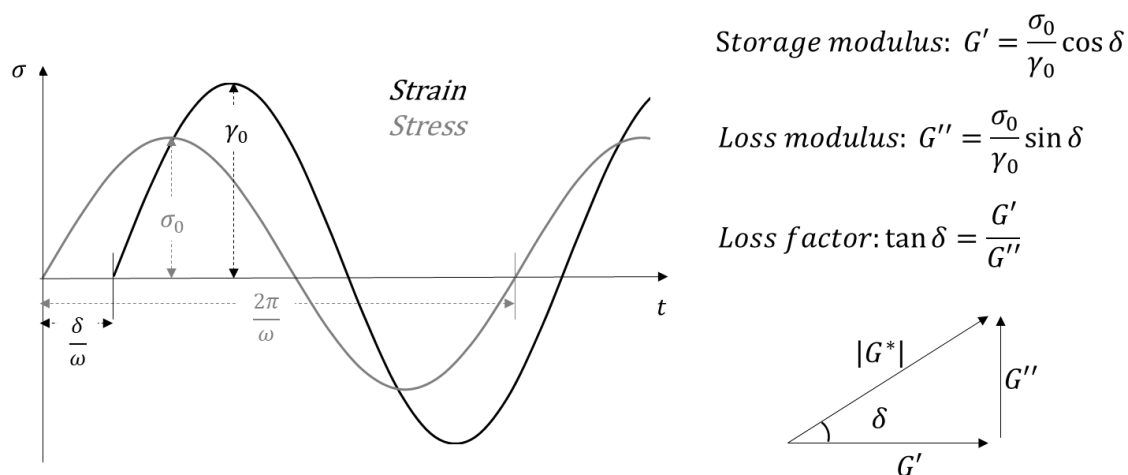


Figure 21: Diagram showing the oscillatory test for viscoelastic behaviour, presented as a sinusoidal function versus time, and the calculations that can be derived from the diagram. Vector diagram illustrating the relationship between complex shear modulus  $G^*$ , storage modulus  $G'$  and loss modulus  $G''$  using the phase-shift angle  $\delta$ .

Viscosity measurements were performed using AR 2000 rheometer, (TA Instruments, USA) with a CP2/40 cone and plate geometry (40 mm radius, 2° opening angle and 15 μm truncation). A silk protein solution or silk/oil emulsion, sufficient to completely fill the geometry, was placed on the fixed plate and the cone was lowered to the required gap setting (15 μm). The cone speed was reduced to the minimum (0.1 mm s<sup>-1</sup>) before the cone touched the sample. Excess sample was allowed to squeeze out from under the cone and was not removed, to avoid shear-induced gelation at the edge of the geometry<sup>69</sup>. To avoid the specimen drying out and forming a skin during the measurements, the area outside the cone was flooded with distilled water and loosely enclosed using an environmental chamber, which was designed to fit around the cone and drive shaft without touching<sup>99</sup>. A constant shear rate of  $\dot{\gamma} = 1 \text{ s}^{-1}$  was applied for 100 s at 25 °C, in order to ensure the specimen was distributed evenly between the cone and plate and to supersede any residual stress from sample loading. The shear viscosity at  $\dot{\gamma} = 1 \text{ s}^{-1}$  was obtained by averaging data from the final 30 s of this stage.

Oscillatory measurements were performed using AR 2000 and Discovery HR-2 rheometers (TA Instruments, USA) with 8 mm parallel plate geometries. Wet silk patterns (immersed in water for 5 minutes before the measurements) or 30  $\mu\text{l}$  of silk/oil emulsion, were carefully placed on the bottom plate and the top plate was gently lowered down to required gap settings (100 - 500  $\mu\text{m}$ ). The experiments were performed in two stages, an oscillatory frequency sweep (20 to 0.1 Hz) followed by a fixed frequency time ramp (1 Hz), both of which were conducted within the sample's linear viscoelastic region (target strain 0.01)<sup>55</sup>. Preliminary experiments were performed on a Bohlin Gemini HR Nano 200 (Malvern Instruments, UK).

#### 4. Infrared spectroscopy

Infrared spectroscopy is an analytical technique commonly used to evaluate the chemical composition of samples based on their molecular vibration transitions, which absorb in the infrared range. The name of the technique: Fourier Transform Infrared (FTIR) spectrometry was given because the collected spectra are deconvoluted by Fourier transformation.

Inside the instrument, IR is emitted from a heated black body emitting mostly between 14000 and 400  $\text{cm}^{-1}$  (0.8 and 25  $\mu\text{m}$ ). After emission, the beam is restricted by an aperture. After the aperture, the beam is directed into the Michelson interferometer for modulation<sup>293</sup>. This interferometer is equipped with a beam splitter which reflects half of the light whilst allowing the other half through, at a 45° angle. This leads to an interference of the beam with itself before being reflected out.

An attenuated total reflection (ATR) accessory collects and focuses the IR beam on the sensor crystal where attenuated total reflection occurs. When a sample is placed in contact with the ATR sensor crystal, a part of the incident radiation can be absorbed without passing through

the sample. This is because the surface of the crystal produces an evanescent wave which interacts with the sample in direct proximity of the crystal surface (0.5 to 2  $\mu\text{m}$ )<sup>294</sup>. It is also possible to measure an ultra-thin film sample by illuminating directly through the sample (via transmission)<sup>105</sup>.

After the sample has absorbed a portion of the IR light, the remaining modulated light is directed to either the pyroelectric Deuterated Tri-Glycine Sulfate (DTGS) or a liquid nitrogen cooled photoconductive Mercury Cadmium Telluride (MCT) detector (Figure 22).

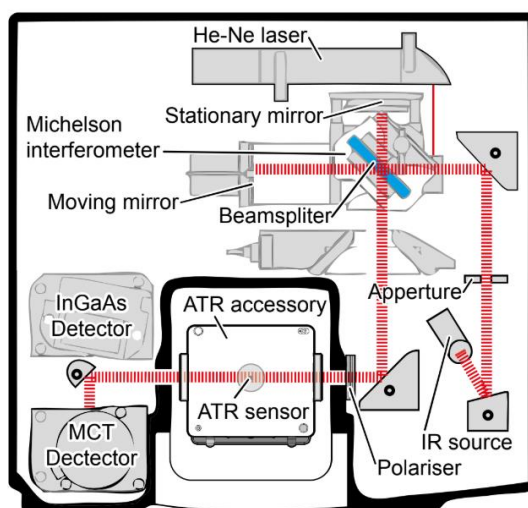


Figure 22: Infrared beam path of Thermo Nicolet 6700 Fourier transform infrared spectrometer (reproduced with permission from<sup>295</sup>).

All FTIR spectra in this thesis were collected by Nicolet 380 spectrometer (Thermo Scientific, Madison, USA) with DTGS detector equipped with diamond ATR accessory (Golden Gate, Specac, UK). Spectral data collected between 800 and 4000  $\text{cm}^{-1}$  using 64 scans, at 4  $\text{cm}^{-1}$  resolution.



#### 4.1. Silk structure characterisation by FTIR spectroscopy

In the silk literature, the crystallisation process ( $\beta$ -sheet structure formation) is usually characterised by FTIR spectroscopy<sup>294,296</sup>. This is mostly done by tracking the positions of the amide I and amide II peaks in the silk spectra and the sub-components of those peaks. The position of amide I peak ( $1500\text{-}1700\text{ cm}^{-1}$ ) can indicate whether the fibroin is amorphous or converted to crystalline state. It is important to note that amide I is not a single peak but a result of a convolution of several structural components<sup>296</sup>. Those structures include: anti-parallel  $\beta$ -sheet ( $1698\text{ cm}^{-1}$ ), un-ordered helical structure ( $1649\text{ cm}^{-1}$ ),  $\beta$ -sheet ( $1615\text{ cm}^{-1}$ ) and tyrosine ring ( $1594\text{ cm}^{-1}$ )<sup>294</sup>.

Crystallisation in the silk can be induced by applying mechanical shear, exposure to organic solvents or due to temperature and pH variations<sup>12</sup>. When the crystallisation process is initiated,  $\beta$ -sheet structures start to form, leading to an increase in the  $\beta$ -sheet content of the amide I peak. This will shift the centre of mass and the ratio between the sub-components of the amide I, resulting in a quantifiable shift of the whole peak toward lower wavenumber values. This shift can be recorded and used to demonstrate the conversion of the silk under various experimental conditions. Figure 23 presents deconvolution of the amide I peak that was performed on an FTIR spectrum collected from an amorphous silk film and one from a converted silk film after methanol treatment. Peak analysis was performed using MagicPlot Student software (version 2.7.2).

For all the silk spectra presented in this thesis, the spectra in the region of interest ( $1200\text{-}1800\text{ cm}^{-1}$ ) were normalized against the amide I band of each sample. This was done to compensate for differences in sample thickness/contact area (which result in absorbance

intensity differences), and for easier comparison between the band position between various samples.

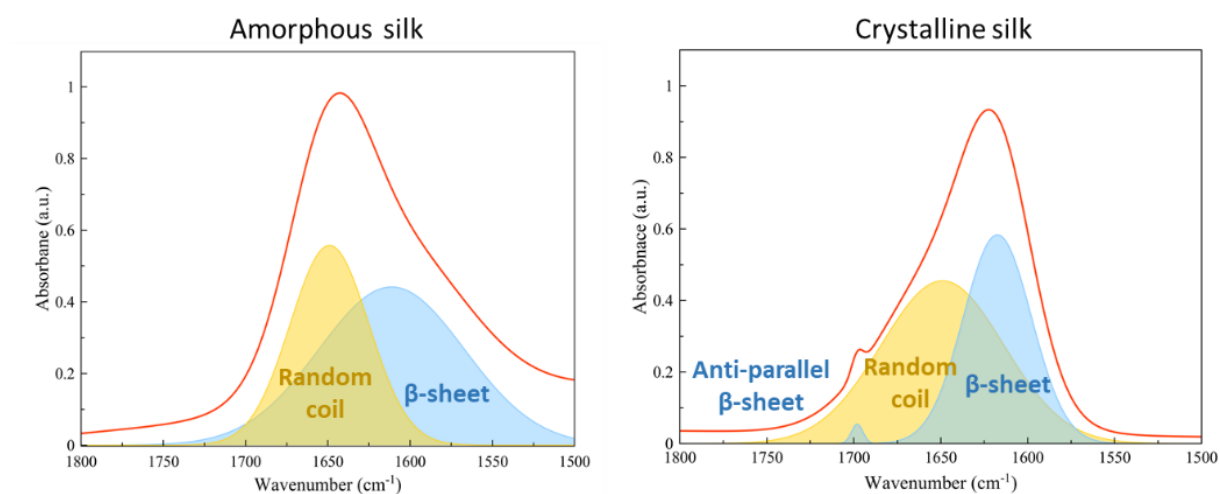


Figure 23: Schematic diagram of the components of silk fibroin Amide I peak. During crystallisation, the  $\beta$ -sheet component is increased, resulting in a shift of the centre of mass in the amide I peak towards lower wavelength values.

## 5. Imaging

### 5.1. Optical and confocal microscopy

All optical images of the silk structures and patterns were collected by a Diaphot TMD300 microscope (Nikon Instruments, Japan) using a Moticam 5MP camera (Motic instruments, Spain) and Stemi 305 (Zeiss, Germany) using an Axiocam 105 colour camera (Zeiss, Switzerland).

Optical profilometry images were collected by ContourGT-X 3D (Bruker, USA).

Fluorescent images were collected by LSM510 Upright Meta laser scanning confocal microscope (Zeiss, Germany) equipped with an objective lens (Achromplan 10x/0.3 NA), lasers emitting light in the UV and visible spectral ranges (Argon/2 - 458, 477, 488, 514 nm, HeNe1

- 543 nm, HeNe2 - 633 nm), and tuneable Ti:Sapphire laser capable of excitation wavelengths between 690 and 1040 nm.

All images were analysed by ImageJ (1.48v).

## 5.2. Scanning Electron Microscopy (SEM)

The characterisation of the microstructure of the silk scaffolds and patterns was performed by XL 30 S FEG (Philips, Netherlands) and Nova NanoSEM 450 (FEI, USA) SEMs. Since the XL 30 S FEG requires high voltage to operate (20 kV), the high sensitivity of silk to the beam and low image quality, it was used only during preliminary experimental work. All SEM images presented in this thesis were taken by Nova NanoSEM 450.

For sample preparation, scaffolds were cross-sectioned using a scalpel and washed with ethyl acetate. Silk patterns and films were fabricated on microscope slides and were directly imaged on the slides without additional processing. All samples were dry during imaging. The samples were placed on an aluminium stub covered with carbon tape. Due to the low accelerating voltage of the Nova (1 kV), no significant charge accumulated on the sample, therefore, no coating was applied. All images were taken at accelerating voltage 1 kV, beam spot 3.0 using an Everhart-Thornley Detector (ETD).

## 6. Summary

A summary of the main equipment used in this thesis can be seen in Figure 24 below. Specific methodology relevant to each chapter may be found accordingly: Direct laser writing (chapter 3); Rheology, UV-vis and IR spectroscopy, projection stereolithography and imaging (chapter 4); Rheology, SEM imaging, IR spectroscopy and mechanical testing (chapter 5).



Figure 24: The main equipment used in the experimental procedures of this thesis.

# Chapter 3

---

## 1D direct laser writing of silk patterns

## Summary

This chapter discusses the suitability of native silk for direct laser writing (DLW) by exploring fabrication methods using a photo-curable silk solution. The parameters required for pattern writing were optimised and the resulting silk structures then discussed. Following this, the photo-curing mechanism is evaluated and discussed alongside post-processing routes including pattern stability, structural conversion and the effect of photo-bleaching. Finally, preliminary cell work has been used to evaluate the potential of silk-DLW structures in biomaterials applications.

## 1. Introduction to Direct laser writing (DLW)

Direct laser writing micro stereolithography ( $\mu$ SL) is a fabrication technique that allows one to fabricate 3D objects<sup>297–300</sup> through photo-polymerisation of a polymeric resin<sup>301</sup>.

### 1.1. Theory and Mechanism

The basic components involved in DLW are a transparent monomeric solution, a photoinitiator and a laser source. To write, a laser beam is focused inside a transparent material, mixed with a photo-sensitive dye resulting in polymerisation at the focal spot. The size of the focal spot, (or structure resolution) can be controlled by the choice of photoinitiator, laser beam, complementary optics and overall experimental parameters<sup>302</sup>.

Photo-polymerisation occurs when a receptive molecule absorbs a photon which then excites said molecule from a ground to a higher energetic state. This excitation generates highly reactive radicals which can then go on to form cross-links between free monomers, inducing polymerisation (Figure 25)<sup>272,301–303</sup>. However, one of the drawbacks of single-photon stereolithography is that the beam is absorbed only within the first 10-50  $\mu$ m from the surface of the resin. This limits the technique to planar patterning. Additionally, radical polymerisation is easily quenched by oxygen, so the reactivity is reduced in an open environment.

Therefore, multi-photon polymerisation can overcome such drawbacks as it allows polymerisation within the volume of the resin. In multiple photon absorption, two (2PP) or more photons are used, with the sum of their energy equal to the energy gap between the ground and an excited state of the target molecule/photoinitiator. Hence to achieve 2PP, the sample is illuminated with double the wavelength of the absorption maximum of the

photoinitiator and the photoinitiator needs to absorb 2 photons, in turn, to go from a ground to intermediate, to an excited state and thus generate radicals.

The probability of simultaneous absorption (A) in a multiphoton polymerisation reaction is given by:

$$(1) \quad A = \frac{P^{N_{abs}}}{T^{N_{abs}-1}}$$

Where P is the laser pulse energy,  $N_{abs}$  is a number of photons absorbed, and T is the laser pulse width. Due to the short lifetimes involved in the process (both photons absorbed within a timescale of  $10^{-16}$  s), these 2PP initiations are rare and require a high photon flux, usually generated by femtosecond lasers, such as Ti:Sapphire<sup>194,218,303,304</sup> which allow the average laser power to be kept low<sup>304</sup>. This is beneficial, especially when dealing with proteins and biological materials which are sensitive to heat generated from high laser powers<sup>305</sup>.

This simultaneous absorption can only happen in the region of the focal area. This is highly beneficial for high-resolution fabrication since the probability for non-specific polymerisation outside the focal region is extremely low. Additional benefits of multi-photon polymerisation are related to the longer wavelength used in this approach which provides greater sample penetration depth<sup>306</sup>.

While in single-photon absorption the number of the absorbed photons ( $N_{abs}$ ) depends linearly on light intensity (I), in multi-photon absorption, it is proportional to the square of the light intensity ( $I^2$ )<sup>301</sup>. Due to the Gaussian laser intensity profile, and the fact that cross-section is dependent on  $I^2$ , a smaller focal volume is exposed in comparison to single-photon polymerisation<sup>307</sup>. This allows the fabrication of structures with a higher resolution. In fact, sub-wavelength structures with a resolution of < 100 nm can be produced by 2PP<sup>308</sup>.



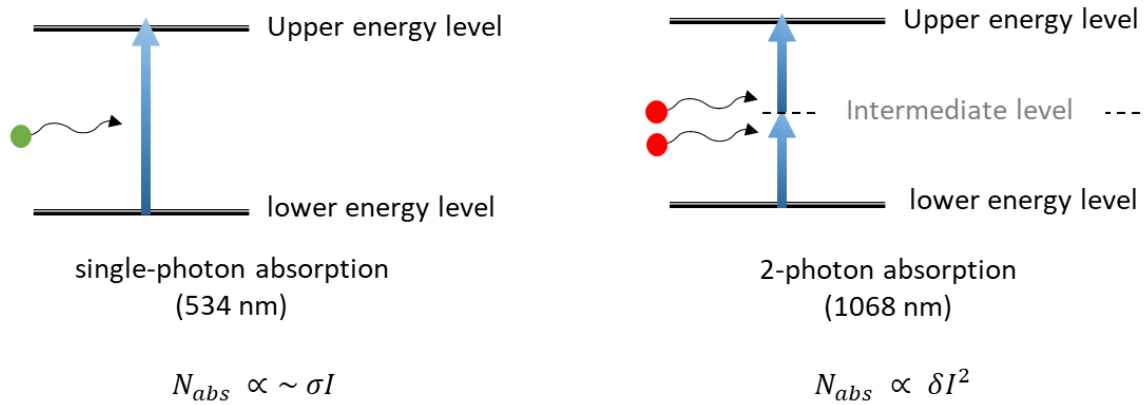


Figure 25: Diagram of energy transition in single-photon and 2-photon absorption. Equations describe the proportion between absorption and light intensities while  $\sigma$  and  $\delta$  are single and 2 photon constants, accordingly.

Despite the broad potential of multi-photon polymerisation in fabricating sub-micron patterns, for reasons of ease of experimental set-up, design flexibility in 2D and 3D and sub-micron structural resolution<sup>272,309</sup>, this chapter will focus on single photon polymerisation as a starting point for the exploration of DLW for silk patterning.

Overall, there have only been a handful of reports in the literature surrounding silk photo-curing, most being published in the last three years with even less for DLW and none that use native silk. Therefore, it is important to first develop and explore the basic fabrication approach and to better understand/control the photo-curing mechanism with easily visible micron-scale structures, before moving onto what is possible with nano-scale high-resolution fabrication.

## 1.2. DLW experimental set-up

A few essential components are required to create a DLW system <sup>218</sup>. An ultrafast laser as a photon source, optical lenses and mirrors to focus and direct the laser beam, a motion stage to generate patterns and a control software to operate the laser and the motion-stage.

A schematic illustration of the DLW set-up, used in this work, can be seen in Figure 26.

The photon source is typically a pico-second advanced diode-pumped solid-state frequency doubled Nd:YAG laser with single frequency green light beam (532 nm). The fundamental wavelength (1064 nm) is removed by a bandpass filter. The beam is expanded by a beam expander and reflected by a mirror at 90 degrees. The reflected beam is focused through a microscope objective lens (e.g. x10, NA 0.3) into a sample holder covered with photo-curable polymeric resin. The sample holder is mounted on an XYZ motion-stage (e.g. Aerotech ANT130XY base). The set-up allows writing across XY directions to produce desired patterns together with Z movement to allow multi-layer fabrication.

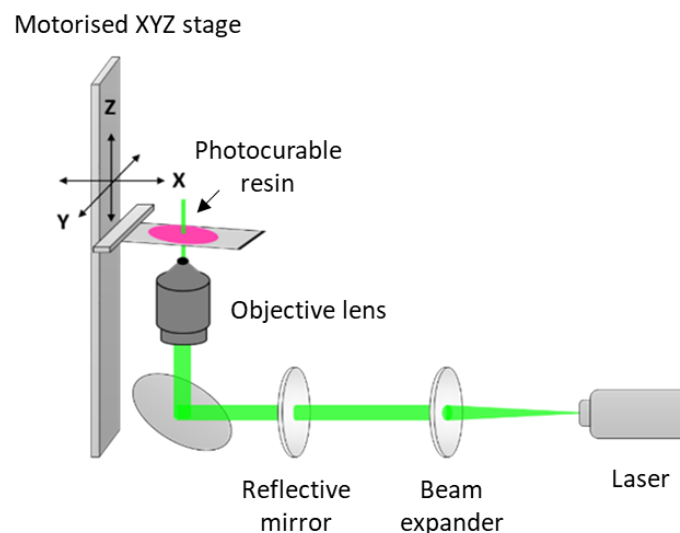


Figure 26: Typical components of a DLW set-up consist of a laser source, focusing optics, photo-curable resin and motorised stage.

### 1.2.1. Motion system

In DLW, writing is possible by the continuous movement of the polymerisation area (laser focal point) in the desired direction. This movement can be produced by 2 approaches: 1) By using a translation stage for sample movement whilst keeping the laser spot at a constant position, or 2) By deflecting the laser spot using a galvanometric mirror system while the sample position is kept constant <sup>272,303</sup>. The set-up choice is dependent on the experimental requirements including fabrication time, pattern resolution, and total sample size to name a few. In general, translation stages tend to be more suitable for small and low-weight samples providing an inexpensive solution, as presented in this work. However galvanometric mirrors are preferred when high speed is required, especially for industrial scale manufacturing <sup>310</sup>.

### 1.2.2. Laser sources in protein DLW

Originally, DLW techniques were developed for non-biogenic materials i.e. mostly polymers or ceramic particles that were embedded into photo-curable resins <sup>306</sup>. With the development of non-toxic photo-curable resins and crosslinking agents, direct write lithography became the state of the art technique for structuring protein-based materials, including alginate <sup>311</sup>, gelatin <sup>253</sup>, collagen <sup>265</sup>, albumin <sup>266,312</sup>, fibroin <sup>276,313</sup> and many more <sup>314</sup>.

The most common laser source in protein photo-lithography is a titanium-sapphire (Ti:Sapphire) femtosecond oscillator <sup>264</sup>. This laser allows a large wavelength range (650-1100 nm) and can generate ultrafast pulses required for multiphoton excitation. During the last two decades, a significant development in the field of protein DLW can be attributed to the work of Campagnola and co-workers who broadly explored the effect of Ti:Sapphire on natural protein polymerisation, activity and function <sup>265,266,270,315-321</sup>. For example, back in 2002, Pitts *et al.* <sup>265</sup> introduced a Rose Bengal-based photo-activator to increase the efficiency

of type 1 collagen crosslinking. In this work, linear patterns with micron and sub-micron resolution were fabricated by multi-photon polymerisation of collagen. A similar method was used by Kaehr *et al.*<sup>266</sup> in 2004 to fabricate patterns from bovine serum albumin (BSA) and avidin, used to guide neural cell growth or confine a cells' position on a surface.

Despite those promising applications, and even though this laser can generate high resolution with nano-range patterns, the price of this system (£80-250K) makes cost a limiting factor for many applications and most research groups. Additional laser sources such as neodymium-doped yttrium lithium fluoride (Nd:YLF)<sup>322</sup>, chromium-forsterite (Cr:forsterite)<sup>323</sup> and ytterbium-doped potassium gadolinium tungstate (Yb:KGW)<sup>253,276,324</sup>, can be appropriate for the generation of multi-photon excitation and have been shown as a suitable choice for multi-photon imaging and fabrication. In 2011, Ovsianikov *et al.*<sup>253</sup> utilised 2PP from a Yb:KGW laser source to fabricate 3D scaffolds made from gelatin, which proved suitable for cell growth. However, the potential of Yb:KGW lasers in DLW has not been fully explored due to limited availability and prohibitive cost.

A decade ago, Kaehr *et al.*<sup>312</sup> suggested the use of neodymium-doped yttrium aluminium garnet (Nd:YAG) laser as a suitable low-cost alternative to the Ti:Sapphire laser for protein DLW. In their work, a sub-micron focal point was reached by focusing the laser output through high numerical aperture optics resulting in successful protein photo-crosslinking. The introduction of this inexpensive (£10-25K) low power (250 mW) laser has led the way to broader protein patterning applications. Turunen *et al.*<sup>304</sup> have demonstrated that when used for micro-patterning of avidin, bovine serum albumin (BSA) and biotinylated bovine serum albumin, Nd:YAG laser can generate comparable feature size and grain characteristics to that achieved by a Ti:Sapphire laser. A literature summary of the different laser sources used in protein direct writing is presented in Table 4 and in the interests of accessibility and

practicality, this chapter explores the suitability of a low-cost Nd:YAG laser for the patterning of native silk protein solutions.

*Table 4: Comparison of the laser parameters used for multi-photon excitations in protein materials as used appears in DLW literature.*

Ref	Laser type	Wavelength	Pulse rate	Laser power	Protein structured
265,266,270,315–321	Ti:Sapphire	650 - 1100 nm	> 100 fs	100 mW – 1 W	Collagen, BSA, avidin, fibrinogen, fibronectin, concanavalin A, silk
322	Nd:YLF	532 nm	150 ps	-	BSA
323	Cr:forsterite	1278 nm	110 fs	3.5 kW	Muntjac deer chromosomes
253,276,324	Yb:KGW	515, 1030 nm	230, 300 fs	-	gelatin
304,312	Nd:YAG	1064, 532 nm	600 ps	250 mW	BSA, biotin, avidin

### 1.3. DLW of Silk

Over the last 20 years, silk-based materials have gained increasing popularity in biomedical research <sup>22,24</sup>. In fact, section 4 in chapter 1 of this thesis presents the broad range of structures and applications that were introduced with the recent progress in silk processing techniques. Currently, some silk research is focusing on the process of laser-based fabrication, investigating the suitability of silk proteins (mostly fibroin) to photo-structuring.

The summary of the silk DLW literature, published so far, is presented in Table 5. As a pioneering step in the field of silk laser writing, Applegate *et al.* <sup>325</sup> investigated multiphoton absorption of reconstituted *Bombyx mori* silk solutions. The study confirmed a 3-photon

absorption for silk at 805 nm and suggested its suitability for DLW tissue engineering (e.g. micro-machining in silk gels for scaffold fabrication). At the end of 2015, Sun *et al.* <sup>270</sup> were the first to report aqueous multiphoton lithography of silk fibroin and silk/metal nanoparticle composites. They fabricated silk lines and patterns using Ti:Sapphire laser and Methylene Blue (MB) photoinitiator. In the next year, Maximova *et al.* <sup>276</sup> used a femtosecond laser for both: patterning of amorphous silk and ablation of crystalline silk films at the micron scale. Most recently, Dickerson *et al.* <sup>271</sup> have demonstrated the ability to print silk/Ru(bpy)<sub>3</sub><sup>2+</sup> self-supporting 3D structures, using Nanoscribe Photonic Professional GT system equipped with a femtosecond solid-state laser.

Currently, all silk-DLW publication used pre-processed reconstituted silk (RS) fibroin solutions in the fabrication process. This work explores the feasibility of the gold-standard native silk (NS) for DLW applications and discusses the benefits of NS in compared to RS. It is also utilises, for the first time, a low-cost Nd:YAG laser in silk DLW providing broad research opportunities for those with a limited budget. Other benefits of native silk in photo fabrication will be discussed in the next chapters.

*Table 5: Comparison of multi-photon direct laser writing publications of silk protein.*

Ref	Laser type	Wave-length (nm)	Pulse rate (fs)	Laser power (mW)	minimal feature size (µm)	Silk type	Photo-initiator	Silk concentration (wt%)
<sup>270</sup>	Ti:Sapphire	800	120	75	< 1	RS, RS/AgNO <sub>3</sub> , RS/HAuCl <sub>4</sub>	Methylene Blue	2.5
<sup>271</sup>	NIR Fibre laser	780	115	100	< 5	RS, RS/Ru(bpy) <sub>3</sub> <sup>2+</sup>	Rose Bengal, Ru(bpy) <sub>3</sub> <sup>2+</sup>	13.5
<sup>276</sup>	Yb:KGW	1030	230	-	3	RS	-	10
This work	Nd:YAG	1064, 532	600K	250	< 20	Native Silk	Rose Bengal	0.5-1

#### 1.4. Photo-dye selection in protein DLW

Another key element in direct writing is the photo-reactive-dye or photoinitiator. The role of the photoinitiator is to initiate the radical coupling reaction after light exposure, by the generation of free radicals <sup>326</sup>. The initiated radicals will, in turn, generate radicals on the residues of the protein, most often aromatic side groups such as tyrosine and tryptophan <sup>327,328</sup>. The aromatic side groups, in turn, will generate a covalent bond by crosslinking to second polymer chain <sup>327</sup>.

It is important to match the absorption spectra of the photoinitiator to the operating laser wavelength to increase the probability of the photon excitation and the crosslinking reaction.

When dealing with native proteins, it is important to keep in mind the high sensitivity of these materials to their surrounding environment. Various conditions such as changes in temperature, pH, mechanical shear, solvents and time, are known to induce denaturation and gelation in protein solutions <sup>22,54,55,62,65,69,87,97,329–332</sup>. Therefore, to achieve control over the fabrication process it is beneficial to keep the fabrication method as simple as possible, introducing the minimum amount of additional chemicals into the protein solution. Furthermore, cellular toxicity of the photoinitiator is highly important and therefore when DLW used in medical application, a photoinitiator is usually chosen from the range of clinically approved materials <sup>333</sup>.

When working with silk proteins, Methylene Blue (MB) <sup>22</sup>, Rose Bengal (RB) <sup>35</sup> and riboflavin <sup>50</sup> have been shown to be suitable choices for photo-lithography depending on the wavelength of the lasers used. Those dye are commonly used for various medical treatments <sup>226,334,335</sup> therefore, should not raise concern when discussing cytotoxicity.

## 2. Materials and Methods

### 2.1. DLW set-up

Direct laser writing of silk/RB was performed using a custom-built DLW set up including a passively Q-switched diode-pumped solid-state (DPSS) Nd-YAG microchip laser with an integrated second harmonic generator, with a sub-ns pulse duration (Alphas, Gottingen, Germany). This laser emits at wavelengths of 1064 and 532 nm (45 kHz repetition rate). The 1064 nm was filtered out by a band-pass filter. The 532 nm laser output was expanded by Galilean beam expander to ~ 8 mm beam diameter, reflected by a silver mirror and focused through a 10× objective lens with NA 0.3 (Carl Zeiss, EC Plan-Neofluar). The beam was focussed through a microscopic glass slide mounted on a high precision XYZ stage (Aerotech ANT130XY base for XY-translation and PRO115 for Z-translation). In each experiment, 10 µl of the silk solution (0.5 – 2 wt%) was dispersed on a glass slide. The patterns were written, by manually focusing the laser just above the glass-silk interface. The focus was defined as the Z position for minimum laser focal spot size.

To explore two-photon polymerisation (2PP), the same set-up was used, however, the 532 nm wavelength was deflected away by a silver mirror and blocked by a beam stopper.

### 2.2. Photoinitiator preparation

Rose Bengal sodium salt, riboflavin 5'-phosphate (water-soluble formulation of riboflavin), Brilliant Blue, Methylene Blue and Direct Red 80, were all purchased from Sigma-Aldrich. A stock solution was fabricated from each photoinitiator by mixing 0.1 g of material with 10 ml of type 2 deionised water (DI). Each stock solution stored in the dark before use.



For UV-Vis spectroscopy analysis, each stock solution was diluted to receive optimal absorption spectra. The dilution ratios were as following:

*Table 6: Photoinitiator dilutions required to collect UV-VIS absorption spectra*

<b>Photoinitiator</b>	<b>Stock solution dilution ratio</b>	<b>Final photoinitiator concentration</b>
Rose Bengal	1:500	0.02 wt%
Riboflavin	1:300	0.03 wt%
Brilliant Blue	1:200	0.05 wt%
Methylene Blue	1:400	0.025 wt%
Direct Red	1:25	0.4 wt%

### 2.3. Photo-curable silk fabrication for DLW

Native silk was extracted from the silk glands of *B. mori* silkworm and diluted with water to produce a range of protein concentrations from 0.3 to 2 wt% (for more details see methods chapter). A photocurable silk solution was produced by the addition of 0.03 wt% of photoinitiator to the silk protein solution. All the experimental set-up was in a dark room, the photoinitiators and the samples were covered with aluminium foil to avoid a premature crosslinking reaction. All solutions were mixed with the photoinitiators immediately before the experiment and the photocrosslinking reaction was initiated when the laser light was switched on.

### 2.4. Optical and confocal microscopy

Images of the silk patterns produced by DLW were collected using a Diaphot TMD300 microscope (Nikon Instruments, Japan) via brightfield, phase contrast and polarisation and a Stemi 305 (Carl Zeiss, Germany) optical microscope operating in reflectance mode. The images were further analysed by ImageJ (1.48v). Confocal and fluorescent images were collected by Upright LSM510 Meta laser scanning confocal microscope (Zeiss, Germany)

equipped with an objective lens (Achromplan 10x/0.3 NA), lasers emitting light in the UV and visible spectral ranges (Argon/2 - 458, 477, 488, 514 nm, HeNe1 - 543 nm, HeNe2 - 633 nm), and tunable Ti:Sapphire laser capable of excitation wavelengths between 690 and 1040 nm.

## 2.5. Characterisation of DLW patterns

DLW patterns were characterised using Fourier-transform infrared spectroscopy (FTIR) on a Nicolet 380 spectrometer (Thermo Scientific, Madison, USA) equipped with an attenuated total reflection (ATR) device (Specac, UK). Spectral data was collected between 800 and 4000  $\text{cm}^{-1}$ , 64 scans, 4  $\text{cm}^{-1}$  scan resolution. UV-VIS absorption spectra were collected using (Spectronic Unicam, UV 330, UK), in a spectral range between 230 nm and 600 nm. Peak fitting of the spectra was performed in MagicPlot software (Magicplot Systems, LLC, Russia). All peaks were fitted as Gaussians.

## 2.6. Cell culture

### 2.6.1. Cell seeding

NG-108-15 neuronal cells originated from mouse (*Mus musculus* neuroblastoma) and rat (*Rattus norvegicus*) glioma. RN-22 Schwannoma cells originated from rat Schwann cell. Both cell types were obtained from the European Collection of Cell Cultures (ECACC) (Public Health England, Porton Down, Salisbury, UK). Human dermal fibroblasts were extracted from abdominoplasty or breast reduction operations in accordance with the local ethical guidelines (under an HTA Research Tissue Bank license number 12179).

All cells were grown in Dulbecco's Modified Eagle Medium (DMEM) containing, fetal calf serum (FCS) 10% (v/v), penicillin/streptomycin 1% (v/v), glutamine 1% (v/v) and amphotericin/ fungizone 0.5% (v/v). The cells were kept in at 37°C with 5% CO<sub>2</sub> throughout the incubation period. After 3 days of incubation, cells were removed from the flask using

0.05% trypsin/EDTA (GIBCO, Invitrogen, Karlsruhe, Germany) and counted using a Neubauer chamber.

NG-108 and RN-22 cells were seeded in a 12 well plate as following: 45k cells per 4 cm<sup>2</sup> for RN22 and 60k cells per 4 cm<sup>2</sup> for NG108-15 cells. NG108-15 cells seeded in serum-free media to avoid proliferation due to the high density of the cell population. Media was changed every 2 days and images were taken 6 days of incubation. NG108-15 and RN22 cell growth was stopped, by cell fixing, after 6 days.

Human dermal fibroblasts were seeded in a 12 well plate (5000 cells/4 cm<sup>2</sup>) and incubated for 24 hours. After incubation, the media was replaced. Cells proliferation was evaluated in both the old media (de-attached cells) and the sample (attached cells) using MTT and Alamar Blue assays.

#### 2.6.2. Alamar Blue and MTT assays

Alamar Blue (Resazurin) (7-Hydroxy- 3H-phenoxazin- 3-one 10-oxide) is a non-fluorescent blue dye. The dye reduction product is resorufin which has a bright pink colour and exhibits strong red fluoresce. This assay is used as an indicator for cell viability as evaluated by the oxidation-reduction reaction which occurs in live cells<sup>336–338</sup>. The main benefit of Alamar Blue is its water solubility which allows one to perform measurements without damaging cells, by avoiding fixing and extraction steps which are commonly used in other assays.

The Alamar Blue assay was performed 24 h after incubation. Firstly, the cell medium was collected (old-media) and replaced by 2 ml of fresh media per well. The old media was placed in a new well-plate to evaluate the viability of the cells which de-attached from the substrate (i.e. sample) during the seeding process. 200 µl of Alamar Blue solution (150 µM in PBS) was added to each well and the plates incubated at 37°C for 2 hours. From each well, 3 batches of

200  $\mu$ l of media were collected and placed in 96-well plate. The fluorescence was measured using a multi-well plate reader with excitation and emission wavelengths of 560 nm and 590 nm respectively.

Another way to evaluate the viability of cells is by a colorimetric assay which measures the metabolic activity of the cells. In viable cells, the metabolic activity can be determined by the reduction reaction of yellow 3-(4,5-dimethylthiazol-2-yl)-2,5-diphenyl tetrazolium bromide (MTT) <sup>339,340</sup>. In viable cells, MTT enters and passes into the mitochondria. In the mitochondria, MTT is reduced to an insoluble dark purple formazan product. The formazan product can be released from the cells by using organic solvents such as isopropanol, and its signal can be recorded by a spectrophotometer <sup>341</sup>.

As a result, an MTT assay was performed 24h after incubation. The media was removed from the wells and transferred to another well plate. The seeded samples were washed twice with PBS. MTT solution (0.5 mg/ml in PBS) was then added to the wells and the plates were placed back in the incubator at 37°C for 40 minutes. Then, the MTT solution was removed and 500  $\mu$ l of acidified isopropanol added to each well. From each well, 3 batches of 150  $\mu$ l of media were collected and placed in a 96-well plate which was then read using a plate reader set at wavelengths of 540 nm and referenced at 630 nm for changes in optical density.

### 2.6.3. Cell fluorescent staining

Cell fluorescent staining was performed according to the following protocol. After the end of the incubation time, the media was removed, and all the samples were washed with PBS. The cells were fixed with 3.7% formaldehyde solution for 20 minutes at room temperature. Following the PBS wash, Triton 0.1% (v/v) was added to each well and incubated for 30 min at room temperature and then washed again with PBS. Phalloidin – Fluorescein

Isothiocyanate labelled (Phalloidin-FITC) and Phalloidin – Tetramethylrhodamine B isothiocyanate (phalloidin-TRITC) were obtained from Sigma-Aldrich and diluted in DMSO to receive 0.05 mg/ml stock solution. Phalloidin-FITC (green) or phalloidin-TRITC (red) 0.2% (v/v) were added to each well and incubated for 30 minutes in the dark. Cell nuclei were labelled by DAPI 0.1% (v/v) and incubated for 10-15 min at room temperature in the dark.

### 3. Results and Discussion

Whilst some research has been performed on reconstituted silk (RS) solutions proving that silk can be structured by light, native silk (NS) has not been used in any light-based fabrication technique. However, due to the major differences between reconstituted and native silk proteins<sup>98,103</sup> it is important to validate this suitability for native silk for DLW fabrication and to explore the photo-curing mechanism. In addition, Nd:YAG lasers have never been used for any silk photo-curing, creating a gap in the field of low-cost silk patterning.

To explore the potential of NS and Nd:YAG lasers in filling this gap, several steps are required. Firstly, is important to fabricate a stable photo-curable NS solution, to allow silk photo-patterning without damaging any protein structure. Secondly, it is important to evaluate the optimal experimental parameters to better control the process. At last, it is important to evaluate the photo-curing mechanism and to examine the stability and characteristics of the fabricated patterns.

#### 3.1. Optimisation of the writing process

##### 3.1.1. Photoinitiator selection

To fabricate a photo-curable silk solution it is important to select an appropriate photoinitiator. Several parameters should be considered when working with native silk:

1. The silk solution used for patterning is highly diluted (1 wt%) native silk protein solution. Thus, the photoinitiator should be hydrophilic and easily dissolve in water.
2. Silk is sensitive to variations in pH<sup>63</sup>, therefore the photoinitiator should be neutral and inert to the silk protein. This eliminates diphenyl(2,4,6-trimethylbenzoyl) phosphine oxide and 2-hydroxy-2-methylpropiophenone photoinitiators commonly used in  $\mu$ SL<sup>342,343</sup>.

3. Silk is shear sensitive<sup>55</sup>, so the photoinitiator should be easily distributed in the sample without the need of stirring or mixing.
4. Silk is a natural material commonly used for medical applications<sup>24</sup> consequently the photoinitiator should be approved for medical use and have minimal toxicity.

In the current set-up tested for silk DLW, the laser source is a Nd:YAG laser which emits at 532 nm. To evaluate the optimal photoinitiator, 5 candidates were tested and a sample without photoinitiator was used as a control. To fit all the criteria the following materials were selected: Rose Bengal (RB) (556 nm), Direct Red (DR) (532 nm) and Brilliant Blue (BB) (554 nm) all with an absorption peak close to the wavelength emitted by the laser (Figure 27a). Pure silk without photoinitiator (280 nm), Methylene Blue (MB) (668 nm) and riboflavin (450 nm) were tested as negative controls (Figure 27b). All photoinitiators were mixed with 1% NS solution (which determined to be the optimal silk concentration for patterning, see section 3.1.1) and stored in the dark before use.

A droplet (2  $\mu$ l) from each solution was spread on a glass slide and the slide was mounted on a motorised stage. The laser was switched on and the stage allowed to move across XY direction to generate grid patterns.

As expected, pure silk and riboflavin controls did not produce any visible patterns. This is an indication that the photo-curing mechanism is indeed dependent on the reaction of the photoinitiator is not a direct effect of the laser's interaction with the silk proteins.

The samples that were mixed with RB, DR and BB, presented a clearly visible pattern after laser exposure (Figure 27c). This shows that those materials can be considered as suitable photoinitiators for native silk DLW. A very weak pattern was received with MB. This is interesting because MB has a significant absorption peak at  $\sim$ 266 nm while negligible

absorption peak at 532 nm. This may indicate that when mixed with MB, silk can undergo 2PP polymerisation under the current experimental conditions.

To choose the most appropriate photoinitiator, the intensity of the absorption peak should be explored when the same photoinitiator concentration is used (0.03 wt%). RB has the highest absorption peak at 532 nm, therefore, it will generate more radicals after illumination, leading to the most effective polymerisation reaction and as a result, to a higher quality pattern. In addition, RB is highly water soluble (1mg/ml) which simplify the solution preparation method and it is widely used in many medical applications<sup>344,345</sup>. Therefore, Rose Bengal was chosen as the most suitable photoinitiator for NS DLW and will be used in all further experiments discussed below.

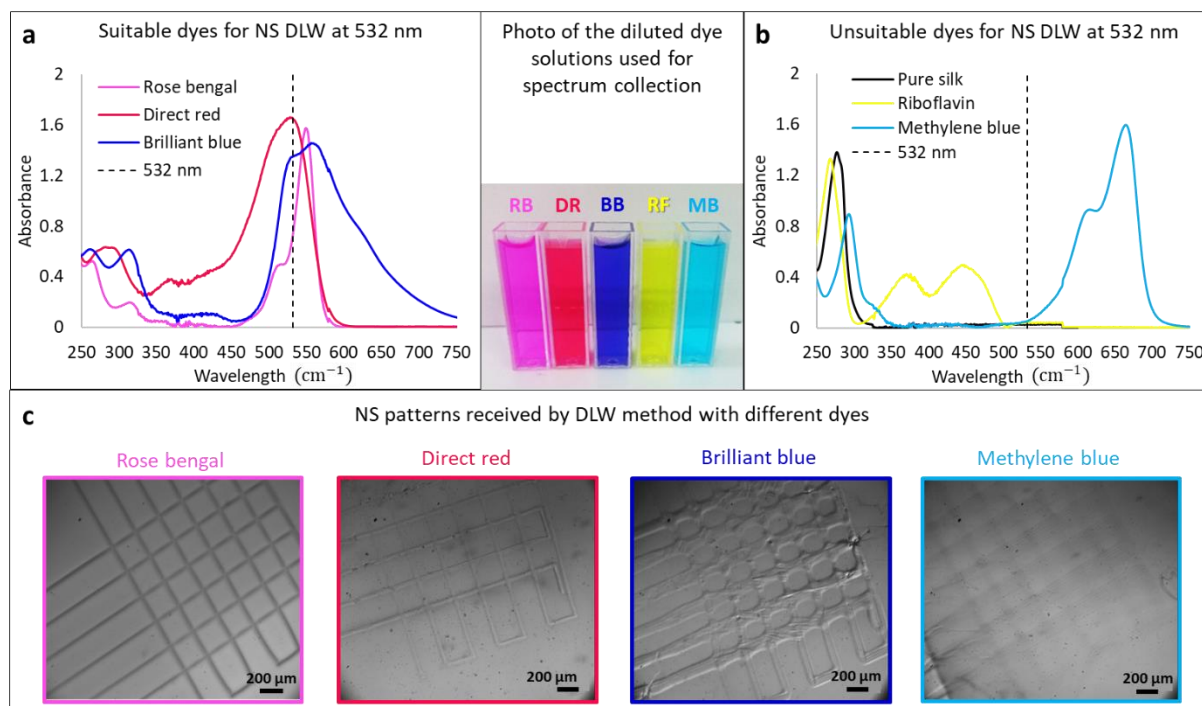


Figure 27: (a) Absorption spectra of Rose Bengal (pink), direct red (red) and brilliant blue (blue). (b) Absorption spectra of pure native silk (black), riboflavin (yellow) and methylene blue (light blue). The dashed line indicates 532 nm wavelength. (c) Silk structures as received by DLW with different photoinitiators. The structures were written at 0.1 mm/sec with maximum laser power.



### 3.1.2. Optimisation of Rose Bengal concentration

The optimal RB concentration was defined as the concentration that allowed to produce stable and elevated patterns without damaging the silk. Damage to the silk was evaluated by visual inspection and defined as local distortion in the pattern or discoloration of the silk as can be seen in the right image of Figure 28a or in Figure 29c (at the focal point).

A range of concentrations was tested from 0 wt% (no RB) to 0.1 wt%. No structure was observed without the addition of RB to the silk solution. The minimal RB concentration that resulted in a visible pattern was 0.01 wt%. However, the pattern was flat and challenging for characterisation. An increase in the RB concentration to 0.1 wt%, resulted in considerable damage to the silk pattern (Figure 28a). Following the structure received during photoinitiator selection experiment, an intermediate concentration of 0.03 wt% was set as the standard for all further experiments.

### 3.1.3. The concentration of native silk solution

When working with natural materials, one of the major challenges is material availability. Due to the fact that the material is extracted from an animal source, it is important to evaluate the minimal amount of protein which can allow the fabrication of sufficient quality patterns which are suitable for scientific analysis. As a key guiding principle used in this work, sacrificed animals were kept to a minimum and all the optimisation process were performed in order to determine the lowest usable concentration to avoid waste.

To define this value, various silk concentrations were tested. Silk solutions varying in concentration from 0.3 to 2 wt% were mixed with 0.03 wt% RB and the DLW system used to fabricate a criss-cross solid-like pattern on top of the liquid unstructured silk layer. The results showed that *B. mori* NS/RB solution can be structured using protein concentrations as low as

0.4 wt% (Figure 28b). This concentration is 6 times lower than the minimal concentration of reconstituted silk previous used in DLW literature (2.5 wt%)<sup>270</sup>. However, when NS concentrations below 0.5 wt% were used, the resulting pattern remained flat on the surface of the slide and was difficult to image and analyse. At concentrations above 1 wt%, the patterns were more pronounced, stable when immersed in water and provided good quality images when assessed by visual inspection. When doubling the concentration (to 2 wt%) no significant improvement in pattern quality was recorded. In the current silk DLW literature, significantly higher concentrations are used for reconstituted silk patterning (>10 wt%)<sup>271,276</sup>. Therefore, whilst increasing native silk concentration might improve pattern stability, it also leads to higher solution viscosity and due to aggregation effects, a shorter shelf life<sup>55</sup> which complicates both handling and storage. In addition, to reach such a high silk concentration large number of silkworms are required, which presents further ethical and practical complications. As a result, when all the factors are considered, a 1 wt% NS solution was set as the standard concentration for all future DLW work.

#### 3.1.4. Sample Z position

In order to investigate the effect of sample positioning, in relation to the laser's focal point, a silk solution was spread on a glass slide and the position of the glass slide was adjusted in the Z direction. The sample was placed at the estimated position of the focal point and 0.4 mm above the focal point. Grid patterns were then written at a speed of 0.1 mm/s. When positioned at the focal point, the line pattern was thin (15  $\mu\text{m}$ ) and raised above the surface after drying (Figure 28c). When the sample was illuminated above the focal point, the pattern was flat and significantly wider (100  $\mu\text{m}$ ). In addition, for these defocussed samples, an internal line architecture was noticed, possibly as a result of silk fibroin alignment occurring under the laser beam or as an artefact of the optical setup. These results show that the

positions of the sample might have a strong effect not only the resolution of the patterns but also their topography and structure. Hence the selection of the focal point position is highly dependent on the final application and will be discussed in the following sections.

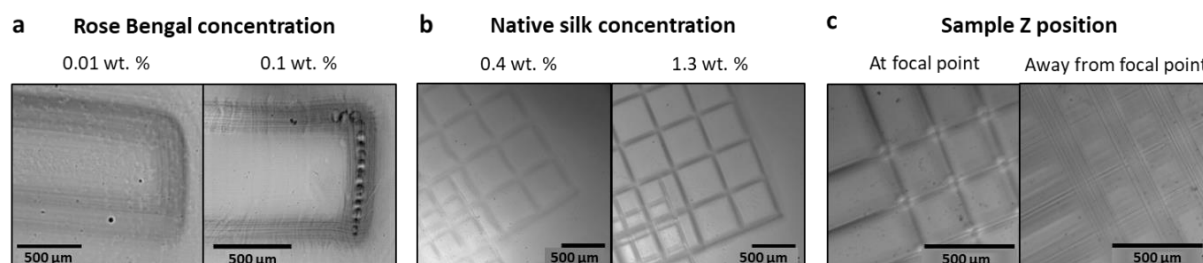


Figure 28: (a) Variation in Rose Bengal concentration, (b) Variation in native silk solution concentration, (c) Variation in sample Z position from the focal point of the laser.

### 3.1.5. Laser parameter optimisation

Various experimental parameters can affect the final resolution and size of the patterns generated. The quality of the pattern, or pattern resolution, was defined by the width of the line created by DLW, with higher resolutions representing narrower lines. However, whilst thinner lines can allow finer structuring, increasing pattern resolution, wider lines can shorten the production time and allow one to cover a larger area with fewer lines, ideal for bulk structuring. The main parameters affecting line width are writing speed, laser power and spot size of the laser beam.

It is important to note that in a nonhomogeneous protein solution, the selection of the writing direction/location might also affect the final line width. This is due to variations in sample viscosity, concentration gradients and different light absorptions across the sample. However, the silk solution used in this work is very dilute (1 wt%) resulting in minimal chances for unwanted protein aggregates. In addition, the RB is highly water soluble which allows full dissolution of the photoinitiator without visible solid residues. Therefore, NS/RB solution may

be considered as homogeneous and the line resolution is not dependent on the writing direction/location.

#### 3.1.5.1. Writing speed

The writing speed was defined as the speed (mm/s) at which the stage moves along X and Y directions. To evaluate the effect of the speed on line thickness, a straight line was written at different speeds (from 0.1 to 3 mm/s) under constant laser power (250 mW). A reverse correlation was found between the writing speed and the final line width after sample drying (Figure 29a). The slowest writing speed (0.1 mm/s) resulted in pronounced line, 20  $\mu\text{m}$  in diameter. By increasing the writing speed to 2.5 mm/s, the line width was reduced to 10  $\mu\text{m}$ . When increasing the writing speed above 2.5 mm/s, the resolution slightly improved (7  $\mu\text{m}$ ), however, the pattern was flat and difficult to analyse. In addition, the pattern was not stable when washed with water and separated from the glass slide. Reducing the writing speed below 0.1 mm/s, was not practical since the writing process was too slow to allow effective fabrication. The optimal writing range was, therefore, determined to be between 0.1 and 2 mm/s, allowing the fabrication of line with a width between 20 and 10  $\mu\text{m}$  accordingly. This writing speed is similar to that used by Sun *et al.*<sup>270</sup> (0.1 mm/s) and significantly faster than the speed of two-photon polymerisation in the publication of Dickerson *et al.*<sup>271</sup> (0.05 mm/s).

#### 3.1.5.2. Laser output

The laser output was defined as the laser power measured after the beam expander, just before the beam was reflected into the objective lens (Figure 26). The DLW set-up did not allow the measurement of the power at a position closer to the sample. The alignment of the DLW set-up, including the position of the lenses and the sample, was kept constant during the optimisation experiments. The writing speed was also kept constant (0.1 mm/s) during

the experiments. When the laser power was attenuated between 335 mW (maximum laser power) and 215 mW, the line width was about 20  $\mu\text{m}$  (Figure 29b). A small drop in line width (to 16  $\mu\text{m}$ ) was measured when the laser power was dropped to below 200 mW. When the laser power was below 100 mW no significant structures were recorded. Therefore, a laser power of 150 mW was defined as the minimal power required for DLW of native silk. However, due to the insignificant difference in resolution, but a faster reaction rate, a power > 250 mW was preferred in all further experiments.

#### 3.1.5.3. Sample alignment

To achieve the optimal resolution, under all experimental conditions, it is essential to accurately define the position of the beam focal point. At this focal point, the intensity is the highest which will result in a maximal energy transfer to the sample and the most effective polymerisation process.

To evaluate the optimal sample alignment across the Z-axis, a glass slide with NS/RB solution was placed at a random position near the focal point and the stage was moved along Z direction, in 0.05 mm steps, above and below the initial sample position. Other experimental parameters were kept constant (laser output: 335 mW, writing speed: 0.1 mm/s). When the sample was placed at the exact focal point of the laser, considerable damage to the sample was recorded (Figure 29c). This might be a result the glass physically breaking down (cracking) underneath the sample, or damage to the sample as a result of overheating. Therefore, writing at the exact focal point should be avoided and the optimal sample position was defined as 0.05 mm above the focal point.

All the optimised experimental parameters are summarised in Table 7 below:

Table 7: The optimised parameters as evaluated for NS/RB DLW writing.

Parameter	Optimised value
Native silk concentration	1 wt%
Photoinitiator	Rose Bengal
Photoinitiator concentration	0.03 wt%
Sample position	<u>Close to the focal point:</u> Thin uniform line (20 $\mu\text{m}$ ) <u>Away from focal point:</u> wide line (100 $\mu\text{m}$ ) with internal architecture
Writing speed	0.1 mm/s < v < 2 mm/s
Laser output power	Minimal (150 mW), optimal > 250 mW
Sample alignment	+ 0.05 mm above the focal point of the beam

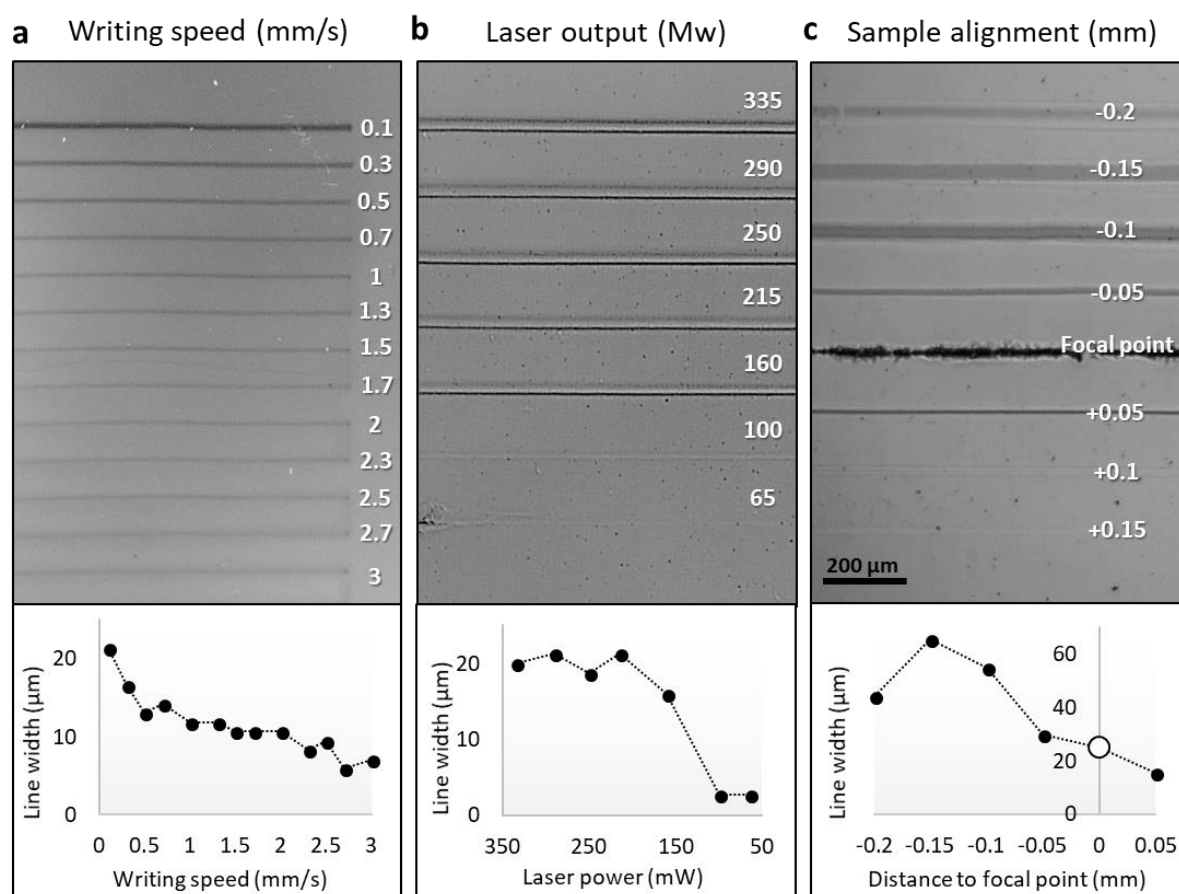


Figure 29: optimisation WLD parameters for (a) writing speed (b) laser output and (c) sample position and the written line pattern using each parameter. Below each image presented the line width as analysed by ImageJ. The hollow circle indicates the predicted width since the line was damaged and not suitable for analysis.

### 3.1.6. The effect of over-heating by the laser

Two of the writing conditions used during the optimisation process clearly led to sample damage. When a high concentration (0.1 wt%) of RB was added to the silk solution or the alignment of the sample was at the focal point of the laser, the written structures appeared black, distorted and had a non-uniform shape. In both cases, it is proposed this might be a result of over-heating the sample, similar to boiling, leading to denaturation of the silk protein<sup>305</sup>. To verify this, it is possible to calculate the heat rise in a sample during laser exposure.

The heat capacity of the sample is defined as the ratio between the heat (energy) added to the sample and the temperature change following this additional heat<sup>346</sup>.

The temperature increase ( $\Delta T$ ) can be estimated by the following relation depending on the energy absorbed by the sample ( $E$ ), the sample mass ( $m$ ) and the specific heat capacity of the sample ( $C$ ):

$$(2) \quad \Delta T(^{\circ}\text{C}) = \frac{E \text{ (J)}}{m(\text{kg}) \cdot C \left(\frac{\text{J}}{\text{kg} \cdot ^{\circ}\text{C}}\right)}$$

The heat capacity is constant, under the given experimental conditions, therefore, an increase in laser energy or a decrease in the beam spot size, might significantly increase the temperature of the sample leading to over-heating.

Since all silk solutions used in this work are dilute (1 wt%), the heat capacity was assumed to be similar to that of water ( $1481 \frac{\text{J}}{\text{kg K}}$ ). The total amount of solution used for a single experiment was 10  $\mu\text{l}$ , therefore, the volume of the sample under the focal spot was assumed to be no more than 1  $\mu\text{l}$ . The average laser power was defined as 250 mW. It is important to note that water has a low coefficient of absorbance at the wavelength of the laser used in the

current set-up (532 nm) resulting in an absorbance of only 5% of the energy<sup>347</sup>. Under those assumptions, an exposure of 1s to the laser beam will lead to a temperature increase by 2.5°C. However, RB salt (RB<sup>2-</sup>) and excited RB (<sup>3</sup>RB<sup>2-\*</sup>) have a strong light absorption at 532 nm<sup>348</sup>. An increase in photoinitiator concentration will increase the amount of energy absorbed by the sample, leading to a significant rise in sample temperature of up to 60°C (for full absorption) and up to 80°C, if the maximum laser power is used. Similarly, the level of absorbed energy can rise due to an increase in laser power, following longer exposure time, or a decrease in laser spot size.

All will result in substantial heating of the sample. It is well known that native *B. mori* silk fibroin is a thermo-sensitive material having a transition temperature of around 67°C<sup>349</sup>. Heating the sample above this temperature results in instability of the hydrogen interactions leading to irreversible protein aggregation and denaturation.

Therefore, it is desirable to avoid significant sample heating when patterning silk. This can be achieved by reducing the laser power, moving away from the focal point of the beam and by minimising the writing time.

### 3.2. Laser beam effects

The optimised parameters, as defined in the previous section were used to fabricate grid patterns from NS/RB solution (Figure 30a). Two regions of interest on the pattern were investigated by optical microscopy. The first interesting observation was a linear alignment of the silk along the writing direction which appeared in the laser exposed area. This can be clearly seen in a cross-section region (Figure 30b) where the silk alignment correlates with the direction of the laser writing.



Another area of interest was the initiation point at which the writing process started. At this position, the laser operated for 5 seconds before the beginning of the writing at 0.1 mm/s. (Figure 30c). At this point, a uniform radial growth of the laser affected region can be seen in all directions.

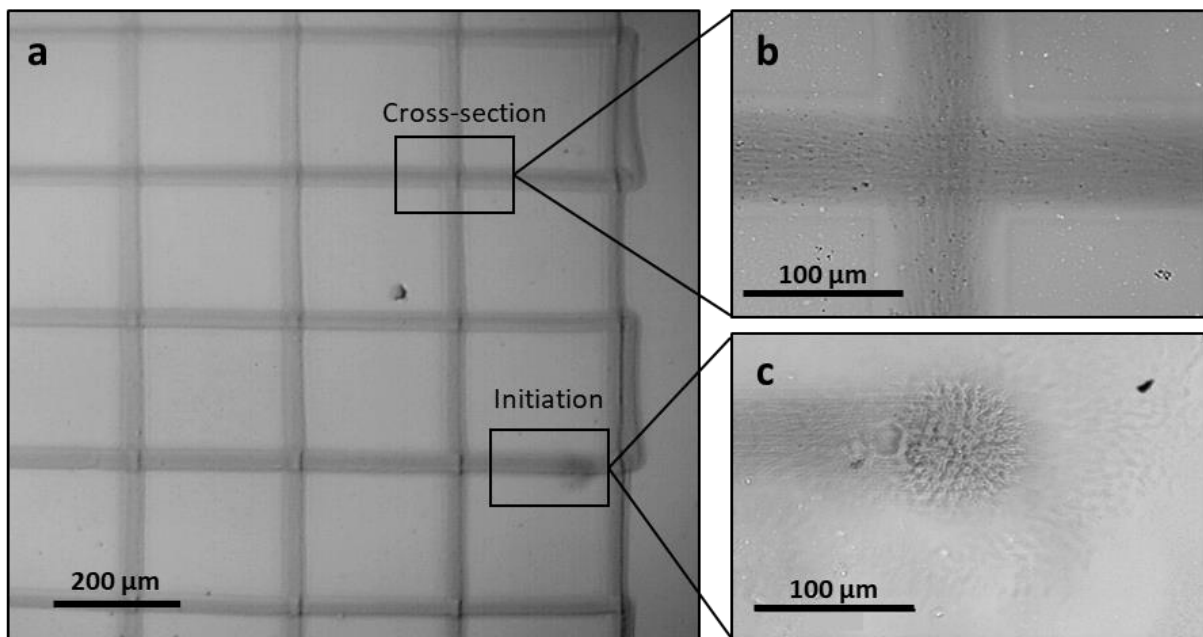


Figure 30: (a) Silk pattern as fabricated by DLW using optimised parameters. (b) Random elongated pattern of the silk along the writing direction. (c) Radial pattern as generated when the laser was kept in a static position for 5 sec.

To explain these observations, it is essential to discuss two main beam-effects, which are commonly seen in samples that were fabricated by laser writing: the formation of speckle patterns following laser light scattering and a radial pattern spread known as the heat affected zone (HAZ) <sup>350</sup>.

### 3.2.1. Speckle patterns

A speckle pattern is a phenomenon that occurs when highly coherent light, such as the light coming from a laser source, interacts with a rough surface <sup>351</sup>. The high degree of scattering of the beam from the surface results in intensity patterns leading to a fine granular structure

appearance. This structure usually appears to be bright and dark random spots with variable shapes and is evidence of intensity distribution and refractive index variation. Speckle patterns do not directly relate to the surface topography. As there is evidence to suggest a polymeric solution is not homogeneous, the results seen in Figure 30b might be a result of higher local polymer concentration leading to a higher refractive index<sup>352</sup>. Despite the fact that silk fibroin and Rose Bengal were fully dissolved in water, it should be noted that the solution was not fabricated in fully sterile conditions, therefore the presence of contaminants such as dust, impurities or other proteins in the silk<sup>353</sup> cannot be eliminated, increasing the chance of light scattering.

Variations in refractive index can also be related to the roughness of the silk layer distributed on the glass. In the current DLW set up, a glass slide with silk solution is illuminated with coherent laser light. When the light interacts with the surface of the silk/glass, wavelets are reflected in random directions from the surface (Figure 31a). The wavelets will interact with each other, at a given point in space, resulting in constructive or destructive interference. This will result in black (destructive) and white (constructive) speckle pattern on the silk. This phenomenon can also explain the linear alignment that was visible in some of the silk samples (Figure 31b). This alignment is formed when the beam is moving along the writing direction resulting in a line-like pattern due to the proximity of the speckle spots. When the distance between the spots is below the special resolution of the DLW technique (which depends on the experimental parameters), it is impossible to distinguish between two individual spots and a continuous pattern is seen.

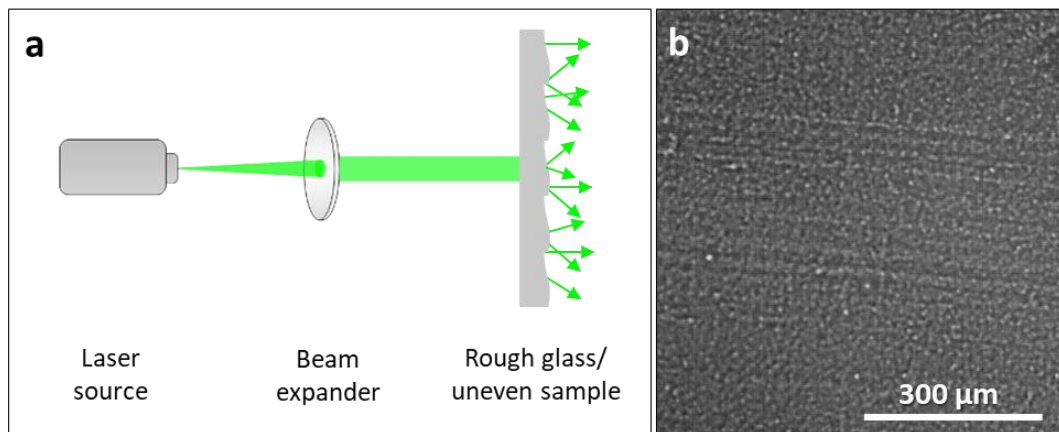


Figure 31: (a) Schematic illustration of speckle pattern formation. Coherent light is transmitted through translucent object with surface roughness and variations in refractive index. The light is scattered from the surface in random directions. (b) a typical speckle pattern received on NS/RB after DLW.

### 3.2.2. Heat affected zone

The Heat Affected Zone (HAZ) is highly discussed in the laser welding literature<sup>350,354,355</sup>. HAZ is defined as the area affected by the laser heat and the re-cooling process, resulting in structural modification and damage to the surface. The size of the HAZ is mainly dependent on the thermal diffusivity of the material or the time it takes to fully cool the material.

To quantify the area of the HAZ, a dot-like pattern was fabricated by DLW. To produce the pattern, the sample was kept at a constant position under the laser, for the duration of 5 s for each spot. The beam was switched off during the movement between the spots (Figure 32a). For each spot, the ratio between the region that was placed directly under the laser (Figure 32a, inner red circle) and the HAZ (Figure 32a, outer red circle) was calculated. It was found out that the area of the HAZ is about 10 ( $9.8 \pm 2.5$ ) times larger than the area directly located under the laser beam. This area size is affected by the laser exposure time and was not noticed when continuous writing was performed at 0.1 mm/s. When the sample was exposed to the

laser beam for longer than 10 secs, considerable damage to the silk was recorded, most likely due sample overheating as discussed previously in section 3.1.5.3.

Harzic *et al.*<sup>355</sup> have studied the effect of laser pulse rate on the size of HAZ in metals. The study showed that by using a femtosecond laser on aluminium sheets, the HAZ can be reduced to <2  $\mu\text{m}$  in compared to 40  $\mu\text{m}$  received for nanosecond laser. This study might suggest that by replacing the laser source of the DLW system and using a femtosecond laser, it is possible to minimize the effect of HAZ in the silk. However, due to the high cost of this modification to the current system, this solution is not practicable.

Lee *et al.*<sup>354</sup> have studied the beam damage effect following sample overheating as a function of the wavelength of the laser. The study was performed on a museum art piece which was made from silk fibres and wrapped in silver ribbon. The aim of the research was to select the appropriate laser wavelength which allows cleaning the silver without damaging the underlying silk. The study found out that laser pulses at a short wavelength (266 nm) resulted in no damage to the silk. However, when long wavelength (1064 nm) was used, significant silk degradation was recorded following sample overheating. These studies indicate that it is possible to control HAZ area by controlling laser parameters such as the laser pulse rate, the wavelength and the laser intensity.

### 3.2.3. Investigation of the surface topography

To enhance the effects of HAZ and speckle patterns described above, a grid pattern was written at a very slow speed of 0.01 mm/s onto the sample. A slow writing speed results in longer interaction times between the beam and the sample, enhancing beam damage effects. As expected, a clear line pattern was observed in the direction of the pattern writing and a large area around the laser pathway was structured (Figure 32b). When a  $300 \times 300 \mu\text{m}^2$

frame was fabricated, more than 83% of the internal area of the frame was affected by the laser and only  $50 \times 50 \mu\text{m}^2$  area did not present any alignment. This result shows that the true resolution should not be defined by the laser spot size alone and emphasizes the importance of beam damage investigation in DLW of silk and other proteins.

To evaluate whether the aligned line structures, as seen in Figure 32b, contributes to the surface topography of the pattern, a multi-layered sample was fabricated. Since the sample is soft and translucent, a single-layered pattern is difficult for characterisation and the surface roughness was below the detection limit of the confocal microscope ( $< 1 \mu\text{m}$ ). To enhance the roughness, 3 layers were written one on top of the other by moving the sample across Z direction,  $+0.05 \text{ mm}$  after the fabrication of each layer. (Figure 32c, top). Confocal microscopy analysis confirmed a grooved surface with a maximal depth of  $10 \mu\text{m}$  (Figure 32c, bottom). This suggests that the visible alignment on the surface is not a sole effect of the speckle pattern, but that a true surface architecture is formed by the laser, creating a grooved topography.

This result can lead the way for many possible applications including the guidance of cell growth along the grooves. As previously shown by Madduri *et al.*<sup>178</sup>, when fabricated by electro-spinning, the directionality of silk blend fibres can direct cell growth. It was also suggested by Lawrence *et al.*<sup>121</sup> that introducing a groove pattern on top of corneal silk films, produced by a soft-lithography method, an improvement in cell alignment, adhesion, mobility and proliferation was observed.

The depth of the grooves can be controlled by controlling the number of silk layers that are printed and by adjusting the writing speed. However, any attempt to add more than 3 layers

was unsuccessful, leading to a separation of the 4<sup>th</sup> layer from the first 3 layers and a distorted pattern.

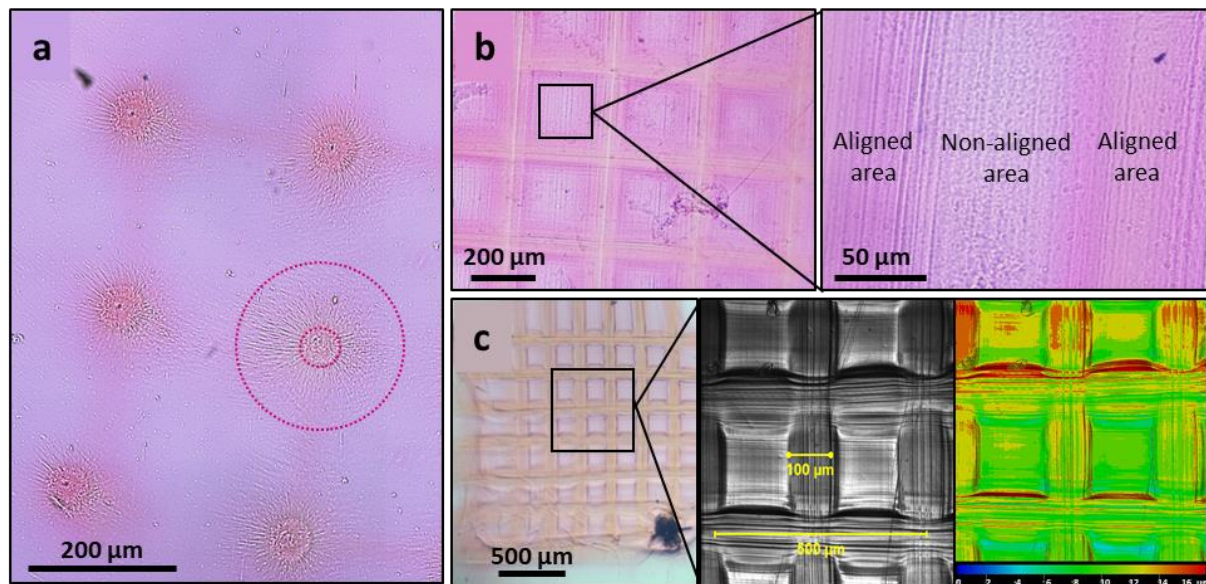


Figure 32: (a) HAZ calculation by dividing the outer red circle (total area) by the internal red circle (area directly affected by the laser). (b) Aligned and non-aligned regions as received with low writing speed (0.01 mm/s). (c) 3-layer pattern with a groove like surface as receive with slow-speed DLW, right images show the confocal images of the surface roughness of the pattern.

### 3.3. SEM analysis of silk DLW patterns

In an attempt to explore the alignment of the silk in response to DLW, the fabricated patterns were analysed by SEM. Images of the samples were collected by 2 different secondary electron detectors: Everhart-Thornley below-the-lens Detector (EDT) (Figure 33a) and immersion- through-the-lens (TLD) (Figure 33b). EDT detectors are widely used in electron microscopy and can provide information about sample topography and composition. The use of in-lens (TLD) detectors allows one to gain higher special resolution and to detect surface contaminations that are not visible by the EDT detector<sup>356</sup>. However, during imaging of the samples, both detectors failed to show any silk alignment and the surface appeared smooth without pronounced topographic contrast. Whilst there was some visible contamination,

probably as a result of dust particles attachment during the drying process, this is in direct contrast to the confocal microscope images (Figure 32c).

The main reasons for the lack of apparent structure may be attributed to a low sample-electron interaction volume. This volume is defined by the accelerating voltage, the atomic number and the density of the sample<sup>356</sup>. A low interaction volume will result in a low signal to noise ratio leading to the reduced contrast between the sample and the background during SEM imaging. An additional outcome of this is a low penetration depth which prevents the user from visualising anything deeper than the top surface features. Hence one possible reason for the lack of contrast might be a thin film layer that formed on top of the pattern during the drying process or as a result of surface restructuring as a result of exposure to ambient humidity<sup>357</sup>.

These effects could shadow the surface topography if the penetration depth is not sufficient. To probe this effect further it is possible to calculate the beam penetration depth,  $d$ , which is given by<sup>356</sup>:

$$d (\mu m) = \frac{0.1V_0^{1.5}}{\rho}$$

Where  $V_0$  (keV) is the acceleration voltage and  $\rho$  ( $g/cm^3$ ) is the density of the material. Since silk is highly sensitive to the electron beam, a low voltage of 1 keV must be used, to avoid denaturation of the protein<sup>358</sup>. The density of dry *B. mori* silk is  $1.34 g/cm^3$ <sup>78,359</sup> resulting in penetration depth of only 75 nm. This indicates that it is unlikely to obtain a reasonable quality images of the topographical contrast under the current imaging. In fact, the current SEM imaging method can only be used for the exploration of the top surface of the pattern.

One way to increase the voltage and the penetration depth is to coat the sample with a thin layer of conductive material such as carbon or gold <sup>360</sup>. However, carbon and gold-coated samples resulted in “black-screen” image without any visible pattern even at higher voltages of up to 5 keV. This is probably because the coating thickness did not allow sufficient penetration of the electron beam, which was < 1 μm even when the higher voltage applied. Considering the sample sensitivity towards the electron beam, and the absence of topographical features under all tested imaging conditions, one can conclude that SEM is not a suitable technique for the visualisation and characterisation of silk DLW patterns.

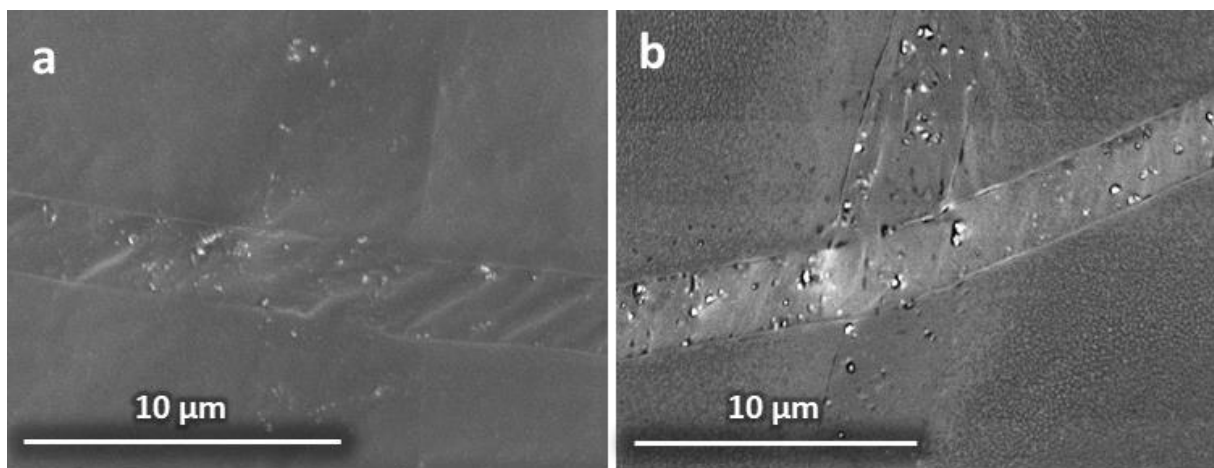


*Figure 33: SEM images of DLW silk structure. (a) EDT detector and (b) TLD detector of FEI Nova NanoSEM 450. No surface topography can be seen due to limited beam penetration depth.*

#### 3.4. Spectroscopic characterisation of the silk patterns

Usually, silk films are transparent <sup>123,361</sup>. As such, they are highly suitable for many applications such as corneal tissue engineering, components in soft electronics and as optical devices <sup>22,121,122,125,141,171,193,362</sup>. Hence it is critical to control the transparent properties of a silk during the patterning process in order to fit the functionality of the final products. However, some polymerisation processes can change the transparency level of the films resulting in a more opaque sample <sup>363</sup>. One such process that can damage the optical transparency is silk's



crystallisation or structural conversion<sup>364</sup>. Therefore, it is beneficial to investigate the mechanism of silk polymerisation during the DLW process in native silk.

Silk conversion level was evaluated by FTIR spectroscopy for unexposed silk solution and silk patterns that were fabricated by DLW. In addition, control spectra were collected after washing the sample with water (to remove unexposed silk) and after controlled conversion with MeOH solution<sup>87</sup>. All samples were air-dried before spectra collection, to avoid any spectral shifts due to the presence of water molecules<sup>365</sup>.

The position of amide I peak in the unexposed sample ( $1640\text{ cm}^{-1}$ ), represents the amorphous/unconverted silk structure (Figure 34, black). The same silk solution was also mixed with RB (0.03 wt%) and exposed to laser light (532 nm, 250 mW) for 5 min. To allow for a sufficient pattern size for uniform FTIR-ATR measurement, multiple lines were written to fully cover a rectangular area of 0.5 x 0.5 cm, a size extending beyond the focal spot size area of the FTIR-ATR accessory. The spectrum was then collected and compared to that of non-patterned silk film (Figure 34, red). No shift in the position of the amide I band was recorded, suggesting that no structural conversion was induced by the laser. This result is in agreement with the literature for RS DLW where no change in crystallinity was recorded in photo-polymerised silk<sup>276</sup>.

To remove the excessive RB and the non-polymerised silk solution, the sample was then washed with water for several minutes, the pattern dried, and spectra collected. Again, no significant shift in the amide I band position was recorded (Figure 34, pink). Though, a slight shift in the centre of mass of this band was noticed and is attributed to a water annealing process in the silk<sup>331</sup>.

Methanol is known to induce structural changes in silk fibroin, resulting in  $\beta$ -sheet formation and an increase in the degree of crystallinity<sup>87,366</sup>. As expected, when the pattern was immersed in methanol, a noticeable shift in the amide I peak was recorded (Figure 34, dashed pink). This confirms that the silk pattern fabricated by the DLW method was not converted prior to the methanol treatment.

The results of this FTIR study clearly show that silk/RB DLW does not induce crystallisation in the silk and the silk remains unconverted. This technique can open the door for many potential applications where specific patterns are required without modification of the silk structure. In addition, it is possible to attenuate the crystallinity of specific regions on the patterns by post-treatment to fabricate multi-structural pattern.

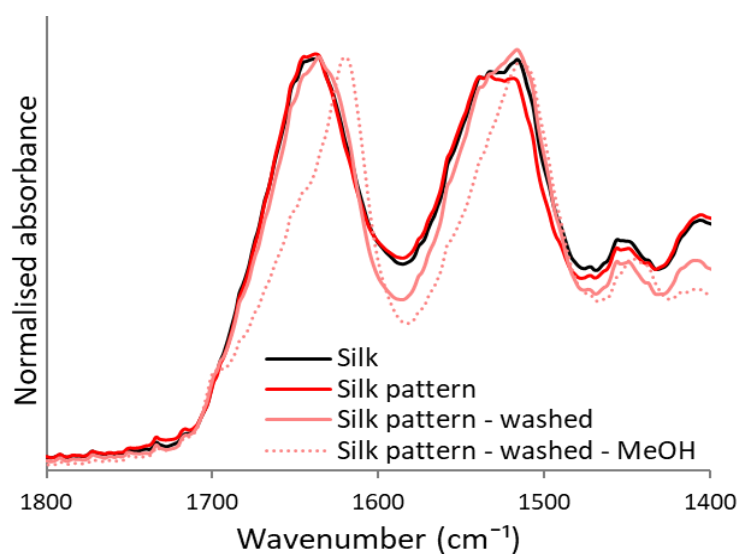


Figure 34: FTIR Spectrum of unexposed silk film (black); silk pattern-fabricated by DLW (red); silk pattern after immersing in water and drying (pink) and silk pattern after methanol treatment (dashed pink). No structural conversion was recorded in the silk after the DLW process.

### 3.5. Pattern transferability

All the DLW patterns described in this chapter were written on standard borosilicate microscope glass slides. This rigid glass slide platform allows a precise and high-speed (up to 3 mm/s) movement of the sample under the beam, without any distortion to the silk solution.

The optical quality of borosilicate glass permits laser penetration with minimal light absorption<sup>367</sup>, however, for many clinical applications, a soft flexible substrate and pattern material is required<sup>193</sup>. To address those needs it is desirable to investigate the capability to transfer the written pattern off the rigid glass substrate to a different surface, post-fabrication, without any significant pattern distortion.

To test sample transferability, a glass slide with a DLW silk pattern was immersed in a container filled with DI water (room temperature) directly after fabrication (Figure 35a). As previously stated in section 3.4 above, under these conditions the photo-crosslinked pattern remained stable while the non-exposed silk/RB solution dissolved (Figure 35b). After being immersed in water for a few seconds, the pattern separated spontaneously from the glass slide and floated on top of the water bath. A second glass slide was placed under the floating pattern and the pattern was carefully attached to the slide, avoiding pattern distortion as possible (Figure 35c). This indicates that the photo-crosslinking mechanism produces stable structures which are rigid enough to enable transfer to another surface but are also flexible to deform which may be useful for coating uneven or curved surfaces.

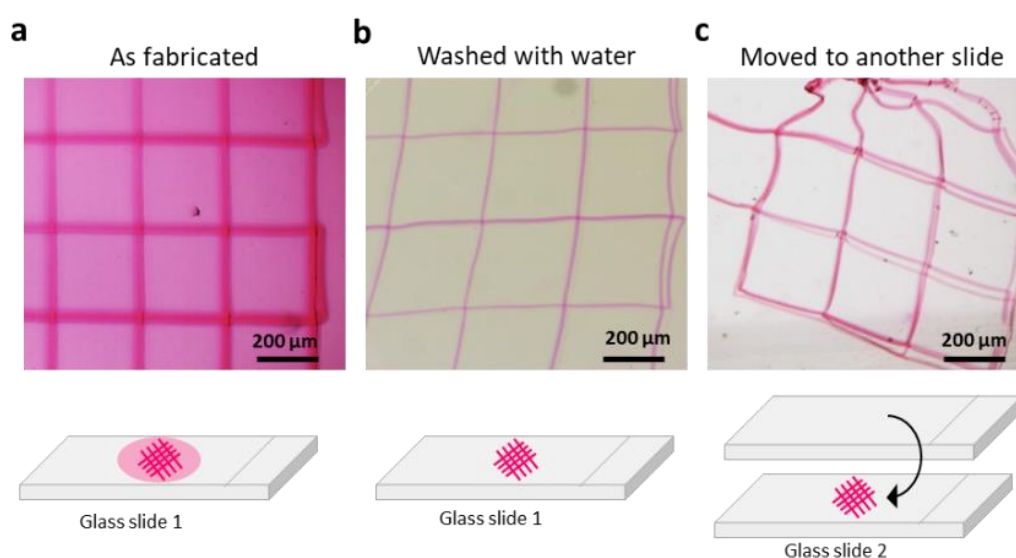
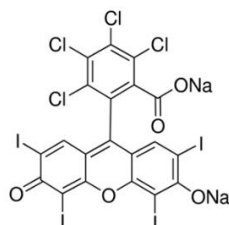


Figure 35: Transformation of the fabricated. (a) As fabricated. (b) After washing with water (c) after transferring to a different surface.

### 3.6. The mechanism of silk crosslinking with rose-bengal

Rose Bengal (4,5,6,7-tetrachloro-2',4',5',7'-tetraiodofluorescein) is a bright pink photoinitiator with a light absorption peak at 532 nm. Its sodium salt formulation, as seen below, is highly water soluble and often used in DLW as the photoinitiator.

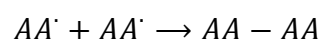
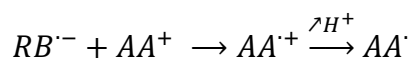
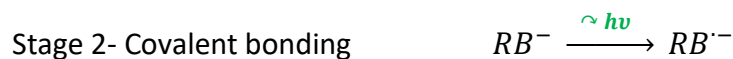


The mechanism of protein polymerisation or crosslinking in the presence of RB and light has been previously explored, especially in collagen photo-curing procedures <sup>265,344,345,348,368</sup>. Possible explanations for the role of RB in silk protein crosslinking can be attributed to the generation of RB radicals which in turn can undergo a variety of chemical interactions with the silk protein <sup>266</sup>.

In 2009, Alarcón *et al.* suggested a non-covalent association between RB and human serum albumin (HSA), leading to the formation of RB/HSA complexes <sup>267</sup>. In fact, up to 10 RB molecules can be bonded to a single HSA protein, due to their high binding affinity. In 2012, the same research group studied the binding between RB and collagen <sup>249</sup>. They suggested that bonding is a result of an ionic interaction between the negatively charged RB and the positively charged amino acid side chains (*e.g.* arginine and lysine) of the collagen. Up to 16 RB molecules were bounded to a single collagen peptide <sup>249</sup>.

Since RB has a dominant pink colour, and the colour is enhanced in all silk polymerised structures, it is reasonable to assume that a similar chemical interaction between the photoinitiator and the silk leading to silk/RB complexes as described in the case of collagen.

A 2-stage mechanism might provide a suitable explanation for the reaction:



At first, the negatively charged photoinitiator ( $RB^-$ ) interacts with the positively charged amino acids ( $AA^+$ ) present in the silk protein. These amino acids occupy 0.81% percents of silk fibroin heavy chain and include Arginine (0.27%), Lysine (0.23%), Histidine (0.1%) and Tryptophan (0.21%)<sup>369</sup>. The ionic exchange takes place until an equilibrium is achieved or until the photoinitiator is fully reacted. As a result, a strong ionic bond is formed, which makes the silk/RB complex non-soluble in water.

At the second stage, light exposure results in excitation of the RB ion ( $RB^{\cdot-}$ ) which in turn will transfer radicals to a nearby amino acid, resulting in excitation of the amino acid ( $AA^{\cdot}$ ). If the radicals are stable for long enough, two excited amino acids in close enough contact will form a covalent crosslink. This will most probably occur between histidine or tryptophan side groups, since the aromatic rings of those amino acids are more likely to preserve the radicals for longer, enabling them enough time to react with a second protein chain<sup>326</sup>.

Therefore, silk photo-crosslinking, in the presence of RB, is probably involves bonds between the histidine and tryptophan amino acids in comparison to the di-tyrosine bonds as has been previously suggested in studies using RB and reconstituted silk<sup>271</sup>.

### 3.7. Cell culture on silk patterns

As described in this chapter's introduction, silk is widely used in many tissue engineering applications specifically demonstrating a high potential for neural regeneration <sup>141,171,177</sup>.

Although silk fibroin and RB solutions are non-toxic when used separately <sup>140,141,157,344,345,370</sup>, it is vital to test that by mixing them their biocompatibility is not affected. In addition, it is useful to verify that the laser polymerised silk pattern can be used as a surface for cell growth.

As a preliminary experiment, two neuronal cell types (NG-108 and RN-22) were seeded on DLW silk patterns to test the toxicity of the silk/RB complex (section 3.7.1 and 3.7.3). This was followed by a more quantitative study to analyse cell viability and the efficiency of cell attachment using human dermal fibroblasts (see section 3.7.4).

NG-108 cells are commonly used as a model cell line to study neurites growth in nerve tissue engineering <sup>371-373</sup>. The cells were seeded on the following samples: 1. silk pattern; 2. silk pattern washed with methanol; 3. RB control; 4. tissue culture plastic (TCP). Images were collected 6 days after the seeding procedure.

Surprisingly, a low level of cell attachment was visualised both on the silk pattern and the RB control. No evidence of neurite growth was present, and the cell shape remained circular indicating no dendritic growth. This might suggest that the concentration of RB photoinitiator (0.03%) used in the process was toxic to NG-108 cells.

In clinical diagnostics, RB is used at 1% concentration to visualise ocular surface damage <sup>334</sup>. However, its toxicity to cells has been studied for various cell types <sup>374</sup>. When its toxicity tested on bovine corneal endothelial cells, a concentration as low as 0.01% was found to significantly reduce cell survival rate and the degree of proliferation, after 1 week of incubation in darkness <sup>375</sup>. The survival and proliferation rate of the cells was even lower when the cells were kept in

the light, demonstrating that the toxicity of RB increases with light exposure. Even a very low RB concentration of 0.001% has shown to reduce the proliferation of fibroblast cells <sup>374</sup>. Therefore, simply reducing RB concentration is not an appropriate solution when wanting to increase the biocompatibility of the silk/RB pattern.

Despite the evident toxicity of the RB photoinitiator, it is clearly seen that methanol wash of the sample increased cell viability. Cell shapes were elongated, indicating dendritic growth similar the one received on the TCP control. This result suggests that increasing the crystallinity of the silk/RB pattern can reduce RB toxicity. This might also be because a significant amount of the RB is removed during the methanol washing process and in addition, the high crystallinity of the silk traps the RB molecules and prevent interaction with the cells. However, to evaluate the true contribution of the methanol washing process to cell viability, it is important to investigate cell attachment to a control sample of silk and methanol without RB. This control was not present in the preliminary set of experiments, however, was added in the second study which performed on fibroblast cells (section 3.7.4).

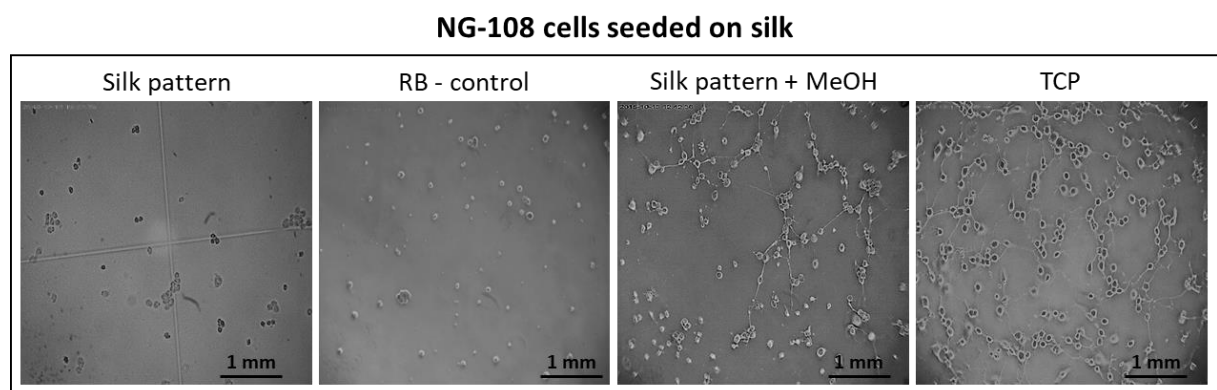


*Figure 36: Optical microscope images of NG-108 cell seeded on: silk pattern fabricated by DLW; RB control made by addition of the photoinitiator to the cell media; silk pattern after washing with methanol and TCP control. All samples were incubated for 6 days before imaging.*

### 3.7.1. Photo-bleaching process of the RB photoinitiator

One feasible way to reduce the presence of RB in the pattern is to bleach the photoinitiator away after pattern fabrication. Silk/RB solution was spread on a glass slide and left to dry. The dry film was then subjected to DLW. As a result, an RB-free pattern was fabricated on the film (Figure 37a). This shows that secondary exposure of the RB to the laser can be used as a mechanism for photoinitiator removal. To confirm the bleaching effect, an FTIR analysis was performed on the silk film before and after the laser bleaching. The results show a decrease in all peak intensities associated with RB on the bleached sample (Figure 37b). This verifies that indeed there are less RB present in the film after laser bleaching.

The photobleaching effect is the result of an electron transfer process in either oxidation or reduction of the RB <sup>376</sup>. In fact, breakdown products of this reaction can be toxic to cells, if the bleaching is done *in situ* <sup>377</sup>. However, since the current photobleaching is done prior to cell seeding, and the radicals formed in the process have extremely short life time <sup>267</sup>, it is safe to assume that no radicals are present in the silk film, when cells are seeded.

As an aside an interesting observation is that whilst it is confirmed in the previous section that there is no conversion of the silk following the laser exposure, and no structural changes were absorbed both visually and by FTIR after the bleaching, DLW might be a suitable technique for marking and labelling coloured silk samples through controlled bleaching of the RB (Figure 37a).



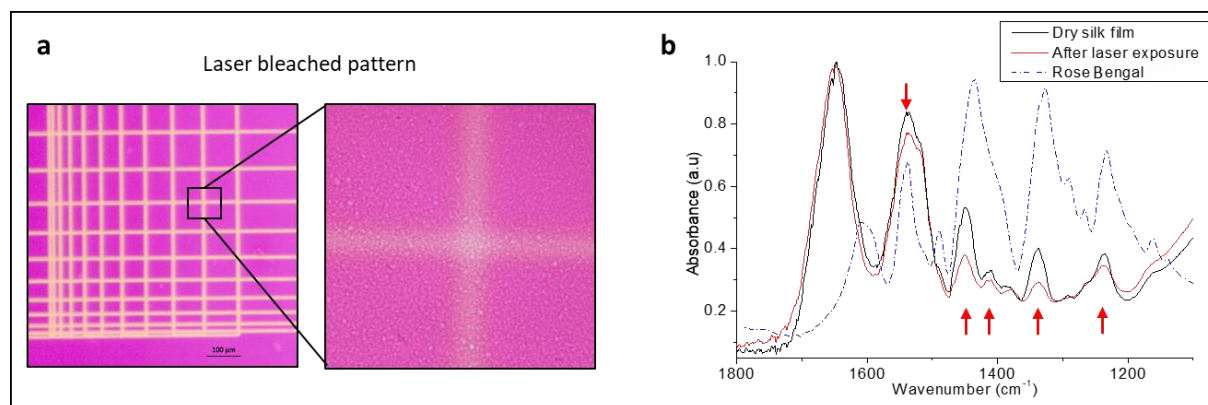


Figure 37: (a) Laser bleached pattern on silk/RB dry film. (b) FTIR spectra of silk/RB film (black), silk/RB film after the laser bleaching (red), RB (dashed blue). Red arrows indicate the RB peaks that decreased in intensity after the bleaching.

Potentially this photo-bleaching approach could be used as a possible route to guide cell growth. This is based on the observation of reduced cell attachment in the RB-rich areas on the silk. Removing the RB in specific locations, will create RB-free regions with reduced toxicity. This might encourage cell migration to the RB-free regions.

To test this hypothesis, silk patterns were fabricated by DLW and left to dry. The dry sample was exposed to the laser for the 2<sup>nd</sup> time, to bleach away the RB in selected regions. NG-108 cells were seeded on the following samples: the original silk pattern as fabricated by DLW, the pattern after bleaching treatment and the pattern after bleaching treatment and then washed by methanol. The average cell number after 24 h of incubation was analysed by ImageJ software using 3 images of each sample type. Representative images and the cell number is presented in Figure 38.

As can be seen from Figure 38, no significant improvement in cell proliferation was recorded on the bleached sample when compared to unbleached one. This suggests that the original hypothesis was not true, and the bleaching method cannot be used for controlled cell growth.

As expected, methanol treatment has significantly improved cell proliferation irrespective of

the photo-bleaching procedure. This suggests that methanol treatment of the patterns, post-fabrication (to induce silk conversion), should be explored as a potential approach to improve cell attachment. However, as commented before (section 3.7.1) an additional control of methanol treated silk (without RB) is required before any firm conclusions can be made.

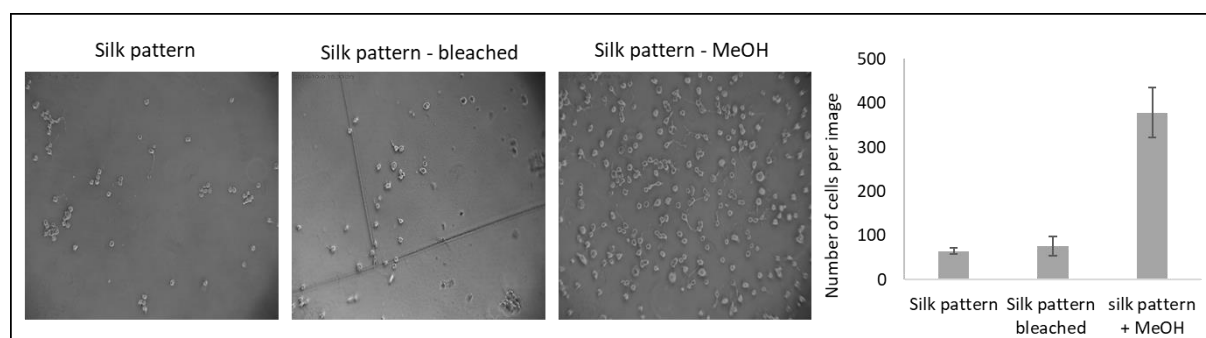


Figure 38: NG-108 cells seeded on: silk pattern fabricated by DLW, same pattern after laser bleach and same pattern after methanol wash. The graph ab average number of cells on each sample type as evaluated by ImageJ. The sample were washed, and the media was replaced to reassure that all the visible cells are attached to the sample. Error bars represent +/- 1SD n=3.

### 3.7.2. RN-22 Schwann cells

Schwann cells are the cells in the peripheral nervous system who has a role in the tissue repair process after an injury<sup>378</sup>. Therefore, they commonly studied and often used in neural tissue engineering, as a model for cell proliferation, especially the RN-22 rat Schwann cells<sup>379–381</sup>.

When RN-22 cells were seeded on the silk/RB pattern, good cell attachment and proliferation was detected on the silk pattern and the RB control (Figure 39). In fact, after 6 days of incubation, all the samples were fully covered with cells. This indicated that the RB was not significantly toxic for the RN-22 cells. To better visualise the area of cell attachment, the silk pattern was stained with fluorescent dyes and images were collected using confocal microscopy.

No difference in the level of cell attachment was recorded between the area with DLW pattern and the un-patterned silk film. This indicates that DLW patterning was not beneficial for guiding cell growth in this study.

One of the clinical uses of RB in the field of neural tissue repair is in photochemical scar ablation<sup>382–384</sup>. In this process, RB is injected into a scar region, and the scar exposed to light. The photochemical reaction following light exposure, leads to scar tissue ablation and induces Schwann cell migration into the area, encouraging axon regeneration<sup>384</sup>. Although in this process RB is used as a destructive component, it remains in the tissue after ablation and does not interrupt the healing process and Schwann cell proliferation. This suggests that Schwann cells are more tolerant to RB when compared to NG-108 cells.

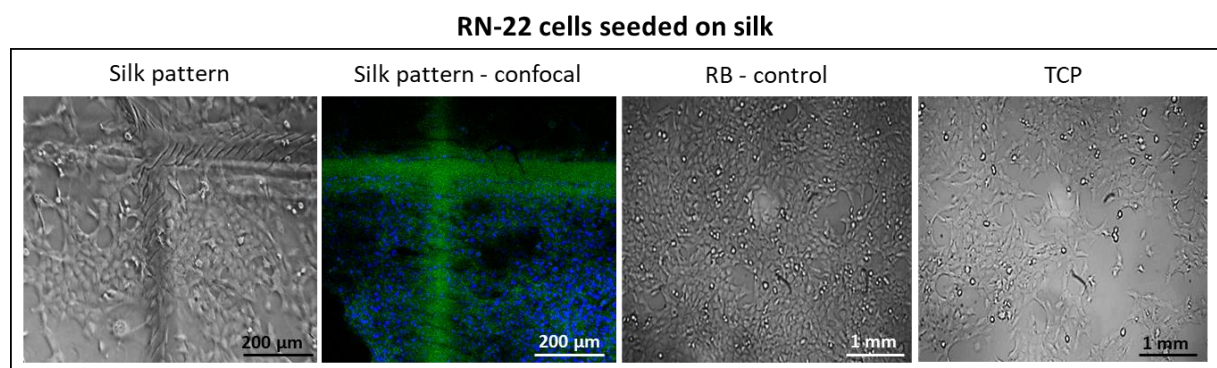


*Figure 39: Optical and confocal images of RN-22 cell seeded on: silk pattern fabricated by DLW; RB control made by addition of the photoinitiator to the cell media and TCP control. All samples were incubated for 6 days before imaging.*

### 3.7.3. Human dermal fibroblasts

In the previous section, neural cells were used due to the extensive research in the field of silk-based neural regeneration<sup>141,171,177,178</sup>. The cells were seeded on silk patterns and their proliferation was visually tracked, following previous studies that suggested that neural growth can be guided by surface topography<sup>177,178,343</sup>. However, the supply of those cells was

limited and characterisation was challenging due to rapid over-population in the samples<sup>168</sup>. Therefore, as an alternative for the neural cells, human skin fibroblasts were used for quantitative data analysis. The goal of the study was to measure cell attachment and growth on amorphous and methanol cross-linked silk. The cells were seeded on a TCP, glass slide, silk film (with and without methanol wash) and unexposed silk/RB film (with and without methanol wash). Alamar Blue and MTT assays were used to assess cell activity, 24h after cell seeding.

When fibroblasts cells were seeded on the DLW samples, both assays indicated significantly reduced cellular activity on the silk sample compared to the glass and TCP controls (Figure 40a). Surprisingly, high cell activity was measured on the silk/RB sample, even higher than that measured on pure silk (without RB). A statistical ANOVA test confirmed a significant difference between the values ( $p < 0.01$ ). Such a result is interesting since RB was found to be toxic to the NG-108 cells in the previous section. An increase in cell activity (absorbance) was measured in both silk samples (with and without RB) following methanol treatment (Figure 40a, right). While in pure silk the activity increased by 75% (from 0.004 to 0.007), only 45% increase in cellular activity (from 0.011 to 0.016) was recorded in silk/RB sample following methanol treatment. Therefore, it can be concluded that methanol treatment enhances cellular activity, but the presence of RB partially inhibits the process. However, the initial value of the absorbance was different between the samples and might be related to a variation in the number of cells attached to the sample after the seeding.

Cell attachment was evaluated by comparing the MTT signal received from the cells on the sample and cells from the media around the sample (Figure 40b). The results clearly show a poor attachment of the cells to the pure silk when only 41% of the seeded cells, remained on

the sample. Surprisingly, the addition of RB to the silk improved cell attachment (64%). This might be a result of the initial polymerisation of the silk/RB solution (under room illumination) which contributes to sample gelation. A more viscous sample can provide better support to the cells increases the number of the attachments<sup>385,386</sup>. Methanol wash slightly improved cells attachment to the pure silk sample (47%) while the highest cell attachment (75%) was recorded on the silk/RB sample after methanol treatment.

To compare the compatibility of the sample and the cells, the cell viability signal was divided by the percent of cells attached to the sample (Figure 40c). Interestingly, the best result was received for the silk/RB sample which was treated with methanol.

These results might indicate that the addition of RB to silk solutions, can significantly improve fibroblast cell attachment. However, currently these results are preliminary and were performed to study the initial cell attachment 24h after the seeding. Due to the potential toxicity of RB, as discussed above, the cell viability expected to be reduced at a longer incubation period, as shown in similar studies with fibroblasts and RB<sup>334,374,375</sup>.

Therefore, it is possible to conclude that post-treatment with methanol of silk samples after DLW fabrication, should be considered as the most appropriate approach to improve cell attachment and viability on the samples.

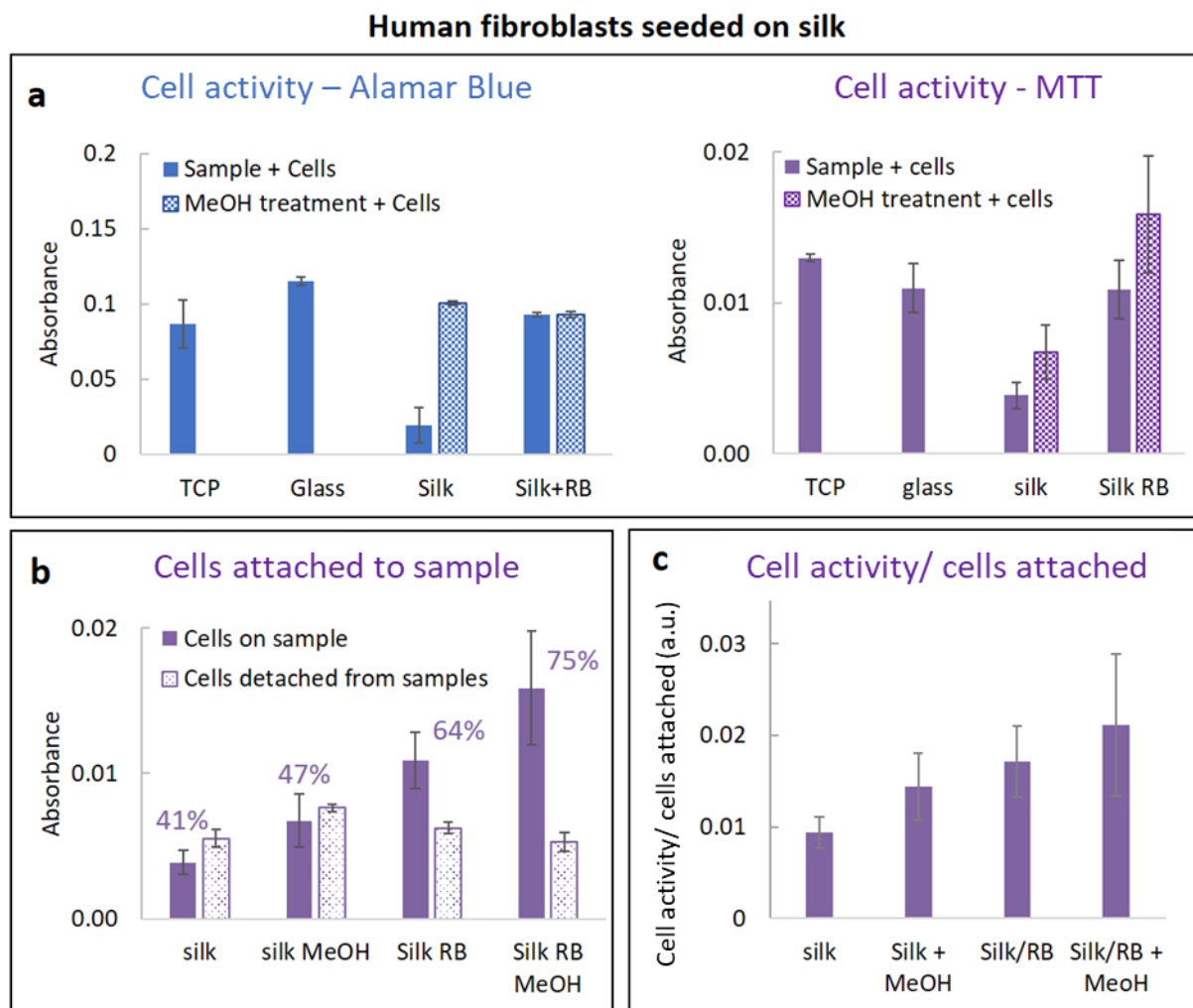


Figure 40: (a) Cell activity of human fibroblast as measured by Alamar blue (left) and MTT assays, 24h after cell seeding. Dashed columns represent methanol washed samples. (b) MTT evaluation of cell attached and detached from the sample by collecting the signal from cells attached to the sample and cells attached to the TCP surface around the sample. Numbers in purple indicate the percentage of attached cells from the total signal. (c) Cell activity as measured by MTT assay divided by the percentage of cells attached to the sample as evaluated in b. ANOVA test indicated a significant difference ( $p < 0.01$ ) between the samples with and without MeOH treatment. Error bars represent  $\pm 1SD$   $n=8$ .

## 4. Conclusions

This chapter has introduced a new, water-based approach for native silk patterning based on single-photon DLW. The fabrication procedure involves the use of a low-cost Nd:YAG laser in comparison to the high-cost laser systems currently used for DLW of silk <sup>270,271</sup>.

In addition, this work explores the use of the gold standard native silk protein in contrast to the processed, reconstituted, silk protein currently used in silk photo-curing publications. The use of native silk allows one to reduce silk concentrations down to 1 wt% without sacrificing quality. This is 2.5 times lower than the minimal concentration of silk used for DLW <sup>270</sup>, and 13 times lower than the one used for silk/RB DLW <sup>271</sup>.

Optimised experimental parameters were evaluated and the fabricated structures discussed. This technique was found to be suitable for the writing of 1 and 2D patterns, with a lateral resolution below 20  $\mu\text{m}$ . However, this resolution was not comparable to the sub-micron resolution (350 - 600 nm) that can be achieved by multi-photon polymerisation <sup>270</sup>. Yet the fact that this is a low-cost silk patterning method and is easily accessible to many research groups, means it should be considered for pilot experiments, optimisation procedures, large area structuring and basic research analysis. The set-up used in this work, allows one to write good-quality patterns 10 times faster (1 mm/s) than multiphoton approaches, in fact, it is possible to produce 1  $\times$  1 cm frame pattern in just 40 seconds, and to fully fill a 1  $\times$  1 cm area in less than 2 hours.

Unfortunately, all attempts to fabricate 3D patterns using a silk/RB solution were unsuccessful and resulted in structural failure during the drying process. However, this lack of success is in agreement with previous silk DLW studies <sup>271,276</sup>. Structure stability can be improved by a secondary crosslinking process using  $\text{Ru}(\text{bpy})_3^{2+}$  and ammonium persulfate <sup>25</sup>, however, these

chemicals might be toxic when used in biological applications<sup>387–390</sup>. Sun *et al.* did demonstrate it is possible to successfully fabricate 3D silk structures by multi-photon polymerisation when using methylene blue photoinitiator<sup>270</sup>. However, their FTIR analysis indicated a full conversion of the silk and is most likely a result of the fs laser source overheating and photo-stimulating the silk to inducing  $\beta$ -sheet formation. In contrast, this work offers a patterning method which maintains the amorphous silk structure and allows high control over the degree of crystallisation, post-processing.

A two-stage mechanism, for silk/RB photo-polymerisation, was introduced, for the first time, contributing to future silk DLW research. The mechanism suggests ionic bonding of the RB salt to the basic side groups of the silk protein, forming silk/RB complexes even prior to light exposure. When the light is turned on, a radical coupling reaction takes place leading to covalent bonding between the amino acids in the side groups (e.g. lysine, histidine and arginine). This mechanism is in contrast to the di-tyrosine bonding mechanism, suggested before, for silk/RB polymerisation<sup>271</sup> and is different to the mechanism of silk/riboflavin photo-curing, proposed in the next chapter.

This ionic interaction between the silk and the Rose Bengal photoinitiator was supported by the strong pronounced rose colour of the fabricated pattern, which remained after intensive washing with water. The covalent crosslinking of the silk protein chains resulted in a stable pattern which allowed to transport the pattern to another surface post-fabrication. This pattern can be applied as a surface coating to introduce topographical features to surfaces which are not suitable for DLW such as opaque or rough materials.

The characterization of the pattern revealed a line-like surface with groves exhibiting a depth of up to 10  $\mu\text{m}$ . However, this topography was not suitable for cell guidance, since the cells



did not show any preference in attachment to the pattern when compared to unstructured silk. This is not surprising since the pattern size was small and in fact, comparable to a single cell size of a fibroblast (10-15  $\mu\text{m}$ ) and neuronal (20-50  $\mu\text{m}$ ) cells <sup>391</sup>. However, this surface topography might be beneficial for the guidance of smaller cell such as platelets (2  $\mu\text{m}$ ) or sperm cells (3  $\mu\text{m}$ ). Another limitation for cell growth was the toxicity of the RB, which resulted in a strong inhibition of cell proliferation and attachment. This was partially resolved when the pattern was pre-treated with methanol before the seeding of the cells.

To conclude, this chapter offers native silk DLW as an alternative and affordable solution, for fabrication of large silk patterns (up to  $\text{cm}^2$  scale) when the sub-micron resolution is not required. However, due to the limitations of the technique such as poor structural stability which cannot support 3D fabrication and the toxicity of RB, other silk structuring techniques should be investigated.



# Chapter 4

---

## Fabrication of 2D Silk Structures by Projection Stereolithography

## Summary

This chapter focusses on the use of projection stereolithography to structure silk and explores the potential range of applications this technology enables. Using a combination of UV-Vis and FTIR the molecular mechanism behind the crosslinking process is probed and rheological analysis is used to directly correlate the effect of light dosage on structure development. Furthermore, to better understand the potential of this technique it compares native silk to the current state-of-the-art; reconstituted silk, with results clearly highlighting that protein molecular weight is a key factor affecting the quality of the fabricated pattern.

## 1. Introduction

The past decade has seen a rapid increase in techniques to facilitate precision control of silk structures at the micro and nanoscale, particularly in the area of bio-optics<sup>193,392</sup>. These approaches can be divided into indirect and direct routes. Indirect fabrication routes such as soft lithography<sup>393,394</sup>, nano-imprinting<sup>395</sup>, and classical photolithography<sup>122,268,396</sup>, whilst inexpensive, require pre-fabrication of fixed templates, masks, and moulds to form the final patterns which can often constrain the resulting structure and its resolution. Direct routes, including e-beam<sup>202,203</sup>, laser machining<sup>397</sup> and multi-photon lithography<sup>270,271</sup>, allow one to achieve much higher pattern resolution; however, these methods usually involve high-cost equipment, small patterning areas, prior chemical modification and require longer fabrication times<sup>193,273</sup>. To address such challenges, projection micro stereolithography (P $\mu$ SL)<sup>297,299,398,399</sup> has been examined as a new route for high-resolution silk patterning.

### 1.1. Projection micro stereolithography (P $\mu$ SL)

P $\mu$ SL is a 3D printing technique based on photocuring a (bio)polymer solution<sup>306,343,400</sup>. Importantly it utilizes a digital micro-mirror device (DMD)<sup>263,399</sup> as a dynamic mask, thus replacing the need of a pre-fabricated static photomask<sup>219</sup>. Furthermore, a dynamic mask such as this enables a sub-micron resolution and does not require the fabrication of a single-purpose mask or the time constraints of single pixel fabrication<sup>401,402</sup>. In addition, stereolithography can print structures in a layer-by-layer manner, rather than in individual pixel-by-pixel structuring used in other fabrication techniques such as DLW (discussed in the previous chapter). Also, the total printing time is dependent only on the thickness of the structure and not on the complexity or the size of the structured layer.

Thus, stereolithography can significantly reduce printing time when compared to other fabrication techniques.

Typically, for P $\mu$ SL a laser beam is expanded and projected onto a DMD, an array of aluminium coated micromirrors which can either reflect or absorb the incoming light to form a binary mask. Afterwards, the reflected image is directed by a mirror and projected onto a container which is filled with a photo-curable solution. The interaction of the laser light and the polymer solution results in a photo-polymerisation reaction, leading to polymer crosslinking and pattern fabrication. The photo-polymerisation reaction is based on an excitation of a photosensitizer and usually occurs through free radical or singlet oxygen generation and is dependent on the excitation wavelength, selected photosensitizer, and accessible polymer surface residues <sup>266</sup> (explained in more detail back in chapter 1). By adjusting the physical properties of the photo-curable polymers (e.g. concentration, viscosity or chemical composition) it is possible to customise the polymerised structures for specific applications <sup>217,233</sup>.

Using the same lithographic approach, 3D structures can be achieved by projecting the image on a motorised z-axis platform. The first layer is projected directly on the platform. After the layer is patterned, the platform moves down, and the next layer is projected on top of the previous layer, generating a multi-layer structure. By altering the projected image between the layers, the stereolithographic system can be used to fabricate complex 3D structures with controlled geometry.

When commercial polymeric resins (e.g. polyethylene glycol) are used for photofabrication, the P $\mu$ SL system which is utilised in this work is suitable for the fabrication of large 3D

structures such as solid tubular nets (Figure 41) with similar geometries to those used for skin and neural regeneration applications<sup>314</sup>. However, when soft natural materials are used in the same system (e.g. silk), it is significantly more challenging to achieve structural stability to support multi-layered structures and requires many years of research and optimisation. Nonetheless, the current photolithographic set-up can be used for single-layer fabrication (patterning) of soft materials and hydrogels. This chapter introduces silk patterning for the fabrication of customised surface topographies, by focussing on the photo-polymerisation process itself and the photocuring mechanism. It also demonstrates the benefits of the native silk in the broad range of applications that require surface patterning (optical devices<sup>119</sup>, labelling<sup>403</sup>, cellular guidance<sup>171</sup> and neural regeneration<sup>343</sup>).

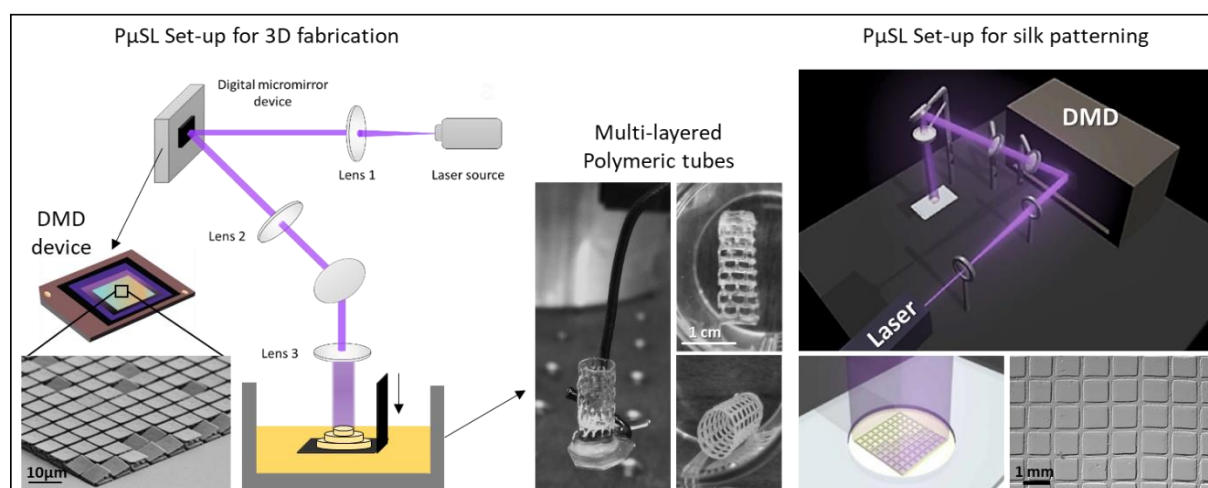


Figure 41: Schematic illustration of a typical projection stereolithography set-up as used in this work for multi-layer (left) and single (right) structure fabrication. In the middle, tubular polyethylene glycol nets that were fabricated by the system used in this thesis are presented. The Image in the right corner shows the native silk grid pattern fabricated by the same system.

## 1.2. Protein stereolithography

Initial research into stereolithography in the early 1980's utilised synthetic materials, mostly polymers or ceramic particles which were embedded into a sacrificial photo-curable resin<sup>306</sup>.

However over the years, with the development of non-toxic photo-curable resins and

crosslinking agents, stereolithography became a powerful technique for structuring biological materials for biomaterial applications, including both proteins and polysaccharides, including alginate<sup>311,404</sup>, gelatin<sup>252,253</sup>, collagen<sup>265,405</sup>, chitosan<sup>136,277</sup>, fibrin<sup>343</sup>, hyaluronic acid<sup>264</sup> and more<sup>314</sup>.

Today, bioprinting by stereolithography can be used to fabricate cell-free scaffolds<sup>406,407</sup> as well as cell-laden scaffolds<sup>407-410</sup>. The fact that stereolithography is a nozzle-free printing technique, results in cell viability higher than 90% and resolution down to 200  $\mu\text{m}$ <sup>408</sup> and makes it suitable for printing of shear-sensitive materials such as silk<sup>69</sup>.

#### 1.2.1. Native silk as a candidate for P $\mu$ SL.

Creation of a silk-based solution prior to patterning is traditionally achieved through reconstitution; a process where spun silk is exposed to chaotropic agents to enable re-solubilisation<sup>22</sup>. Unfortunately, if reconstitution is not carefully controlled, it can result in a certain degree of collateral damage to the fibroin and may lead to a decrease in the molecular weight of the protein, which also impacts the properties of the final restructured material<sup>411,412</sup>. In fact, it is possible that reconstitution's degrading effect on the silk protein may explain why current silk photo-curing techniques require relatively high silk concentrations (>5 wt.%) in order to generate stable structures<sup>122,271,276</sup>.

Alternatively, it is possible to obtain a soluble, native silk solution directly extracted from the animal's silk gland<sup>47,103,106</sup>. The use of such native silk solutions has previously been shown to be advantageous not only in setting the gold standard for biomimetic spinning technologies<sup>53-55,69,103</sup> and even perhaps as a model biopolymer<sup>20,98</sup>, but also recently in creating silk based encapsulation devices<sup>189</sup> and in the development of silk-based biophotonics<sup>392</sup> at relatively low silk concentrations (~1 wt.%). However, the potential of native



silks for deployment in photolithographic applications have yet to be fully exploited, and hence the impetus for this thesis chapter.

### 1.2.2. Photoinitiators for protein stereolithography

The success of stereolithography bioprinting is strongly dependent on the availability of suitable photoinitiators, which will allow effective photocuring process without damaging or modifying biomaterials. Several publications utilised an ultra-violet (UV) light source to polymerise reconstituted silk using Irgacure 2959 dye as a photoinitiator<sup>193,220,268,269,275,277</sup>. However, UV light has been reported to damage cellular DNA<sup>228,229</sup> and protein structures (e.g. lysozymes, antigens, antibodies and silk)<sup>413,414</sup>. Moreover, UV light can damage the DMD device itself<sup>416</sup>, reducing its service life.

Additional important parameters that should be considered when structuring native silk proteins, are the toxicity of the photoinitiator and its chemical composition. It is desired to introduce the minimum number of chemical reagents into the silk solution, to avoid unwanted silk gelation as a result of the high sensitivity of silk to variations in pH and ionic composition of the solution<sup>63,105</sup>. In addition, the photoinitiator should strongly absorb at a wavelength of the laser used in the stereolithographic set-up.

Riboflavin, also known as vitamin B2, is naturally present in the body<sup>417,418</sup> and, at the appropriate concentrations, is biocompatible and suitable for *in vivo* applications<sup>419</sup>. It has been previously demonstrated to be a suitable photo crosslinker for many natural materials including collagen<sup>225,226,250,368</sup>, alginate<sup>420,421</sup> and silk<sup>122</sup>. A key advantage over other photoinitiators is that the riboflavin chromophore absorbs strongly in the violet-blue part of the visible spectrum<sup>422</sup>, enabling visible light to be used as opposed to previous work where UV light was utilised<sup>193,423</sup>. The chemical structure of riboflavin<sup>422</sup> can be seen in Figure 42a.

Several studies suggest that the key mechanism for riboflavin photo-gelation in silk and other proteins is attributed to the formation of di-tyrosine bonds <sup>122,225,250,368</sup>. This is because riboflavin absorbs UV, violet or blue light (350-500 nm) (Figure 42b) and acts as a type II photoinitiator where it extracts a proton from the hydroxyphenyl ring of the tyrosine <sup>424</sup> resulting in a crosslinking of 2 tyrosine moieties via the formation of a di-tyrosine bond <sup>425</sup>. This mechanism will be further explored in the results section of this chapter.

Consequently, in this research, photo-curable native silk was fabricated by the addition of water-soluble riboflavin formulation (riboflavin 5'-monophosphate) which acted as the photoinitiator to a light-based polymerisation reaction.

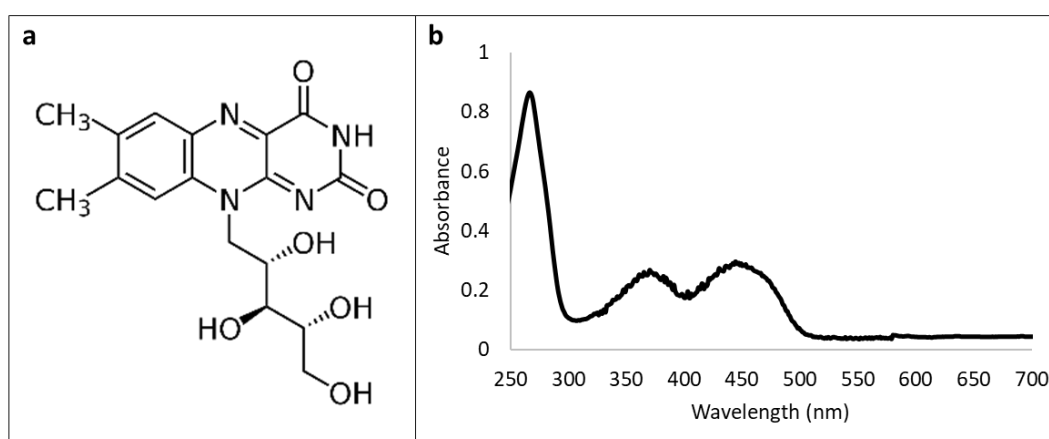


Figure 42: (a) the chemical structure of riboflavin (b) absorption spectra of riboflavin.

This chapter presents a direct, water-based route, for micro silk patterning using photo-curable *Bombyx mori* native silk dope solution and PμSL without prior chemical modification. This method not only allows control over the pattern on a micron resolution level but also produces large-scale (1 cm<sup>2</sup>) repetitive patterns. In addition, it explores the influence of molecular weight in this structuring approach by comparing native silk dope, reconstituted silk protein and a tyrosine-rich synthetic protein solution to validate the structuring mechanism.

## 2. Methodology

### 2.1. Protein solution fabrication

Native silk dope was extracted from the posterior section of the middle division of the silk glands from final instar *B. mori* silkworms and diluted in distilled water so that the protein concentration was 1 wt%. No further purification was required. Reconstituted silk (RS) solution was prepared in accordance with the protocol described in chapter 2. The resulting RS solution was diluted to 2 wt%. Poly (Glu-co-Tyr) solution was prepared by diluting Poly (Glu-co-Tyr) (Sigma-Aldrich) in Type II water to achieve 5 wt%.

After preparation, all solutions were stored at 4°C and were used within 1 week to avoid any age-related degradation/gelation of the polymers.

#### 2.1.1. Photo-curable solution fabrication

Photocurable poly(ethylene glycol) diacrylate (PEG-DA, 250 g/mol, Sigma Aldrich, UK) solution, was prepared with the addition of 2% (wt/wt) diphenyl-(2,4,6-trimethylbenzoyl)-phosphine oxide/2-hydroxy-2-methylpropio-phenone 50/50 (Sigma Aldrich, UK) photoinitiator in a similar method to described by Pateman *et al.*<sup>343</sup>.

Photo-curable protein solutions were produced by the addition of 0.02 wt% of riboflavin 5'-monophosphate (Sigma-Aldrich) to each solution prior to the photo-curing process. All solutions were kept in the dark to avoid premature crosslinking.

### 2.2. Silk PμSL patterning

The patterns were fabricated by projection-based lithography using a digital micro-mirror device (DMD). Light from a violet diode laser (405 nm, Vortran laser technology Inc, Sacramento, CA, USA) was expanded to a 5 mm diameter beam and was reflected from a

DLP® 0.55 XGA DMD with 5.4 µm mirror size (Texas Instruments Incorporated, TX, USA). The reflected image was directed by a silver coated mirror and projected onto a glass slide covered with photo-curable protein solution, located below the mirror. The solution was confined in a frame to ensure a flat surface area and covered during the photo-curing process to avoid water evaporation. The laser power varied from 50 mW to 250 mW and projection time varied from 10 s to 10 min for all types of samples.

### 2.2.1. Optimisation of the fabrication parameters

To evaluate the optimal fabrication conditions for silk/riboflavin solution, complex images of the 'University of Sheffield' logo, were projected on the solutions and the resulted patterns were visually investigated (Figure 43).

Longer projection times produced higher-quality patterns probably due to higher crosslinking in the sample which contributes to pattern stability. Short projection times (<1 minute) failed to produce a recognisable pattern. Longer projection times (> 10 min) did not improve pattern quality if comparing it the pattern that was fabricated after 5 minutes of projection and led to a reduction in the yield of the process (amount of sample produced in a given time). Therefore 5 min was selected as the optimal projection time for silk PµSL fabrication.

Silk solutions at concentrations ranging from 0.4 to 2 wt% were tested to evaluate the minimum silk concentration required for good-quality fabrication. Visible patterns were received even at a concentration as low as 0.5 wt%. However, to produce good-quality patterns (with high similarity to the projected image) with pronounced and controlled surface topography, a native silk concentration of 1 wt% was defined as the optimal concentration in all further experimental protocols. When the fabrication process was repeated with RS

solutions, the same concentration of silk did not produce a full pattern and only a partial image was observed. Therefore, a concentration of 2 wt.% was used for all RS patterning.

Setting the laser output to between 150 and 250 mW was found to produce high-quality patterns (visually similar to the projected image with full image details). Laser powers below 50 mW did not allow the fabrication of a visible pattern. Since the polymerisation process is dependent on the amount of light energy that is transferred into the sample, a higher light energy (laser power) will require shorter projection time to deliver the same energy dose. As a result, 250 mW (maximum laser power) was used in all further patterning for both silk types. This is to provide the maximum energy flux, minimising fabrication time.

All the optimised experimental parameters that were used for the fabrication of patterns presented in this chapter are summarised in Table 8.

*Table 8: Optimised experimental parameters for the fabrication of native silk patterns by P $\mu$ SL*

Parameter	Optimised values
Silk concentration	Native silk: 1 wt.% Reconstituted silk: 2 wt.%
Photo-responsive dye	riboflavin 5'-monophosphate
Riboflavin concentration	0.02 wt.%
Laser output power	250 mW
Projection time	5 min

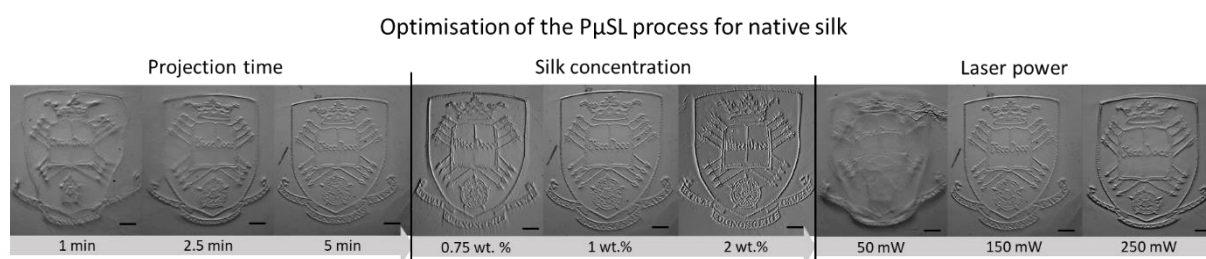


*Figure 43: Native silk patterns of the 'University of Sheffield' logo as received during the optimisation of the image projection time, silk solution concentration and the laser output power. Scale bar 1mm.*

### 2.3. Post-fabrication treatment

After fabrication, dry samples were immersed in LiBr solution (9.3 M) for 10 min at 60°C and then in DI water for 10 min at room temperature. This dissolved any non-structured protein solution prior to subsequent mechanical analysis. To induce silk crystallisation, the patterns were immersed for 1 min in MeOH/DI solution at a concentration range from 10% to 100% (v/v). The samples were left for drying and rehydrated with DI water (5 min) prior to the rheological measurements.

### 2.4. Imaging of the fabricated patterns

Optical images of the structures were collected using a Diaphot TMD300 microscope (Nikon Instruments, Japan) with a Moticam 5MP camera (Motic instruments, Spain) and a Stemi 305 microscope (Zeiss, Germany) using an Axiocam 105 colour camera (Zeiss, Switzerland). Optical profilometry images were collected by ContourGT-X 3D (Bruker, USA). All images were analysed by ImageJ (1.48v).

### 2.5. Spectroscopic characterization of the crosslinked patterns

All spectral data were acquired at room temperature ( $25\pm 2^\circ\text{C}$ ). Samples were characterized by Fourier-transform infrared spectroscopy (FTIR) using a Nicolet 380 spectrometer (Thermo Scientific, Madison, USA) equipped with a Golden Gate attenuated total reflection (ATR) device (Specac, UK). Spectral data were collected between 800 and  $4000\text{ cm}^{-1}$ , using 64 scans, at  $4\text{ cm}^{-1}$  resolution. UV-VIS absorption spectra were collected (using Spectronic Unicam, UV 330, UK), in the spectral range between 230 nm and 600 nm. Peaks in the spectra were fitted using MagicPlot Student Version 2.7.2. All peaks were fitted as Gaussians.

## 2.6. Similarity analysis of the patterns

A similarity index was defined to evaluate how similar the fabricated patterns were to the original projected pattern. To achieve this, a photo of each pattern was collected by an optical microscope. Then the image was transferred to ImageJ software for further analysis. For each image (original projected image and the resulted pattern), a threshold was adjusted to 70 % and a binary function was applied. Then any noise or contamination in the image, outside of the pattern, was removed by colouring the relevant pixel in black, assuring that no pixel from the pattern was removed. The fabricated pattern was coloured in grey to introduce a colour contrast. Then the binary images of the fabricated pattern (grey) and the original image (white) were overlaid to evaluate the correlation between the images (Figure 44). The histogram of the overlay image was plotted, containing 4 peaks corresponding to pixel counts of the following regions on the image:

**Black**- background (no pixels in original and fabricated images).

**Dark grey**- no correlation (pixel present in fabricated pattern but not in the original image).

**Light grey** – correlation (pixel present in both images).

**white** - original pattern (pixel present in the original image but not in the fabricated pattern).

The similarity percent was defined as the number of correlating pixels between the original image (a) and the received pattern (b) divided by the original image, as seen below:

$$\% \text{ Similarity } (a, b) = \frac{\text{Correllating pixels } (a, b)}{\text{Pixels in original pattern } (a)} = \frac{\text{Light grey pixels}}{\text{white pixels}}$$

For each sample type, at least 3 images were analysed, and similarity values were averaged.

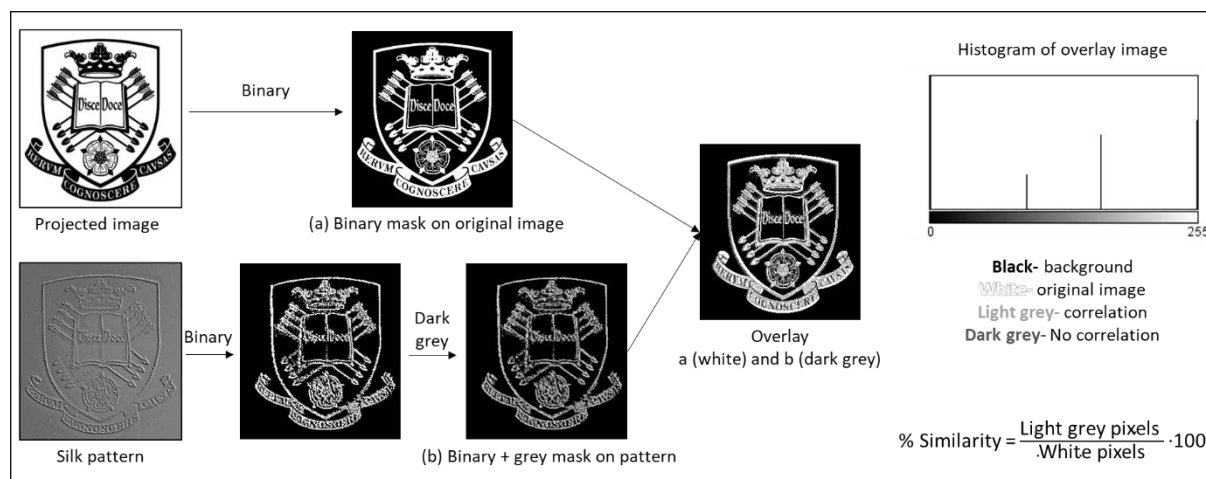


Figure 44: The process of Image similarity evaluation. The projected image and the fabricated pattern are transferred to binary images. The dark grey filter is applied on the pattern. As overlay image is generated and a histogram of the overlay image is plotted. The light grey values of the histogram (correlating pixels in both images) are divided by the white pixels (original image) to calculate the similarity between the images.

## 2.7. Image analysis of the QR code patterns

Optical images of the QR codes patterns were collected using a Diaphot TMD300 (Nikon Instruments, Japan) microscope. Images analysed by ImageJ (1.48v). Since the original patterns are transparent, they were not suitable for direct scanning by commercial QR code readers which require black-on-white contrast. Consequently, a small amount of image processing was applied (brightness and contrast adjustments), to enhance the contrast between the pattern and the background. The images were transferred to ImageJ software and the following image processing steps were used: (1) Binary (to enhance the contrast) → (2) Invert (to allow black on white pattern) → (3) Erode (To remove background contaminations).

The processed images of the codes were scanned by a free QR Scanner app (version 0.52) installed on a mobile phone (Sony Xperia Z3 compact). The original pattern (left) and the pattern after image processing (right) can be seen in Figure 45. No cropping was applied to



emphasize that the printing of the code doesn't affect the surrounding areas on the silk sample.

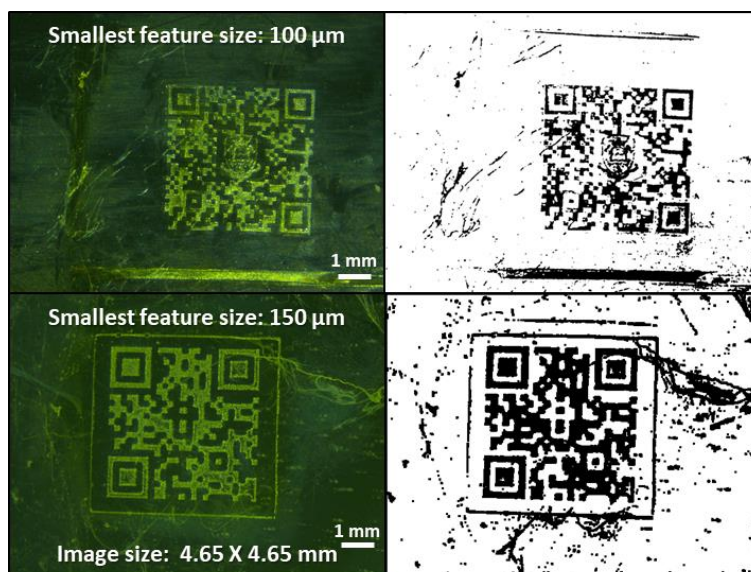


Figure 45: Native silk QR codes fabricated by P $\mu$ SL. The original image of the pattern (left) and the pattern after minimum processing in ImageJ (right) as can be detected by a commercial QR scanner. Both codes lead to <https://www.sheffield.ac.uk> website. The top QR code embedded with The University of Sheffield logo.

## 2.8. Rheological measurements

Rheological measurements were made using an AR 2000 and a Discovery HR-2 rheometer (TA Instruments, New Castle, DE, USA). The latter was equipped with the modular microscope accessory, with a transparent lower plate and a 405 nm LED light source (minimum power output 870 mW), to enable *in situ* photo-curing experiments. The LED was turned on and off during the experiment at given intervals to explore the change in elastic modulus upon irradiation. All measurements were taken using an 8 mm diameter parallel plate geometry at room temperature ( $25 \pm 2^\circ\text{C}$ ). To avoid water evaporation, few millilitres of water were added around the sample (and had no contact with the sample) and the sample was covered with a customized environmental chamber. The experiments were performed in two stages,

recording the elastic modulus ( $G'$ ) throughout an oscillatory frequency sweep (20 to 0.1 Hz) followed by a fixed frequency time ramp (1 Hz), both of which were conducted within the sample's linear viscoelastic region (target strain 0.01). For the oscillatory test, displayed modulus values were calculated as the average  $G'$  value in the range between 1 to 10 Hz.

## 2.9. Protein analysis by gel electrophoresis

A small portion of each solution (1 wt.%) was mixed with an equal volume of a solution containing sodium dodecyl sulfate (SDS, 4 %, to disrupt non-covalent bonding) and 2-mercaptoethanol (4 mM, to reductively cleave disulfide bonds in the proteins). 20  $\mu$ L of each solution was loaded onto on a 4–20 % polyacrylamide (PA) gradient gel and the protein components were separated by electrophoresis (GE) (90 minutes, 160 V, 100 mA). The gel was immersed for 30 minutes into a fixation solution (400 mL ethanol, ethanoic 100 mL acid, 500 mL water) and protein bands were stained by Coomassie blue. The gel was imaged using a Perfection 2450 Photo scanner (Seiko Epson Corp. Suwa, Japan) at 1200 DPI.

Molecular weights of the proteins were evaluated by comparing their movement with reference standards (HiMark™ Pre-stained High Molecular Weight Protein Standard).

### 3. Results and discussion

Silk patterns were fabricated by P $\mu$ SL using a native silk solution containing riboflavin dye (Figure 46a). Glass slides were used as substrates for the semi-solid patterns to allow easy transfer for imaging and post-processing. When dried, the samples were solid, transparent and flat, resembling silk films. However, when hydrated the patterns swelled, resembling gel-like materials (Figure 46b) and were defined as silk hydrogels <sup>426</sup>.

The fabricated patterns were transparent when placed over a plain text, although the patterns exhibited light diffraction under illumination (Figure 46c). This is probably a result of secondary sub-pattern in the structure which will be discussed in the next section.

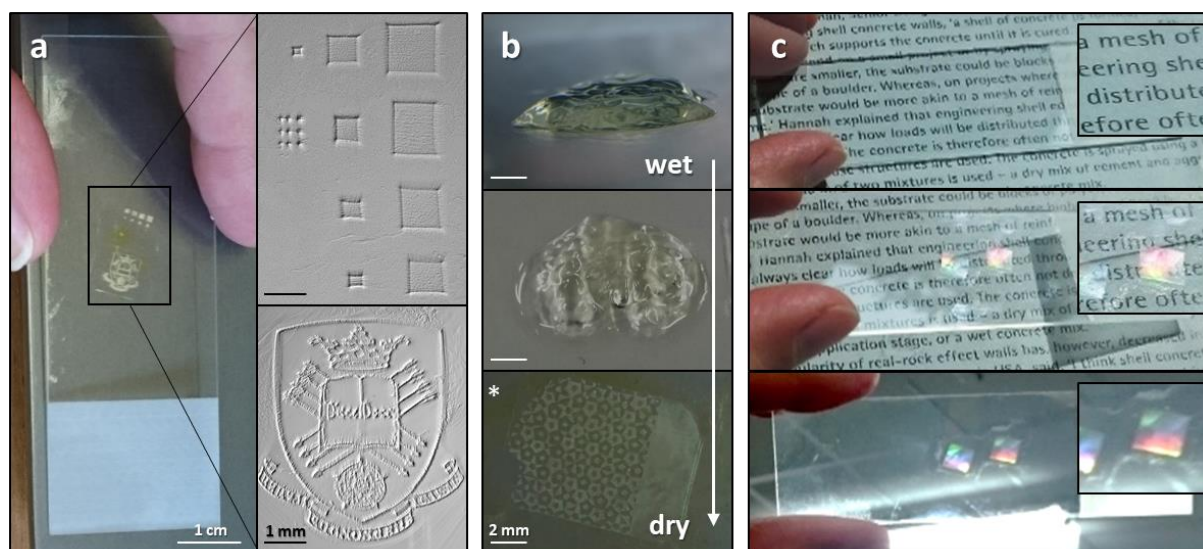


Figure 46: (a) Native silk patterns as fabricated by P $\mu$ SL in the presence of riboflavin. (b) silk patterned hydrogels, swelling when immersed in water. (c) The pattern is transparent with light diffraction properties. Asterisk in (b) indicates a pattern of quasicrystalline symmetry (quasicrystals) <sup>427</sup> discovered by Prof. Dan Shechtman (awarded the 2011 Nobel Prize in Chemistry).

A linear expansion in the size of the pattern, when compared to the DMD image, was observed as a result of a deviation from the precise focal point and the associated scattering

events within the sample which effects the photo-crosslinking process <sup>428</sup>. To evaluate the expansion coefficient, a  $4 \times 4$  pixel<sup>2</sup> ( $21.6 \times 21.6 \mu\text{m}^2$ ) image was projected from a DMD system producing a  $40 \times 40 \mu\text{m}^2$  pattern on the silk film. This value was used to determine the projected pixel size vs the DMD pixel area multiplier as:

$$\text{Area Multiplier}_{\text{DMD} \rightarrow \text{Silk surface}} = 3.43$$

For the DMD system used in this work, a single micro-mirror size was  $5.4 \times 5.4 \mu\text{m}^2$ . Thus, the minimum theoretical feature size that can be produced by the current set-up (considering the mathematical multiplier) is  $10 \times 10 \mu\text{m}^2$ .

According to Bragg's law <sup>429</sup>, light diffraction can occur when the light passes around the edge of an object and is dependent on the wavelength of the light ( $\lambda$ ) the distance between to neighbouring objects ( $d$ ) and the light scattering angle ( $\theta$ ). The minimum distance required for the diffraction is given by:

$$d = \frac{\lambda}{2 \cdot \sin(\theta)}$$

Given the fact that the smallest value a sinus function can have is 0.5 (excluding 0), the maximum distance between the pattern on the image which will produce visible light diffraction is:

$$d_{max} = \lambda_{max} = 700 \text{ nm}$$

Therefore, it can be concluded that the diffraction visible in the silk patterns cannot be a direct result of the projected features and that a periodic sub-micron structure must be present in the silk.

### 3.1. Sub-patterns and biocompatible diffraction grids

Closer investigation of the structured samples revealed a secondary, highly regular sub-pixel pattern with features below 5  $\mu\text{m}$ . This sub-pattern is most likely a result of the DMD mirror geometry and their spacing in the optical setup <sup>416</sup>. Interestingly these features produced a diffraction pattern under direct laser illumination (Figure 47a).

To evaluate the fabrication conditions that should be used for controlled generation of diffraction patterns, two stereolithographic set-ups available in the lab were explored. In fact, those sets of experiments aimed to explore whether the location of the projected image in the stereographic system (above or below the sample) can influence pattern fabrication.

A thin layer of photocurable silk solution was placed on top of a glass slide. In the first set-up, the image was reflected from the DMD and projected through the glass slide on the bottom layer of the solution (bottom projection). It resulted in a clear image of the projected pattern and the long-range order of the sub-pattern was confirmed by measuring the light diffraction pattern spacings <sup>430</sup> (Figure 47b). In the second set-up, the reflected beam was projected on the solution from above and focused on the glass surface (top projection). The semi-solid pattern produced on the glass was distorted and the sub-pattern presented an irregular structure with a ring pattern diffraction indicating that there is no repeated order in the sub-pattern, similar to that seen in amorphous or polycrystalline materials <sup>430</sup>. This can be explained by sufficient scattering of the laser light while moving inside the solution volume.

One potential use of such reflective patterns is for the fabrication of biocompatible implantable photonic devices <sup>431</sup> which can be used as specific sensors or electrodes <sup>432</sup>, light delivery systems <sup>433</sup> and optical elements <sup>434</sup>. This can be achieved by changing the distance

between the elements of the pattern to generate specific diffraction patterns as a function of the light wavelength <sup>203</sup>.

To investigate the potential of the native silk diffraction grids in similar applications, a glass slide with a photo-responsive solution was placed precisely at the focal point of the laser (0 mm), 8 mm below the focal point (- 8 mm) and 8 mm above the focal point (+ 8 mm). Fast Fourier Transform (FFT) performed on the images of the patterns indicated a shift with the variation in sample position. This confirms that precise sample alignment in P $\mu$ SL allows controlling the spacing of the sub-pixel patterns (Figure 47c).

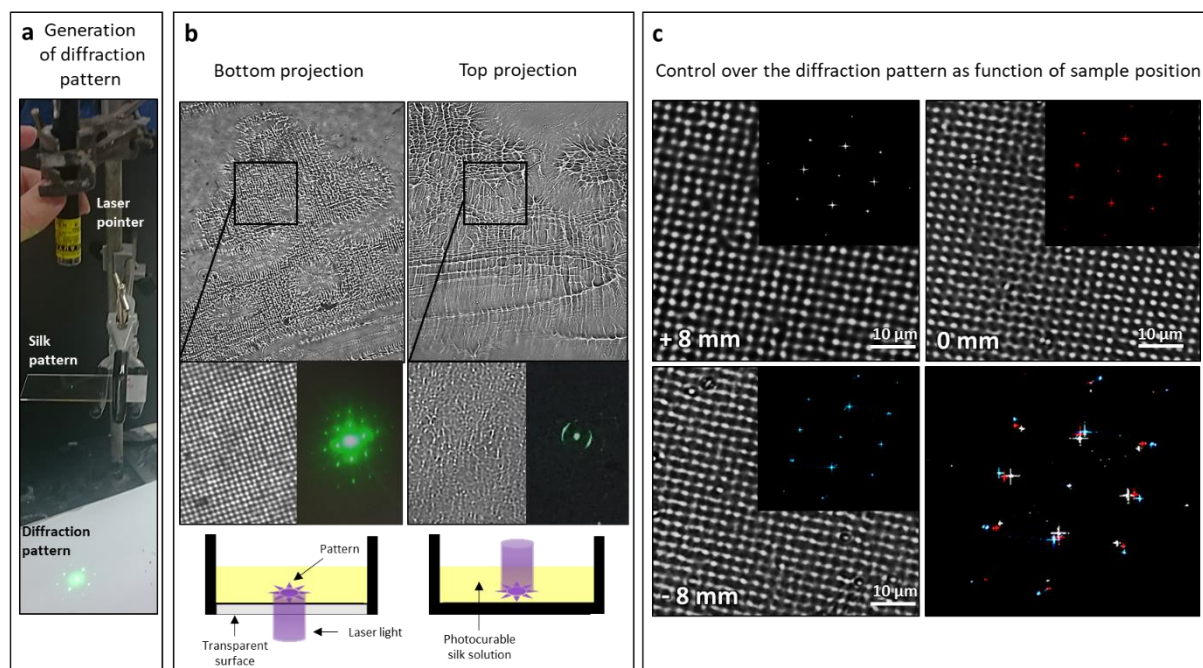


Figure 47: (a) Diffraction pattern generated by projection of laser light on the fabricated pattern. (b) The stereolithographic set-up used to generate patterns. In bottom projection, the image is projected through the glass surface minimising light scattering are resulting in a regular ordered pattern. In top projection, the image is projected through the silk solution which increases light scattering and results in an irregular pattern. (c) Diffraction grids with various spacing values as fabricated by moving the sample position from the focal point (0 mm), above the focal point (+ 8 mm) and below the focal point (- 8 mm). FFT images represent the shift in the spacing between the patterns.



Since the total area of the projected patterns was up to 1 cm<sup>2</sup>, and the spacing between the sub-pattern was about 3 μm, this technique can be defined as being suitable for micro-patterning of silk on the micron scale.

### 3.2. Silk-based photonic components for labelling and data storage

The major benefit of PμSL is the fact that images are projected directly onto the sample without intermediate masks which can lead to practically unlimited flexibility in design. This can be used for the fabrication of elaborate photonic components which can be realised in a few seconds (Figure 48). Pattern topography was analysed by optical profilometry, confirming that the patterns are raised above the surface, with an average height of ~5 μm.

Back in 2008, similar silk-based photonic components were produced by Fiorenzo and Kaplan using soft-lithography methods<sup>435</sup>, by generating repetitive silk patterns on pre-fabricated polymeric moulds. More recently, the same research group proposed the use of electron-beam lithography to create similar silk structures<sup>203</sup> from dry, polymerised silk film and liquid, amorphous silk solutions. The exposure of the silk protein to the electron beam resulted in protein degradation (in dry silk films) and intermolecular crosslinking (in silk solutions) both creating the desired pattern. In their work, they were able to control the light scattering by generating patterns with a specific spacing of 500, 600 and 700 nm. This spacing is 5 times smaller than the spacing achieved in the method described in this work (3 μm), however, this may be possible in the future with the developments of high-resolution DMD devices.

This combination of silk's mechanical, biological and optical properties combined with process/manufacturing flexibility and speed, make silk-PμSL fabricated patterns ideal candidates for a broad range of labelling applications, for example, food, drugs, tissues in tissue engineering or organs for transplantation. The control over the diffraction patterns and

the unlimited pattern design can also be beneficial for security and identification purposes. When designing labels for packaging and food industries <sup>117</sup>, one desire is to include product information, allowing correct identification and to provide storage/use guidance. When labelling implants and medical devices <sup>436–438</sup> it can be beneficial to include patient personal information and medical history to minimise human errors.

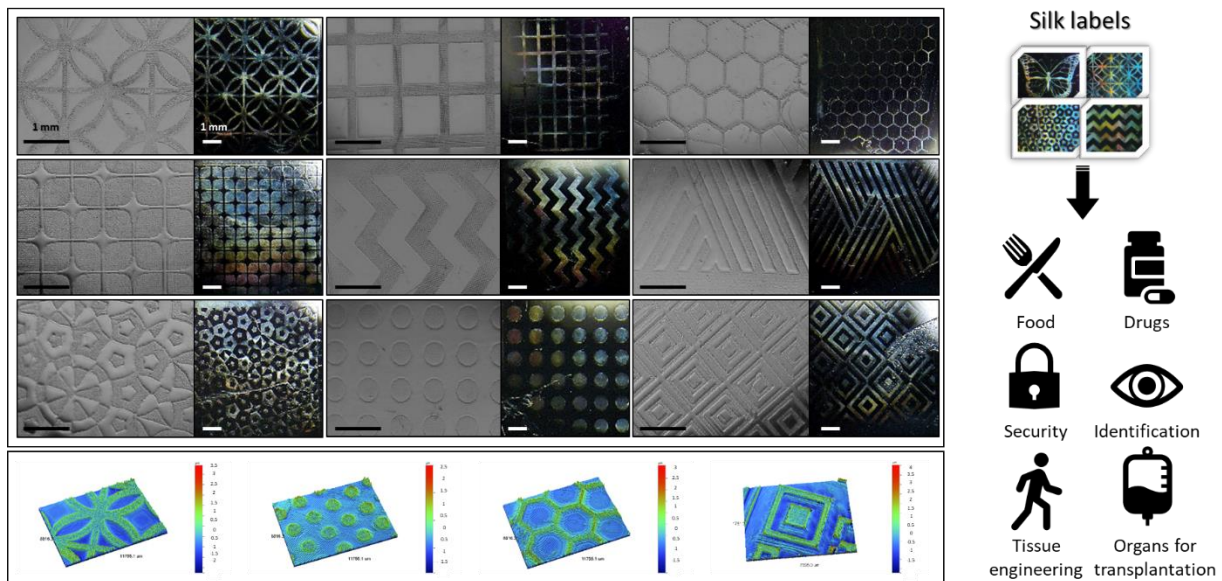


Figure 48: Optical microscopy images of native silk photonic patterns and the light scattering received with the change of illumination angle. (Bottom row) Pattern topography as received by optical profilometry. (Right) schematic diagram of the proposed potential labelling applications of the silk patterns. Scale bar 1 mm.

As proof of concept, silk QR codes <sup>439</sup> were fabricated by P $\mu$ SL to allow reference to complex and dynamic databases (Figure 49). After minimum image processing (see methodology section), the codes were readable by all QR Scanner apps installed on mobile phones (Android and iOS).



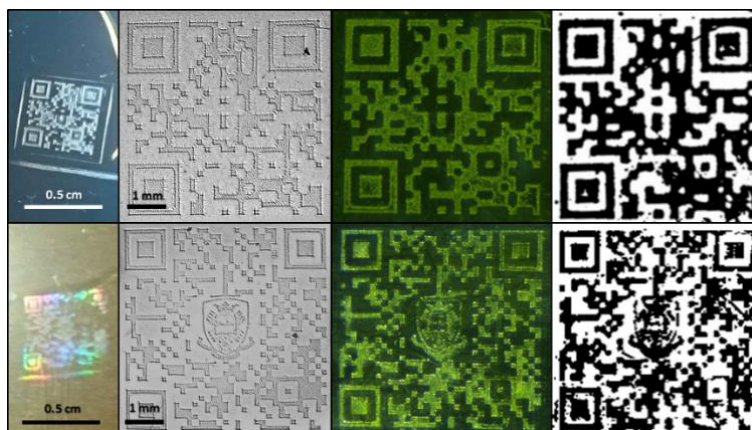


Figure 49: Native silk QR codes. Photograph (left), optical microscopy images (middle) and the scannable pattern after minimum image processing (right).

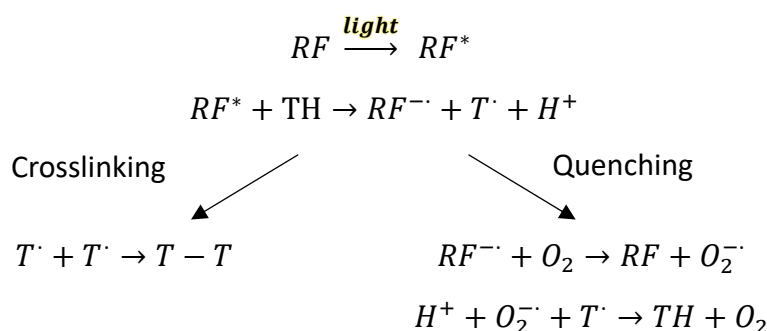
### 3.3. Mechanism

Previous studies have shown that protein solidification in the presence of light and a photo crosslinker is usually attributed to chemical crosslinking of the protein<sup>440</sup>. This crosslinking most often occurs through tyrosine side groups of the protein, forming di-tyrosine bonds<sup>368,441</sup>. When exposed to light, riboflavin (*RF*) absorbs photons and shifts to an excited state (*RF\**). As a result, the tyrosine (*TH*) is oxidized by the photoexcited riboflavin and form tyrosyl radicals (*T·*). The radicals can react in two possible mechanisms:

1. Crosslinking - When two tyrosyl radicals react with each other to form a single di-tyrosine bond ( $T - T$ ) leading to chemical crosslinking of the protein.
2. Quenching - In the presence of oxygen the riboflavin radicals can generate superoxide anion radicals ( $O_2^-$ ) which in turn can react with the tyrosyls, prevent the formation of di-tyrosine bonds leading to quenching of the polymerisation reaction.

Hence, the rate of the reaction should dependent of the number of riboflavin radicals generated (light flux), the number of tyrosyls (protein concentration) and the oxygen

concertation in the environment during the photopolymerisation process. The mechanism is summarised below:



To validate the crosslinking mechanism, for the native protein solution, UV spectroscopy was employed to examine the tyrosine peak (275 nm) of native silk/riboflavin samples before and after exposure to laser light. Photo-exposed samples revealed a shoulder on the tyrosine peak which was not present in the spectra of the pure native silk solution or the riboflavin dye (Figure 50a).

It is also interesting to note that the photocured sample does not show any peaks between 350-500 nm, where the riboflavin strongly absorbs. This indicates that no direct crosslinking between the native silk and the dye has occurred and that the riboflavin was fully removed after washing with DI water. This, in fact, may have future utility in creating dye-free silk structures for tissue engineering applications or potentially recycling of the photoinitiator.

The shoulder on the main tyrosine peak was fitted and a second peak was recognised (325 nm), which was attributed to the presence of a di-tyrosine bond<sup>442</sup> (Figure 50b). This strongly suggests chemical crosslinking under laser illumination. As an additional confirmation of the chemical crosslinking in the silk/riboflavin system, the silk-patterns were immersed in LiBr solution for 10 min at 60°C. LiBr is a chaotropic agent known to solubilize silk through disruption of hydrogen bonds<sup>22</sup>. As expected, the photo-cured pattern remained stable while

the non-exposed silk fully dissolved (Figure 50c), confirming that the patterns are in fact a chemically crosslinked structure.

Further analysis of structure development was undertaken using FTIR to detect if there is any protein secondary structure conversion in the native silk after photo-curing. The typical structural conversion in silk associated with fibre spinning can be characterised by a shift of the amide 1 peak position ( $\sim 1650\text{ cm}^{-1}$ ), indicating the formation of  $\beta$ -sheet crystalline units which are present in silk fibres<sup>95,294,296,443,444</sup>. However, the FTIR analysis performed on the photo-cured native silk patterns indicated a primarily amorphous structure. This is particularly interesting as it means that structuring without conversion/crystallization of the native silk can be achieved as previously proposed<sup>122,276</sup>. This suggests a different mechanism for silk photo-gelation, compared to native silk spinning<sup>103</sup> and methanol-induced silk gelation<sup>87</sup>. In fact, the amorphous state of the patterns endows additional flexibility as it is possible to undertake further controlled conversion by washing the sample with MeOH (Figure 50d). By doing this the level of crystallinity can be controlled by adjusting the concentration of MeOH aqueous solution towards full conversion at concentrations above 50% v/v.

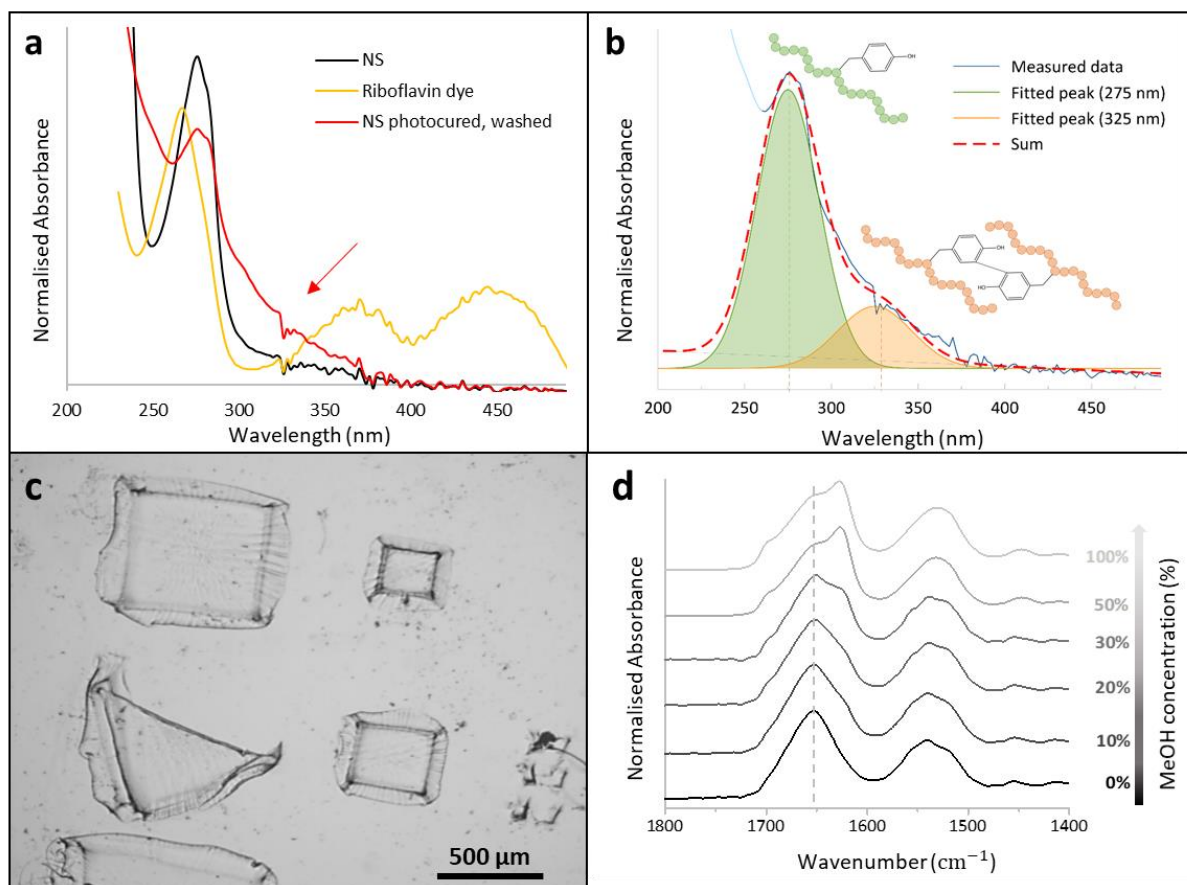


Figure 50: (a) UV-VIS spectra of native silk (black), riboflavin dye (yellow) and photocured native silk washed with water (red). The red arrow indicates the shoulder in the photocured sample. (b) Peak fitting of the photocured sample indicating the appearance of 325 nm peak corresponding to di-tyrosine bonds formation. (c) Silk pattern after washing with LiBr solution. The photocured areas remained while the non-exposed silk dissolved. (d) FTIR spectra of silk hydrogels, as fabricated (0%), after a wash with various MeOH/DI water solutions (10%, 20%, 30%, 50%) and pure MeOH (100%). A gradual crystallisation can be seen with the shift in Amide 1 (1654 cm<sup>-1</sup>) peak position (grey dashed line indicates the initial position).

### 3.4. Mechanical characteristics

One of the challenges in hydrogel-based applications the control of mechanical properties <sup>404,426,445,446</sup>. Linking these insights into structure development with function, the effect of illumination on the stiffness (elastic modulus, G') was explored during and after the photocuring process.

Using a rheometer equipped with a LED light source at the same wavelength as the laser in the P $\mu$ SL setup (405 nm), *in-situ* measurements of the elastic modulus were performed under constant illumination (Figure 51a). All measurements began in darkness and illumination was applied after 300 s. This is to allow the system to stabilise and to diminish effects which do not directly related to the photo-curing process.

After an induction period, significant increases in the values of  $G'$  were recorded during illumination periods with the rate of modulus growth is proportional to the light flux irradiating the sample (Figure 51a, inset). This suggests that by adjusting the light intensity, the number of riboflavin radicals that are generated can be regulated and, as a result, direct control over the reaction rate can be achieved. The presence of an induction period may be attributed to several reasons such as crosslinking of other low molecular weight proteins naturally present in the silk gland<sup>98</sup>. Alternatively, the induction period could be a result of the time required for generating sufficient amount of di-tyrosine bonds to form a fully interconnected protein network which can begin to distribute the applied stress and manifests itself as a stiffness increase. The induction period can also be a result of tyrosine radicals quenching the reaction, which occurs in the presence of oxygen (see section 3.3) and leads to recovery of the radicals and decrease in the rate of the photo-crosslinking reaction<sup>447</sup>.

To investigate the mechanical properties of the silk hydrogels post-fabrication, native silk solution was exposed to laser light to generate large (1 cm<sup>2</sup>) rectangular patterns. Both the photo-exposed and non-exposed silk did not dissolve in deionised water. This is in contrast to the silk/Rose Bengal patterns in which the non-exposed silk fully dissolved when immersed in water (see chapter 3). Afterwards, the fabricated patterns were dried, and the unexposed

silk was removed by washing the patterns with 9.3 M LiBr solution. Then, the samples were hydrated again by immersing them in DI water for 5 minutes.

Subsequent dynamic shear analysis<sup>448–451</sup> of the hydrogels revealed an increase in the storage modulus with an increase in the projected energy dose. The maximum modulus value was ~500 Pa, making the photo-cured silk much stiffer in comparison to unexposed silk (~30 Pa) (Figure 51b). This value for native silk is higher than previously reported stiffness values by Applegate *et al.*<sup>122</sup> by over 200 Pa, wherein that study a photo-curable reconstituted silk (RS) was used. Furthermore, when patterns were post-treated with increasing concentrations (v/v) of MeOH solution, the storage modulus reached 2000 Pa for 50% MeOH and increased up to 16000 Pa for 100% solution (Figure 51c). Combining these results indicates that the  $G'$  of native silk/riboflavin hydrogels can be controlled over 4 orders of magnitude, thus replicating the mechanical properties of various human tissues such as brain (< 10<sup>2</sup> Pa), lungs (< 10<sup>3</sup> Pa), liver (10<sup>3</sup>-10<sup>4</sup> Pa) and muscles (> 10<sup>4</sup> Pa)<sup>452</sup> (Figure 51c).

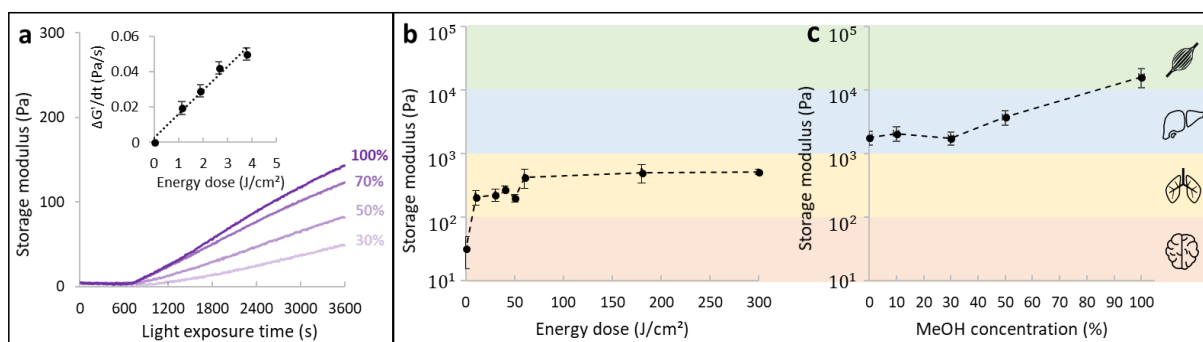


Figure 51: (a) Elastic modulus ( $G'$ ) values over time as a function of the light intensity. (Inset)  $G'$  gradient as a function of the total energy dose. (b)  $G'$  value as a function of energy dose projected during pattern fabrication. (c)  $G'$  value as a function of MeOH concentration used to wash the sample post-fabrication. Error bars represent +/- 1SD n=3.

### 3.5. Silk vs. PEG in P $\mu$ SL patterning

One of the most common materials used in projection stereolithography is polyethylene glycol (PEG)<sup>398,453</sup>. To compare the potential of native photo-curable silk solution developed in this work, and PEG which has been previously used in our lab, the pattern of 'The University of Sheffield' logo was fabricated from both solutions. For each solution, optimised fabrication parameters were chosen to enable the best image quality possible, thus testing the current limits of these materials.

The optical images clearly show the benefits of native silk in the printing of fine structures (Figure 52). When exploring the 'Yorkshire rose' feature in the pattern, which has a diameter of 1 mm, the PEG pattern does not allow to distinguish between the internal features in the rose, limiting the resolution of the technique to 1 mm. In contrast, the silk pattern has distinguishable features of  $\sim 50$   $\mu\text{m}$  in size suggesting that by using silk solution in the  $\mu\text{PSL}$ , instead of PEG, pattern resolution can be significantly improved. Yet, PEG has more pronounced surface topography creating a more 3D-like pattern.

These results emphasise that native silk can be proposed as an alternative material for P $\mu$ SL patterning when fine and complex 2D and 2.5D patterns are required. This is especially relevant in biological applications when the use of natural polymers is preferable. However, silk is not perfect, when moving to 3D fabrication, native silk failed to generate stable multi-layer structure and is not suitable, under the current fabrication method, for the generation of hollow or porous structures multi-layer structure.

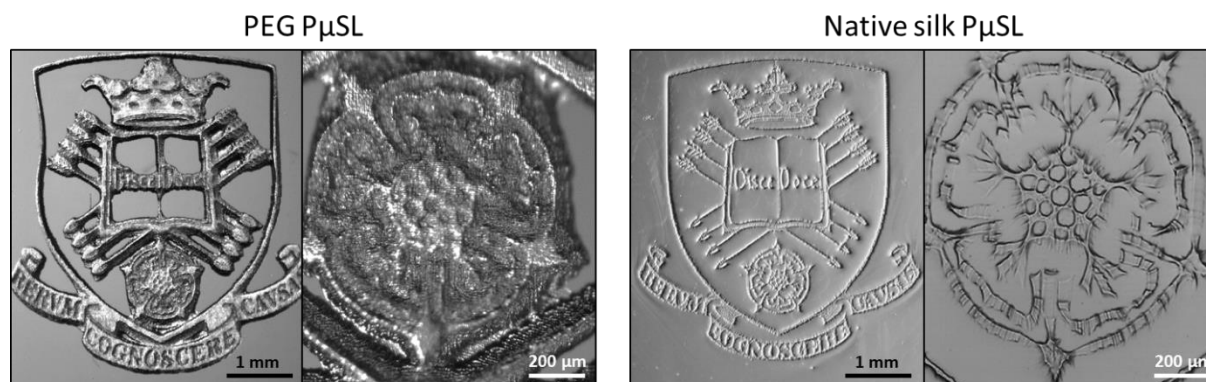


Figure 52: 'University of Sheffield' logo pattern fabricated by P $\mu$ SL from PEG and native silk solutions.

### 3.6. Protein quality in silk P $\mu$ SL patterning

A wide range of publications show that photolithography is a suitable approach for protein patterning <sup>192,221,250,252,268,269,405,454,455</sup>. However, to unravel the influences of protein processing on pattern quality and complexity, the performance of the silk community's standard reprocessed silk, known as regenerated or reconstituted silk, was compared to the gold standard, native silk.

Given that the mechanism of the silk photo-gelation is dependent on di-tyrosine crosslinking, it was hypothesised that to initiate the photo-gelation process, sufficient tyrosyl radicals need to be produced and so the concentration of the tyrosine in the solution, the light intensity applied, and the chain lengths of the polymers, combined, will ultimately determine the crosslinking rate and the final quality of the pattern. Given that there is no difference in the amount of tyrosines present per weight of protein between a native and a reconstituted silk, the major difference should be the molecular weight <sup>369,456,457</sup>. As a further means to test the tyrosine crosslinking/molecular weight hypothesis, of a tyrosine-rich polymer, (Glu-co-Tyr), was used as a control which has the potential to form 25 times more di-tyrosine bonds than silk but is of a lower molecular weight (15 times shorter average chain length).



Two different images were projected onto native silk, RS and poly (Glu-co-Tyr) solutions containing riboflavin. Minimum feature size was tested by a grid pattern with patterns ranging from  $4 \times 4 \text{ pixel}^2$  to  $100 \times 100 \text{ pixel}^2$  (Figure 53a-c, top). The quality of the image was tested by projecting the 'University of Sheffield' logo pattern (Figure 53a-c, bottom). For each sample type, the lowest concentration which provided the best pattern was selected. Image quality was assessed by a quantitative parameter of similarity between the original image projected from the DMD and the resulting pattern as described in the methodology section of this chapter.

Native silk offered a minimum feature size of  $40 \mu\text{m}$  and the highest Similarity value of 80% (Figure 53d, e) at just 1 wt% concentration. This concentration was found to be at least 2.5 times lower than any reconstituted silk solution used for photo-fabrication in the currently reported literature <sup>270,271,273,275-277</sup>, 6 times lower than the RS/fibroin photocurable resin recently reported by Applegate *at al.* <sup>122</sup> and 2 times lower than the reconstituted silk (2 wt%) used in this research which was the minimum concentration required to fabricate recognisable patterns. Furthermore, by using native silk it was possible to produce images with a similarity index  $>75 \%$  at all tested concentrations (0.5-3 wt%). Hence, it can be concluded that the suitability of a protein for complex image fabrication is not solely a factor of protein concentration. This is also supported by the lower quality image produced from poly (Glu-co-Tyr) solution despite the high concentration of tyrosine units in the sample (1.25 mol %) when compared to native silk solution (0.05 mol %). The improvement in the performance of native silk, when comparing it to other proteins that were used for patterning in this work, is most likely a result of its higher molecular weight.

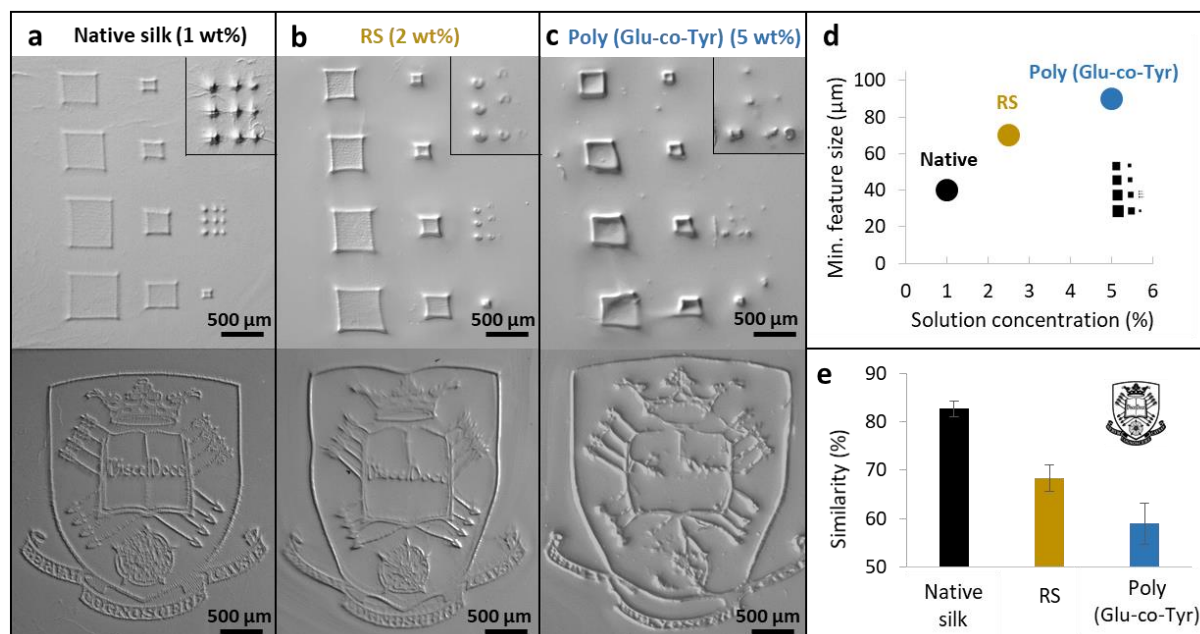


Figure 53: Comparison between feature size grid and logo patterns as received for (a) native silk, (b) reconstituted silk (RS), (c) Poly (Glu-co-Tyr) protein. (d) Minimum feature size measured for each sample as a function of optimal solution concentration. (e) Similarity value indicating how similar is, the fabricated pattern was, to the original projected image. Error bars represent +/- 1SD n=3.

### 3.6.1. The effect of RS quality on PμSL silk patterning

It is known that the process of silk reconstitution reduces the molecular weight of the silk fibroin<sup>85</sup>. The degradation of silk proteins is not attributed to the solubilisation in LiBr but rather to the degumming process. Degumming has been clearly shown to reduce silk's molecular weight with exposure time and concentration of Na<sub>2</sub>CO<sub>3</sub><sup>22,85,103,458</sup>.

To confirm that image quality is correlated to protein molecular weight, RS solutions were fabricated by directly dissolving cocoons in LiBr (no degumming) and chemical degumming cocoons by boiling them in 0.3%, 0.03% and 0.003% Na<sub>2</sub>CO<sub>3</sub> solutions prior to the dissolution in LiBr. As a result, RS with different molecular weights/degradation of the fibroin was produced and the M<sub>w</sub> was evaluated by gel electrophoresis (Figure 54a). The results demonstrated that the M<sub>w</sub> of native silk was significantly higher (≥ 420 kDa) than that of all

chemically degummed RS solutions ( $\leq 250$  kDa). While the fibroin only native silk solution was dominated by a single band on the gel (indicating the presence of a single protein chain with a uniform  $M_w$ ), the reconstituted silk had a smeared band across the whole column of the gel, indicating broad molecular weight distribution of polypeptide chains. The presence of a smeared band was also seen in the non-degummed sample which might suggest that even the process of dissolution in LiBr alone, degrades silk proteins, reducing their  $M_w$  and affecting their physical properties. This was previously confirmed by Cho *et al.*<sup>140</sup> and Wang *et al.*<sup>456</sup> who both recorded a decrease in fibroin molecular weight and storage modulus following dissolution in LiBr solution. However, it should be mentioned that the smeared band can also be attributed to the presence of sericin protein in the silk, which separates from the fibroin fibres during the silk reconstitution process. The molecular weight of the sericin ranges from 10 to 400 kDa<sup>459,460</sup> and its structure and molecular weight depend on the method of its extraction, purification and processing<sup>461,462</sup>. When sericin extraction was performed at a high temperature or acidic conditions, the molecular weight distribution was 35 – 150 kDa whereas when sericin was extracted in alkaline solution the molecular weight was 15 – 75 kDa<sup>462</sup>. This large distribution in the molecular weight of both proteins in the silk solution, the fibroin and the sericin, generate multiple bands of molecular weights on the gel resulting in the appearance of a smeared band on the gel.

To evaluate the dependence of image quality on the degumming process, the university logo pattern was printed on the various RS solutions. While the non-degummed RS was able to generate a full logo pattern, all the chemically degummed silk solutions resulted in incomplete, low-quality patterns (Figure 54b).

Rheological measurements during *in situ* photo-curing were performed, as described before, to compare the crosslinking reaction rate between native and reconstituted silks (Figure 54c). In both samples, a significant increase in the mechanical stiffness of the pattern ( $G'$ ) was measured during illumination while the reaction rate declined when the light was switched off. When compared to RS, native silk presented superior mechanical properties following light exposure resulting in a higher stiffness during each period of illumination. In contrast to the native samples, a slight increase in  $G'$  values, during the period of darkness, was noticed in some of the RS samples.

This increase was not noticed when the samples were measured in darkness during the same period without illumination. This suggests that light activates secondary reactions in the RS which do not occur in the native protein solution. Those reactions might result from the broad molecular weight distribution in the reconstituted silk solution, leading to multiple rates of the gelation in the sample. At the beginning of the process, the solution contains many fibroin fragments with short protein chains. When the crosslinking reaction is initiated, the rate of protein migration in the sample decreases due to sample gelation and molecular mobility restrictions reducing the rate of the photo-crosslinking reaction<sup>463</sup>. When the light is switched off, the slow reactions can still be recorded. When the reaction proceeds and the chains are beginning to crosslink, the probability for entanglement in the chains is increased, raising the rate of the crosslinking process<sup>102</sup>. The rate of polymerisation can increase with the light intensity to an upper limit which is defined as the rate in which the reaction kinetics are not controlled by the rate of protein/peptide fragment migration/movement in the sample, but only by the diffusion rate of the reactive species<sup>463</sup>. This can also be seen in Figure 54c where the reaction rate in the reconstituted silk is increased with every cycle of photo-exposure. In contrast, the molecular weight distribution in the native silk is more uniform, leading to a

constant rate of gelation with light exposure. Due to the long polymeric chains of the native silk, the reaction rate is rapid and terminates immediately when the light is switched off.

The effect of RS degumming on the development of pattern stiffness was evaluated by measuring  $G'$  for each sample under constant illumination. As predicted, RS without degumming demonstrated the highest  $G'$  value and the best image quality while chemical degumming significantly reduced the stiffness reaching less than 50% of the values for non-degummed samples (Figure 54d). In addition, the induction period for the highly degummed samples (0.3% of  $\text{Na}_2\text{CO}_3$ ) was longer, as expected, due to the presence of shorter polymer chains requiring more crosslinked regions to form a stable protein network.

These results strongly suggest that the process of silk reconstitution and thus the quality of the resulting protein solution significantly affects the potential applications of photopatterning and printing in silk. In addition, these findings are in good agreement with the wider photolithography literature which has previously shown a decrease in feature size with the increase in the molecular weight of the polymer<sup>464,465</sup>. However, whilst native silk is a convenient gold standard, it is not really an industrially scalable alternative as it has to be manually extracted from the animal, which is both time-consuming and technically challenging.

The use of reconstituted silk can be beneficial when industrial scales are required due to the ability to produce high quantities of silk solution by using controlled and well-established fabrication protocols. However, even though RS is broadly used across many fields in the silk literature, the current research introduces its limits when high-resolution patterning is required, emphasising the fact that by improving the current reconstitution approach, better quality silk can be fabricated and the application range for silk-based materials can be

expanded. Some examples of improved quality RS can be attributed to the use of  $\text{CaCl}_2$  for the dissolution of the silk fibres which allows preserving the nanofibril structure of the silk <sup>142,279,457,466</sup>. Alternatively, Boulet-Audet *et al.* <sup>467</sup> suggested that nearly native-quality reconstituted silk can be fabricated by degumming dry-spun silk cocoons in demineralised water. This was confirmed in this study, whereby using RS without prior degumming, it was possible to achieve patterns with comparable quality to that of native silk, as can be seen in Figure 54b. However, the process of chemical degumming was initially introduced to remove the sericin protein, which can potentially evoke an inflammatory response of the body when used in medical applications <sup>24,137</sup>. Therefore, the content of sericin in the silk solution, fabricated by alternative degumming methods should be broadly explored prior to using this approach for any medical-related applications. Following the fact that no sericin was recorded by Boulet-Audet *et al.* <sup>467</sup> following water degumming, alternative silk degumming is a highly promising approach for improving the field of silk manufacturing.

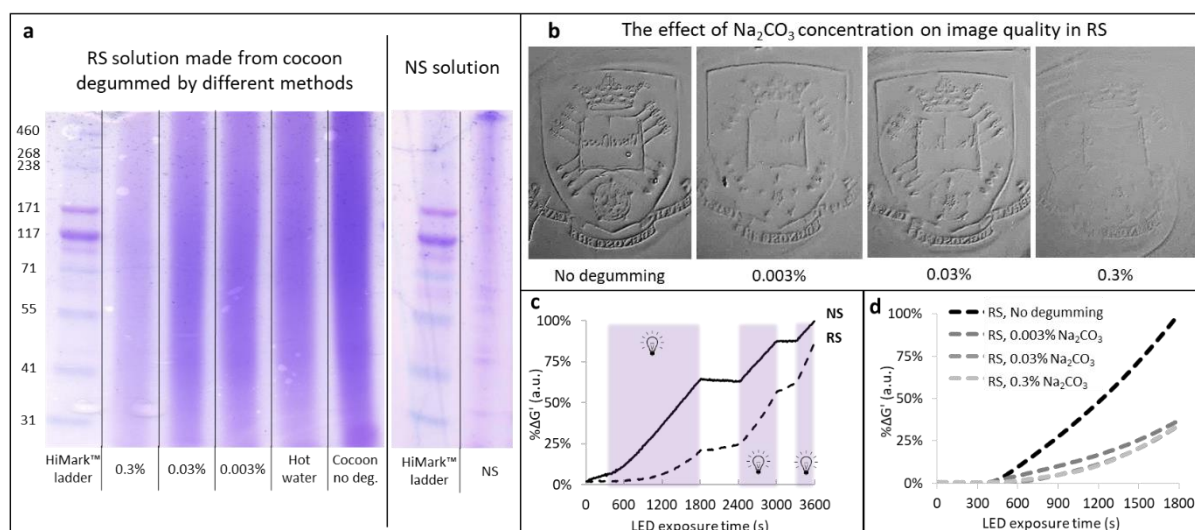


Figure 54: (a) Gel electrophoresis results for RS solutions degummed by the addition of 0.3%, 0.03%, 0.003%  $\text{Na}_2\text{CO}_3$ , by boiling the cocoons in hot water or direct dissolution in LiBr (no degumming). (a, right) Gel electrophoresis results for native silk. (b) Patterns fabricated by  $P\mu\text{SL}$  from the same solutions of RS at 2 wt% concentration. (c) Change in  $G'$  values (in %) of native silk (full line) (taken as 100%) and RS (dashed line) with (purple area) and without (white area) illumination. (d)  $G'$  values of RS patterns fabricated from solution that were degumming at various  $\text{Na}_2\text{CO}_3$  concentrations.

### 3.6.2. Enzymatic degradation of silk patterns

The previous section discussed the effect of degumming on pattern quality. However, the degumming process is relevant only when dealing with reconstituted silk. To evaluate the effect of the molecular weight in native silk proteins and move further beyond correlation towards causation, controlled enzymatic degradation was explored. Protease XIV is often used in silk literature to mimic biodegradability<sup>142,145,197</sup> because it causes protein catabolism by hydrolysis of the peptide bonds which break the peptide backbone leading to sample degradation (for silk this include both the crystalline and non-crystalline regions)<sup>468,469</sup>.

Numata et al.<sup>468</sup> investigated the enzymatic degradation of crystalline (methanol converted silk with  $\beta$ -sheet structure) reconstituted silk particles that were exposed to protease XIV. Each particle was composed of several nanofibrils. The thickness of the particle was approximately 5 nm containing 53 % beta-sheet, 36 % alpha-helix and random coil, and 11 % turns. Initial degradation of the particles, following the exposure to the enzyme, was observed after 12 h and resulted in the breakage of the particle into separate fibril-like fragments (nanofibrils) around 5 nm thick and 80–100 nm wide. While after 24 h degradation nanofilaments (160 nm length) were observed and the average thickness of the filaments decreased to 2 nm.

To understand the effect of the enzymatic degradation on image quality, protease XIV solution was added to the protein solution prior to patterning or was applied on the dry pattern after fabrication. At first, the appropriate concentration of protease was evaluated and found to be 0.0175 U/ml which allow for full degradation of the pattern after 30 min

(Figure 55a). Higher concentrations of the enzyme resulted in a very fast pattern degradation, which was hard to record.

Subsequently, protease was added to silk fibroin solution and a pattern was produced immediately after protease addition (with about 1-minute delay due to experimental set-up) and after 10 and 15 minutes (Figure 55b). No visible pattern was recorded 30 min after the addition of the enzyme. The molecular weight of the silk was evaluated using gel electrophoresis method (Figure 55c), as described before. The sample with the minimum exposure to the protease mainly presented a single band at high molecular weight (> 460 kDa), similar to that of a non-degraded native silk. This indicated a narrow distribution of the molecular weight and a more intact, native-like protein. As expected, this sample produced a good quality pattern reproducing all the features of the projected pattern. When investigating the ability for a silk solution to be structured after 10 and 15 minutes of enzymatic degradation, the protein bands on the gel were divided into multiple bands indicating smaller molecular weight fragments, and the average molecular weight was reduced. As expected, the pattern quality was reduced accordingly, resulting in only a partial pattern.

This result is in good agreement with the silk literature, indicating a wide molecular weight distribution after fibroin degradation with protease XIV, with molecular weights in the range of 3–370 kDa, <sup>144,468–471</sup>. Numata *et al.* <sup>468</sup> also reported that after enzymatic digestion of crystalline silk, several low molecular weight fragments (< 50 kDa), and more than 30 high molecular weight fragments (< 240 kDa) were received, suggesting that the silk molecules are digested at several hydrophilic domains.

As discussed in section 3.3, photocured silk patterns have a different crosslinking mechanism than that of silk fibres that were spun in physiological conditions <sup>122,268,276,414</sup>. Therefore, it



was assumed that the enzymatic degradation would not affect an already formed, crosslinked, pattern. Similarly to the use of water in chapter 3 and LiBr in the previous section, enzymatic degradation was tested as a potential route to reveal the pattern after fabrication by degrading the un-exposed silk solution around the photo-exposed pattern. However, when the patterns were immersed in the protease solution the entire sample and pattern degraded over time (after ~10 minutes of immersion (Figure 55d)). Nevertheless, a silk aggregate can be recognised in the top left corner in all images taken after enzyme addition, suggesting that the silk is not degraded by the enzyme but separates from the glass slide and aggregates. Understanding this effect of protease degradation, on photo-crosslinked silk might be beneficial for future research applications. However, it can be concluded that it is not a suitable technique for pattern development post-printing.

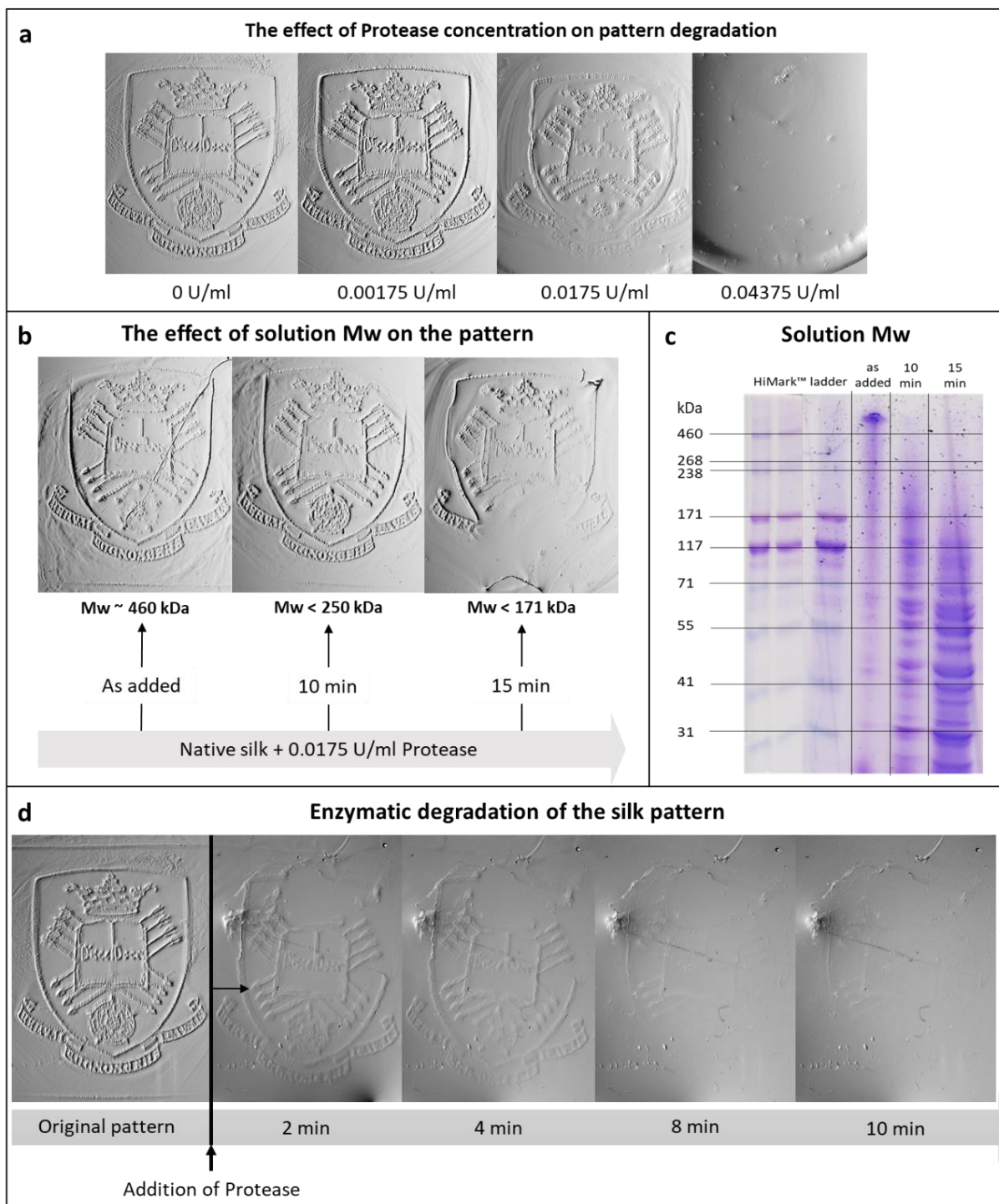


Figure 55: Enzymatic degradation of silk solutions and patterns by protease XIV. (a) The effect of enzyme concentration in the silk solution pre-fabrication on the printed pattern. The patterns were produced 10 minutes after the addition of the enzyme. (b) The patterns as produced immediately, 10 min and 15 min after the addition of 0.0175 U/ml enzyme to the silk solution. (c) Gel electrophoresis results of silk solutions used to fabricate the patterns presented in b. (d) Enzymatic degradation over time of silk pattern post-fabrication.

## 4. Conclusions

This chapter demonstrates that native silk is not only suitable for photo-lithography, but also enables one to achieve patterns with smaller feature sizes, better image quality and at lower concentrations when compared to using a standard reconstituted silk. The experimental conditions and pattern characteristics that were evaluated in this chapter are summarized in Table 9.

*Table 9: The summary of the experimental conditions and the pattern characteristic as evaluated in this chapter*

<b>Parameter</b>	<b>Values in the current set-up</b>
Native silk solution concentration	1 wt.%
Dye	riboflavin
Light source	GaN laser, 405 nm, 250 mW
Fabrication time	5 min/layer
Minimum feature size	40 $\mu\text{m}$
Subpattern spacing	3 $\mu\text{m}$
Maximum area for structuring	1 x 1 cm
Similarity to original image	> 80 %
pattern area multiplayer	3.43
Post processing (removal of un-polymerised solution)	LiBr 9.3M, 10 minutes
The elastic modulus of hydrogel patterns	30 – 16000 Pa

From Table 9 it is clear that patterns down to 40  $\mu\text{m}$  were fabricated, a resolution improvement of 20 % compared to previously reported riboflavin/RS photocuring<sup>122</sup>. On the macro-scale, by using the P $\mu$ SL method, photonic components were produced alongside larger scale patterns such as readable QR codes. The similarity index was introduced, for the first time in the field of silk structuring, to assess image quality in addition to feature size, for a better comparison between various structuring techniques and materials. Furthermore, the mechanism behind native silk photo-gelation was explored, with findings supporting previous

studies that suggested the formation of di-tyrosine bonds and the resulting chemical crosslinking of the proteins present.

However, it was observed that no protein structural conversion ( $\beta$ -sheet formation) occurred during the photo-curing of native silk, allowing us to decouple structuring with conversion and opening up the possibility to control protein crystallinity and mechanical properties. Finally, by comparing native silk to reconstituted silk, it was proposed that molecular weight is the main parameter contributing to the quality of the fabricated image and the mechanical stiffness of silk patterns. This was also confirmed by enzymatic degradation experiments. As a result, the author of this thesis proposes that to allow a fair comparison between various light-based structuring techniques in the future, the protein molecular weight should be stated in addition to protein concentration.

In conclusion, the approach presented in this chapter towards silk pattern generation and the insights gained into light-based silk structuring can hopefully contribute towards a fundamental understanding of natural silk solidification and potentially find application in food, packaging, security marking and medical devices industries in the future.

# Chapter 5

3D fabrication of silk structures  
by emulsion templating route

## Summary

This chapter introduces emulsion templating as a means to fabricate 3D interconnected porous silk structures known as poly-HIPEs. From a practical perspective, several ways to fabricate these structures are explored including creating the emulsion, stabilising it and finally phase removal and solidification. In order to gain a deeper understanding of why certain approaches are more successful than others, key physical properties are evaluated including emulsion viscosity, silk concentration, silk quality and solution pH. Finally, rheological studies are introduced to determine the mechanical properties of both the liquid emulsions and the solid scaffolds before discussion surrounding the potential range of applications these new materials could be used for.

## 1. Introduction

Previous chapters explored the suitability of silk as a structuring material in 1D and 2D fabrication. Despite promising results, creating 1D and 2D topographical architectures, many applications require rigid, porous and 3D structures to act as functional scaffolds/foams <sup>23,24,135,142</sup>.

One of the main applications of porous biodegradable scaffolds is in tissue engineering <sup>23,24,120,142,181</sup> where a porous matrix is used as a tissue grafting element to preserve volume, provide temporary mechanical support and to deliver bio-factors such as cells, growth factors and drugs <sup>24,172,182,183,472,473</sup>. Ideally, the scaffold degradation rate is matched to tissue regeneration rate to allow complete recovery and provide sufficient mechanical support during this process <sup>142</sup>. Key challenges in scaffold design are controlling porosity and building the many complex 3D shapes required to match the different geometries in the human body <sup>182,474–477</sup>. Furthermore creating an openly porous structure is desirable to allow mass-transport for cell nutrition and migration, and to provide enough surface features for cell attachment <sup>477</sup>. Looking beyond structure it is also important to control the surface chemistry of the scaffold which can determine the type of degradation and cellular interactions <sup>182,476</sup>.

Additional applications of porous scaffolds/foams might include insulation (thermal and sound), filtration and low-weight space fillers <sup>478–481</sup>. In addition, the high surface area of the foams makes them appropriate as substrates for catalysis, chromatography, separation, absorption, ion exchange, insulation, drug delivery and sensing <sup>284,478,482–485</sup>.

It is well-known silk exhibits the characteristics of a thermal insulator <sup>486,487</sup> and it has been used in thermal clothing for years <sup>488,489</sup>. However if we look to the biological role of the cocoon it has been recently found that wild silk has an even lower thermal diffusivity than

domesticated *B. mori* silk, which is attributed to the presence of calcium oxalate crystals trapping air inside the cocoon structure<sup>486</sup>. Learning from this natural approach for thermal insulation<sup>490</sup>, the combination of silk fibroin and air, as seen in porous silk foams, could be an ideal solution. Moreover, the thermal conductivity of the silk can be controlled by adjusting its crystallinity level (*e.g.* by methanol treatment), with lower crystallinity levels being poorer conductors, which can allow for customization of the foam properties to suit the desired application<sup>487,491</sup>. In a similar manner, the acoustic properties of silk have also been shown to be dependent on its crystallinity level ( $\beta$ -sheet content) which can be modified to fit specific sound insulation applications<sup>492</sup>.

Clearly, there is a need to develop new means to create 3D structures, therefore, this chapter explores emulsion templating route as a novel approach for the fabrication of silk scaffolds together with the preliminary routes that led to the selection of this specific fabrication method. In order to set the appropriate context of the work it is first beneficial to define the main terms used in this thesis chapter including emulsions, HIPes and poly-HIPes which are to follow:

## 1.1. Emulsion

An emulsion is a two-phase system composed of a matrix phase (matter) and droplet phase (colloids). Both phases are liquid and are usually immiscible (such as aqueous and lipophilic phases)<sup>493,494</sup>. Some of the most common examples might include milk (oil in water, O/W), body cream (water in oil W/O) and mayonnaise (O/W stabilised by the egg protein, lecithin). Generally, an emulsion is an unstable system which does not tend to form spontaneously and will separate over time<sup>495</sup>. An input of energy is required to form an emulsion, which is commonly provided by shaking, stirring or sonication of both phases<sup>496,497</sup>. The resulting



droplets of one phase are usually randomly distributed in the matrix without defined internal structure. Hence it is desirable to achieve long-term stability of the system to allow enough time for matrix solidification and the preservation of any porous geometry created <sup>495</sup>.

The stability of an emulsion is mainly affected by the droplet size distribution and the chemical composition of the droplet phase. Increased stability is achieved when droplets size decreases <sup>498</sup>. However any temperature increase will result in higher thermal energy in the droplets leading to more frequent droplet collision and as a result, larger droplet size <sup>499</sup>. To combat this, surface-active agents (surfactants), can be used as emulsifiers which create an interfacial film around the droplets, obstructing the droplet coalescing process <sup>500</sup>. The volume fraction between the oil and the water phases and the nature of the surfactant will define the type of the emulsion (W/O or O/W) <sup>495,501</sup>. The Bancroft rule <sup>502</sup>, introduced by Dwight Bancroft in 1913, states that the continuous phase (matrix) is defined as the phase in which the surfactant is more soluble in <sup>503</sup>. Therefore, proteins will promote the formation of O/W emulsion due to their high solubility in water <sup>495</sup>.

### 1.1.1. The mechanism of emulsion formation

The process of emulsion formation, known as emulsification, can be described as the transition from a single large oil droplet with an area  $A_1$ , into multiple smaller droplets with a total area of  $A_2$  (Figure 56).

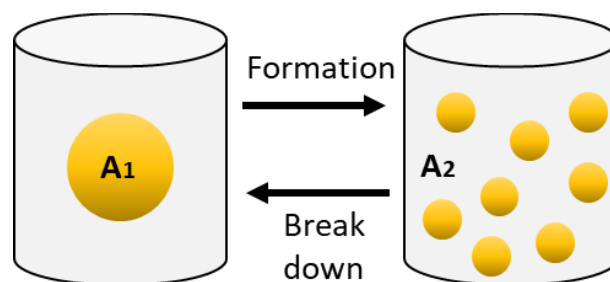


Figure 56: A diagram of emulsion formation and break down process. A large droplet with surface area  $A_1$  is separated into smaller droplets with a total surface area of  $A_2$  and vice versa.

The change in free energy ( $\Delta G^f$ ), required for the formation of an emulsion, can be represented by two terms:

1. The surface energy term:  $\Delta A\gamma_{12}$

In which  $\Delta A$  is the difference in surface areas:  $\Delta A = A_2 - A_1$ , and  $\gamma_{12}$  is the interfacial tension between the oil and the water. In the case of large droplet area ( $> 1 \mu\text{m}^2$ ) the interfacial tension  $\gamma_{12}$  is the same for both the large and the smaller droplets.

2. The entropy of dispersions term:  $T\Delta S$

Which represents the increase in the configurational entropy following the production of a large number of droplets.

From the second law of thermodynamics  $\Delta G^f$  is given by:

$$(1) \quad \Delta G^f = \Delta A\gamma_{12} - T\Delta S$$

For most emulsions  $\Delta A\gamma_{12} \gg -T\Delta S$  which leading to  $\Delta G^f > 0$  meaning that the formation of the emulsion is a non-spontaneous process, and the system is thermodynamically unstable.

When stabilizing the emulsion by the addition of a surfactant and/or polymer to the continuous phase, an energy barrier is created between the droplets, inhibiting the breakdown reaction and leading to a kinetically stable system.

It is fairly easy to form large droplets ( $> 1 \mu\text{m}^2$ ) to generate a macro-emulsion, by applying high speed stirring or mixing to both phases. This can be achieved by various techniques including vibrational stages, magnetic stirrers, centrifuges and ultrasonic probes<sup>503</sup>.

However, the formation of nano-emulsions with droplets having a sub-micron surface area is challenging and requires high energy input or sufficiently high surfactant concentrations<sup>504</sup>.

This is a result of the pressure difference between the inside area and outside surface of the droplet, known as Laplace pressure ( $\Delta p$ )<sup>501,505</sup>.

This pressure is determined by the two principal radii of curvature of the droplets ( $r_1, r_2$ ) and is given by:

$$(2) \quad \Delta p = \gamma \left( \frac{1}{r_1} + \frac{1}{r_2} \right)$$

In a perfectly spherical droplet  $r_1 = r_2$ . However, as a droplet begins to break apart following the stirring, the droplet is strongly deformed which leads to an increase in the value of  $\Delta p$  (Figure 57)<sup>495</sup>. Due to the inverse ratio between the pressure and the radii, the stress needed to deform small droplets is much higher than the one required to deform larger droplets and requires more vigorous agitation/ higher energy input. This can be ameliorated in part by the use of surfactants which serve to lower the interfacial tension, reducing in the value of  $\Delta p$  and the total energy input required for the process<sup>495</sup>.

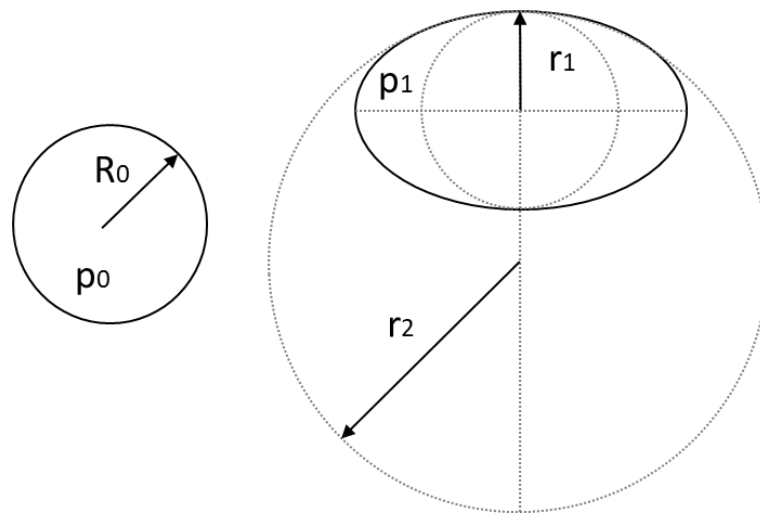


Figure 57: Schematic illustration of the radii of curvature in a perfectly spherical droplet ( $R_0$ ) and a droplet deformed to ellipsoid shape ( $r_1, r_2$ ). The pressure in the drops is  $p_0$  and  $p_1$  accordingly, while  $p_1 > p_0$ .

When droplets are in close contact with each other they can coalesce, forming larger droplets and reducing the stability of the system. There are a few factors which affect this collision such as matrix viscosity, electrical repulsion and the presence of surfactants. At first, the viscosity of the matrix (such as the water phase) prevents the droplets from approaching their collision point. An increase in matrix viscosity (*e.g.* by the addition of salts) will inhibit droplet coalescence, while a decrease in matrix viscosity (*e.g.* by heating) will enhance the coalescence rate<sup>499</sup>. The second collision barrier is the presence of a double charge electronic layer surrounding the droplets. Two nearby droplets, having the same chemical composition, will have the same surface charge, which will result in a repulsive force between the droplets, preventing the collision process<sup>495</sup>. Finally, the surface film on the droplet, created by the surfactant, contributes to emulsion stability and prevents coalescence of the drops<sup>505</sup>.

#### 1.1.2. Emulsification methods

Emulsification can be achieved by various methods classified by the level of energy introduced into the system during the emulsification process<sup>505</sup>. Low energy input methods including pipe flow<sup>506,507</sup> and droplet injection<sup>508,509</sup> cause minimal distortion to the continuous phase. Medium energy input methods involving shakers, vibration stages and low-speed stirring can induce flow of the matrix phase, generating frictional and inertial forces<sup>494,495,498</sup>. High speed mixing or stirring, centrifugation and ultrasonication can provide the high energy input required for the generation of small droplets, however in so doing it will result in significant flow in the system and high shear stresses on the interface between the droplets and the continuous phase<sup>495,496,503</sup>.

When a solution flows, shear stresses are generated as a result of two flow regimes: laminar and turbulent. These flow regimes are described by their Reynolds number ( $Re$ ) which is

defined as the ratio between the inertial forces and viscous forces acting during flow. The value of  $Re$  is dependent on the linear liquid velocity ( $v$ ), liquid density ( $\rho$ ), the liquid viscosity ( $\eta$ ) and the characteristic flow length ( $l$ ) as follow:

$$(3) \quad Re = \frac{\text{Inertia forces}}{\text{Viscous forces}} = \frac{v l \rho}{\eta}$$

When  $Re > \sim 1000$  the flow is laminar and when  $Re > \sim 2000$  the flow is turbulent<sup>510</sup>. Thus, for two equal emulsions having the same viscosity and density, vigorous mixing will lead to an increase in the flow speed  $v$  resulting in a more turbulent flow regime. This in turn will generate increased shear stress on the droplets and will lead to droplet breakdown resulting in smaller droplet sizes in the emulsion (Figure 58).

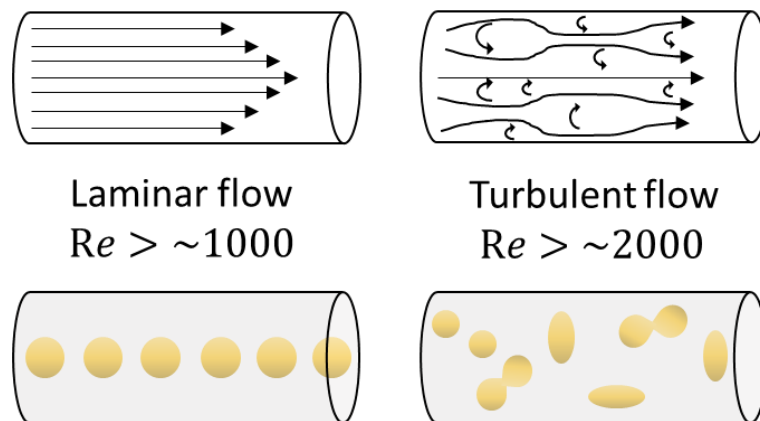


Figure 58: Schematic illustration of laminar flow (left) and turbulent flow (right). The droplets shape (yellow) is presented for each flow regime.

An additional parameter that affects the breakup of the droplets is the viscosity of the oil in the droplet phase. Droplet deformation time ( $\tau_{def}$ ) is the ratio between the viscosity of the oil ( $\eta_{oil}$ ) and the stress acting externally on the droplet ( $\sigma$ ) as follow:

$$(4) \quad \tau_{def} = \frac{\eta_{oil}}{\sigma}$$

Therefore, it will take longer to deform droplets with higher viscosity.

## 1.2. High Internal Phase Emulsion (HIPE)

Emulsion stability is dependent on the packing factor ( $\phi$ ) which is defined as the fraction of the total emulsion volume occupied by the droplet phase<sup>505</sup>. The maximum packing factor ( $\phi_{max}$ ) that spherical undeformed droplets can reach 0.74. In the special case of high internal phase emulsions (HIPEs), the packing factor exceeds this value ( $\phi > \phi_{max}$ ). This can be achieved following deformation of the spherical droplets, resulting from emulsion compression which occurs when a high ratio of droplet phase is added to the solution<sup>282</sup>. As a result, the spherical droplets deform into tightly packed polygon-shaped particles that occupy the space more efficiently (Figure 59).

From thermodynamic perspective, HIPEs are created as a result of an outer pressure which acts on the droplets and compresses them. This pressure is equivalent to the internal osmotic pressure ( $\Pi$ ) of the droplet. During the shape transformation, from spherical to polygonal, the droplet surface area ( $s$ ) is also increased. The stored energy from this shape transformation is equal to the work produced by the outer pressure during HIPE formation<sup>501</sup>. This equality means that the osmotic pressure following the decrease in volume ( $dV$ ) is equal to the work needed to create an additional surface ( $ds$ ). This relationship is described in the equation below, where  $\sigma$  the interfacial tension:

$$(5) \quad -\Pi dV = \sigma ds$$

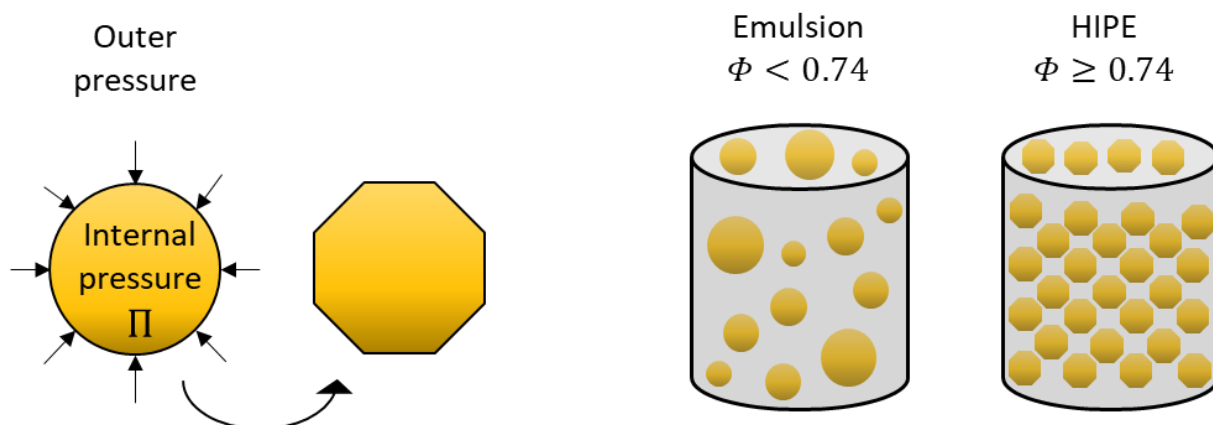


Figure 59: Schematic illustration of droplet shape transformation during the process of HIPE formation.

### 1.3. Poly-HIPES

Poly-HIPES are emulsion-templated polymers with unique interconnected porous structures synthesized from high internal phase emulsions (HIPES) <sup>282-284,511</sup>. These structures are the result of closely packed droplets (with packing factor  $> 0.74\%$ ) embedded in a continuous matrix. After polymerisation and the removal of the droplet phase, the cavities left will form the main pores known as voids. During the polymerisation processes, the continuous matrix phase usually shrinks, causing the void walls to rupture and forming interconnected holes known as windows. As a result, an interconnected open-cell porous structure is formed. Some of the major advantages of a poly-HIPE include high levels of porosity (over 90 %), the ability to fabricate variable void sizes (from 10 to 100  $\mu\text{m}$ ) by controlling the droplet size, low densities of the foams (down to 0.03  $\text{g}/\text{cm}^3$ ), large surface areas (up to 700  $\text{m}^2/\text{g}$ ), high permeabilities and the ability to absorb large volumes of liquids <sup>283</sup>. Due to the extremely high surface area of the poly-HIPES, they are commonly used to support chemical reactions, acting as separation membranes and used as tissue engineering scaffolds <sup>282,284,512</sup>. Surface

functionalised poly-HIPEs can be used for cell culture, controlled drug delivery or as responsive and smart materials <sup>513–515</sup>.

### 1.3.1. Poly-HIPEs from natural materials

A review of the Literature indicates that poly-HIPEs are usually made from synthetic polymers, with or without surface modification <sup>282,284,513,514</sup>. Some poly-HIPEs can be fabricated from a blend of natural and man-made polymers or can be incorporated with bioactive particles, (e.g. hydroxy appetite) to improve scaffold biocompatibility and cell attachment <sup>516–518</sup>.

Despite the broad use of poly-HIPEs in tissue engineering <sup>477</sup>, there is very limited evidence in the current literature for poly-HIPEs which are purely made from natural materials <sup>251,512,519</sup>. The first instance of the development of a natural poly-HIPE was by Barbetta *et al.* <sup>251,519</sup> who fabricated a gelatin methacrylated poly-HIPE more than a decade ago. However, this was not entirely natural as the production process of this gelatin-based poly-HIPE involved the use of toxic solvents such as dimethyl sulfoxide (DMSO) and toluene which can affect biocompatibility. In 2012, Zifu *et al.* <sup>512</sup> introduced protein poly-HIPEs fabricated from bovine serum albumin (BSA) as the solution phase and hexane as the droplet phase. Those pioneering publications indicate that there is much to explore in the fields of natural material poly-HIPEs.

The combination of the poly-HIPE structure with the benefits of natural materials, such as high biocompatibility and physiologically relevant biodegradation rates <sup>142,144,145,520,521</sup>, holds promising potential in the fabrication of next-generation medical materials. In addition, natural materials, such as silk, exhibit unique physical properties <sup>522</sup> which cannot be fully reproduced by the current routes of artificial silk production <sup>14,103</sup>. At last, the fabrication methods of the natural poly-HIPEs explored in this chapter, are water-based processes which



are environmentally friendly, without toxic waste products and with low energy consumption using ambient fabrication conditions.

The following chapter discusses the optimisation of silk poly-HIPE's fabrication. Several fabrication steps are deliberated such as the fabrication of stable emulsions, routes for emulsion stabilisation and the process of scaffold solidification. The mechanism is explored, and the mechanical and rheological properties are investigated. The fabricated scaffolds and the poly-HIPEs are characterised and potential application range is explored.

## 2. Methodology

### 2.1. Materials

All the experiments were performed using reconstituted silk solutions. This is due to the limitations of native silk when applying shear-based mixing methods such as shaking and stirring as described in section 3.1.

#### 2.1.1. Reconstituted silk solution fabrication

Chemically reconstituted silk solution was fabricated in according to the method described in chapter 2. Mechanically degummed silk was prepared from dry-spun *B. mori* silk cocoons by cutting them into small pieces and degumming in hot water for 30 minutes. Drying, dissolution and filtration stages were the same as for chemical degumming. Non-degummed silk was received by directly dissolving the whole *B. mori* cocoon in 9.3 M LiBr solution for 2 h at 60°C. Dissolution and filtration stages are the same as described for chemically degummed silk. All solutions were stored at 4°C and used within 1 week. This is to avoid any age-related degradation of the polymers or premature gelation. Prior to the experiment, the solution concentration was adjusted by mixing with DI water (to dilute the solution) or concentrated by dialysis (MWCO 12-14 kD, Spectra/por®) against 30 wt.% PEG (Mw 35,000 g/mol). Final solution concentration varied from 2.5 to 6 wt.%.

#### 2.1.2. Photo-curable silk solution

Photo-curable silk solution was fabricated by the addition of 0.2% Riboflavin 5'monophosphate sodium salt (Sigma-Aldrich) to the silk solution.

#### 2.1.3. Oil phase

The oil phase in all the emulsions was a pure rapeseed oil (Tesco, UK). No further purification was required.

### 2.1.3.1. Oil selection

In the current emulsion templating literature, the organic phase (oil) is commonly made of materials containing formamide (FA), dimethylformamide (DMF), dimethylsulfoxide (DMSO) and toluene<sup>284,518,523</sup> which hazardous to the human body with increased potential to cause damages such as skin irritation and liver failure together with proven carcinogenic and teratogenic activity<sup>524–526</sup>.

Rapeseed oil is one of a vegetable-derived renewable resource which applied in the production of biodegradable polymers<sup>527</sup>. This is due to its availability and a relatively low cost (600€/Metric Ton (IndexMundi database)). Rapeseed oil-based polymeric materials can be used in a variety of biomedical applications in tissue engineering, pharmacology, surgery, wound healing, and drug delivery, suggesting the potential biocompatibility of this oil<sup>527</sup>.

Therefore, in this work, rapeseed oil was selected as a natural, non-toxic alternative for the organic phase of the HIPes, which together with the natural silk solution can generate structures and scaffolds made fully from natural materials and suitable for medical applications.

An additional benefit of the rapeseed oil includes its low viscosity values (0.04 Pa·s)<sup>528</sup>, which allow to break it into droplets by applying low shear and preventing silk gelation, as discussed in chapter 3.3. In addition, preliminary experiments revealed that there is no chemical interaction between the silk and the oil which allow to avoid potential damage to the silk.

## 2.2. Direct methods for the fabrication of porous silk scaffolds

### 2.2.1. Pure silk freeze drying

Chemically reconstituted silk solution (4 wt. %) was cast into a mould and left to gel at room temperature for 1 week. The gelled structure was then freeze dried by first cooling to -4°C

overnight and then transferred to a container with a controlled freezing rate of  $-1^{\circ}\text{C}/\text{min}$ . The sample was then kept at  $-20^{\circ}\text{C}$  for 24 h to remove water.

### 2.2.2. Air foaming

1 ml of chemically reconstituted silk solution (4 wt. %) was placed into a 10 ml glass beaker. A 5 mm flexible pipe was connected at one end to a pressurised air supply (3 bar) and at the other end was fixed to a 25G needle (BD, USA). The needle was placed in the solution for 1 minute and the air supply was opened to allow foaming. The foam was transferred to a petri dish and air dried for 1 week.

### 2.3. Silk HIPEs fabrication

Reconstituted silk solution was transferred into a glass beaker and placed on a vibration unit (Vibrax-VBR, IKA, Germany). Pure repassed oil (Tesco, UK) was loaded into a disposable syringe (BD, USA) and mounted on a programmable syringe pump (AI-1000, World Precision Instruments, Herts, UK). The syringe tip was connected by a 5 mm flexible pipe to a 21G needle (BD, USA). The needle was placed above the surface of the silk solution (to avoid shearing by contact) and the oil was added drop-by-drop at a rate of 60 ml/min as illustrated in Figure 60. The stage vibration rate varied between a minimum of 600 and a maximum of 2200 rpm. After full addition of the oil, the needle was removed, and the fabricated emulsion was left on the shaker for 20 minutes. This is to allow homogeneous droplet distribution and the formation of the HIPE structure.

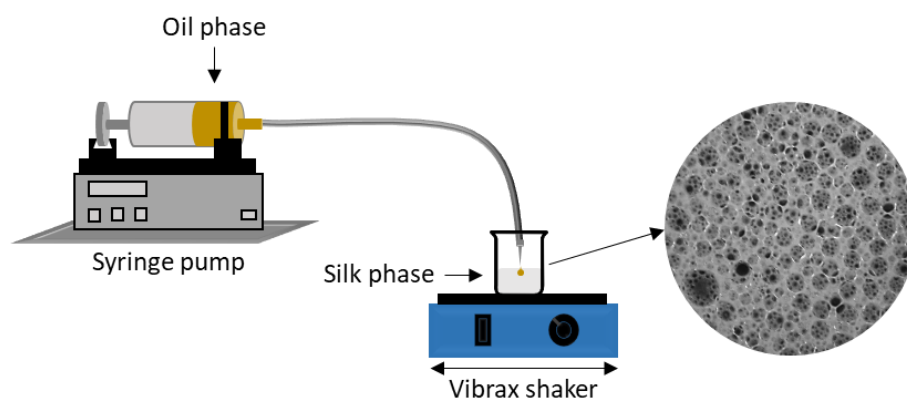


*Figure 60: Schematic illustration of the oil-in-silk HIPEs fabrication method, and an optical image of the fabricated HIPE structure.*

The HIPE was cast into several moulds including a microcentrifuge tube, spectroscopy cuvette, petri-dish and moulds with custom designed geometries. For some samples, a magnetic bar was added to the HIPE and the sample was mixed at 2000 rpm for 10 minutes on a magnetic stirrer (Stuart US151, Cole-Parmer, UK). After the mixing, a white viscous semi-solid foam was produced. The foam was transferred to the same moulds as described for the non-mixed samples and left for 1 week at room temperature to allow gelation.

## 2.4. Poly-HIPEs fabrication

Three solidification approaches were used to form solid poly-HIPEs from the produced HIPEs.

### 2.4.1. HIPEs stabilisation by natural gelation

In most cases, the mould with the HIPE was left to solidify for 1 week (7 days) at room temperature to allow natural silk gelation. The solid samples were gently separated from the mould and immersed in ethyl acetate solution for 24h, to dissolve the oil phase and reveal the porous structure. Then, the porous scaffold was placed on a paper towel and left to dry for several hours, until solid scaffold was received. A summary of the process can be found in Figure 61. The full protocol for the fabrication process can be found in Appendix A.

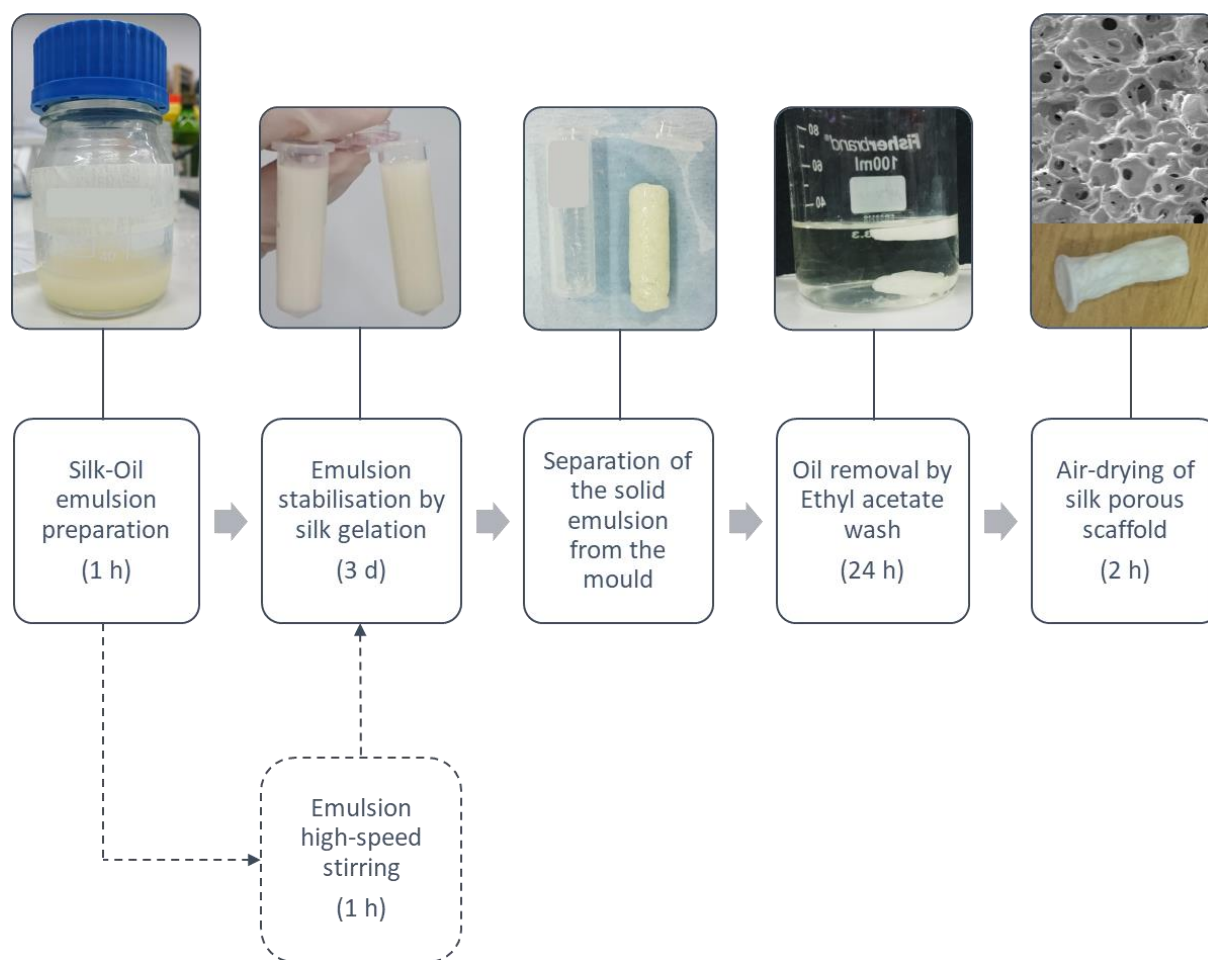


Figure 61: The fabrication of silk poly-HIPES by natural gelation solidification process.

#### 2.4.2. HIPES stabilisation by freeze drying

In some cases, to reduce the time of the natural gelation process, the HIPES were freeze dried directly after fabrication, in a similar method to that used in direct freeze drying of silk solution as described above. The solid samples were immersed in ethyl acetate for 24 h to remove the oil and then air dried for several hours until white solid scaffold is received.

\*This method was most suitable for flat samples (in a petri-dish), which provides a large exposed surface of the HIPE. When the HIPES were frozen inside 2ml microcentrifuge tubes, the samples remained liquid in the bottom of the tube and as a result, the sample collapsed during the attempts to separate it from the mould.

### 2.4.3. HIPEs solidification by freeze drying in water

The HIPEs were stabilised by the natural gelation method and oil was removed by ethyl acetate. After complete oil removal, the samples were immersed in DI water for 24 h to allow full water penetration into the pores. The wet samples were freeze dried using the standard freeze-drying process described above. The dried scaffolds were analysed without additional processing.

## 2.5. Mechanical characterisation

### 2.5.1. Compression test

The compression stiffness of the scaffolds was evaluated using Zwick Roell, Z0.5 material testing machine with a 500 N load cell (Zwick, Germany). A cylindrical silk scaffold (1 cm diameter, 0.2 mm thickness) was placed between two compression plates. The cross-head speed (top plate) was 0.5 mm/min.

The average stress, acting of the sample, was recorded at 0.2%, 20%, 40% compression strain and used as a representative value for sample stiffness.

### 2.5.2. Rheological measurements

Sample viscosity and elastic modulus were recorded using AR 2000 and Discovery HR-2 rheometers (TA Instruments, New Castle, DE, USA). The geometry for all measurements was an 8 mm parallel plate. All rheological data were acquired at room temperature ( $25 \pm 2^\circ\text{C}$ ). To avoid water evaporation, the sample was covered with a customized environmental chamber which was not in contact with the geometry of the rheometer at any time.

During the viscosity measurements a constant shear rate of  $\dot{\gamma} = 1 \text{ s}^{-1}$  was applied for 100 s to ensure the specimen was distributed evenly on the rheometer and to supersede any residual stress from sample loading. The shear viscosity at  $\dot{\gamma} = 1 \text{ s}^{-1}$  was obtained by

averaging data from the final 30 s of this stage. The oscillatory measurements were performed in two stages, an oscillatory frequency sweep (20 to 0.1 Hz) followed by a fixed frequency time ramp (1 Hz), both of which were conducted within the sample's linear viscoelastic region (target strain 0.01). For the oscillatory test, presented modulus values were calculated as the average  $G'$  value in the range between 1 to 10 Hz.



### 3. Results and discussions

The goal of the current thesis chapter is to present the development process of a simple water-based technique for the fabrication of 3D silk scaffolds having a poly-HIPE structure. To do so, several approaches were tested as preliminary routes to evaluate the best fabrication technique. Those sets of experiments, starting from simple single-phase fabrication and moving to two-phase emulsion templating are presented below.

#### 3.1. Selection of silk solution

Following the positive results for native silk structuring, described in the previous chapters, native silk was the first candidate for the current set of experiments. Therefore, native silk was tested in each preliminary experiment described in section 3.2. However, due to its rapid gelation when mechanical shear is applied, it was unsuitable for structure fabrication in most experimental approaches. In fact, when used in stirring or vibrational experiments, silk solution (concentration range of 0.5 – 2 wt%) gelled immediately, restricting possible experimental designs. Another limitation of native silk is its low quantity and limited availability. Each silkworm can provide 2 ml of silk solution (1 wt%) while to allow full process optimisation, larger quantities are desired. This will allow to perform multiple repeats and to gain better control over the process. Therefore, at this early stage of process development, only reconstituted silk solutions were used.

#### 3.2. Preliminary stages of process development

To investigate the best approach for silk poly-HIPE fabrication, several fabrication methods were tested, starting from direct single-phase fabrication routes including freeze drying and air foaming.

### 3.2.1. Direct methods for the fabrication of porous silk scaffolds

As described in chapter 1 of this thesis, there are few methods which can be used for the fabrication of porous scaffolds. Direct methods can be described as methods which do not require a sacrificial material such as salts (e.g. NaCl in salt-leaching) and solvents (e.g. methanol) which can interact with the silk affecting its properties <sup>49,529</sup>.

Two common direct assembly routes, including freeze drying and air foaming, were examined to evaluate the benefits and limitation of each fabrication approach when designing the optimal scaffold. Both techniques were tested for their suitability for the fabrication of pure silk scaffold with poly-HIPE structure.

#### 3.2.1.1. Freeze drying

The current silk literature is widely discussing freeze drying as the main solidification process for scaffold fabrication <sup>135,182,476</sup>. This is probably due to the simplicity of this technique as it permits a high level of control over the final pore size and the bio-friendly nature of the process <sup>182</sup>. During the process of freeze drying (lyophilisation), the sample is cooled down to water freezing temperature and ice crystals are formed. Then, the pressure is reduced, and the ice is removed by sublimation resulting in fully dried, solid sample. Scaffold porosity is generated from the ice crystals and can be controlled by adjusting sample concentration, freezing temperature and freezing/drying rates <sup>135,182,474,476</sup>. In general, slow freezing rates will allow the formation of large ice crystals generating macro-porous structures. While rapid freezing rates lead to supercooling (cooling below the freezing point without crystallization), preventing the formation of large ice crystals and leading to smaller pores. The pore sizes are usually uniform under given experimental conditions, however it is possible to introduce poly-

dispersed porosity by the addition of electrolytes to silk solution generating graduated ice nucleation rates <sup>474</sup>.

To explore this fabrication approach, silk solutions were produced as described in the methodology section and allowed to gel at room temperature for 1 week. The gelled sample was freeze-dried, and the final structure was explored. The fabricated foam had a white solid appearance with partial interconnectivity and open porosity, with pore diameter below 100  $\mu\text{m}$ . The scaffold had an uneven pore size distribution (Figure 62). The majority of the foam volume had a typical lamellar structure often seen in freeze-dried scaffolds <sup>530</sup>. Overall, the structure was similar to that previously observed in the literature and no poly-HIPE structure was present in the scaffold <sup>135,474,476</sup>.

Despite the popularity of freeze drying for foam fabrication, this method alone offers limited control over the interconnectivity of the scaffolds and produces insufficient pore size (< 100  $\mu\text{m}$ ) for tissue engineering applications <sup>531</sup>.

Following the fact that freeze drying fabrication route for silk scaffolds is well explored and optimised in the literature, and yet no silk poly-HIPEs were reported, little improvement can be achieved by further exploration of this route. Therefore, freeze drying alone was defined as unsuitable for silk poly-HIPEs fabrication.

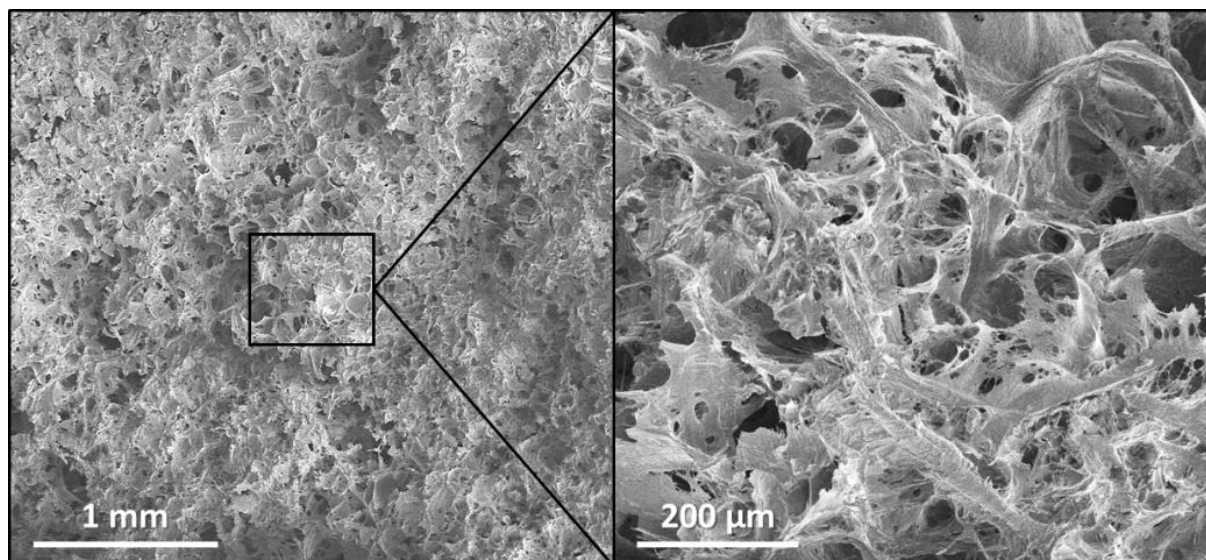


*Figure 62: Reconstituted silk scaffold fabricated by freeze drying process.*

#### 3.2.1.2. Air foaming

As an alternative route to freeze drying, gas foaming approach can also be suitable for the fabrication of silk-based porous scaffolds<sup>135,278,532</sup>. In this technique, a foaming agent such as ammonium bicarbonate is added to the silk phase to generate an inert gas such as N<sub>2</sub> or CO<sub>2</sub> under moderate acidic conditions. Then, the gas phase is removed, creating porosity in the remaining liquid phase. Usually, a highly viscous solution is used to avoid the drainage of the liquid phase, which might occur due to a significant difference between the densities of the gas and the solution. This fabrication method usually results in a highly interconnected openly porous structure, however, the structures have limited shape stability over time, and post-processing is required such as immersion in methanol/water solution or freeze drying to maintain the structure<sup>135,532</sup>.

This approach served as inspiration for the idea to use air pressure to generate porosity in the silk. This led to the attempt to fabricate silk scaffold by introducing air bubbles into the silk under high pressure using a pressure gun similar to that used in spray painting. Since the

bubbles are injected under pressure into the protein solution, the solution is expected to foam, as can be witnessed when beating an egg white (albumen). The shear-induced in the sample following the interaction between the bubbles (injected at high speed) and the silk (static) are expected to generate gelation of the silk and as a result solidification and stabilisation of the porous structure.

As expected, when air foaming was tested on the silk solution, a stable semi-solid foam was produced. No further processing was required apart from air drying in ambient condition to allow water evaporation and silk solidification. The fabricated solid scaffold was examined under SEM (Figure 63).

The scaffold showed fine-porosity with average pore size  $< 5 \mu\text{m}$ . Due to the small size of the pores and uneven distribution of the pores along the scaffold (as a result of manual fabrication) it was challenging to explore the interconnectivity of the pores.

However, this potentially low-cost and single stage approach for silk scaffolds fabrication might be beneficial for some applications requiring fine porosity and can be a potential route for exploration in future research. In fact, a better control over the foaming process (by designing an automated injection system) might allow a more uniform distribution of the pores and better control over the pore size.

Nevertheless, since the aim of this research was to generate a poly-HIPE structure which was not witnessed in the air foamed silk and keeping in mind that tissue engineering scaffolds require large interconnected pores ( $> 100 \mu\text{m}$ ), this fabrication method was not investigated any further in the current research.

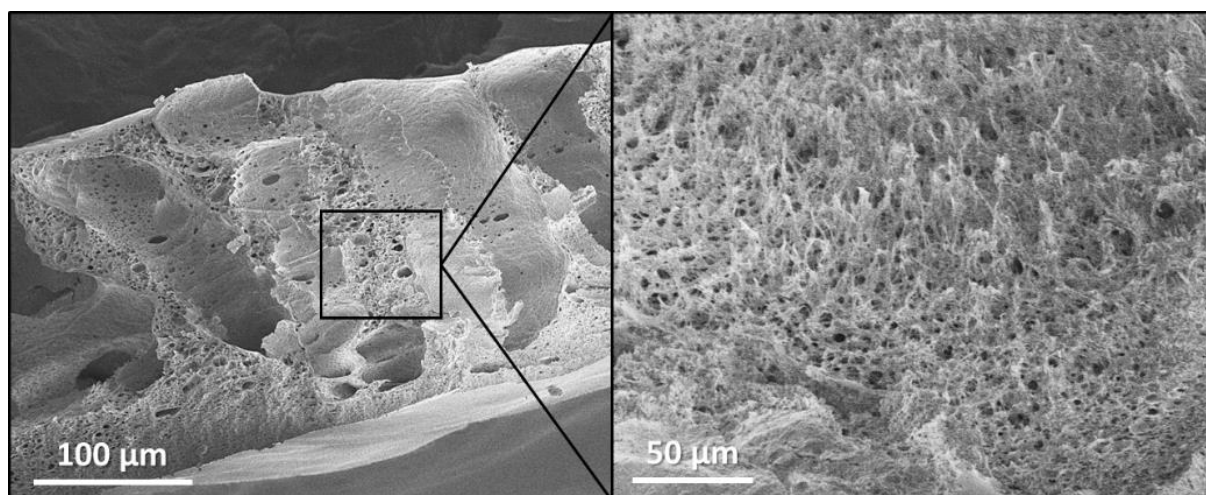


*Figure 63: Reconstituted silk scaffold fabricated by air foaming process.*

Both fabrication methods, described above, had strong limitations when precise control over the porosity is required and were therefore deemed not suitable for the fabrication of scaffolds with poly-HIPE structures. Hence it was concluded that a second liquid phase is required for the process.

The introduction of a second phase allows one to generate an emulsion and to develop a new approach for silk fabrication utilising an emulsion templating method. In this method, the porosity is generated by the addition of a secondary phase (oil) into the main phase (silk solution). By precisely controlling the ratio between the phases, it is possible to fabricate HIPE structure which will generate poly-HIPEs after solidification and oil removal. This structure is usually stabilised by the uniform dispersion of the small droplets in the continuous matrix.

### 3.2.2. Indirect method for scaffold fabrication – two-phase emulsion

When developing a new approach for the fabrication of silk and oil emulsion, the first step in is to evaluate the optimal method to distribute the oil phase in the silk matrix. To do so, it is required to incorporate the oil bubbles/droplets into the aqueous silk matrix and to evenly distribute them across the matrix. Due to the limited stability of emulsions, it will tend to

separate<sup>505</sup>. Therefore, it is especially important to achieve long enough stability to cover the duration of the matrix solidification. This can be reached by both increasing the rate of matrix solidification and reducing the rate of droplet collision.

Emulsion stability is mainly affected by droplet size distribution and the chemical composition of the matrix. Reducing the size of the oil droplets will contribute to stability<sup>495</sup>. This can be achieved by two main approaches: The first is breaking the oil into small particles (e.g. by spraying the oil under pressure) and distributing those particles in the solution, or by the addition of the oil phase on top of the matrix and applying high speed mixing (e.g. by a magnetic stirrer or a centrifuge) to break the oil into small droplets *in situ*.

To test those approaches, rapeseed oil and reconstituted silk solutions were used in a ratio of 3:1 (oil to silk), which is the minimum ratio required for HIPE formation (matching a packing factor of  $\Phi=0.74$ )<sup>282</sup>. After fabrication, all the emulsions were transferred to moulds and left at room temperature for 1 week to allow complete gelation of the silk matrix. After gelation was achieved, the oil phase was removed, and the sample was dried. The final scaffolds were examined by SEM.

#### 3.2.2.1. Oil spraying

In this fabrication approach, small oil bubbles were created by spraying the oil using a paint pressure gun. This is in an analogous manner to the air foaming process described in section 3.2.2.1. By modifying the gun pressure, it should be possible to control the droplet diameter and the subsequent pore size of the scaffold. However, the maximum gun pressure that was generated in the current process, was not sufficient enough to allow significant bubble penetration into the silk solution phase. As a result, the oil was localised mostly on the surface of the silk solution phase. This is probably a result of the high surface tension of the oil-water-

air interface<sup>533,534</sup> which requires higher energy input to allow oil penetration. SEM analysis indicated a closed-pore structure with minimal interconnectivity, similar to that seen in scaffolds which were fabricated by standard freeze drying method (Figure 64, left). Therefore, this method was excluded for HIPE fabrication.

It might be possible to improve the penetration of the oil with by increasing the gun pressure. However, this might result in significantly high shear on the silk and potentially induce premature silk gelation<sup>12</sup>.

#### 3.2.2.2. Fast stirring

One of the common approaches for emulsion stabilisation is high-speed stirring, introducing shear, which overcomes the interfacial tension between the oil and the water layers breaking the oil droplets and generating smaller bubbles<sup>495</sup>. The introduction of shear can lead to both droplet coalescence or droplet break-down. Applying medium shear levels promotes droplet coalescence and therefore increase the average pore size of the final scaffold. However, applying high shear levels, as can be done by fast stirring, results in a turbulent flow regime which can cause significant droplet deformation followed by droplet break-down. This will result in a highly dispersed emulsion with smaller average droplet size<sup>498</sup>. Since the stability of the small-droplet emulsion is higher than a large-droplet emulsion, this approach can be a suitable emulsion stabilisation. This method is commonly used on synthetic polymers which are not usually not sensitive to high shear<sup>342,484,485</sup>.

To explore the potential of this approach for silk HIPEs fabrication, a rapeseed oil layer was added on top of the silk solution. The sample was placed on a magnetic stirrer and mixed at maximum speed by using a stirrer bar, with the aim to break the oil layer into microscopic droplets. It was hypothesised that the addition of the oil will reduce silk response to shear by



further dilution of the silk solution. However, as expected, due to the shear-sensitive nature of the silk proteins<sup>69</sup>, full silk gelation occurred before the droplets were small enough to form a stable emulsion. SEM images confirmed closed cell porosity with no evidence of a poly-HIPE structure (Figure 64, centre). Therefore, stirring alone, cannot be a suitable method for the fabrication of oil/silk emulsions.

#### 3.2.2.3. Centrifugation

Centrifugation can be used as an alternative method to stirring since it allows one to generate high turbulence in the solution (to break oil droplets) at much lower shear rates when compared to high-speed stirring<sup>535</sup>. During stirring, the magnetic stir bar is in a direct contact with the silk solution which increases the shear acting on the silk protein, due to friction between the bar and the silk. In centrifugation, the centrifugal force acts externally, without the need for an internal stirring bar, reducing any localised high degrees of shear on the silk<sup>535</sup>.

To test the applicability of centrifugation for silk emulsion stabilisation, the oil phase was added on top of the silk solution and the sample was put in a centrifuge. The centrifuge was operated at 13,000 rpm for 10 min. SEM images indicated that the scaffold fabricated by centrifugation had similar structure to that seen in scaffold fabricated by high-speed stirring and oil spraying (Figure 64, right) confirming the lack of emulsion formation and the absence of a poly-HIPE structure. Visual inspection indicated that the pore size was smaller when compared to scaffold fabricated by fast stirring with more uniform pore size distribution. This method can be suitable for the fabrication of silk scaffolds when closed porosity is required (e.g. for thermal insulation in environments with high humidity level such as wet cavities) but is not suitable for the fabrication of interconnected silk poly-HIPEs.

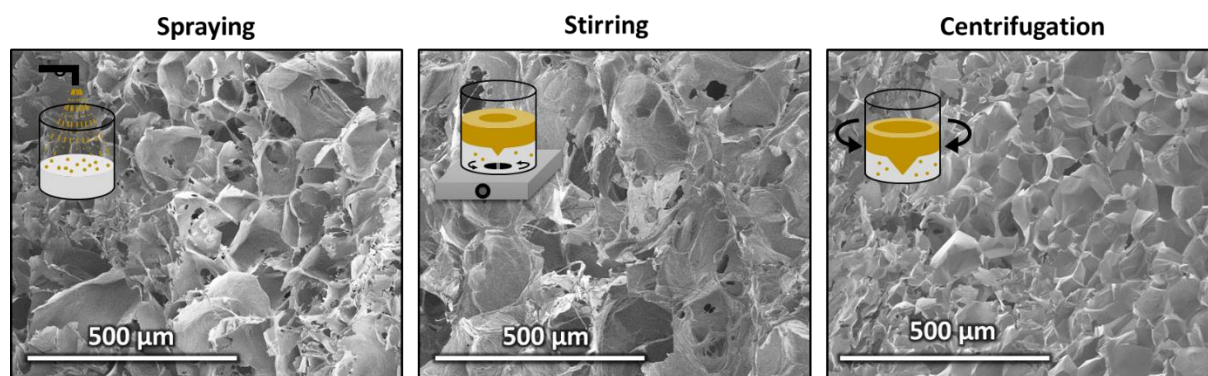


Figure 64: SEM image of the cross-sections of the silk scaffold as fabricated by oil spraying (left), stirring (middle) and centrifugation (right) methods.

#### 3.2.2.4. Drop-by-drop oil injection

Silk solution gels when shear is applied<sup>69</sup>. Therefore, it is important to minimise the turbulent flow in the solution. All of the methods proposed above failed to form an emulsion and as a result, no poly-HIPE structures were produced. Hence an alternative method is required, which will provide uniform distribution of the droplets in the silk matrix with minimal flow disturbance. This can possibly be achieved by controlled injection of the oil in a drop-by-drop manner into the solution and gently shaking the emulsion to allow even distribution of the droplets across the full emulsion volume<sup>536–538</sup>. To test this approach, the silk solution was placed on a vibrational stage and the oil was slowly injected. As a result, a stable white emulsion was produced. The emulsion remained stable until full gelation of the silk was recorded (1 week).

It is important to note, that an oil in water emulsion does not show similar long-term stability<sup>511</sup>, and usually separates after few minutes or hours (dependent on the droplet size). Therefore, it is possible that in the oil/silk system the fibroin protein acts as a stabiliser agent (surfactant) contributing to the stability of the emulsion. In fact, proteins can often act as stabilising agents in HIPEs<sup>511,512</sup>. Therefore, silk solution can potentially act as both, the matrix

phase and the surfactant layer contributing to successful HIPE fabrication. In addition, silk can undergo natural gelation under ambient conditions <sup>15,22,62</sup>, which can assist to preserve the HIPE structure during the process of poly-HIPEs solidification.

SEM analysis revealed uniform interconnected porosity across the whole volume of the drop-by-drop injection fabricated scaffold save for a thin film layer on the top (Figure 65). This type of structure a poly-HIPE and indicates the formation of HIPE structure between the oil droplets and the silk matrix <sup>282-284</sup>. Therefore, due to the success of this approach, the drop-by-drop oil injection into the silk matrix was chosen as the main fabrication approach for silk poly-HIPEs and will be explored in the sections below.

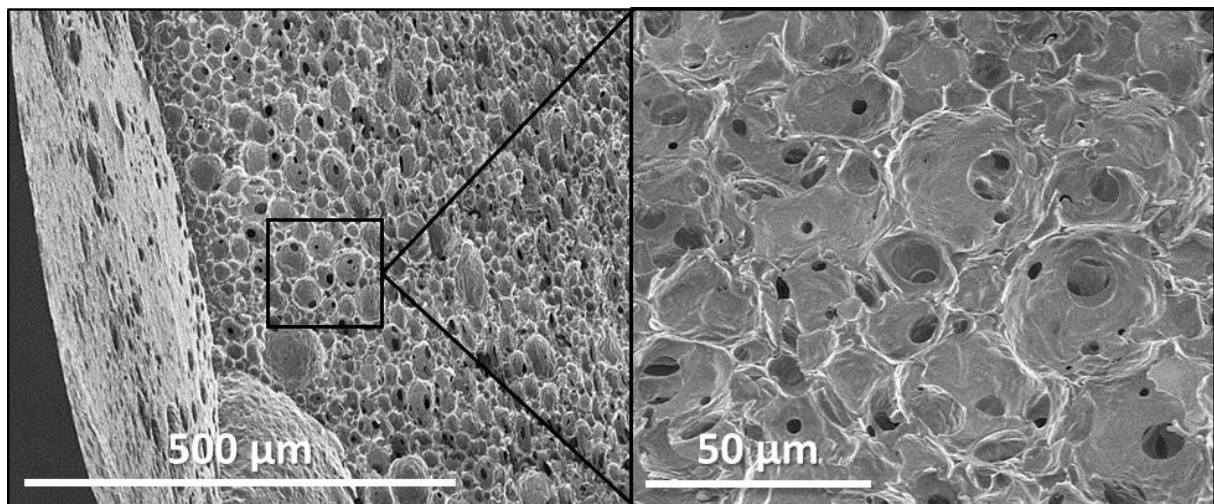


*Figure 65: SEM image of silk scaffold fabricated by drop-by-drop oil injection method. The scaffold has uniform pore size distribution with interconnectivity.*

### 3.2.3. The conclusion from preliminary experiments

A few key conclusions were dawned from the preliminary experiments:

1. Native silk is not suitable for 3D scaffold fabrication when used in the current experimental set-up.

2. Single phase fabrication routes (freeze drying and air foaming) were not suitable for the generation of silk poly-HIPEs and the addition of the second phase is required.
3. Drop-by-drop oil injection method was the only one that allowed the production of stable silk poly-HIPEs without premature silk gelation.

The conclusions of the preliminary experiments suggest that oil-in-silk HIPEs can be generated and stabilised in a green and low-cost method, without any additional additives. Furthermore, after the solidification of the silk and removal of the oil phase, the poly-HIPE structure was recorded and the diagnostic voids and windows geometries were observed <sup>283</sup>.

However, the initial process had low repeatability level and resulted in the inconsistent porosity of the scaffolds, indicating that a full optimisation of the fabrication approach is required.

The sections below (3.3 – 3.13) describe the optimisation process of each fabrication step including emulsion formation, emulsion stabilisation and emulsion solidification. In addition, it explores the contribution of various experimental parameters to the final porosity, structure and shape of the scaffolds.

### 3.3. The fabrication and study of Oil-in-silk (O/S) emulsions

This section explores the process of oil-in-silk HIPEs fabrication using emulsion templating approach that was evaluated during the preliminary experiments in section 3.2.

To form O/S emulsions, oil droplets were added into to the silk solution and the solution was gently shaken to allow even distribution of the droplets to promote the formation of HIPE <sup>282,511</sup>. In addition, a control oil-in-water (O/W) emulsion was fabricated by the distribution of oil droplets to DI water at the same ratio as for O/S and then vigorously stirring the mixture

until a uniform emulsion was achieved. High-speed mixing was required to generate the emulsion. The O/W emulsion was not stable and separated a few minutes after fabrication. In contrast, the O/S emulsion was stable and did not separate during the whole experimental procedure.

Rheological measurements of the viscosity revealed that O/S emulsion had a higher viscosity ( $\sim 3 \text{ Pa}\cdot\text{s}$ ) by an order of magnitude, when compared to that measured for pure rapeseed oil ( $0.04 \text{ Pa}\cdot\text{s}$ )<sup>528</sup>, diluted silk solution (4 wt%,  $0.05 \text{ Pa}\cdot\text{s}$ ) and the O/W emulsion prior to separation ( $0.14 \text{ Pa}\cdot\text{s}$ ) (Figure 66a). Those viscosity values suggest that the silk protein acts as a stabiliser, increasing the viscosity of the emulsion and its stability over time. This result is in an agreement with the literature, previously suggesting proteins as suitable surfactants for emulsion fabrication and HIPEs stabilisation<sup>511,512,539</sup>.

No significant variation in the viscosity of O/S emulsions was recorded in the short period of the measurement (100 sec) indicating that the measuring procedure alone does not affect the emulsion's viscosity. However, when measured for longer periods of time, a slight increase in viscosity from  $\sim 3 \text{ Pa}\cdot\text{s}$  (immediately after fabrication) to  $\sim 15 \text{ Pa}\cdot\text{s}$  (3 hours after fabrication) was recorded (Figure 66b). Due to the presence of an environmental trap to prevent moisture loss and skin formation, this is probably a result of natural silk gelation that is initiated by the shear during the shaking process used to distribute the oil droplets in the silk<sup>55,69,95,329</sup>. In addition, when sample viscosity was measured 160 minutes after fabrication, the initial viscosity was high ( $17 \text{ Pa}\cdot\text{s}$ ), with a gradual decrease in the first 50s of measurements, down to a value of  $10 \text{ Pa}\cdot\text{s}$ . This might be a result of a weak protein network which started to form in the silk which breaks down following the non-linear rheological

measurements <sup>329</sup>. For all samples, the viscosity was defined as the viscosity value recorded after 100s of measurement.

To evaluate the rate of viscosity increase as a function of time since fabrication ( $d\eta/dt$ ), a fresh emulsion was produced and kept at room temperature. A sample from the emulsion was measured occasionally over a period of 5 hours (Figure 66c). Subsequently, the viscosity increase rate was evaluated from a linear fit to the results and was found to be about:

$$d\eta/dt = 0.04 \frac{Pa \cdot s}{min}$$

The linear increase in emulsion viscosity suggests that the selected fabrication method initiates the natural silk gelation process which usually follows similar gelation rates <sup>69</sup>. This process can be used as a stabilisation stage to maintain the structure of the emulsion and to allow the fabrication of solid silk scaffolds.

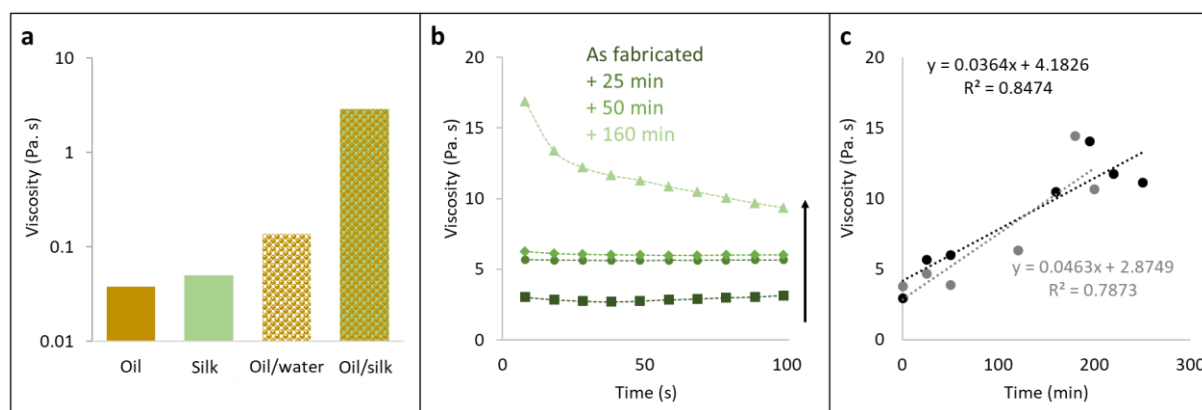


Figure 66: (a) Viscosity values for pure rapeseed oil (brown) <sup>528</sup>, reconstituted silk solution 4 wt% (green), oil/water mixture (brown/white) and oil/silk emulsion (brown/green). (b) Viscosity over time of oil/silk emulsion immediately after fabrication and after 25, 50, 160 minutes storage at room temperature. (c) Viscosity vales of oil/silk emulsion measured during first 5 hours after fabrication.

### 3.4. Silk HIPes

During the process of O/S emulsion fabrication, oil droplets are added to the silk solution. As stated earlier in this chapter, when the ratio between the oil and silk phase is increased above

74 % (3:1 oil to silk solution) a HIPE structure can be formed<sup>282,511</sup>. When external pressure is applied on the droplets (e.g. during silk gelation) droplet deformation can occur, transforming them to polygonal shape<sup>282</sup>, increasing their thermodynamic stability of the system leading to the formation of a HIPE structure. The stability of the HIPE is also increased since the silk protein can also act as surfactants, preventing droplet collision<sup>511</sup>. In this work, stable HIPES were defined as emulsions with HIPE structures that did not separate after 1 week of gelation. After the gelation process had finished, the semi-solid HIPES were immersed in ethyl acetate to remove the oil and expose the voids. Ethyl acetate immersion can also increase the crystallinity level of the silk<sup>540,541</sup>, further contributing to sample stability. During the final drying process (solvent evaporation), it is thought complete silk solidification occurs. The solidification process results in a contraction of the silk which allows for the formation of interconnected windows between the voids. A scheme of the poly-HIPE fabrication process is presented in Figure 67, left.

To analyse the level of silk conversion/crystallinity during the process, FTIR spectra were collected from a semi-solid HIPE after gelation and from the solid poly-HIPE scaffold. The HIPE had an unconverted structure similar to that of an amorphous silk<sup>22,77</sup>, while the solid poly-HIPE was fully converted indicating a high degree of  $\beta$ -sheet structures<sup>45</sup> (Figure 67, right). It is also important to note that the oil peak ( $1740\text{ cm}^{-1}$ ) was present in all samples, indicating that the washing process was not sufficient to completely remove all oil residues.

This might be a result of a partly closed porosity of the scaffold and can be solved by generating scaffolds with higher interconnectivity together with an increase in the duration of the oil removal stage.

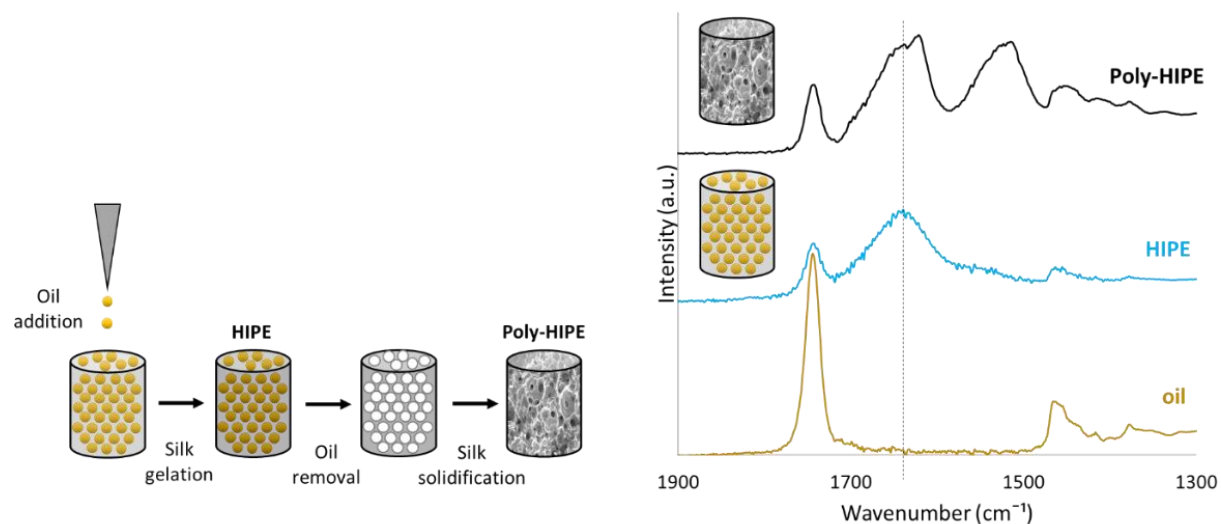


Figure 67: Schematics of Poly-HIPE fabrication. The oil is added drop-by-drop, the sample stabilises by natural gelation process, the oil is removed, and the sample is solidified during solvent evaporation.

### 3.5. The effect of vibration speed on the stability of O/S emulsions

To evaluate the optimal method for the preparation of stable HIPEs, it is important to understand the effect of the vibration speed of the sample on emulsion stability and droplet distribution (Figure 68a).

To test emulsion stability, the silk solution was placed of a vibrational rotational stage (see section 2.3) and the stage was set to different vibration rates (slow, medium and high). The oil was added drop-by-drop to the silk solution during the vibration.

A fast vibration rate (2200 rpm), resulted in immediate silk gelation and failure to form an emulsion as a result of the high shear applied. The fast solidification of the silk matrix prevented the uniform distribution of the oil droplets and as a result, did not generate any usable samples. A slow vibration rate (600 rpm) was not sufficient to stabilise the emulsion and a full separation between the oil and the silk phases was recorded. One reason might be the larger droplet size generated with slower vibration rates. The fast rate of large droplet



collision might overcome the slower rate of droplet migration in the silk matrix preventing emulsion formation. Since applying high-speed vibration resulted in immediate gelation of the silk, one of the experimental approaches included low-speed vibration during oil addition (when the silk phase is dominant), and high-speed vibration (when the oil is fully added and dominates the emulsion). After oil addition at low vibration rates, an increase of sample vibration speed, up to the maximum of 2200 rpm, or alternatively high-speed stirring, did not contribute to emulsion stability and the oil and silk phases remained separated. In fact, this process was analogous to the fast stirring method which also failed to form a stable emulsion (section 3.2.2.2). Applying a medium vibration rate (1200 rpm) during oil addition resulted in a stable emulsion without noticeable gelation of the silk. Therefore, this vibration rate was selected as the optimal rate for the fabrication of silk HIPEs.

After the emulsion was fabricated, it was stirred by a magnetic stirrer for 10 minutes to improve emulsion stability. An increase in the viscosity of the emulsion was measured for both slow and medium rate samples (Figure 68b). No sample gelation was recorded following the stirring. This indicated that after a stable emulsion is formed, it is possible to manipulate its viscosity without damaging the silk. The viscosity threshold for stabilisation of O/S emulsion was defined as 1 Pa·s, which was the viscosity of the medium vibrated sample.

- All samples with viscosity < 1 Pa·s showed full phase separation.
- All samples with viscosity > 1 Pa·s remained stable over 1 week of gelation and some had HIPE structure.

One important observation from this set of experiments is related to silk solution gelation. When the oil phase is added on top of the solution the shear acting on the silk during high-speed vibration process caused rapid silk gelation. As a result, the protein aggregates and

forms silk gel which is fully separated from the oil phase. However, when the oil phase is evenly distributed in the silk (medium speed vibration) a stable emulsion is formed, and the emulsion remains stable even after vigorous stirring, without noticeable phase separation. Yet, following the stirring process, the viscosity of the emulsion is increased, influencing the final properties of the scaffolds.

The scaffolds fabricated at medium vibration rate with and without post stirring were investigated by dynamic shear analysis<sup>450,451</sup> to evaluate their mechanical stiffness. The average elastic modulus of the vibration-only scaffolds was  $18 \pm 11.2$  kPa, while after stirring the modulus slightly increased to  $20 \pm 7.2$  kPa (Figure 68c). These results support the finding that stirring after emulsion fabrication can improve the mechanical stability of the scaffolds.

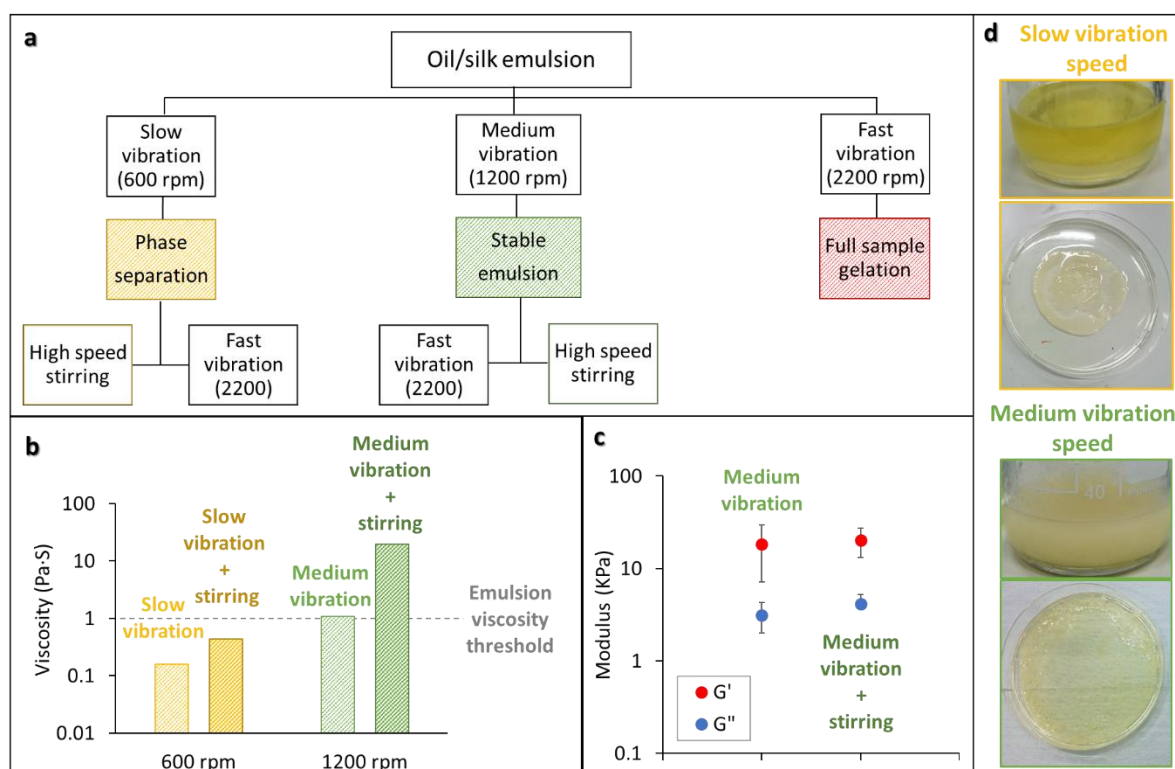


Figure 68: (a) The optimisation routes of silk solution vibrational speed during the oil addition process. (b) viscosity values of the samples fabricated by slow vibration and medium vibration with and without post stirring. (c) The elastic ( $G'$ ) and storage ( $G''$ ) moduli of the scaffolds fabricated at medium vibration speed, with and without post stirring, as evaluated by dynamic shear analysis measurements. (d) A photo of the emulsions directly after fabrication (top) and after 1 week of gelation in a petri-dish (bottom).

Alongside the process of HIPE fabrication, interesting structures were observed in the samples that were fabricated by the slow vibration method. At first, full separation of silk and oil phases was recorded. This is probably a result of hydrophobic repulsion between the oil phase and the aqueous silk solution. When high-speed vibration or stirring was applied on the separated mixture, the silk layer aggregated to form a continuous protein network on the bottom of the container. The network that was formed following high-speed stirring presented elongated lace-like structure (Figure 69, left). The structure that was formed following high-speed vibration, presented a network of spherical particles (Figure 69, right).

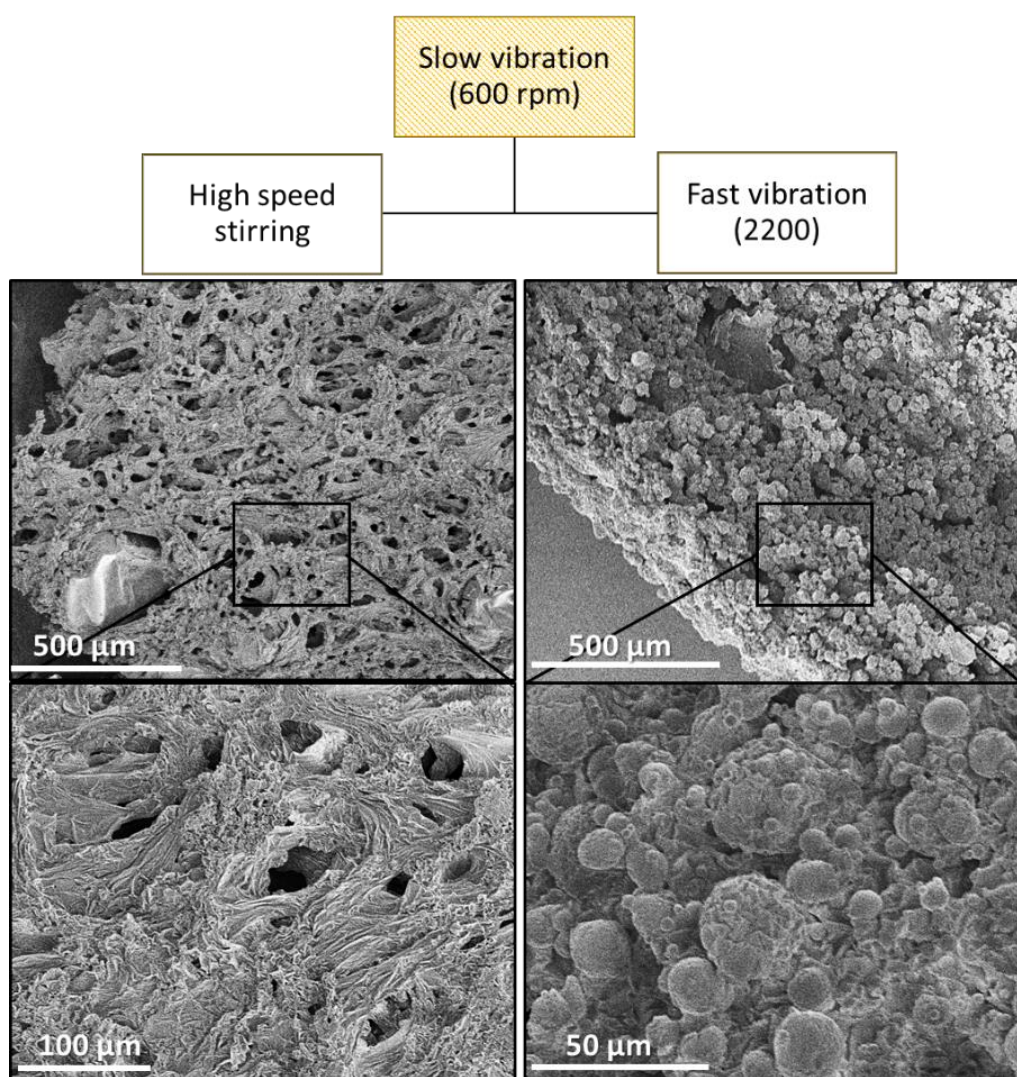


Figure 69: SEM images of the structure of the silk fibroin network received by slow vibration of the solution during the oil addition process followed by high-speed stirring (left) or fast vibration (right).

This can be explained by different flow regimes between the two mixing mechanisms which will be investigated in section 3.8. In short, when the sample is mixed by external vibration, the shear is evenly distributed through the centre of the sample with an elevated shear level at the borders. As a result, the flow is uniform with minimal deformation and spherical silk particles are formed. However, when the sample is stirred by a magnetic stirrer, high shear rates develop at the interface between the stirrer bar and the solution, resulting in turbulent flow which causes particle deformation and elongation.

### 3.6. The effect of viscosity on the thickness of the voids' walls

As established in section 3.5, one key parameter that can affect HIPE stability and structure is the viscosity of the O/S emulsion<sup>282,511</sup>. It was hypothesised that the viscosity of the emulsion can influence HIPE structure by several routes. At first, the rate in which the oil droplets are distributing in the matrix during the vibration is dependent on matrix viscosity. Higher matrix viscosity will reduce droplet migration rates, leading to non-uniform droplet distribution. High matrix viscosity can also contribute to the external pressure acting on the droplet, increasing the probability of droplet deformation and breakage. Therefore, higher matrix viscosity can potentially reduce the final pore size of the scaffold. In addition, matrix viscosity also defines the value of the external pressure acting on the droplets during the contraction (solidification) process. A high viscosity matrix will generate higher external pressure, increasing the probability of rupture in a void's walls (or windows formation). This will affect the interconnectivity level of the scaffold.

To test this hypothesis and to evaluate the effect of matrix viscosity on scaffold porosity, several HIPEs were fabricated, their viscosity measured, and porosity visually evaluated. A distribution in HIPE viscosities was achieved by slight variation of the vibrational speed around

the value of 1200 rpm and as a result of a natural variation in viscosities of the silk solution <sup>55</sup>.

The viscosity of the emulsions was measured directly after fabrication and the dry solid scaffolds were evaluated by SEM.

A direct correlation was found between the viscosity of the emulsion and the thickness of void walls in the scaffold (Figure 70). When the emulsion viscosity was below 3.2 Pa·s, partial interconnectivity was observed. However, all the samples with higher viscosity values (3.8 Pa·s, 5.1 Pa·s, 10.7 Pa·s) had fully closed pores and did not form a poly-HIPE structure. Pore size distribution was similar for all samples with a slight reduction in pore diameter in the most liquid samples. This is probably a result of higher level of sample shrinkage (during the solidification process) in comparison to the minimal contraction of samples with close porosity. The threshold for emulsion viscosity immediately after fabrication ( $\eta_e$ ) which is required to allow successful poly-HIPE fabrication was found to be:

$$1 \text{ Pa}\cdot\text{s} < \eta_e < 3.2 \text{ Pa}\cdot\text{s}$$

In this viscosity range, the sample is viscous enough to allow emulsion formation but liquid enough to allow the formation of interconnected pores.

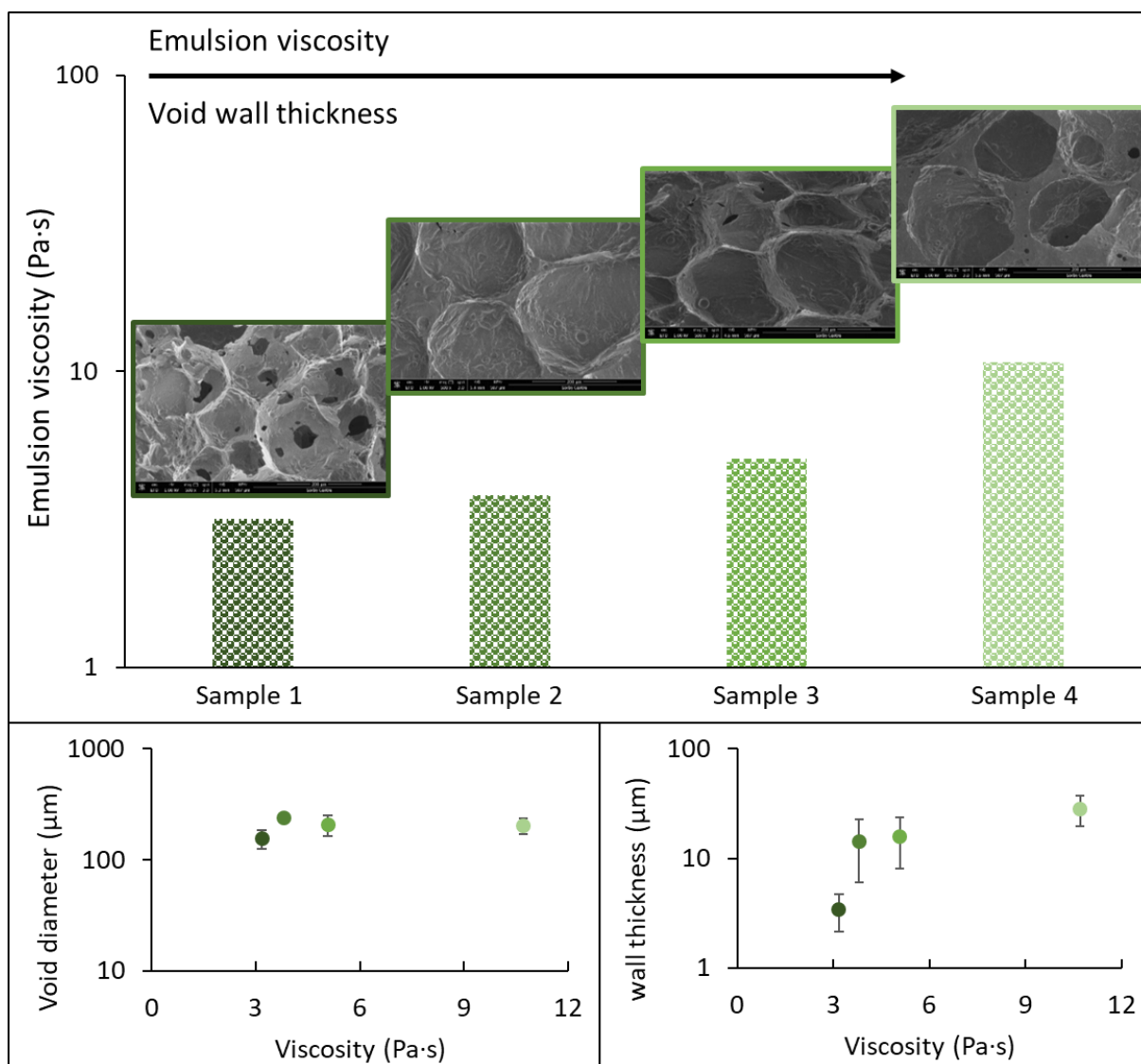


Figure 70: Scaffold porosity as a function of emulsion viscosity. The thickness of the void's wall is increased with the increase in emulsion viscosity, leading to close porosity structure (left). Void diameter (right, top) and void wall thickness (right, bottom) as a function of the emulsion viscosity.

### 3.6.1. Sample viscosity values as a function of container fixation

During the vibration, the solution container was fixed to the vibrational stage to avoid sample spillage and to allow uniform shaking. It was noticed during the experimental work that the fixation method influenced the probability of successful HIPE formation. At first, the bottle was fixed at the top using several rubber bands and the bottom of the bottle could freely

move on the vibrational stage in rotational motion (Figure 71a). Due to inconsistency in the results, an additional fixation method was introduced where the bottle was fixed in the centre, using custom-made holder, and could move across the vibrational platform in translation motion (Figure 71b).

When the bottle moved by rotational motion during the vibration, centrifugal shear forces were acting on the silk. The shear was high at the top of the container (due to restricted motion) and lower at the bottom (due to free motion) and a flow velocity gradient developed in the solution. This results in uneven shear distribution in the sample and non-uniform emulsion viscosity<sup>535</sup>. In contrast, using a central fixation mode, all the emulsion was moving simultaneously at the same speed, resulting in a more uniform mixing.

An additional parameter contributing to variations in sample viscosity is a disparity in droplet sizes between the two fixation modes. This is a result of an experimental set-up in which the oil is added to the solution from a needle which is fixed at the top of the bottle. In top bottle fixation mode, the restriction on the motion of the top part of the bottle will result in more frequent collisions (knocking) of the needle with the walls of the bottle. As a result of the collision, droplets can separate from the needle leading to smaller droplet sizes in the emulsion. In central fixation mode, due to uniform movement of the bottle, the needle collision is minimal which results in larger droplets falling directly into the silk solution. Rheological measurements indicated, as expected, a more uniform viscosity distribution across samples that were prepared via the central fixational mode while large viscosity variations were recorded in those prepared via the top fixation mode. However, the average viscosity values in the central fixation mode were significantly lower ( $0.94 \pm 0.15$  Pa·s) when



compared to top fixation ( $5.6 \pm 2.9$  Pa·s) (Figure 71c). In fact, the viscosity of the emulsions fabricated with central fixation was just sufficient enough for HIPE formation ( $\sim 1$  Pa·s).

Those results show that central fixation mode is preferable when desiring to achieve better control over sample viscosity. However, in this specific experimental set-up, top fixation mode was preferable in order to achieve the minimal viscosity requirements for the fabrication of a stable HIPE. This minimal viscosity is required to maintain the emulsion structure and to prevent phase separation. When the viscosity of the matrix is too low, the surface tension around the droplets is not sufficient to maintain the round droplet shape of the oil, resulting in a continuous layer of oil on top of the silk solution. It would be beneficial, in the future, to explore alternative fixation routes which will allow fabricating samples with lower viscosity variations in the desired viscosity range.

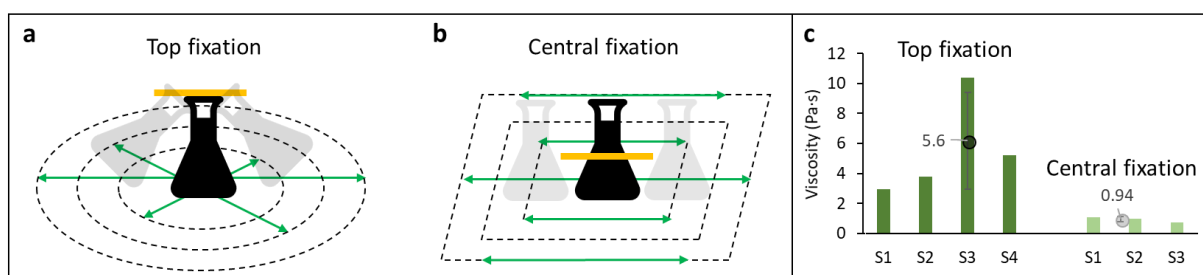


Figure 71: A schematic illustration of the (a) top and (b) central fixation modes and sample bottle movement range during the vibration. (c) The variation in O/S emulsion viscosity and the average viscosity measured for each fixation method.

### 3.7. The fabrication of silk Poly-HIPes

After the first batch of silk poly-HIPes were fabricated, and the oil phase was removed, a significant contraction of the scaffold was recorded after solidification (Figure 72a). A substantial difference between the top layer of the scaffold and its internal area was observed. While the top layer consisted of a white solid foam with open porosity and a poly-HIPE structure (Figure 72b), the internal layer did not fully solidify during the gelation stage



resulting in a weak unstable structure which collapsed during the drying process (Figure 72c). FTIR spectra indicated higher  $\beta$ -sheet content in the top layer in compared to the internal area (Figure 72d). This structural instability limits the maximum dimensions of the poly-HIPE scaffolds, restraining scaffold shape to flat disks, with a thickness of few millimetres.

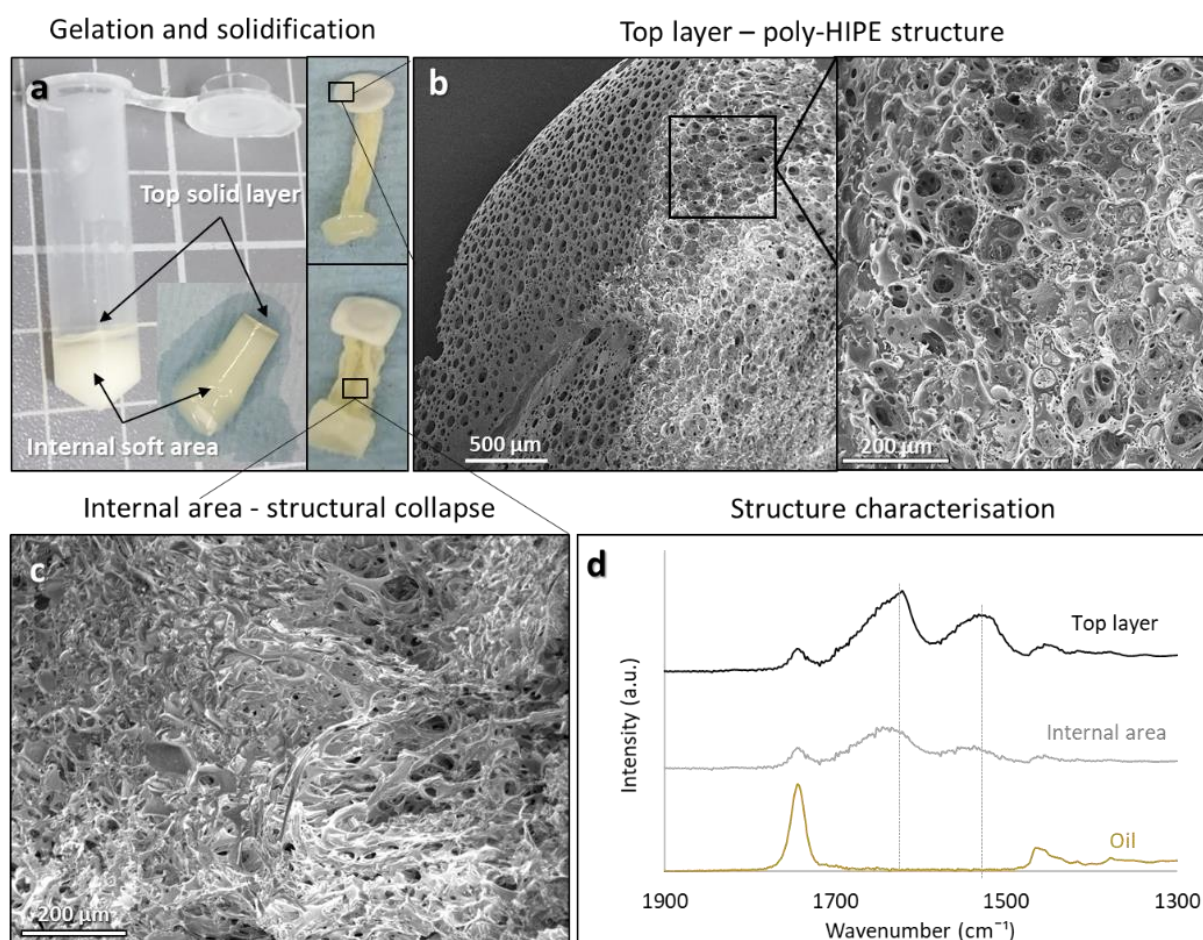


Figure 72: Silk scaffolds fabricated by drop-by-drop oil injection methods and solidified by natural gelation. (a) Silk HIPE after 1 week of gelation with rigid top layer and soft internal structure before (left) and after (right) the air-drying process. (b) SEM image of the top layer showing a highly-interconnected Poly-HIPE structure. (c) SEM image of the internal area showing structural collapse. (d) FTIR spectra of the oil (brown), dry internal phase (grey) and dry top layer (black) indicating higher  $\beta$ -sheet content in the top layer as can be seen from the position of the amide 1 peak.

During the whole gelation period, the HIPE was kept in an open microcentrifuge tube, at room temperature, exposed to air. Therefore, air could play a significant role in the solidification of the top layer. When the process was repeated but the microcentrifuge tube was closed, no

top solid layer was observed after 6 days of gelation, and the whole structure remained uniform and soft. When the gelation was performed in a flat petri-dish, a solid disk was produced after 48 hours, with open porosity at the top layer (which was exposed to air) and close structure at the bottom layer (not exposed to air) with trapped oil remaining (Figure 73a). The contribution of air to the gelation and solidification of the HIPEs can be attributed to a few possible mechanisms:

1. Oxygen-induced silk crystallisation – The interaction of silk with oxygen in the air can induce silk crystallisation and therefore improve the stability of the oxygen-exposed surfaces <sup>441,447,542</sup>.
2. Sample drying – The water evaporation rate from the surface is higher than that from the internal phases which result in higher silk concentration on the top layers and therefore enhanced structural stability.
3. Skin formation – When water evaporates from the silk solution, it leads to an increase in the local concentration on the top layer, which will promote skin formation and significantly inhibit water evaporation rate trapping residual solvents in the lower layers of the structure <sup>116</sup>.

Following FTIR results, which confirm higher crystallinity of the top layer (Figure 72d) when compared to the internal layer and the visual difference in porosity between the air-exposed top layer and non-exposed bottom layer in the flat sample, it can be suggested that the process of solidification is a combination of all the mechanisms described above.

The process of skin formation can be described by Peclet number ( $Pe$ ) which defines the balance between hydrodynamic forces and Brownian motion during evaporation <sup>543</sup>. This parameter is used to describe the relative strength of evaporative drying, leading to an

increased surface concentration of the polymer solution and polymer diffusion in the solution. This reaction tends to equilibrate on the border layer, spatially.

The  $Pe$  number is given by the ratio between the thickness of the layer ( $H$ ), the evaporation rate ( $E$ ) and the diffusion coefficient in the polymeric solution ( $D$ ) as follow:

$$(1) \quad Pe = \frac{HE}{D}$$

When  $Pe \gg 1$ , the evaporation rate is too fast (or the layer is too thick) to allow inter-diffusion in the polymer. Therefore, a concentration gradient is expected leading to non-uniform drying rates. Here the concentration on the top layer is higher, resulting in a more rigid structure and closed porosity (skin layer). When  $Pe \ll 1$ , the evaporation rate (and diffusion) in the polymer is uniform, resulting in similar crystallinity levels across the sample, leading to no skin layer and open porosity at the top of the scaffold (Figure 73b).

The use of freeze drying as the solidification process can significantly reduce the evaporation rate, reducing the value of  $Pe$  number<sup>544,545</sup>. (The calculation of  $Pe$  values for silk drying by air and by freeze drying processes are provided in Appendix B). To explore this theory, scaffolds were solidified by freeze drying as described in section 2.4.3. As expected, a uniform open porosity was observed in the scaffold without noticeable skin formation (Figure 73c).

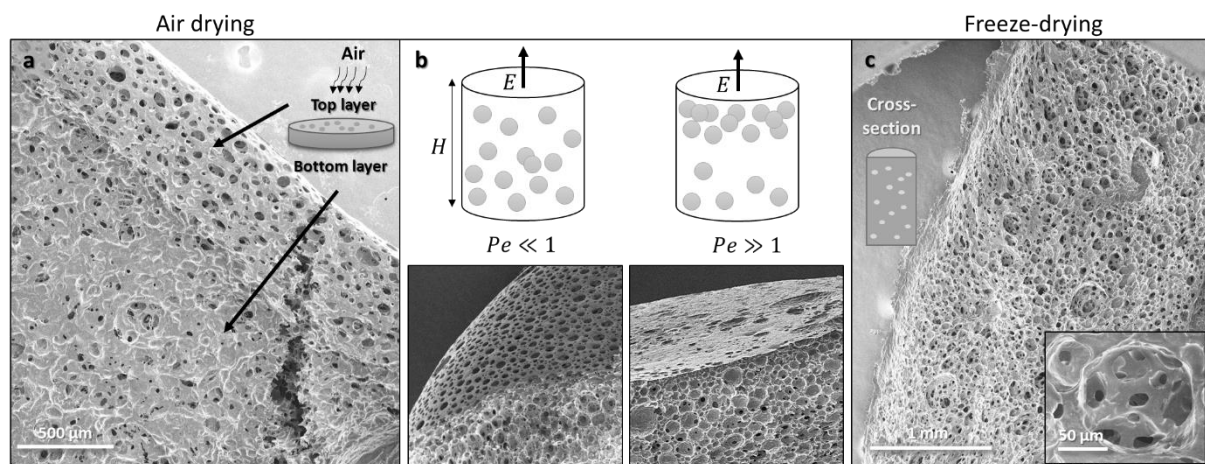


Figure 73: (a) SEM image of silk scaffolds fabricated by air-drying in a petri-dish. The top layer (air exposed) show open porosity while the bottom layer (non-exposed) had close porosity. (b) Top layer porosity as generated from a sample with a low Peclet number (left, open porosity) and high Peclet number (right, skin layer). (c) Cross-section of a silk scaffold fabricated by freeze drying. Fully open porosity on the top layer and the internal structure is observed.

These results indicate that by controlling the drying rate, it is possible to control the surface porosity of the scaffolds. Open surface porosity can allow better penetration into the scaffold for filtration or tissue engineering applications<sup>546,547</sup>, while a closed surface is beneficial for insulation (from humidity)<sup>548,549</sup> and allows the storage of liquids and gases in the internal space for control release with scaffold degradation<sup>142,182,478</sup>.

### 3.8. The effect of stirring on the stability of silk HIPes and Poly-HIPes

One possible method to improve emulsion stability, in order to avoid structural collapse during the drying process, is to apply high shear (by stirring) on the HIPes to initiate gelation of the silk<sup>550</sup>.

In the current experimental approach, the samples were stirred on a vibrational platform, by using a magnetic stirrer or by both methods combined. A computational fluid dynamics study, performed by Bai *et al.*<sup>535</sup>, analysed the fluid stresses in the bulk liquid (water) and near the air-liquid and solid-liquid interfaces. The study found that when a sample is mixed by an

orbital vibrational shaker, high shear rates are localised on the container wall and in a small area in the centre of the air–liquid surface. In the case of mixing by a magnetic stirrer, higher shear rate values are located near to the container walls and at about the same height as the position of the magnetic stirring bar, but over a smaller area compared to the orbital shaker. At the air-liquid interface, a magnetic stirrer was shown to generate relatively high shearing near the stirring bar. Those surfaces, which are most commonly Teflon<sup>®</sup> (i.e. PTFE) coated, are hydrophobic and can contribute significantly to protein aggregation<sup>551</sup>.

A schematic diagram of shear distribution in the sample reproduced after Bai *et al.*<sup>535</sup>, and the emulsions produced by each method can be seen in Figure 74.

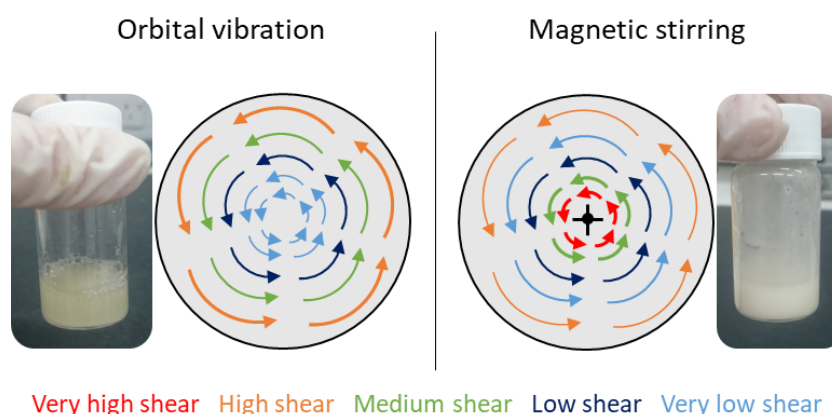


Figure 74: Schematics of the shear distribution in an orbital shaker (high shear rate values are located near the container wall) and a magnetic stirrer (very high shear near the stir bar interface). The emulsions fabricated by each method are shown next to each diagram.

Thus, the introduction of the high shear to the centre of the sample, by stirring the emulsion after fabrication, could contribute to the stability of the HIPEs by two main mechanisms:

1. Shear-induced droplet break-up which will result in smaller droplet size<sup>550,552</sup>.
2. Shear-induced silk gelation which will contribute to sample stability and shorten the gelation period post-fabrication<sup>69</sup>.

To examine the effect of stirring, HIPEs were fabricated using a vibrational orbital shaker, as described before, and then exposed to high speed stirring for 10 minutes using a magnetic stirrer. Following stirring, a stable white foam was produced. The viscosity of the stirred sample was significantly higher (3.5 Pa·s) than the viscosity of the emulsion produced by vibration alone (0.5 Pa·s) (Figure 75a). This viscosity was sufficient enough to allow extrusion through a syringe needle and the fabrication of stable 2.5D structures and stand-alone fibres (Figure 75b). In fact, this shows that the sample can potentially be suitable for 3D fabrication techniques such as inkjet printing. However, a few challenges need to be overcome to allow 3D printing of silk poly-HIPEs, including the fact that the viscosity of the emulsion is not stable and increases linearly during the printing process. This will require *in situ* adaptation of the printing parameters and the development of fast solidification methods for stabilising each printed layer individually.

In addition to the increased viscosity, the stirred sample appeared whiter and had more uniform droplet size distribution. After 1 week of gelation, the stirred HIPE was more solid and did not break when it was separated from the mould. While the HIPE which was fabricated by vibration alone was not fully solid and broke during the separation from the mould. A skin layer on the top surface was observed in both samples.

An interesting observation relates to the density of the samples. While the stirred sample floated in ethyl acetate and water solutions, the vibration-alone sample sank. This might indicate a closed porosity structure in the vibrational sample, which traps air in the scaffold and does not allow solvent/water penetration, reducing the total density of the sample. While the stirred sample most likely has an open porosity, allowing for full penetration of the solvent and higher density of the wet scaffold. Furthermore, the stirred sample maintained its

original shape after oil removal, with minimal contraction, while the vibration-only sample collapsed during oil removal. The comparison between the samples at various fabrication stages can be seen in Figure 75c.

To evaluate the level of sample contraction, vibration only and vibration and stirring emulsions were cast into a petri-dish (32 mm diameter) to fabricate flat disks with 0.5 mm thickness. Petri-dishes were used to maximize the surface area exposed to air to improve solidification. The samples were left for 48 hours to reach full gelation. After 48 hours, the samples were removed from the petri-dish and placed on a paper towel to absorb excess oil. The area of the disks was measured using ImageJ software and was defined as the initial area (as fabricated). The area was measured again after of 1 h of oil absorbance. Since the diameter of the disk is significantly larger than its thickness ( $32 \gg 0.5$  mm), sample contraction was evaluated in 2D and contraction in Z direction was neglected due to low contribution to the total volume of the sample. The vibration-only sample contracted to 77% of its original area. This is probably due to oil leakage from the open porosity in the sample. This is also supported by the large oil stain which formed around the sample. The stirred sample remained the same and no shrinkage was recorded. This is probably due to its closed porosity structure which stops oil leakage and provides higher mechanical stability, preventing contraction. To dissolve the oil that remained in the scaffold, both samples were immersed in ethyl acetate for 24 h, and placed on a tissue paper to allow solvent evaporation and sample drying. The vibration-only sample underwent additional contraction and the final surface area was 66% of its the initial size. No significant contraction was recorded in the vibration + stirring sample (Figure 75d). FTIR analysis of the vibration and stirred sample indicated a fully converted structure in both the top and the internal layers of the poly-HIPE (Figure 75e). While the vibration only sample was fully converted only at the top layer with no structural conversion in the internal



phase (Figure 72d). This is expected following the large surface area that is exposed to oxygen and the high shear levels acting on the sample during the stirring process, both result in silk crystallisation <sup>69</sup>.

These results support the assumption that stirring can improve structural stability, preventing sample contraction and collapsing. However, the internal porosity should be investigated to evaluate the effect of stirring on the process of poly-HIPE structure formation.

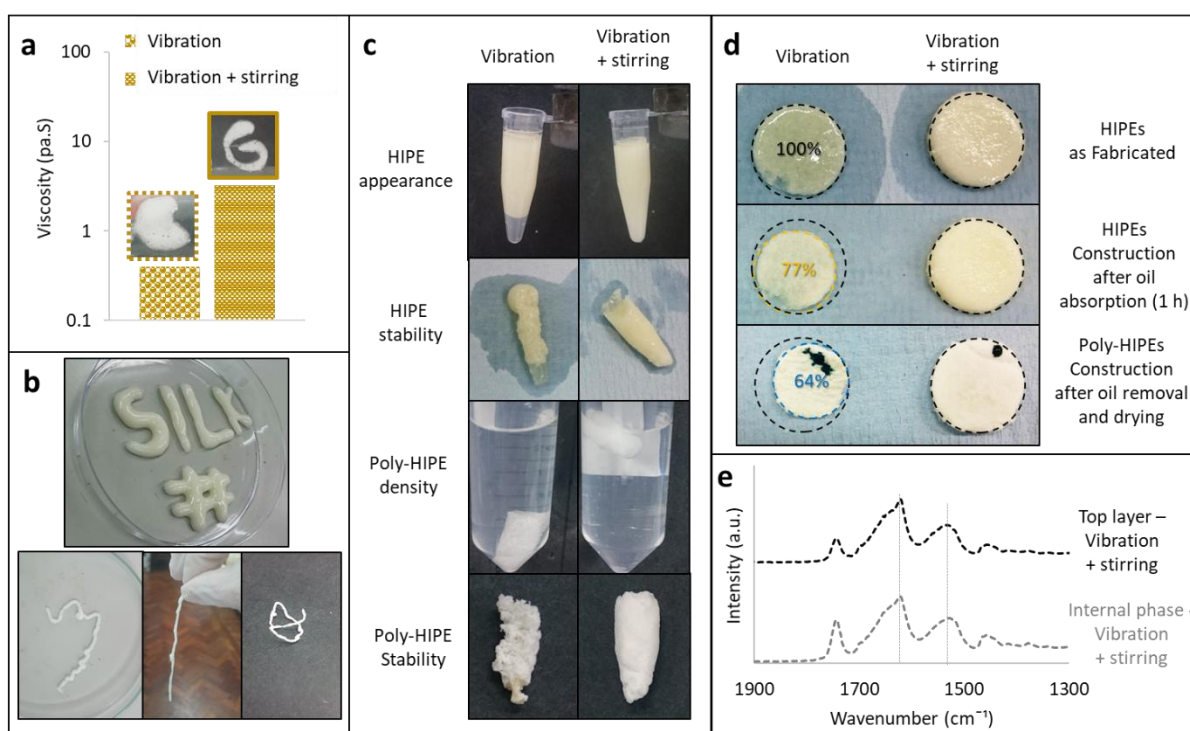


Figure 75: (a) Viscosity values of oil-in-silk emulsion fabricated by vibration-only and by vibration + stirring methods. Images above the graph present the letter “G” as written by extrusion from a 27G syringe. (b) 2.5D writing and poly-HIPE fibres fabricated by HIPE extrusion from a 27G syringe needle. (c) Comparison between vibration only and vibration + stirring samples. (d) Samples construction during post-processing. (e) FTIR spectra of the mixed sample indicating full conversion of the structure.

The porosity of the vibration + stirring sample was evaluated by SEM. The top layer of the scaffold consisted of closed-porosity film layer while the internal layer presented interconnected poly-HIPE structure (Figure 76). This skin formation is a result of an increase



in the evaporation rate from the surface during the mixing and reduction in the diffusion rate in the sample, most likely due to increased emulsion viscosity.

The closed porosity of the surface, acting as a protective frame around the fragile poly-HIPE structure, providing enhanced stability and protection from collapse. In addition, the smaller droplet size and more uniform droplet distribution, following fast stirring of the sample, when compared to a sample that was fabricated by vibration alone, could also contribute to scaffold stability minimizing sample contraction.

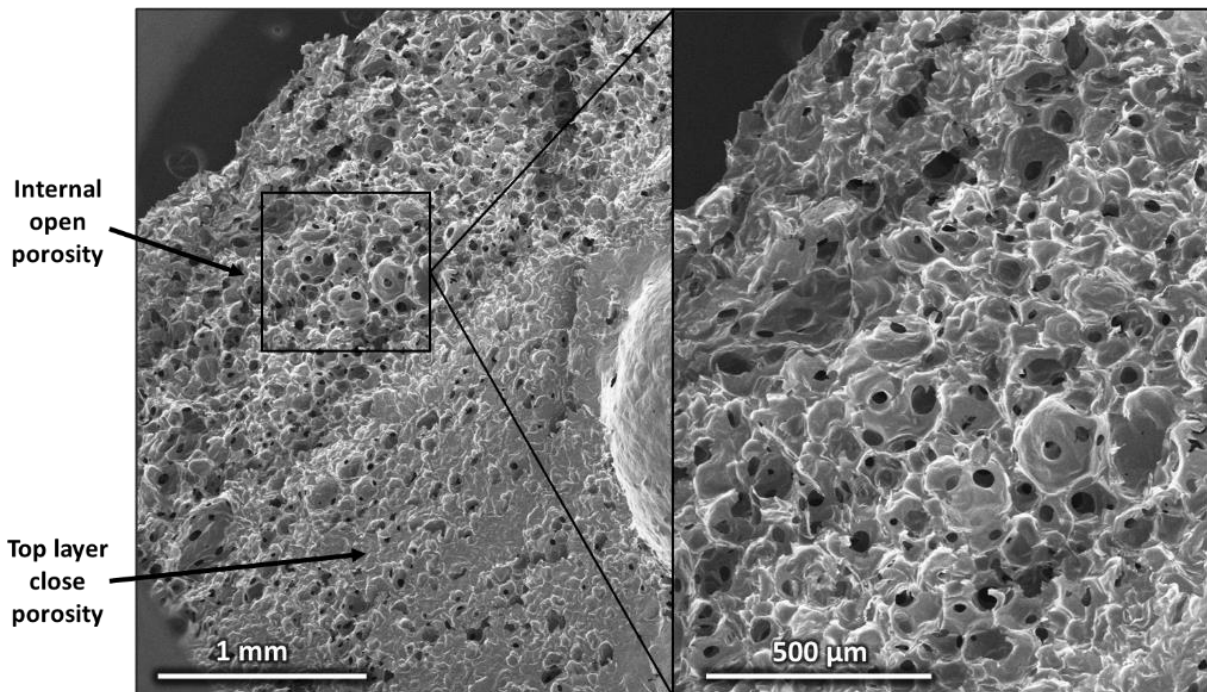


*Figure 76: Silk poly-HIPE fabricated by drop-by-drop injection method followed by high-speed stirring. External skin layer is formed. The internal area presented uniform interconnected poly-HIPE.*

### 3.9. Optimisation of the HIPE solidification procedure

When designing the ideal scaffold, especially for tissue engineering, it is important to avoid skin layer formation (to allow open porosity) and to prevent the collapse of the structure (to maintain the desired geometry) <sup>135</sup>. To achieve this goal, several solidification mechanisms

were investigated including air drying (solidification by natural gelation), freeze drying (solidification of the HIPE structure after fabrication) and water-based freeze drying (solidification of the poly-HIPE structure after oil removal).

As seen in section 3.7, air drying alone is not a suitable technique for large scaffolds fabrication due to scaffold collapse. The addition of high-speed stirring to the process improved structural stability but encouraged the formation of a surface skin layer limiting the application range. In addition, stirring resulted in smaller pore size which again limits the application range. As also seen in section 3.7, Freeze drying can prevent skin formation and allow to maintain the internal porosity of the sample.

Scaffolds that were fabricated by air drying were compared to scaffolds that were fabricated by two freeze drying methods: direct freeze drying and water-based freeze drying.

In the direct method, freeze drying of the HIPEs was performed directly after fabrication to avoid the time-consuming process of gelation (1 week). The HIPEs were transferred to a petri-dish after emulsification and the petri-dish placed in a freeze drying system for 48 hours according to the method described in section 2.4.2.

The samples prepared by water-based freeze drying were first allowed to fully gel for 1 week after emulsification. Then, the oil phase was removed, and the sample was immersed in water to allow water penetration into the empty voids prior to the freeze drying, according to the method described in section 2.4.3. The surface tension of the water and the mechanical stability of the ice forming during the freezing was expected to prevent structural collapse by supporting the voids during the drying of the matrix.

All samples were compared after full solidification by SEM analysis. As expected, the air-dried sample had open surface porosity with partial structural collapse. A deformation in the shape of the voids (elongated and not spherical voids) can also be a result of this partial collapsing (Figure 77, left). The Freeze-dried sample had a top skin layer (non-continuous) with internal poly-HIPE structure (Figure 77, middle). However, the additional stability offered during solidification by the water-based freeze drying solidification method resulted in the best scaffold geometry, with open surface porosity and internal and uniform interconnected poly-HIPE structure (Figure 77, left). Therefore, the water-based freeze drying method was selected as the optimal solidification method in silk poly-HIPEs fabrication. However, one main limitation of this solidification method relates to the time-scale of the process. To allow full water penetration into to voids, the samples were immersed in water for an additional 24 h, after oil removal. This extended the fabrication time to 11 full days in compared to 8 days for air drying and 4 days for direct freeze drying.

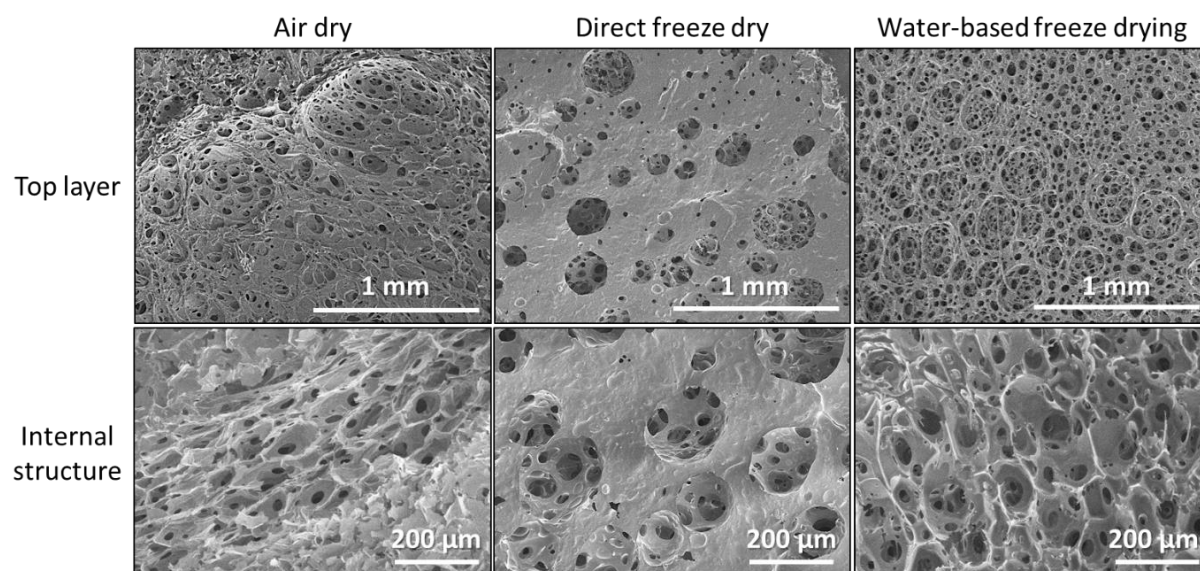


Figure 77: SEM images of the top layer (top) and internal structure (bottom) of silk scaffolds fabricated by air drying (left), direct freeze drying (centre) and water-based freeze drying (right) methods.

### 3.10. The effect of silk concentration

Protein concentration plays a key role in the stability of HIPEs and poly-HIPE structures<sup>512</sup>. It is known that a minimum ratio of 0.74 oil to water is required to achieve stable HIPE<sup>511</sup>. However, this ratio is valid when two-phase emulsions are generated. In the current experimental setup, the matrix phase is in fact, a dilute protein solution (2.5 to 6 wt%). During the solidification process, water is evaporated from the matrix and the scaffold is formed solely from the remaining network of silk proteins. Therefore, it is important to evaluate the true protein content in the emulsion in addition to the ratio between the phases.

All the fabricated emulsions had an oil to silk solution ratio of 3:1. However, the protein content in the silk solution was adjusted to achieve protein to emulsion ratios of 1:200, 1:100 and 1:80. For each sample, fabricated from those ratios, the images of the gelled emulsion after 1 week of gelation and the final solid scaffolds were recorded for to samples fabricated by vibration alone and vibration + stirring methods (Figure 78).

All the samples fabricated by vibration alone presented significant contraction regardless of protein concentration. As expected, a reduced contraction was recorded for all samples that were stirred after fabrication. However, the intermediate 1:100 sample resulted in the most uniform scaffold suggesting this range to be the most suitable ratio for poly-HIPE fabrication. This is probably because at this protein content, the silk network is stable enough to support the scaffold structure, but the emulsion is liquid enough to prevent premature silk gelation.

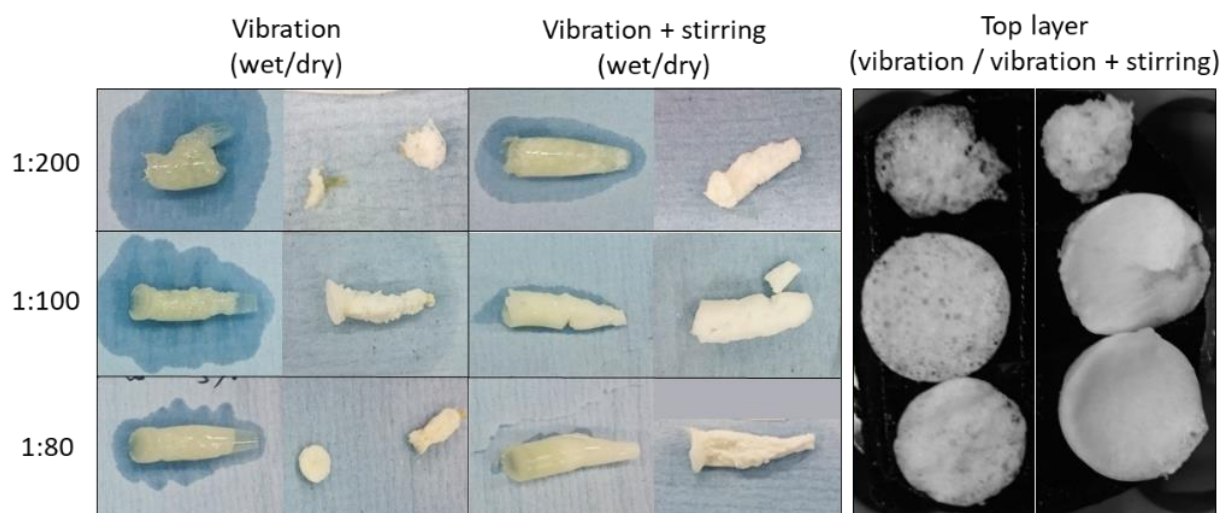


Figure 78: A photo of oil-in-silk emulsions after 1 week of gelation and the solid scaffolds fabricated from silk solution with various protein content. This is including protein to emulsion ratios of 1:200 (top), 1:100 (middle) and 1:80 (bottom). The left image presents the top layer of the same samples.

All scaffolds that were fabricated with protein content below 1:200 (1:250, 1:300) failed to generate poly-HIPE structures and resulted in closed porosity samples. It was challenging to increase the ratio of the protein above 1:70 due to a few limitations:

- A minimum of 1:3 ratio between the oil and silk solution phases is required to stabilise the HIPE.
- Concentrated silk solutions (>10 wt%) can have a high viscosity (> 1 Pa·s)<sup>553</sup> which will result in immediate silk gelation when vibrational shear is applied.

Both limitations define the maximal theoretical silk protein content as 1:40. In addition, the current fabrication process for reconstituted silk solution is time-consuming (1 week) and results in a low yield of 45% (0.45 gr reconstituted protein out of 1 gr of cocoon). Therefore, it is important to optimise the silk concentration to increase productivity.

An investigation of the fabricated scaffolds revealed that poly-HIPEs can be fabricated at ratios between 1:70 and 1:165 (Figure 79). However, 1:100 ratio resulted in the highest



porosity level (> 90 %) and full interconnectivity. Therefore, 1:100 was chosen as the optimal protein content for the fabrication of silk poly-HIPes.

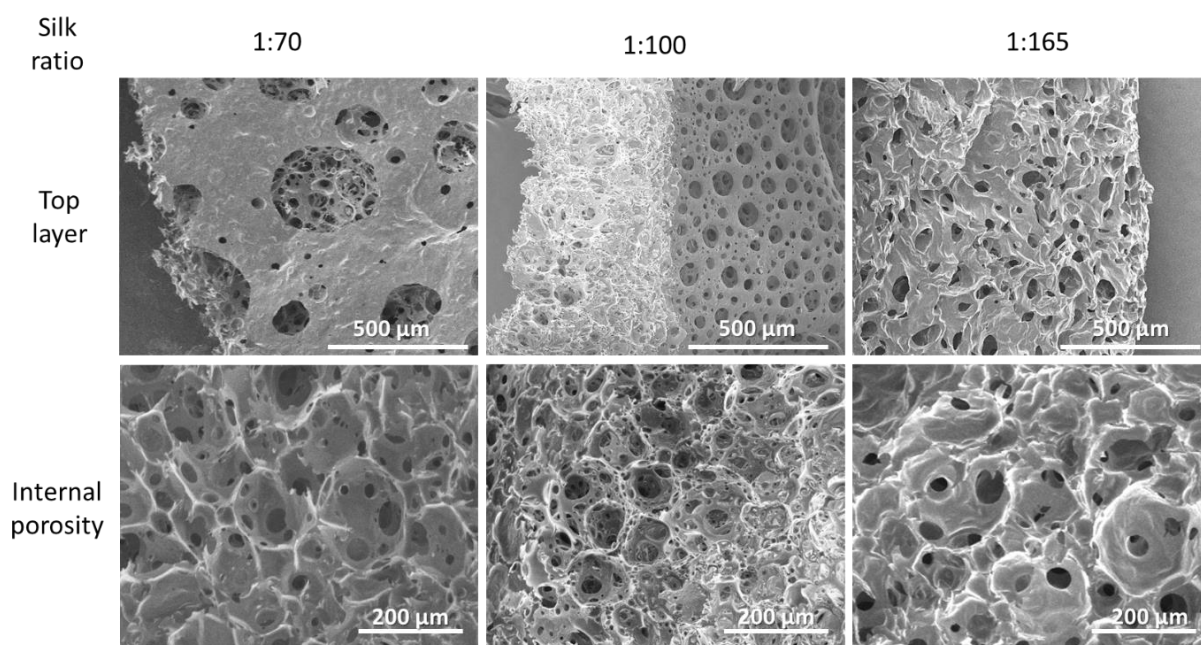


Figure 79: Silk poly-HIPes fabricated at different silk protein content including 1:70 (left), 1:100 (middle) and 1:165 (right). The ratio is defined as the protein content out of the total emulsion volume. The top row shows the structure of the top layer while the bottom later shows the internal structure.

### 3.11. The effect of silk degumming method on the poly-HIPE structure

As broadly discussed in chapter 4 of this thesis, silk quality (or molecular weight) can affect silk mechanical properties<sup>456</sup> and can influence the stability of the silk scaffolds<sup>24</sup>. Even though native silk is considered to be the gold standard, having a higher molecular weight when compared to reconstituted silk<sup>103</sup>, in the current set-up, it was not possible to use native silk for emulsion fabrication (section 3.1).

Reconstituted silk can act as an alternative candidate to native silk, however, there is no standardised scale for the evaluation of the quality of reconstituted silk and its properties might vary with its production method<sup>85,91,554</sup>.

The most common reconstitution method currently used is based on chemical degumming of silk cocoons<sup>22,86</sup>. To evaluate the effect of the degumming process of the reconstituted silk on the stability of poly-HIPE scaffold, three reconstitution procedures were tested: chemical degumming (with Na<sub>2</sub>CO<sub>3</sub>), mechanical degumming (with water instead of Na<sub>2</sub>CO<sub>3</sub>), and direct dissolution of the cocoon (no degumming). The mechanical degumming and the no degumming methods intend to increase the molecular weight of the protein, potentially leading to better emulsion stability with the aim to reduce the level of scaffold contraction.

As can be seen from Figure 80, all silk degumming methods were suitable for the fabrication of the poly-HIPEs structure. As expected, the internal structure of the chemically degummed sample collapsed during the air-drying process while the top layer remained stable. Similar sample contraction was observed in the mechanically degummed sample. However, the non-degummed solution produced a uniform scaffold with minimal contraction even during simple air-drying solidification. The pore size of the chemically degummed sample was smaller than the mechanically degummed and the non-degummed sample. This is a result of the lower molecular weight of the chemically degummed sample, which reduces sample viscosity and allows for the formation of smaller droplets.

To evaluate the mechanical stiffness of the scaffolds, 10 small round disks (1 cm in diameter, 0.5 cm high) were fabricated from each silk solution and tested under compression. The scaffolds were compressed to 2%, 20% and 40% of their original height and the stiffness were recorded at this compression levels. Surprisingly, the mechanically degummed scaffold presented the highest stiffness at 40% compression ( $1 \pm 0.06$  kPa) when compared to the non-degummed ( $0.77 \pm 0.38$  kPa) and the chemically degummed ( $0.78 \pm 0.11$  kPa) samples (Figure 80). However, the non-degummed sampled had a larger standard deviation ( $0.77 \pm 0.38$  kPa),

with some values that were comparable to the mechanically degummed sample. It might be possible to improve the average stiffness of the non-degummed sample by gaining better control over the fabrication process.

The fabrication of scaffolds from non-degummed silk is significantly simpler, faster and greener (no  $\text{Na}_2\text{CO}_3$  is required) process and given the fact that the mechanical properties of some of the scaffolds were comparable to that of scaffolds fabricated from chemically degummed silk, this process should be widely explored. After some process optimisation, non-degummed silk solutions should be considered as a suitable source for silk poly-HIPes fabrication.

However, when designing silk poly-HIPes for tissue engineering applications, the presence of sericin in the silk, which is usually removed by degumming, can influence the biocompatibility of the fabricated scaffolds<sup>555</sup> as discussed in chapter 4. For those applications, it is preferable to use chemically or mechanically degummed silk and water-based freeze drying process.



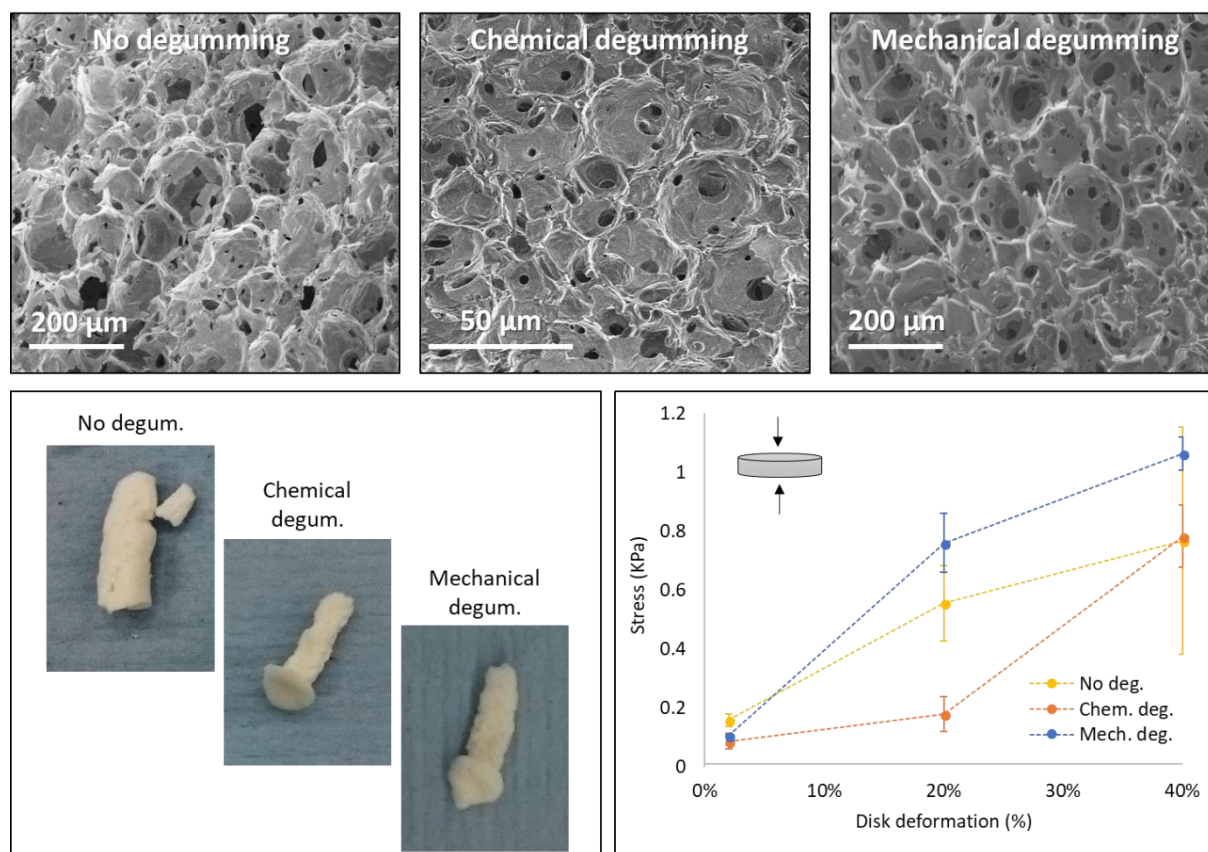


Figure 80: Top: SEM images of silk poly-HIPes fabricated from non-degummed (left), chemically degummed (centre) and mechanically degummed (right) silk solutions. Bottom left: The dry scaffolds used for the SEM analysis. Bottom right: Stress values for solid scaffolds fabricated from non-degummed (yellow), chemically degummed (orange) and mechanically degummed (blue) silk solution measured under compression of 2%, 20% and 40% from its original height. Error bar represents at least 3 samples of each type.

### 3.12. The effect of silk pH on the structure of poly-HIPes

Silk proteins are sensitive to variations in pH and undergo gelation when the pH is reduced below the value of 6<sup>63,330,556</sup>. Since the viscosity of the emulsion should be controlled for successful poly-HIPE fabrication, it is important to evaluate the effect of the pH on the viscosity of the emulsion and as a result the final structure of the scaffold. During the stage of silk dissolution, when reconstituted silk is fabricated, the cocoons are dissolved in LiBr solution (strong alkali)<sup>138</sup>. Following the dissolution stage, the silk solution is filtered against de-ionised water to remove LiBr remains<sup>22</sup>. The duration of the filtration stage will define the concentration of the LiBr and will influence the pH of the solution. However, it should be

noted that in the process of filtration, low molecular weight proteins are also removed, increasing the average molecular weight of the silk solution. Thus higher molecular weights should lead to higher solution viscosities<sup>557</sup>, obstructing HIPE formation.

To test this effect, two filtration times were compared, and the pH of the solution was recorded. At first, the solution was filtered for 24 hours, as described in chapter 2. Half of the solution was collected for further analysis. The pH was measured to be 9.5 indicating some LiBr remained. The remaining solution was filtered for an additional 24 h, and the pH was reduced to 8. FTIR analysis of silk films, cast from those solutions, did not reveal any recordable difference in the crystallinity level of the silk (Figure 81).

Both solutions were used in the same experimental procedure to fabricate HIPEs and Poly-HIPEs. The mechanical properties and the structures were evaluated by rheological and compression measurements and are summarised in Table 10.

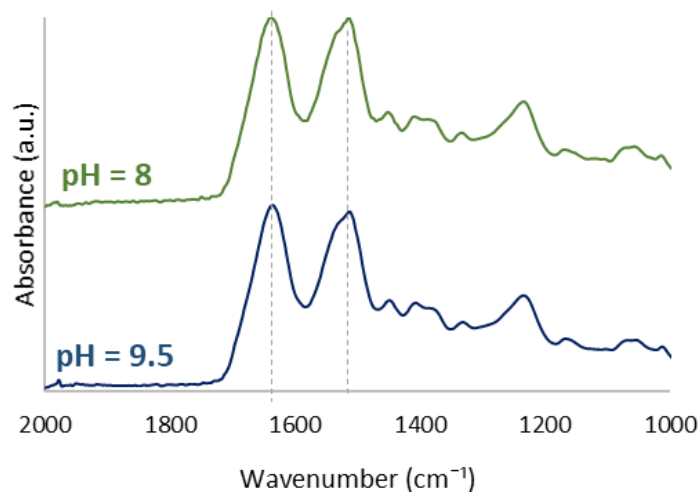


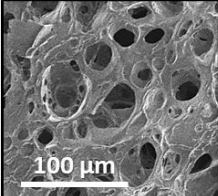
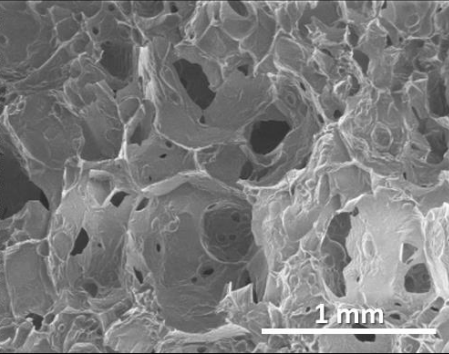
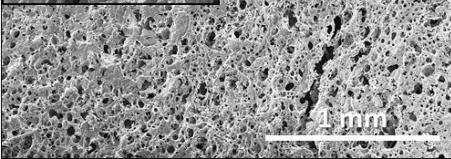
Figure 81: FTIR spectra of silk films cast from reconstituted silk solution collected after 24h (pH=9.5) and 48h (pH=8) of filtration.

The scaffold that was fabricated from the alkaline solution (pH=9.5), had a significantly smaller pore size ( $74 \pm 9 \mu\text{m}$ ) when compared to the more neutral solution (pH=8) ( $764 \pm 68 \mu\text{m}$ ).

This is probably a result of a lower solution viscosity, which allowed more drop breakdown and faster migration of the droplets in the matrix when same vibrational speed is used. As expected, smaller pore size contributed to the stiffness of the scaffold, leading to higher stress values ( $0.62 \pm 0.25$  kPa) in comparing to the pH 8 sample ( $0.12 \pm 0.04$  kPa), when the scaffold was compressed to 20% of its original height.

Dynamic shear analysis <sup>450</sup>, performed on wet scaffolds (which were immersed in water for 10 minutes prior to the measurements), revealed higher elastic modulus for the pH 9.5 sample. These results suggest that it is beneficial to limit the filtration time to 24 h to avoid full removal of the LiBr ions. Since the process of scaffold fabrication involves additional stages such as ethyl acetate wash and water immersions, it is safe to assume that the ion residues in the final scaffold were kept to a minimum.

*Table 10: The comparison of pore diameter and mechanical properties of silk poly-HIPE scaffolds fabricated from the same silk solution after different filtration times.*

pH = 9.5	pH = 8
Filtration time: 24 h	Filtration time: 48 h
Pore diameter : $74 \pm 9 \mu\text{m}$	Pore diameter : $764 \pm 68 \mu\text{m}$
Stress (20% compression): $0.62 \pm 0.25$ kPa	Stress (20% compression): $0.12 \pm 0.04$ kPa
Elastic modulus (from DSA): $28 \pm 3.1$ kPa	Elastic modulus (from DSA): $6.8 \pm 5.3$ kPa
	
	

### 3.13. Photo-curing of HIPEs

Following the discussion in chapter 4, it was shown that when silk is mixed with riboflavin, it will undergo gelation under UV and visible light. Therefore, photocuring was tested as a potential approach to increase the rate of the gelation (which usually takes 1 week) during the poly-HIPE fabrication process.

Silk solution mixed with riboflavin prior to the addition of the oil phase and an emulsion was fabricated according to the standard method described in section 2.3. The emulsion was placed under a UV lamp for 30 min to achieve gelation by the initiation of chemical crosslinking between the tyrosine side groups of the fibroin<sup>122</sup>. As expected, the photo-exposed samples gelled while the unexposed emulsions remained liquid. In addition, a slight discolouration was noticed in the photo-exposed samples probably due to the reaction of the riboflavin and light resulting in partial photobleaching of the riboflavin<sup>422</sup> (Figure 82).

FTIR spectra collected from the emulsions indicated improved emulsion stability 1h after fabrication in the photo-exposed sample. This can be seen from the fact that the FTIR spectrum was similar to that of a freshly fabricated emulsion. However, the un-exposed sample did not show a typical FTIR spectrum for silk, having strong peaks from the oil phase, suggesting possible phase separation between the oil and the silk solution (Figure 82, right).

Both samples were left at room temperature for 1 week, to allow gelation. After this gelation period, no visible difference in the appearance of the unexposed and photo-exposed sample was recorded.

SEM analysis indicated a closed porosity structure for the photo-exposed sample, with very large pore sizes (~ 1 mm). This is probably a result of the rapid gelation process, occurring under the UV light, potentially leading to droplet collision. In addition, it can also be a result

of the heat from the UV light source which reduces sample viscosity increasing droplet migration rate raising the probability of droplet collision.

In a stable emulsion, droplet collision is prevented by several mechanisms (see section 1.1). Photo-exposure can interfere with those mechanisms, leading to droplet collision by several methods:

1. Reducing the viscosity of the water phase - Usually, the viscosity of the water phase prevents droplets from approaching the collision point. When placed under light, significant heating of the emulsion occurs, which can lead to a reduction in water viscosity and an increase in droplet motion rate. This will increase to the probability of close-contact between the droplets and lead to more frequent collision events.
2. Disturbance of the charged layer around the droplets – An additional collision barrier is the presence of a charged layer around the oil droplets which cause electrostatic repulsion between the droplets. It is probable that during the radical coupling reaction, which occurs in the presence of light, the charged layer is affected reducing the electrostatic repulsion between the droplets and increase the probability for droplet collision.
3. Interfacial tension balance interference - Droplet collision can also be prevented as a result of the interfacial tension between the oil and the water phases. Rapid crosslinking of the matrix phase can interrupt the balance between the internal droplet pressure and the external interfacial tension, affecting the probability for collision.

Due to the very large pore size of the photo-exposed samples with lack of interconnectivity, photo-curing was defined as an unsuitable technique for silk HIPes gelation.

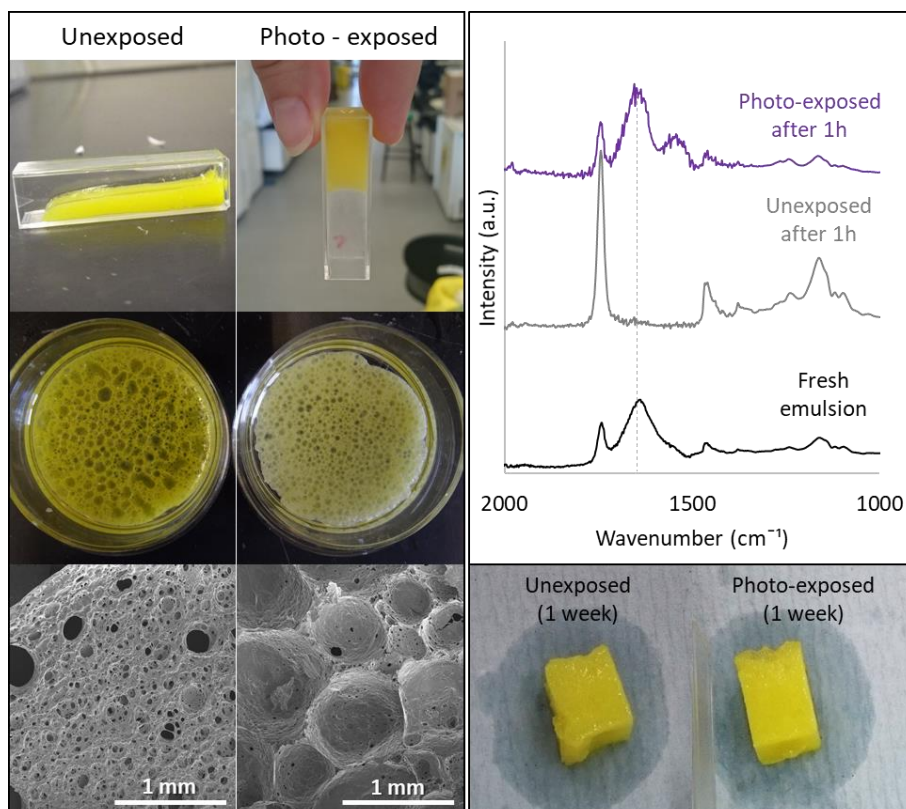


Figure 82: Comparison between photo-exposed and unexposed silk HIPES fabricated in the presence of riboflavin. Silk HIPE after fabrication (Top, middle right), (bottom right) SEM images of the solid scaffolds. (top, left) FTIR spectra of the fresh emulsions, and 1h after fabrication. (bottom, right) Gelled HIPES, 1 week after fabrication.

### 3.14. Porosity and interconnectivity of the fabricated silk scaffolds

Many parameters can affect the porosity of silk scaffolds<sup>135,547</sup>. It was shown in previous sections (3.5 to 3.12), that by controlling the experimental conditions during emulsion fabrication and solidification, the level of interconnectivity might vary from fully closed isolated pores (received from highly viscous emulsion) to fully open interconnected structures (fabricated from an emulsion with low viscosity and alkaline silk solution). In addition, the pore size of the scaffold can be modified by adjusting the fabrication method of the scaffold and by post-processing. In this work scaffolds were fabricated with various pore diameters ranging from very small pores, a few micrometres in size (by air foaming) ideal for gas



filtration or particle separation applications, to scaffolds with very large pore sizes ~1-millimetre (by photo-exposure), which could be suitable for insulation and for the storage of humidity-sensitive materials. By optimising of the process of poly-HIPE fabrication, it was also possible to achieve medium size pores in the range of 50-200  $\mu\text{m}$ , which are most suitable for tissue engineering applications and cell growth <sup>531</sup>.

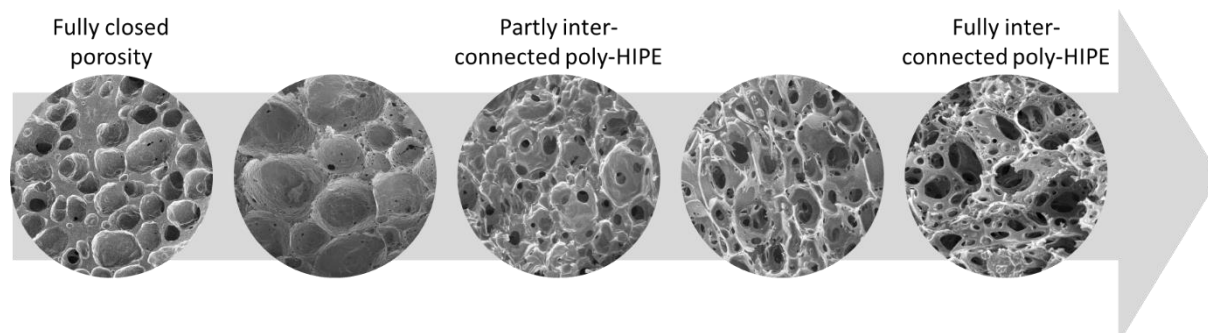


*Figure 83: Interconnectivity levels of silk scaffold as received in this work by process optimisation methods. The interconnectivity level varied from fully closed structure to a fully-interconnected network.*

### 3.15. Applications of porous scaffolds

Scaffolds with open and closed porosity are widely used for many applications <sup>135,283,284,546,558</sup>.

Open cell foams are usually softer due to the interconnectivity of the pores forming a continuous internal network. This network can be filled with additional material, to fit desired functionality, or to influence foam stability and mechanical properties. Closed cell foams are made of individual voids fully separated from each other. This structure usually contributes to the higher compressive strength of the foam (section 3.12). Such foams are denser and require more matrix material and are isolated from environmental effects such as moisture, solvents or gases.

### 3.15.1. Application of silk poly-HIPes with open porosity

In tissue engineering, open porosity is important to allow cell migration into the scaffold, to support the penetration of newly formed blood vessels and allow diffusion of nutrients to support cell growth<sup>477</sup>. If the scaffold is fabricated from a biodegradable material, like silk<sup>145</sup> and open pore structure will lead to a more uniform degradation of the structure<sup>120,145</sup> (Figure 84, left). The degradation rate can be further controlled by controlling the crystallinity level of the silk, enabling one to match it to the natural healing rate of the surrounding tissue<sup>145</sup>.

Moreover, open porosity scaffolds have extremely high surface areas, which provide a platform for surface modification to allow incorporation of drugs or growth factors, improving cellular migration and growth in the scaffold and supporting tissue regeneration process<sup>472,559</sup>.

In addition, the large surface area of these scaffolds makes them ideal candidates for filtration systems<sup>478</sup>. This is because they can capture ions/particles/pollutants without restricting the flow of solvents or gases through the scaffold<sup>49,560,561</sup>.

Alternatively, open porosity foams can be suitable as thermal insulators<sup>480,488</sup>. They are also suitable for application that requires isolating materials which are flexible and compressible such as refrigerator bags or thermal fabrics, due to their increased compressibility level when compared to closed porosity foams<sup>548</sup>.

### 3.15.2. Application of silk foams with closed porosity

One limitation of thermal insulators with open porosity is that they are not suitable for insulation in wet or humid environments<sup>562</sup>. Water can penetrate the voids, reducing the insulation properties of the foam<sup>487,549</sup> and promoting the growth of fungi and bacteria. Therefore, scaffolds with closed porosity are a more appropriate choice for insulation in



humid conditions, since they can trap the air (or alternative filler) in the structure, and to prevent the penetration of water vapour<sup>549</sup>. Those scaffolds can also be used as sealants or gaskets, creating isolated environment<sup>563,564</sup> when required, or to act as a barrier in wound dressings and skin grafts to minimise infection<sup>565</sup>.

In medicine, separated closed pores can be used as carriers of chemicals, nutrients and drugs<sup>566</sup>. The biodegradation of a closed-cell scaffold is usually a gradual process (from the outer shell to inner core (Figure 84, right)). These scaffolds could be ideal candidates when gradual treatment is required because it is possible to load each layer/pore individually, post-fabrication, and to allow step-by-step drug release during scaffold biodegradation. Variation in chemical compositions, materials and concentrations between the individual pores, can allow customisation of complex treatment procedures or similar applications requiring a gradual material release.

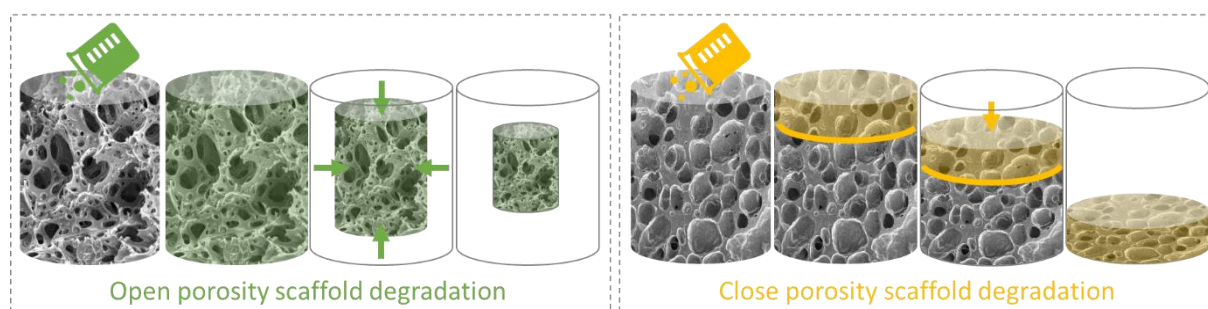


Figure 84: Schematic illustration of the degradation regime for open porosity (left) and close porosity (right) scaffolds.

### 3.15.3. Applications of typical silk foams

In some instances, the fabrication procedures described in this chapter failed to form a stable HIPE and a poly-HIPE structure. In those cases, standard silk foams were produced, similar to

those commonly found in the wider silk literature <sup>135,136,142,567</sup>. These foams are usually from a lamellar structure, with a large pore size (> 100  $\mu\text{m}$ ) and some interconnectivity <sup>280</sup>.

This foam structure can be used for acoustic applications such as sound shielding, or noise isolation <sup>492,568</sup>. When acoustic wave penetrates the foam, the acoustic energy is converted to heat. The movement of the sound wave results in vibrations of the pore walls and the air that is trapped inside the pores. Those vibrations result in sound energy wave damping, by converting it to heat energy <sup>568</sup>. During this process the pores are stretched, bent and buckled under the vibrational pressure, transforming the sound waves into kinetic energy. Larger pores will contain more trapped air and lead to larger damping effect acting as a better acoustic insulator than foams with smaller pores <sup>568</sup>.

Since the production process of typical foams is simpler and faster than that of foam with a poly-HIPE structure, typical foams can provide solutions when large area insulation is required. Standard foams can also absorb mechanical shock, due to their ability to bend and deform under mechanical pressure <sup>132</sup> because of their lamellar structure <sup>569</sup>.

It is also assumed that standard silk foams have lower production costs in comparison to poly-HIPEs, as a result of fewer production stages (direct freeze drying without gelation or oil removal), slightly faster process speed (48 hours instead of 1 week required for poly-HIPE fabrication) and the fact that no additional materials are required (such as oil or ethyl acetate). However, when discussing applications in tissue engineering, the limited control over structure porosity and low interconnectivity levels make these foam suitable candidates for only basic applications such as void filling, providing mechanical support and physical protection to wounded or missing tissues, or as a temporary solution during the tissue regeneration process <sup>135</sup>.

As a convenient summary for the reader, selected structures of the porous silk structures presented in this chapter and the list of possible applications for each structure are presented in Figure 85 below.

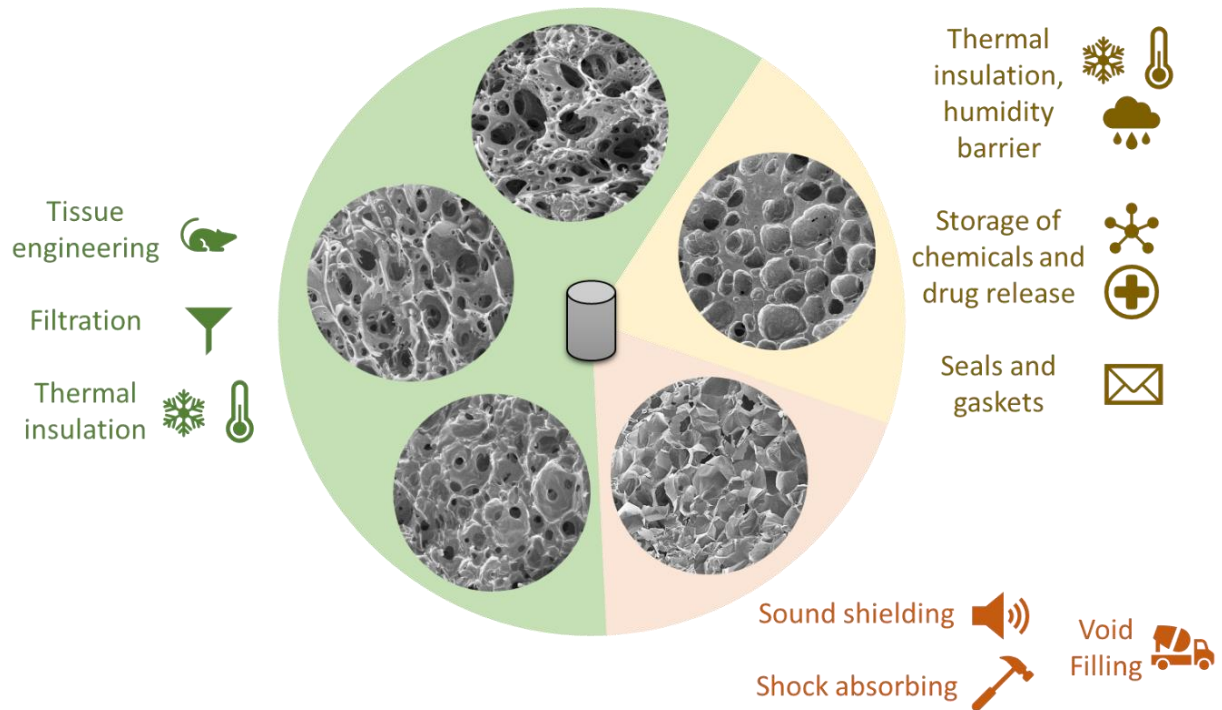


Figure 85: Selected structures of porous silk including open-porosity scaffolds (green), closed porosity scaffolds (yellow) and typical foams (orange) fabricated by emulsion templating and direct freeze drying methods and the list of possible applications for each foam.

## 4. Conclusions

Until now, there has been no prior literature describing the successful fabrication of 3D silk scaffolds with poly-HIPE structures. This chapter addresses this fundamental and technical gap in our knowledge and the optimal parameters for the fabrication of consistent silk poly-HIPEs scaffolds are summarised in Table 11 below:

*Table 11: The optimal experimental parameters for the fabrication of silk poly-HIPEs*

<b>Parameter</b>	<b>Optimal value</b>
Silk protein source	Whole cocoon (no degumming)
Silk solution pH	9.5
Silk protein concentration	1:100
Oil to Silk solution ratio	3:1
Oil induction method	Drop-by-drop injection
Emulsion stabilisation	Orbital vibrational shaker
Vibration speed	1200 rpm
Required emulsion viscosity	$1 < \mu < 3.5 \text{ Pa}\cdot\text{s}$
Emulsion gelation method	Native gelation – 1 week
Oil removal	Immersion in ethyl acetate – 24 h
Structure stabilisation	Immersion in water – 24 h
Emulsion solidification	Freeze drying

To develop the optimal fabrication process, different fabrication methods were explored. At first, preliminary experiments were performed to evaluate the most suitable fabrication approach. It was established that a second phase (oil) is required to generate controlled porosity and interconnectivity in the silk phase. This is because single-phase techniques such as freeze drying and foaming failed to provide the desired structures.

Secondly, several methods were tested with the aim to fabricate uniform and stable emulsions from oil and silk. It was found that drop-by-drop injection of the rapeseed oil (see section 2.1.3.1) into the silk solution allows the fabrication of stable emulsions with HIPE structure. This method was optimised, and the fabricated scaffolds were characterised.

To better understand why certain processing parameters were preferable to others the optimal fabrication process was evaluated by a close investigation of the quality of the silk solution, the stability of the oil-in-silk emulsion and the effect of experimental conditions such as sample vibration speed, mixing mechanism, gelation process and solidification method. Spectroscopic and rheological measurements alongside SEM analysis were used to evaluate the properties and the structures of the fabricated materials.

Several experimental parameters were evaluated as contributing factors affecting successful poly-HIPE fabrication. The viscosity of the oil-in-silk emulsion was found to have a major effect on the interconnectivity and porosity of the scaffold. Increased viscosity ( $> 3.2 \text{ Pa}\cdot\text{s}$ ), resulted in a complete closed cell structure, without interconnectivity. Low viscosity emulsions ( $< 1 \text{ Pa}\cdot\text{s}$ ), failed to form stable HIPEs and separated shortly after fabrication.

The shear applied on the sample, during emulsion fabrication, influenced the porosity of the surface layer and the pore size. When the sample was mixed, using magnetic stirrer, the surface skin was created on the scaffold limiting its permeability. However, the pore size was

reduced, and the scaffold had higher stability and did not contract during sample drying. The use of freeze drying after sample gelation was seen to reduce surface skin formation and improve the structural integrity of the scaffold preventing contraction, even in samples that were not mixed after vibration.

The silk solution pH was found to affect the pore size of the scaffold and as a result its mechanical properties. Higher pH values (9.5) resulted in smaller porosity and higher mechanical stiffness. Optimal concentration of the silk protein was defined as 1:100 protein to the emulsion, which allowed sufficient mechanical integrity to support poly-HIPE structure while maintaining the emulsion viscosity below the maximal threshold for emulsion formation.

Somewhat surprisingly in light of the previous findings for silk structuring in 1D and 2D (Chapters 3 and 4) the quality of the silk which is defined by the degumming process did not have a significant effect of the structure of the poly-HIPEs. All the tested silk solutions (chemically degummed, mechanically degummed and non-degummed) were suitable for the fabrication of silk poly-HIPEs. However, since non-degumming is the simplest and most environmentally friendly fabrication method, it was selected as the first choice for most silk poly-HIPEs. However, due to the presence of sericin in the non-degummed sample, the biocompatibility of these scaffolds should be explored in future research. Until it will be fully evaluated, it is preferable to use chemically or mechanically degummed silk source when fabricating scaffolds for medical applications.

It is important to note that the emulsion templating technique used in this chapter, is significantly different from the photo-fabrication approach that was used in chapter 3 and 4. Photo-curing allows to produce stable hydrogel structures by chemically crosslinking between

the side groups of the protein, but the silk remains unconverted (no  $\beta$ -sheet formation) with weak mechanical integrity, limiting this fabrication technique to the production of 1D and 2D structures. However, in emulsion templating route, structural conversion of the silk occurs following the physical shear which is applied on the silk during the emulsion fabrication process and following the chemical conversion occurring when the scaffolds are washed with ethyl acetate. This converted silk structure has higher mechanical stability and can support 3D constructions.

## Appendix A - An optimised protocol for the fabrication of silk poly-HIPes.

### 1. Fabrication of reconstituted silk solution:

- a. Dissolve 1 gr of dry *B. mori* cocoons in 10 ml 9.3M LiBr solution (2 h, 60°C).
- b. Place the solution in dialysis membrane and filter against 1 litre of DI water (24 h, 20°C). Water should be exchanged 5 times during the dialysis process.
- c. Filter the solution using standard filtration paper.
- d. Adjust solution concentration to 4 wt.%.  
If required, dilute the solution with DI water or re-concentrate in 30 wt% PEG.

### 2. Fabrication of silk HIPes:

- a. Place 8 ml of silk solution in a 200 ml glass bottle.
- b. Place the bottle on an orbital shaker stage and fix on the top. Set shaker speed to 1200 rpm.
- c. Fill the syringe with 24 ml rapeseed oil.
- d. Place the syringe on a syringe pump and adjust the speed to 60 ml/h. Connect the syringe to the bottle using 1mm pipe with a 21G needle at the end.
- e. Turn on a syringe pump and the shaker and leave until the full addition of the oil (about 30 min).
- f. Disconnect the syringe and leave the bottle on the shaker for a further 20 minutes.

### 3. Fabrication of silk poly-HIPes:

- a. Transfer the emulsion to the desired template.
- b. Leave at room temperature for 1 week to allow silk gelation.
- c. Remove gently from the template and transfer to 20 ml ethyl acetate for 24 h.
- d. Remove from ethyl acetate and transfer to 20 ml DI water for an additional 24 h.
- e. Place the sample in a freeze drier and freeze for 24h.
- f. Dry the sample under vacuum for 24 h.

### 4. Scaffold preparation for SEM analysis:

- a. Cut gently a cross-section of the scaffold with a sharp scaffold.
- b. Place the sample in ethyl acetate for 24 hours to remove excess oil and reveal the surface.
- c. Remove the sample and place on a paper tissue until dry.
- d. Place on the SEM sample holder and investigate at low keV.



## Appendix B

### 1. Estimations for the Peclet number in silk/oil emulsions

As described in section 3.7, the  $Pe$  number is given by the ratio between the layer thickness ( $H$ ), the evaporation rate ( $E$ ) and the diffusion coefficient for the polymeric solution ( $D$ ) as follow:

$$Pe = \frac{HE}{D}$$

Alternatively, it can be described as a function of air velocity above the solution ( $v$ ) the density ( $\rho$ ) and heat capacity ( $c_p$ ) of the solution, the characteristic length ( $D$ ) along which the evaporation process occurs, and thermal conductivity ( $k$ ) of the sample as follow <sup>570</sup>:

$$Pe = \frac{v\rho c_p D}{k}$$

#### 1.1. Air velocity

The evaporation rate of water from the sample into the atmosphere is a function of temperature, humidity, and air velocity. The evaporation is the diffusion of water molecules out of a water surface through the air layer covering the water surface. In this research, silk emulsions were transferred into microcentrifuge tubes with a diameter of 1 cm and a height of 3 cm. The tubes were stored in a closed drawer in the lab with a relative humidity of about 50%. The drawer protected the samples from external air flow (e.g. wind, large humidity gradients or human activity in the lab). Therefore, it can be assumed the air velocity is laminar and was maintained constant during the drying process.

The velocity can be calculated from the ratio between the quantity of flow ( $Q$ ) and the cross-section area of the vessel ( $A$ ) as follow:

$$v = \frac{Q}{A}$$

The total emulsion volume was 2ml (3:1 oil to silk ration). Water evaporation time was assumed to be 1 h. In fact, stable emulsions were received after 6 days of storage however it is hard to separate between the process of silk gelatine and the effect of water evaporation. Longer evaporation time will decrease the air speed even farther, reducing the values of Pe number. Therefore, the maximum evaporation rate was used.

The quantity of flow can be calculated as follow:

$$Q = \frac{V_{total}}{t_{evaporation}} = \frac{0.5 \text{ ml}}{1 \text{ h}} = 1.4 \cdot 10^{-10} \frac{m^3}{s}$$

The evaporation process occurs only on the surface area of the vessel:

$$A = \pi r^2 = \pi(0.005)^2 = 7.85 \cdot 10^{-5} \text{ m}^2$$

Therefore, the air velocity is:  $v = 1.8 \cdot 10^{-6} \frac{m}{s}$ .

## 1.2. Comparison between air-drying and freeze drying

The silk solutions used for emulsion fabrication were at ~4 wt% concentration. For the simplicity of the calculation and for comparison to a frozen state, silk solution was considered as water. The corrected values for the silk solution are presented, indicating that no significant difference is expected in the evaporation regime due to the presence of the silk.

No evaporation of oil or silk protein was assumed.

The Pe number was calculated and compared between the two samples:

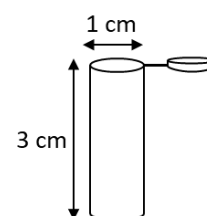
1. Pure water evaporation at room temperature (air drying on the lab bench)
2. Ice evaporation (freeze drying).

The parameters used for the calculations and the values of Pe number are given in the table below:

Parameters	Water (25°C)	Ice (0°C)	Silk solution
Velocity (v) [m/s]	$1.8 \cdot 10^{-6}$	$1.8 \cdot 10^{-6}$	$1.8 \cdot 10^{-6}$
Density ( $\rho$ ) [kg/m <sup>3</sup> ]	1000	917	1015.9
Heat capacity ( $C_p$ ) [J/kg·K]	4185.5	2090	4073.3
Characteristic length (D) [m]	0.03	0.03	0.03
Thermal conductivity (k) [W/m·K]	0.591	2.22	0.578
<b>Peclet Number (Pe)</b>	<b>0.38</b>	<b>0.05</b>	<b>0.39</b>

The parameters of the silk fibroin are as follow <sup>491,571</sup>:

Parameters	Silk fibroin
Density ( $\rho$ ) kg/m <sup>3</sup>	1398
Heat Capacity ( $C_p$ ) J/kg·K	1380
Thermal Conductivity (k) W/m·K	0.256



It should be noted that for both drying processes the value of  $Pe < 1$ . However, to allow uniform drying and avoid skin formation, Pe should be significantly lower than one.

This can be achieved in a freeze-drying process when the solution undergoes sublimation from solid state (ice) directly to water vapours (gas). Therefore, the process of freeze drying is preferable if one desires to maintain the structure of the emulsion and to allow open porosity on the surface avoiding skin formation.



# Chapter 6

---

## Conclusions & Author's Remarks



## Thesis summary

This PhD project was set out with the main question: "Can we spin silk with light?"

My main desire was to introduce a new approach for silk spinning (protein gelation) which can be used alongside well-established techniques such as flow-induced spinning, solvent induced gelation and thermal changes (heating and cooling), which are currently used. This is with the idea in mind that photo-curing provides a non-contact, well-controlled technique for silk-based fabrication, expanding the application range and leading to a new era for this well-explored natural material.

At the beginning of my journey in silk research, the field a photo-curable silks were just beginning, utilising chemically modified silk proteins and UV light sources for the curing of bulk silk structures.

Few initial questions were guiding me during the initial stages of the project:

- Is it possible to produce a photo-curable resin from a native silk dope?
- Is it possible to cure silk by laser light without damaging its structure?
- What is the molecular mechanism behind the photo-curing process?

During the attempt to answer those questions a few key principles were always kept in my mind. The first, keeping the process as simple as possible, avoiding complex and time-consuming chemical modifications and maintaining the main benefits of the silk: its biocompatible and mechanical integrity. The second, to keep the cost of the process to a minimum to introduce a low-cost alternative for current silk photo-gelation research which involves high-end commercial equipment with very limited access to the broad silk community. Finally, since the silk material is the focus of this work, it was important to keep it as the main ingredient in any process. This allows exploring its full structuring potential

avoiding silk-based composites, which are broadly used in the literature to improve structural stability<sup>19,22,23,172,572</sup>. The scientific attention of this work was mainly on silk structuring mechanisms while the final structure integrity and applications were secondary to this cause.

It is important to note that all published silk-based photofabrication, up to this day, utilise processed proteins (reconstituted silk) as the raw material. As discussed in this thesis this protein is significantly different in its properties, having much lower molecular weight and larger distribution in chain sizes when compared to the native silk. Hence the main novelty of this thesis can be attributed to the exploration of the unprocessed native material and its potential for utilisation in industrial applications.

The results chapters of this thesis (chapter 3-5) present the experimental techniques and the key findings of each experimental approach. However, as it always seen in experimental research, this does not fully reflect the whole process of exploration leading to those specific silk processing techniques. This section will discuss the intellectual journey of the author and summarise the challenges along the way. The methods and result discussed in this thesis are summarised in Table 12.

## 1. Intellectual journey and challenges

The research journey described in this thesis can be divided into 3 major milestones which are classified by the dimensionality of the structure that was achieved by each route.

### 1.1. The initial approach to silk photo-gelation, 1D writing

The first step in photo-curing was the development of a photocurable silk which can be cured with the available laser systems in our lab. The first challenge appeared when all the standard photoinitiators, that are typically used for polymer photo-curing,<sup>343,485</sup> damaged the native



silk and resulted in immediate gelation. Therefore, a range of dyes that are typically used with natural materials, mostly in medical applications, were explored, leading to the selection of Rose Bengal dye for direct laser writing (DLW) and Riboflavin for projection micro stereolithography (P $\mu$ SL) fabrication. Both of these dyes have been previously used for native materials photocuring, especially for corneal collagen crosslinking <sup>225,345</sup>, and supporting evidence for their suitability for silk photo-fabrication was published during the period of this research <sup>122,249</sup>.

Once the photocuring solution was developed, the Rose Bengal / silk was tested using a lab-built direct write laser system which allows pixel-by-pixel polymerisation and fabrication of linear structures, classified as 1D writing. An investigation into the photo-crosslinking mechanism revealed that the dye is actively cross-linked to the silk, creating silk-dye complexes which cannot be removed afterwards by rinsing. That fact that the Rose Bengal dye was chemically bound to the silk might have been one of the reasons that raised an issue of cytotoxicity which was not resolved even after additional exposure to the laser which was performed try and photo-quench the dye in order to remove it. The issue of cytotoxicity was resolved by methanol treatment improving cell attachment to the treated silk. This was probably a combined effect of structural conversion in the silk which can improve cell attachments and the fact that Rose Bengal dye molecules are restricted in the converted structure and their interaction with the cells is minimal. However, cell alignment on the photo-cured structure was not observed.

A further realisation during this study was that even though the silk proteins are chemically bound in the photo-cured sample, no structural conversion in the silk was recorded (as was shown by FTIR in chapters 3 and 4). Those results were enlightening and were investigated

extensively as an approach to control the mechanical properties of the structural post-fabrication. However, this finding was not in agreement with the original hypothesis, suggesting that whilst silk can be spun by light, structures are created via a different mechanism of gelation. In fact, by using photo-gelation, silk can be structured and aligned by light, maintaining its amorphous, hydrogel-like nature. This can later then be converted post-fabrication to crystalline silk by methanol treatment, decoupling these two processes and offering increased versatility to those wishing to work with this material.

One of the benefits of the DLW approach is the ability to generate 2-photon polymerisation (2PP) which significantly reduce the voxel size and improves resolution <sup>218</sup>. Since the crosslinking mechanism of this polymerisation is similar to that of single-photon polymerisation, and the resolution of the structure was not a key factor in this section of the thesis, 2PP was not explored. However, the current silk literature exploits the process of 2PP to generate sub-micron reconstituted silk structures achieving complex 3D shapes <sup>271</sup>. Therefore, I believe that the potential of 2PP structuring should be explored in the future for native silk proteins which might allow outperform the current achievements in this area.

One major methodological problem was related to the self-built nature of the DLW system. This system is composed of a laser source and optical elements which are aligned on an optical table. When used frequently, by multiple users, it is very common to see misalignments in the laser path that can affect the position of the focal point, the optimal experimental conditions and structural resolution. This has led to a certain inconsistency in the quality of the patterns, preventing accurate standardisation of the experimental parameters. To avoid this problem, each set of experiments were conducted under the same alignment conditions, on the same day and using the same batch of silk. The optimal DLW parameters that are presented in

chapter 3, were chosen as the experimental conditions that led to the best quality patterns across all the batches.

Additional limitations of the technique is related to the fact that the fabricated patterns were very fragile and difficult to handle. In addition, when washed with water (to remove excess dye and silk), the patterns often separated from the glass substrate used for mechanical support during the writing process. Thus, whilst useful in terms of creating free-standing structures, their fragility meant that any attempt to perform mechanical characterisation of the samples resulted in significant damage to the silk and thus no valuable data was collected.

## 1.2. Progress in silk photo-gelation, the introduction of 2D fabrication

Following those challenges, the next research approach was to simplify the process by generating stable and large structures which are easier for visualisation and characterisation. This led me to explore the idea of mask-less P $\mu$ SL which allows one to print the entire image directly on the silk solution, in a layer-by-layer fabrication approach. Such silk images were previously fabricated by classic lithographic techniques using pre-fabricated patterns and moulds <sup>119</sup> or by photo-lithography using masks <sup>220</sup>. During the period of this research, an alternative approach was proposed in the literature, suggesting the use of high-cost electron beam system to generate complex images on a sub-micron scale <sup>203</sup>. In contrast, the P $\mu$ SL approach introduced in chapter 4 of this thesis allowed rapid, low-cost and dynamic fabrication on larger scales (tens of microns up to centimetres). Although this approach cannot compete with e-beam over resolution, it can provide an accessible and industrial scale solution for a broad range of applications where sub-micron resolution is not required.

Silk P $\mu$ SL patterns were generated by placing a thin layer of a solution under the reflected beam and projecting the desired image directly onto the silk. After an optimisation process

which included the concentration of the silk, the laser parameters and the exposure time, complex silk patterns were fabricated. The process was highly repeatable with similar pattern qualities being created using the same experimental conditions. This major improvement in pattern repeatability when compared to the DLW system, is a result of a static optical system in the P $\mu$ SL set-up.

Surprisingly the riboflavin dye was completely removed when the sample was immersed in water, suggesting a different mechanism of photo-gelation from that suggested for silk photocuring in the presence of Rose Bengal dye. It was confirmed that riboflavin-initiated radicals on the tyrosine side groups of the protein which in turn can interact and form di-tyrosine bonds. No traces of the riboflavin dye were found in the photo-cured sample, suggesting that riboflavin does not directly crosslink to the silk protein. This result is very enlightening, amplifying the fact that dye selection has a major effect on the photo-gelation process and should not be driven solely by the absorption spectra of the dye.

The mask-less P $\mu$ SL system used in this section was previously used in our lab for the fabrication of polymeric 3D tubes and scaffold for tissue regeneration<sup>342,343</sup>. However, to attempt structuring with silk a few adaptations were required, such as the use of a more powerful laser source to initiate the polymerisation in the silk/riboflavin solution (250 mW vs. 10-50 mW). This is because riboflavin is a weaker light absorbent than the commercial photoinitiators at the wavelength of the current laser<sup>230</sup>.

After complete photo-curing of the silk, the pattern had a consistency of a stable sticky gel which was easier to handle and characterise than the DLW patterns. This is probably a result of a larger sample and a higher level of energy dose delivered to the silk. In DLW the energy is delivered only to a specific point on the sample, and even when extremely low writing

speeds are used (0.01 mm/s), each area on the sample is exposed to light radiation for a maximum duration of few seconds. However, in P $\mu$ SL the whole sample is exposed to a uniform radiation dose for much longer (minutes). In chapter 4 of this thesis, it was shown by *in situ* rheological measurements that were performed during the photo-curing process, that the radiation dose delivered to the sample is directly connected to the stiffness of the resulting gel. As a result, stiffer gels are easier to handle and therefore are more practical for most applications.

The simplicity of this method, the large flexibility in pattern design and the higher stiffness of the patterns, make P $\mu$ SL the preferred choice for rapid, repeatable large-scale patterning. Therefore, I recommend using P $\mu$ SL for further research in native silk photo-fabrication.

Following the success of P $\mu$ SL in native silk, I have decided to explore the benefits of this material by comparing it to typical reconstituted silk solutions. Whilst this material is more commonly seen and used in the silk structuring literature, the process of reconstitution is known to have a strong effect on the final properties on the silk, and it was no surprise to me that the reconstituted silk was without a doubt inferior to the native protein. This can be seen from the higher concentrations required for structuring (2 wt.%), the larger variability in the results, and the inferior quality of the final patterns.

Following the concept that the mechanism of crosslinking occurs through the tyrosine side groups on the silk protein, the initial hypothesis was that the number of tyrosine groups on the protein is the main factor contribution the photo-curing process. This idea was explored by using a tyrosine-rich co-polymer (poly tyr-co-glu) which was used as a control in the photocuring process. However, this hypothesis was ruled out after the co-polymer did not produce in a good quality pattern. In fact, only a high concentration of the polymer (5 wt. %),

at its solubility limit, resulted in a visible structure reproducing only a partial image of the projected pattern (chapter 4). Those results brought me to the idea that the key benefit of native silk is in fact, its high molecular weight, which is also the main factor contributing to image quality during the photo-gelation.

This hypothesis was tested by comparing the quality of the pattern achieved by photo-curing of the native protein and reconstituted silk produced by standard degumming. As just mentioned, the process of degumming is known to degrade the protein<sup>85</sup> and here was used as a method to study the effect of protein degradation level on the quality of the printed patterns. The hypothesis was confirmed and a significant reduction in pattern quality was recorded with protein degradation/degumming time. Affirming this, a similar degradation in molecular weight was also achieved by enzymatic breakdown of the native protein and resulted in similar outcomes for pattern quality. This confirmed that pattern quality is directly related to molecular weight and not primarily affected by other differences between the native and reconstituted silk proteins.

The most important outcome of this part of my research was that when the degumming stage in the process of silk reconstitution was avoided, a significant improvement in the pattern quality was recorded, and the pattern was comparable to that achieved for native silk printing. Therefore, I suggest that the current field of silk bioprinting can be significantly improved by alteration of the sample preparation method, and removal of the degumming step from silk reconstitution process. However, this raises an additional issue which was not addressed in this work regarding the role of the sericin protein in the photo-gelation process. Sericin is removed during the degumming process<sup>86</sup>. This process also degrades the fibroin and reduces its molecular weight. A broader investigation is required to answer if the sericin

has a role in the photo-curing process or how it affects the pattern quality. This can be partially answered by comparing the patterns produced from native silk that was extracted from a sericin free zone of the duct (0 wt.% sericin) and those of a non-degummed reconstituted sample where sericin was not removed at all (~30 wt.%). The result; both materials generated similar patterns. Therefore, one can assume that the sericin does not play an active role in the photocuring process but its presence can still have an effect on pattern properties and application range <sup>31</sup>.

Despite the promising results, silk P $\mu$ SL still has a few challenges to overcome. At first, the system used in this set-up was limited to a 250 mW laser source operating on maximum power. The use of a stronger source might reduce the fabrication time which is currently 5 minutes per sample and can lead to an increase in sample stiffness post-fabrication. This allows tuning the stiffness of the silk gels over a broader range of values, expanding potential applications. This improvement in sample stiffness might also contribute to sample stability during multi-layer fabrication which currently cannot be achieved.

Although the fabricated patterns are classified as hydrogels with pronounced surface topography (~ 10  $\mu$ m) and can be defined as 2.5D structures, it is fair to say that it has not been possible to generate true 3D objects in the current P $\mu$ SL set-up.

### 1.3. The limits of photo-gelation in 3D fabrication

One of the main limitations is this set up is the fact that the object is polymerised inside a resin pool. This requires an additional step to separate the photo-gelled silk structure from the surrounding non-exposed silk solution. Even if a stable 3D object is fabricated, it is extremely challenging to separate it from the viscous sticky silk surrounding the object and all of the many attempts to do so resulted in a complete collapse of the structures. One of the

reasons is because the un-exposed silk solution undergoes partial gelation which as a result of reflected beam elements in the solution. It is also a result of the fact that riboflavin absorbs in the visible light and despite my attempts to conduct the experiment in complete darkness, external light exposure during sample loading and experiment preparation is sufficient to initiate gelation in the silk. Increasing laser power and the stiffness of the photo-cured sample might simplify the process of separation but might also result in a higher scattering level of the laser beam and thus more gelation of the surrounding silk.

In fact, when discussing the photo-gelation approach for 3D fabrication, only a single paper from Sun *et al.* <sup>270</sup> published in 2015 reporting a true 3D structure of pure silk, can be found from the whole literature of silk photo-fabrication <sup>573</sup>. In this work, Sun *et al.* were able to generate free-standing structures, a few microns in size, by combining multi-photon lithography and reconstituted silk. In this process a Ti:Sapphire femtosecond laser was used to induce the polymerisation. This laser is significantly more expensive and powerful than the Nd:YAG laser used in the current work. In addition, the small size of those structures can make them unsuitable for most medical applications which usually require larger scaffolds about few millimetres in size <sup>574</sup>.

This study together with the many limitations of the photo-curing process discussed above led me to the conclusion that pure-silk 3D applicable structures cannot be readily achieved with the systems currently available in our lab. Therefore, the process of native-silk P $\mu$ SL is currently limited to 2.5D fabrication.

#### 1.4. An alternative route for 3D structuring of silk – emulsion templating

When reaching this point in my research, I decided to put the photo-fabrication approach on hold and to develop a novel and alternative 3D fabrication route to generate silk scaffolds.



This was done with the aim to contribute the broad field of silk structuring on the multi-dimensional scale and following a preliminary success achieved by Jack Rutter from the Natural Materials Group during his final research project.

The idea behind the emulsion templating approach was to generate silk porous structures. This was achieved by the addition of oil droplets to liquid silk to generate a stable high internal phase emulsion (HIPE). Then solidification of the silk (by gelation) and removal of the oil to fabricate pure-silk poly-HIPE (chapter 5). Such poly-HIPE structure has not been reported before in the silk literature but the HIPE structure has proven to be very beneficial for many applications<sup>283</sup>, especially in tissue engineering<sup>484,485</sup>.

Initially, native silk was tested as a candidate for poly-HIPEs fabrication. However, any attempt to fabricate a stable emulsion from native silk is failed due to immediate silk gelation. Alternatively, non-degummed reconstituted silk was chosen based on my previous findings in chapter 4 that non-degummed reconstituted silk behaves similarly to natural silk during photocuring.

During the initial stages of poly-HIPEs fabrication process development, the true nature of silk complexity was fully revealed to me, where it was difficult to control the large number of parameters that affected the final structure porosity, resulting in poor repeatability. It was a very long journey, but the outcome was clear: pure silk poly-HIPEs scaffolds can be made.

The resulting fabrication process is simple, water-based and biofriendly, involving two main materials: silk and rapeseed oil. The fabrication is done in ambient conditions and does not require complex lab equipment, reducing cost and increasing accessibility. In fact, the poly-HIPEs can be fabricated in any basic chemical lab and provide unlimited research opportunities for this unique silk scaffold.

The main scientific conclusion from this part of my research was that the viscosity of the silk/oil emulsion plays the key role in the final porosity of the structure. If the viscosity is too high ( $> 3.2 \text{ Pa}\cdot\text{s}$ ) the scaffold will result in a fully closed porosity, failing to provide the interconnectivity required for tissue engineering applications. If the viscosity is too low ( $< 1 \text{ Pa}\cdot\text{s}$ ) the oil and silk will separate and fail to produce a scaffold.

This narrow range of appropriate viscosities requires a high level of control over the process of emulsion fabrication. This can be achieved by precise control over the oil droplet size and by improving the method for distributing the droplets in the silk, which is currently done by a simple shaking of the silk solution by placing it on an orbital vibration stage. Additional challenges were to generate an emulsion with sufficient viscosity to allow the stable printing of complex 3D structures (*via* sample extrusion) without affecting the HIPE structure of the emulsion.

One main drawback of this process is the amount of sample required for each experiment. Currently, each batch of reconstituted silk provides up to 20 ml of solution. Each emulsion templating experiment requires 8 ml of silk. Therefore, it is challenging to optimise the process with a single batch of silk. Due to batch-to-batch variations in the reconstitution process, it is also challenging to use multiple batches for the optimisation.

Therefore, I propose that the current process of poly-HIPE fabrication urgently requires an alternative emulsification system which allows one to reproduce the fabrication process on a smaller scale. When this goal is achieved, process optimisation will be significantly improved resulting in a much higher level of repeatability.

In conclusion, as summarised in Table 12, native silk is a suitable material for photo-fabrication and enables the improvement of quality and complexity of hydrogel patterns,

which are currently limited due to the use of processed silk proteins. Moreover, it was also established that by simple modification of the current degumming methods for reconstituted silks, it is possible to achieve high-quality structures which are comparable in complexity to that fabricated from native silk. Additionally, it was shown that porous interconnected 3D structures can be fabricated for high-quality reconstituted silk using a simple and environmentally friendly approach that was originally introduced in chapter 5 of this thesis. This thesis provided an insight into the photo-gelation mechanism and provides the optimised values for the multiple parameters that affect the properties of the structures.

To finish, I hope that this work will inspire the current and future researchers in the area of biomaterials and advanced manufacturing and will contribute to the development of low-cost commercial systems improving the accessibility of silk-based medical products worldwide.

Table 12: Summary of the methods and result discussed in this thesis

	Chapter 3 1D direct laser writing of silk patterns	Chapter 4 Fabrication of 2D Silk Structures by Projection Stereolithography	Chapter 5 3D fabrication of silk structures by emulsion templating route
Main Scientific question	<ul style="list-style-type: none"> <li>• Can silk be spun by light?</li> </ul>	<ul style="list-style-type: none"> <li>• What are the benefits of the native protein in photo-fabrication?</li> </ul>	<ul style="list-style-type: none"> <li>• Is it possible to fabricate pure silk poly-HIPes?</li> </ul>
Research goals	<ul style="list-style-type: none"> <li>• Development of the process of DLW for native silk protein and exploration of the photo-gelation mechanism</li> </ul>	<ul style="list-style-type: none"> <li>• Development of low-cost approach for native silk patterning by P<math>\mu</math>SL</li> <li>• Exploration of native silk benefits in photo-fabrication</li> </ul>	<ul style="list-style-type: none"> <li>• Fabrication of pure-silk scaffolds with poly-HIPE structure</li> </ul>
Method used	Direct laser writing	Projection stereo-lithography	Emulsion templating
Sample type	Native silk	Native silk Reconstituted silk	Reconstituted silk
Additives to the silk	Rose Bengal dye	Riboflavin dye	Rapeseed oil
Key findings	<ul style="list-style-type: none"> <li>• Native silk can be used for patterning by DLW technique</li> <li>• Rose Bengal dye is chemically bound to the protein in the photo-cured silk</li> <li>• The written patterns are not suitable for cells guiding applications</li> </ul>	<ul style="list-style-type: none"> <li>• Native silk is suitable for complex patterning</li> <li>• Riboflavin dye is not bound to the silk</li> <li>• Native silk provides better image quality than reconstituted silk</li> <li>• The DMD used in P<math>\mu</math>SL generates photonic silk elements</li> </ul>	<ul style="list-style-type: none"> <li>• Silk poly-HIPes can be fabricated by low-cost emulsion templating method</li> <li>• Emulsion viscosity is the key factor affecting the porosity and interconnectivity of the scaffold</li> <li>• Photo-curing does not contribute to the fabrication process</li> </ul>
Contribution to the field	<ul style="list-style-type: none"> <li>• Development of biocompatible photo-curable silk resins</li> <li>• Demonstrating that native silk is suitable for photo-fabrication</li> <li>• Evaluation of the differences between Rose Bengal and Riboflavin in the mechanism of photo-gelation</li> </ul>	<ul style="list-style-type: none"> <li>• Introduction of new low-cost approach for complex silk patterning</li> <li>• Developing a novel method for rapid fabrication of silk optical elements</li> <li>• Establishing that protein molecular weight is the key parameter defining image quality</li> <li>• Introduction of the term Similarity for comparison between silk patterning techniques</li> </ul>	<ul style="list-style-type: none"> <li>• First evidence of pure-silk poly-HIPes and one of the pioneering works on natural materials poly-HIPes</li> <li>• Introduction of low cost and environmentally friendly method for the fabrication of silk scaffolds with controlled porosity and interconnectivity</li> <li>• Establishing viscosity range for successful fabrication</li> </ul>
Improvements and additional research	<ul style="list-style-type: none"> <li>• Improvement of repeatability of the results by modifying the current DLW set-up</li> <li>• Investigation of the two-photon polymerisation process in native silk</li> </ul>	<ul style="list-style-type: none"> <li>• Implementation of laser with higher power to boost the cross-linking process</li> <li>• Investigation of the potential of photo-gelation in silk 3D fabrication by redesigning of the current P<math>\mu</math>SL set-up</li> <li>• Fabrication of controlled diffraction grids to generate specific colours in the optical patterns</li> </ul>	<ul style="list-style-type: none"> <li>• Redesigning the experimental set-up to gain better control over the final porosity of the scaffold</li> <li>• Down-scaling the set up to reduce sample amount</li> </ul>

## References

- (1) Shear, W. A.; Palmer, J. M.; Coddington, J. A.; Bonamo, P. M. A Devonian Spinneret: Early Evidence of Spiders and Silk Use. *Science* (80-. ). **1989**, *246* (4929), 479–481.
- (2) Sutherland, T. D.; Young, J. H.; Weisman, S.; Hayashi, C. Y.; Merritt, D. J. Insect Silk: One Name, Many Materials. *Annu. Rev. Entomol.* **2010**, *55* (1), 171–188.
- (3) Eisoldt, L.; Smith, A.; Scheibel, T. Decoding the Secrets of Spider Silk. *Mater. Today* **2011**, *14* (3), 80–86.
- (4) Vollrath, F.; Knight, D. Biology and Technology of Silk Production. In *Biopolymers Online*; Wiley-VCH Verlag GmbH & Co. KGaA, 2005; Vol. 8, pp 25–46.
- (5) Bini, E.; Knight, D. P.; Kaplan, D. L. Mapping Domain Structures in Silks from Insects and Spiders Related to Protein Assembly. *J. Mol. Biol.* **2004**, *335* (1), 27–40.
- (6) Koh, L.-D.; Cheng, Y.; Teng, C.-P.; Khin, Y.-W.; Loh, X.-J.; Tee, S.-Y.; Low, M.; Ye, E.; Yu, H.-D.; Zhang, Y.-W.; et al. Structures, Mechanical Properties and Applications of Silk Fibroin Materials. *Prog. Polym. Sci.* **2015**, *46*, 86–110.
- (7) Belanger, W. A. The Silk Road in World History. By Xinru Liu. Oxford: Oxford University Press, 2010, 168 Pp. *J. Asian Stud.* **2011**, *70* (04), 1156–1157.
- (8) Mackenzie, D. The History of Sutures. *Med. Hist.* **1973**, *17* (02), 158–168.
- (9) Moy, R. L.; Waldman, B.; Hein, D. W. A Review of Sutures and Suturing Techniques. *J. Dermatol. Surg. Oncol.* **1992**, *18* (9), 785–795.
- (10) Shao, Z.; Vollrath, F. Surprising Strength of Silkworm Silk. *Nature* **2002**, *418*, 741.
- (11) Markus, H.; David, K.; Thomas, S. Spider Silk: From Soluble Protein to Extraordinary Fiber. *Angew. Chemie Int. Ed.* **2009**, *48* (20), 3584–3596.
- (12) Liu, X.; Zhang, K.-Q. Silk Fiber — Molecular Formation Mechanism, Structure- Property Relationship and Advanced Applications. In *Oligomerization of Chemical and Biological Compounds*; 2014.
- (13) Mortimer, B.; Holland, C.; Vollrath, F. Forced Reeling of Bombyx Mori Silk: Separating Behavior and Processing Conditions. *Biomacromolecules* **2013**, *14* (10), 3653–3659.
- (14) Koepfel, A.; Holland, C. Progress and Trends in Artificial Silk Spinning: A Systematic Review. *ACS Biomater. Sci. Eng.* **2017**, *3* (3), 226–237.
- (15) Jin, H.-J.; Kaplan, D. L. Mechanism of Silk Processing in Insects and Spiders. *Nature* **2003**, *424* (2002), 1057.
- (16) Gosline, J. M.; DeMont, M. E.; Denny, M. W. The Structure and Properties of Spider Silk. *Endeavour* **1986**, *10* (1), 37–43.
- (17) Tashiro, Y.; Otsuki, E. Studies on the Posterior Silk Gland of the Silkworm Bombyx Mori. IV. Ultracentrifugal Analyses of Native Silk Proteins, Especially Fibroin Extracted from the Middle Silk Gland of the Mature Silkworm. *J. Cell Biol.* **1970**, *46*, 1–16.
- (18) Mondal, M.; Trivedy, K.; Kumar, S. N. The Silk Proteins, Sericin and Fibroin in Silkworm, Bombyx Mori Linn.,-a Review. *Casp. J. Env Sci* **2007**, *5* (2), 63–76.
- (19) Ude, A. U.; Eshkoo, R. A.; Zulkifili, R.; Ariffin, A. K.; Dzuraidah, A. W.; Azhari, C. H. Bombyx Mori Silk Fibre and Its Composite: A Review of Contemporary Developments. *Mater. Des.* **2014**, *57*, 298–305.
- (20) Porter, D.; Vollrath, F. Silk as a Biomimetic Ideal for Structural Polymers. *Adv. Mater.* **2009**, *21* (4), 487–492.
- (21) Meng, X.; Zhu, F.; Chen, K. Silkworm: A Promising Model Organism in Life Science. *J. Insect Sci.* **2017**, *17* (5), 97.
- (22) Rockwood, D. N. D. D. N. D. D. N.; Preda, R. C. R. R. C.; Yücel, T.; Wang, X.; Lovett, M. L.; Kaplan, D. L.; Yucel, T.; Wang, X.; Lovett, M. L.; Kaplan, D. L.; et al. Materials Fabrication from Bombyx Mori Silk Fibroin. *Nat. Protoc.* **2011**, *6* (September), 1612–1631.
- (23) Altman, G. H.; Diaz, F.; Jakuba, C.; Calabro, T.; Horan, R. L.; Chen, J.; Lu, H.; Richmond, J.; Kaplan, D. L. Silk-Based Biomaterials. *Biomaterials* **2003**, *24* (3), 401–416.
- (24) Vepari, C.; Kaplan, D. L. Silk as a Biomaterial. *Prog. Polym. Sci.* **2007**, *32* (8–9), 991–1007.
- (25) Klymenko, V. V. Animal Species for Developmental Studies. **1990**, No. January 1990.
- (26) Quatrefages, A. De. SILK-WORMS AND SERICULTURE. *Pop. Sci. Mon. Mon.* **1873**, *3*.
- (27) Craig, C. L. Evolution of Arthropod Silks. *Annu. Rev. Entomol.* **1997**, *42*, 231–267.
- (28) Li, G.; Zhou, P.; Shao, Z.; Xie, X.; Chen, X.; Wang, H.; Chunyu, L.; Yu, T. The Natural Silk Spinning Process: A Nucleation-Dependent Aggregation Mechanism? *Eur. J. Biochem.* **2001**, *268*, 6600–6606.
- (29) Sehna, F.; Akai, H. Insect Silk Glands: Their Types, Development and Function, and Effects of Environmental Factors and Morphogenetic Hormones on Them. *Int. J. Insect Morphol. Embryol.* **1990**, *19* (2), 79–132.

## PhD Thesis: Multi-dimensional Structuring of Native Silk

- (30) Takiya, S.; Tsubota, T.; Kimoto, M. Regulation of Silk Genes by Hox and Homeodomain Proteins in the Terminal Differentiated Silk Gland of the Silkworm *Bombyx Mori*. *J. Dev. Biol.* **2016**, *4* (2), 19.
- (31) Kunz, R. I.; Brancalhão, R. M. C.; Ribeiro, L. de F. C.; Natali, M. R. M. Silkworm Sericin: Properties and Biomedical Applications. *Biomed Res. Int.* **2016**, *2016*, 8175701.
- (32) Gage, L. P.; Manning, R. F. Internal Structure of the Silk Fibroin Gene of *Bombyx Mori*. I The Fibroin Gene Consists of a Homogeneous Alternating Array of Repetitious Crystalline and Amorphous Coding Sequences. *J. Biol. Chem.* **1980**, *255* (19), 9444–9450.
- (33) Nowick, J. S.; Insaf, S. The Propensities of Amino Acids To Form Parallel  $\beta$ -Sheets. *J. Am. Chem. Soc.* **1997**, *119* (45), 10903–10908.
- (34) Matsumoto, A.; Lindsay, A.; Abedian, B.; Kaplan, D. L. Silk Fibroin Solution Properties Related to Assembly and Structure. *Macromol. Biosci.* **2008**, *8* (11), 1006–1018.
- (35) Pace, C. N.; Treviño, S.; Prabhakaran, E.; Scholtz, J. M. Protein Structure, Stability and Solubility in Water and Other Solvents. *Philos. Trans. R. Soc. B Biol. Sci.* **2004**, *359* (1448), 1225–1235.
- (36) Bratzel, G.; Buehler, M. J. Sequence-Structure Correlations in Silk: Poly-Ala Repeat of *N. Clavipes* MaSp1 Is Naturally Optimized at a Critical Length Scale. *J. Mech. Behav. Biomed. Mater.* **2012**, *7*, 30–40.
- (37) Rathore, O.; Sogah, D. Y. Self-Assembly of  $\beta$ -Sheets into Nanostructures by Poly (Alanine) Segments Incorporated in Multiblock Copolymers Inspired by Spider Silk. *J. Am. Chem. Soc.* **2001**, *123* (22), 5231–5239.
- (38) Yamane, T.; Umemura, K.; Nakazawa, Y.; Asakura, T. Molecular Dynamics Simulation of Conformational Change of Poly(Ala-Gly) from Silk I to Silk II in Relation to Fiber Formation Mechanism of *Bombyx Mori* Silk Fibroin. *Macromolecules* **2003**, *36* (18), 6766–6772.
- (39) Buyong, M.; Ruth, N. Molecular Dynamics Simulations of Alanine Rich B-sheet Oligomers: Insight into Amyloid Formation. *Protein Sci.* **2009**, *11* (10), 2335–2350.
- (40) Keten, S.; Buehler, M. J. Nanostructure and Molecular Mechanics of Spider Dragline Silk Protein Assemblies. *J. R. Soc. Interface* **2010**, *7* (53), 1709–1721.
- (41) Guerette, P. A.; Ginzinger, D. G.; Weber, B. H. F.; Gosline, J. M. Silk Properties Determined by Gland-Specific Expression of a Spider Fibroin Gene Family. *Science* (80-. ). **1996**, *272* (5258), 112–115.
- (42) The UniProt Consortium. UniProt: The Universal Protein Knowledgebase. *Nucleic Acids Res.* **2017**, *45* (D1), D158–D169.
- (43) Zhou, C.-Z.; Confalonieri, F.; Medina, N.; Zivanovic, Y.; Esnault, C.; Yang, T.; Jacquet, M.; Janin, J.; Duguet, M.; Perasso, R.; et al. Fine Organization of *Bombyx Mori* Fibroin Heavy Chain Gene. *Nucleic Acids Res.* **2000**, *28* (12), 2413–2419.
- (44) Joseph, Z.; Ishay, J. S. Silk Structure in the Hornet Cocoon. *J. Electron Microsc. (Tokyo)*. **2004**, *53* (3), 293–304.
- (45) Lotz, B.; Colonna Cesari, F. The Chemical Structure and the Crystalline Structures of *Bombyx Mori* Silk Fibroin. *Biochimie* **1979**, *61* (2), 205–214.
- (46) Chen, X.; Shao, Z.; Vollrath, F. *The Spinning Processes for Spider Silk*; 2006; Vol. 2.
- (47) Holland, C.; Porter, D.; Vollrath, F. Comparing the Rheology of Mulberry and “Wild” Silkworm Spinning Dopes. *Biopolymers* **2012**, *97* (6), 362–367.
- (48) Knight, D.; Vollrath, F. Liquid Crystals and Flow Elongation in a Spider’s Silk Production Line. *Proc. R. Soc. London* **1999**, *266* (November 1998), 519–523.
- (49) Zhou, L.; Chen, X.; Shao, Z.; Huang, Y.; Knight, D. P. Effect of Metallic Ions on Silk Formation in the Mulberry Silkworm, *Bombyx m Ori*. *J. Phys. Chem. B* **2005**, *109* (35), 16937–16945.
- (50) Dicko, C.; Kenney, J. M.; Knight, D.; Vollrath, F. Transition to a Beta-Sheet-Rich Structure in Spidroin in Vitro: The Effects of PH and Cations. *Biochemistry* **2004**, *43*, 14080–14087.
- (51) Asakura, T.; Umemura, K.; Nakazawa, Y.; Hirose, H.; Higham, J.; Knight, D. Some Observations on the Structure and Function of the Spinning Apparatus in the Silkworm *Bombyx Mori*. *Biomacromolecules* **2007**, *8* (1), 175–181.
- (52) Wohlrab, S.; Thamm, C.; Scheibel, T. *The Power of Recombinant Spider Silk Proteins*; 2014; Vol. 5.
- (53) Sparkes, J.; Holland, C. Analysis of the Pressure Requirements for Silk Spinning Reveals a Pultrusion Dominated Process. *Nat. Commun.* **2017**, *8* (1), 594.
- (54) Holland, C.; Terry, A. E.; Porter, D.; Vollrath, F. Comparing the Rheology of Native Spider and Silkworm Spinning Dope. *Nat Mater* **2006**, *5* (11), 870–874.
- (55) Laity, P. R.; Gilks, S. E.; Holland, C. Rheological Behaviour of Native Silk Feedstocks. *Polymer (Guildf)*. **2015**, *67*, 28–39.
- (56) Vollrath, F.; Knight, D. P. Liquid Crystalline Spinning of Spider Silk. *Nature* **2001**, *410* (March), 541.
- (57) Knight, D. P.; Vollrath, F. Liquid Crystals and Flow Elongation in a Spider’s Silk Production Line.

- Proc. R. Soc. London. Ser. B Biol. Sci.* **1999**, *266* (1418), 519 LP-523.
- (58) Wang, X.; Zhao, P.; Li, Y.; Yi, Q.; Ma, S.; Xie, K.; Chen, H.; Xia, Q. Modifying the Mechanical Properties of Silk Fiber by Genetically Disrupting the Ionic Environment for Silk Formation. *Biomacromolecules* **2015**, *16* (10), 3119–3125.
- (59) Xiao, S.; Stacklies, W.; Cetinkaya, M.; Markert, B.; Gräter, F. Mechanical Response of Silk Crystalline Units from Force-Distribution Analysis. *Biophys. J.* **2009**, *96* (10), 3997–4005.
- (60) Krasnov, I.; Diddens, I.; Hauptmann, N.; Helms, G.; Ogurreck, M.; Seydel, T.; Funari, S. S.; Müller, M. Mechanical Properties of Silk: Interplay of Deformation on Macroscopic and Molecular Length Scales. *Phys. Rev. Lett.* **2008**, *100* (4), 2–5.
- (61) Sakka, S.; Kozuka, H. *Handbook of Sol-Gel Science and Technology. 1. Sol-Gel Processing*; Springer Science & Business Media, 2005; Vol. 1.
- (62) Nagarkar, S.; Nicolai, T.; Chassenieux, C.; Lele, A. Structure and Gelation Mechanism of Silk Hydrogels. *Phys. Chem. Chem. Phys.* **2010**, *12* (15), 3834–3844.
- (63) Foo, C. W. P.; Bini, E.; Hensman, J.; Knight, D. P.; Lewis, R. V.; Kaplan, D. L. Role of PH and Charge on Silk Protein Assembly in Insects and Spiders. *Appl. Phys. A Mater. Sci. Process.* **2006**, *82*, 223–233.
- (64) Im, D. S.; Kim, M. H.; Yoon, Y. Il; Park, W. H. Gelation Behaviors and Mechanism of Silk Fibroin According to the Addition of Nitrate Salts. *Int. J. Mol. Sci.* **2016**, *17* (10).
- (65) Wang, X.; Kluge, J. A.; Leisk, G. G.; Kaplan, D. L. Sonication-Induced Gelation of Silk Fibroin for Cell Encapsulation. *Biomaterials* **2008**, *29* (8), 1054–1064.
- (66) Matsumoto, A.; Chen, J.; Collette, A. L.; Kim, U.-J.; Altman, G. H.; Cebe, P.; Kaplan, D. L. Mechanisms of Silk Fibroin Sol–Gel Transitions. *J. Phys. Chem. B* **2006**, *110* (43), 21630–21638.
- (67) Greenfield, N. J. Using Circular Dichroism Spectra to Estimate Protein Secondary Structure. *Nat. Protoc.* **2006**, *1* (6), 2876–2890.
- (68) Yang, Y.; Shao, Z.; Chen, X.; Zhou, P. Optical Spectroscopy to Investigate the Structure of Regenerated Bombyx Mori Silk Fibroin in Solution. *Biomacromolecules* **2004**, *5*, 773–779.
- (69) Laity, R. P.; Holland, C. The Rheology behind Stress-Induced Solidification in Native Silk Feedstocks. *International Journal of Molecular Sciences* . 2016.
- (70) Chi-Hao, L.; Dean, H. R.; U., P. K.; W., U. D. Differential Scanning Calorimetry Studies of the Inverse Temperature Transition of the Polypentapeptide of Elastin and Its Analogues. *Biopolymers* **2018**, *29* (14), 1699–1706.
- (71) Ashish, N.; John, C.; Mary, C.; Franco, F.; Joseph, C.; Hamidreza, G. Genetic Synthesis and Characterization of PH- and Temperature-Sensitive Silk-Elastinlike Protein Block Copolymers. *J. Biomed. Mater. Res.* **2002**, *62* (2), 195–203.
- (72) Edsall, J. T.; McKenzie, H. A. Water and Proteins. II. The Location and Dynamics of Water in Protein Systems and Its Relation to Their Stability and Properties. *Adv. Biophys.* **1983**, *16*, v–vi.
- (73) W., U. D. Molecular Machines: How Motion and Other Functions of Living Organisms Can Result from Reversible Chemical Changes. *Angew. Chemie Int. Ed. English* **2018**, *32* (6), 819–841.
- (74) Urry, D. W.; Peng; Xu, J.; McPherson, D. T. Characterization of Waters of Hydrophobic Hydration by Microwave Dielectric Relaxation. *J. Am. Chem. Soc.* **1997**, *119* (5), 1161–1162.
- (75) Sohn, S.; Strey, H. H.; Gido, S. P. Phase Behavior and Hydration of Silk Fibroin. *Biomacromolecules* **2004**, *5*, 751–757.
- (76) Shao, Z.; Vollrath, F. The Effect of Solvents on the Contraction and Mechanical Properties of Spider Silk. *Polymer (Guildf)*. **1999**, *40*, 1799–1806.
- (77) Valluzzi, R.; He, S. J.; Gido, S. P.; Kaplan, D. Bombyx Mori Silk Fibroin Liquid Crystallinity and Crystallization at Aqueous Fibroin–Organic Solvent Interfaces. *Int. J. Biol. Macromol.* **1999**, *24*, 227–236.
- (78) Chen, F.; Porter, D.; Vollrath, F. Structure and Physical Properties of Silkworm Cocoons. *J. R. Soc. Interface* **2012**, *9* (74), 2299–2308.
- (79) Agarwal, N.; Hoagland, D. a; Farris, R. J. Effect of Moisture Absorption on the Thermal Properties of Bombyx Mori Silk Fibroin Films. *Therm. Prop. Silk Fibroin Film.* **1996**, 401–410.
- (80) Boutry, C.; Blackledge, T. A. Evolution of Supercontraction in Spider Silk: Structure-Function Relationship from Tarantulas to Orb-Weavers. *J. Exp. Biol.* **2010**, *213* (20), 3505–3514.
- (81) Yang, Z.; Liivak, O.; Seidel, a.; LaVerde, G.; Zax, D. B.; Jelinski, L. W. Supercontraction and Backbone Dynamics in Spider Silk: <sup>13</sup>C and <sup>2</sup>H NMR Studies. *J. Am. Chem. Soc.* **2000**, *122* (14), 9019–9025.
- (82) Shao, Z.; Vollrath, F.; Sirichaisit, J.; Young, R. J. Analysis of Spider Silk in Native and Supercontracted States Using Raman Spectroscopy. *Polymer (Guildf)*. **1999**, *40*, 2493–2500.
- (83) Pérez-Rigueiro, J.; Elices, M.; Guinea, G. V. Controlled Supercontraction Tailors the Tensile Behaviour of Spider Silk. *Polymer (Guildf)*. **2003**, *44*, 3733–3736.

- (84) Liu, Y.; Shao, Z.; Vollrath, F. Relationships between Supercontraction and Mechanical Properties of Spider Silk. *Nat. Mater.* **2005**, *4*, 901.
- (85) Wang, H.-Y.; Zhang, Y.-Q. Effect of Regeneration of Liquid Silk Fibroin on Its Structure and Characterization. *Soft Matter* **2013**, *9* (1), 138–145.
- (86) Gulrajani, M. L. Degumming of Silk. *Color. Technol.* **1992**, *22* (1), 79–89.
- (87) Tsukada, M.; Gotoh, Y.; Nagura, M.; Minoura, N.; Kasai, N.; Freddi, G. Structural Changes of Silk Fibroin Membranes Induced by Immersion in Methanol Aqueous Solutions. *J. Polym. Sci. Part B Polym. Phys.* **1994**, *32* (5), 961–968.
- (88) Seidel, a; Liivak, O.; Calve, S.; Adaska, J.; Ji, G.; Yang, Z.; Grubb, D.; Zax, D. B.; Jelinski, L. W. Regenerated Spider Silk: Processing, Properties, and Structure. *Macromolecules* **2000**, *33*, 775–780.
- (89) Hirota, N.; Mizuno, K.; Goto, Y. Group Additive Contributions to the Alcohol-Induced Alpha-Helix Formation of Melittin: Implication for the Mechanism of the Alcohol Effects on Proteins. *J. Mol. Biol.* **1998**, *275*, 365–378.
- (90) Vollrath, F.; Knight, D. P.; Hu, X. W. Silk Production in a Spider Involves Acid Bath Treatment. *Proc. R. Soc. B Biol. Sci.* **1998**, *265* (January), 817–820.
- (91) Jiang, P.; Liu, H.; Wang, C.; Wu, L.; Huang, J.; Guo, C. Tensile Behavior and Morphology of Differently Degummed Silkworm (*Bombyx Mori*) Cocoon Silk Fibres. *Mater. Lett.* **2006**, *60*, 919–925.
- (92) Walters, K. Rheology of Polymers. *J. Nonnewton. Fluid Mech.* **1981**, *8*, 193.
- (93) Osswald, T.; Rudolph, N. Polymer Rheology; Osswald, T., Rudolph, N. B. T.-P. R., Eds.; Hanser, 2015; pp I–XI.
- (94) Tabatabai, A. P.; Kaplan, D. L.; Blair, D. L. Rheology of Reconstituted Silk Fibroin Protein Gels: The Epitome of Extreme Mechanics. *Soft Matter* **2015**, *11* (4), 756–761.
- (95) Chen, X.; Knight, D. P.; Shao, Z.; Vollrath, F. Regenerated Bombyx Silk Solutions Studied with Rheometry and FTIR. *Polymer (Guildf)*. **2001**, *42* (25), 9969–9974.
- (96) Iizuka, E. Mechanism of Fiber Formation by the Silkworm *Bombyx Mori*. *Biorheology* **1966**, *3*, 141–152.
- (97) Terry, A. E.; Knight, D. P.; Porter, D.; Vollrath, F. PH Induced Changes in the Rheology of Silk Fibroin Solution from the Middle Division of *Bombyx Mori* Silkworm. *Biomacromolecules* **2004**, *5* (3), 768–772.
- (98) Laity, P. R.; Holland, C. Native Silk Feedstock as a Model Biopolymer: A Rheological Perspective. *Biomacromolecules* **2016**, *17* (8), 2662–2671.
- (99) Hossain, K. S.; Nemoto, N.; Magoshi, J. Rheological Study on Aqueous Solutions of Silk Fibroin. *XIIIth Int. Congr. Rheol.* **2000**, 1–372.
- (100) Pople, J. a.; Hamley, I. W.; Fairclough, J. P. a; Ryan, a. J.; Hill, G.; Price, C. A Shear Induced Transition of Lamellar Alignment in a Concentrated Diblock Copolymer Solution. *Polymer (Guildf)*. **1999**, *40*, 5709–5714.
- (101) Ferry, J. D.; Ferry, J. D. *Viscoelastic Properties of Polymers*; Wiley, 1980.
- (102) Watanabe, H. Viscoelasticity and Dynamics of Entangled Polymers. *Prog. Polym. Sci.* **1999**, *24* (9), 1253–1403.
- (103) Holland, C.; Terry, A. E.; Porter, D.; Vollrath, F. *Natural and Unnatural Silks*; 2007; Vol. 48.
- (104) Manning, R. F.; Gage, L. P. Internal Structure of the Silk Fibroin Gene of *Bombyx Mori*. II. Remarkable Polymorphism of the Organization of Crystalline and Amorphous Coding Sequences. *J. Biol. Chem.* **1980**, *255* (19), 9451–9457.
- (105) Laity, P. R.; Baldwin, L.; Holland, C. Changes in Silk Feedstock Rheology during Cocoon Construction: The Role of Calcium and Potassium Ions. *Press* **2018**, *1800188*, 1–11.
- (106) Hou, Y.; Xia, Q.; Zhao, P.; Zou, Y.; Liu, H.; Guan, J.; Gong, J.; Xiang, Z. Studies on Middle and Posterior Silk Glands of Silkworm (*Bombyx Mori*) Using Two-Dimensional Electrophoresis and Mass Spectrometry. *Insect Biochem. Mol. Biol.* **2007**, *37* (5), 486–496.
- (107) SHIMURA, K.; KIKUCHI, A.; KATAGATA, Y.; OHOTOMO, K. The Occurrence of Small Component Proteins in the Cocoon Fibroin of *Bombyx Mori*. *J. Sericultural Sci. Japan* **1982**, *51* (1), 20–26.
- (108) Dong, Z.; Zhao, P.; Wang, C.; Zhang, Y.; Chen, J.; Wang, X.; Lin, Y.; Xia, Q. Comparative Proteomics Reveal Diverse Functions and Dynamic Changes of *Bombyx Mori* Silk Proteins Spun from Different Development Stages. *J. Proteome Res.* **2013**, *12* (11), 5213–5222.
- (109) Horie, Y.; Ito, T. Nutrition of the Silkworm, *Bombyx Mori*—X. Vitamin B Requirements and the Effects of Several Analogues. *J. Insect Physiol.* **1965**, *11* (12), 1585–1593.
- (110) Legay, J. M. Recent Advances in Silkworm Nutrition. *Annu. Rev. Entomol.* **1958**, *3* (1), 75–86.
- (111) Vollrath, F.; Madsen, B.; Shao, Z. The Effect of Spinning Conditions on the Mechanics of a Spider's Dragline Silk. *Proc. R. Soc. London B Biol. Sci.* **2001**, *268* (1483), 2339–2346.
- (112) Xia, Q.; Zhou, Z.; Lu, C.; Cheng, D.; Dai, F.; Li, B.; Zhao, P.; Zha, X.; Cheng, T.; Chai, C. A Draft Sequence for



- the Genome of the Domesticated Silkworm (*Bombyx Mori*). *Science (80- )*. **2004**, *306* (5703), 1937–1940.
- (113) Ma, S.; Zhang, S.; Wang, F.; Liu, Y.; Liu, Y.; Xu, H.; Liu, C.; Lin, Y.; Zhao, P.; Xia, Q. Highly Efficient and Specific Genome Editing in Silkworm Using Custom TALENs. *PLoS One* **2012**, *7* (9), e45035.
- (114) Xia, Q.; Guo, Y.; Zhang, Z.; Li, D.; Xuan, Z.; Li, Z.; Dai, F.; Li, Y.; Cheng, D.; Li, R. Complete Resequencing of 40 Genomes Reveals Domestication Events and Genes in Silkworm (*Bombyx*). *Science (80- )*. **2009**, *326* (5951), 433–436.
- (115) Zhang, Y. Q. Applications of Natural Silk Protein Sericin in Biomaterials. *Biotechnol. Adv.* **2002**, *20*, 91–100.
- (116) Routh, A. F. Drying of Thin Colloidal Films. *Reports Prog. Phys.* **2013**, *76* (4), 46603.
- (117) Marelli, B.; Brenckle, M. A.; Kaplan, D. L.; Omenetto, F. G. Silk Fibroin as Edible Coating for Perishable Food Preservation. *Sci. Rep.* **2016**, *6* (November 2015), 1–11.
- (118) Ling, S.; Jin, K.; Kaplan, D. L.; Buehler, M. J. Ultrathin Free-Standing *Bombyx Mori* Silk Nanofibril Membranes. *Nano Lett.* **2016**, *16* (6), 3795–3800.
- (119) Lawrence, B. D.; Cronin-Golomb, M.; Georgakoudi, I.; Kaplan, D. L.; Omenetto, F. G. Bioactive Silk Protein Biomaterial Systems for Optical Devices. *Biomacromolecules* **2008**, *9* (4), 1214–1220.
- (120) Kearns, V.; MacIntosh, A. Silk-Based Biomaterials for Tissue Engineering. *Top. tissue Eng.* **2008**, *4* (114), 1–19.
- (121) Lawrence, B. D.; Marchant, J. K.; Pindrus, M. a.; Omenetto, F. G.; Kaplan, D. L. Silk Film Biomaterials for Cornea Tissue Engineering. *Biomaterials* **2009**, *30* (7), 1299–1308.
- (122) Applegate, M. B.; Partlow, B. P.; Coburn, J.; Marelli, B.; Pirie, C.; Pineda, R.; Kaplan, D. L.; Omenetto, F. G. Photocrosslinking of Silk Fibroin Using Riboflavin for Ocular Prostheses. *Adv. Mater.* **2016**, *28* (12), 2417–2420.
- (123) Perry, H.; Gopinath, A.; Kaplan, D. L.; Negro, L. D.; Omenetto, F. G. Nano- and Micropatterning of Optically Transparent, Mechanically Robust, Biocompatible Silk Fibroin Films. *Adv. Mater.* **2008**, *20* (16), 3070–3072.
- (124) Tow, K. H.; Chow, D. M.; Vollrath, F.; Dicaire, I.; Gheysens, T.; Thévenaz, L. Spider Silk: A Novel Optical Fibre for Biochemical Sensing; 2015; Vol. 9634, p 96347D–9634–4.
- (125) Tao, H.; Hwang, S.; Marelli, B.; An, B.; Moreau, J. E.; Yang, M.; Brenckle, M. a; Kim, S.; Kaplan, D. L.; Rogers, J. A.; et al. Silk-Based Resorbable Electronic Devices for Remotely Controlled Therapy and in Vivo Infection Abatement. *Proc. Natl. Acad. Sci.* **2014**, *111* (49), 17385–17389.
- (126) Kim, D.-H.; Viventi, J.; Amsden, J. J.; Xiao, J.; Vigeland, L.; Kim, Y.-S.; Blanco, J. A.; Panilaitis, B.; Frechette, E. S.; Contreras, D.; et al. Dissolvable Films of Silk Fibroin for Ultrathin Conformal Bio-Integrated Electronics. *Nat Mater* **2010**, *9* (6), 511–517.
- (127) De Rossi, D.; Kajiwarra, K.; Osada, Y.; Yamauchi, A. Polymer Gels. In *Fundamentals and Biomedical Applications*; Springer, 1991.
- (128) El-Sherbiny, I. M.; Yacoub, M. H. Hydrogel Scaffolds for Tissue Engineering: Progress and Challenges. *Glob. Cardiol. Sci. Pract.* **2013**, *2013* (3), 316–342.
- (129) Ruel-Gariepy, E.; Leroux, J.-C. In Situ-Forming Hydrogels—review of Temperature-Sensitive Systems. *Eur. J. Pharm. Biopharm.* **2004**, *58* (2), 409–426.
- (130) Chao, P.-H. G.; Yodmuang, S.; Wang, X.; Sun, L.; Kaplan, D. L.; Vunjak-Novakovic, G. Silk Hydrogel for Cartilage Tissue Engineering. *J. Biomed. Mater. Res. B. Appl. Biomater.* **2010**, *95* (1), 84–90.
- (131) Tao, H.; Brenckle, M. A.; Yang, M.; Zhang, J.; Liu, M.; Siebert, S. M.; Averitt, R. D.; Mannoor, M. S.; McAlpine, M. C.; Rogers, J. A.; et al. Silk-Based Conformal, Adhesive, Edible Food Sensors. *Adv. Mater.* **2012**, *24* (8), 1067–1072.
- (132) Mills, N. *Polymer Foams Handbook: Engineering and Biomechanics Applications and Design Guide*; Elsevier, 2007.
- (133) Lefebvre, L. P.; Banhart, J.; Dunand, D. C. Porous Metals and Metallic Foams: Current Status and Recent Developments. *Adv. Eng. Mater.* **2008**, *10* (9), 775–787.
- (134) Sachlos, E.; Czernuszka, J. T. Making Tissue Engineering Scaffolds Work. Review: The Application of Solid Freeform Fabrication Technology to the Production of Tissue Engineering Scaffolds. *Eur Cell Mater* **2003**, *5* (29), 39–40.
- (135) Nazarov, R.; Jin, H. J.; Kaplan, D. L. Porous 3-D Scaffolds from Regenerated Silk Fibroin. *Biomacromolecules* **2004**, *5* (3), 718–726.
- (136) Kim, U.-J. J.; Park, J.; Kim, H. J.; Wada, M.; Kaplan, D. L.; Joo Kim, H.; Wada, M.; Kaplan, D. L.; Kim, H. J.; Wada, M.; et al. Three-Dimensional Aqueous-Derived Biomaterial Scaffolds from Silk Fibroin. *Biomaterials* **2005**, *26* (15), 2775–2785.
- (137) Aramwit, P.; Kanokpanont, S.; De-Eknamkul, W.; Srichana, T. Monitoring of Inflammatory Mediators

- Induced by Silk Sericin. *J. Biosci. Bioeng.* **2009**, *107* (5), 556–561.
- (138) Phillips, D. M.; Drummy, L. F.; Conrady, D. G.; Fox, D. M.; Naik, R. R.; Stone, M. O.; Trulove, P. C.; De Long, H. C.; Mantz, R. A. Dissolution and Regeneration of Bombyx Mori Silk Fibroin Using Ionic Liquids. *J. Am. Chem. Soc.* **2004**, *126* (44), 14350–14351.
- (139) Meng, Z.; Zheng, X.; Tang, K.; Liu, J.; Qin, S. Dissolution of Natural Polymers in Ionic Liquids: A Review. *e-Polymers* **2012**, *12* (1).
- (140) Wray, L.; Hu, X.; Gallego-Illamas, J.; Georgakoudi, I.; G Omenetto, F.; Schmidt, D.; Kaplan, D. *Effect of Processing on Silk-Based Biomaterials: Reproducibility and Biocompatibility*; 2011; Vol. 99.
- (141) Yang, Y.; Chen, X.; Ding, F.; Zhang, P.; Liu, J.; Gu, X. Biocompatibility Evaluation of Silk Fibroin with Peripheral Nerve Tissues and Cells in Vitro. *Biomaterials* **2007**, *28* (9), 1643–1652.
- (142) Kundu, B.; Rajkhowa, R.; Kundu, S. C.; Wang, X. Silk Fibroin Biomaterials for Tissue Regenerations. *Adv. Drug Deliv. Rev.* **2013**, *65* (4), 457–470.
- (143) Liu, W.; Merrett, K.; Griffith, M.; Fagerholm, P.; Dravida, S.; Heyne, B.; Scaiano, J. C.; Watsky, M. A.; Shinozaki, N.; Lagali, N.; et al. Recombinant Human Collagen for Tissue Engineered Corneal Substitutes. *Biomaterials* **2008**, *29* (9), 1147–1158.
- (144) Arai, T.; Freddi, G.; Innocenti, R.; Tsukada, M. Biodegradation of Bombyx Mori Silk Fibroin Fibers and Films. *J. Appl. Polym. Sci.* **2004**, *91* (4), 2383–2390.
- (145) Cao, Y.; Wang, B. Biodegradation of Silk Biomaterials. *Int. J. Mol. Sci.* **2009**, *10* (4), 1514–1524.
- (146) Pharmacopeia, U. S.; Revision, X. US Pharmacopeial. *Inc., Rockville, MD.* 1995, pp 1161–1162.
- (147) Soong, H. K.; Kenyon, K. R. Adverse Reactions to Virgin Silk Sutures in Cataract Surgery. *Ophthalmology* **1984**, *91* (5), 479–483.
- (148) Rossitch, E.; Bullard, D. E.; Oakes, W. J. Delayed Foreign-Body Reaction to Silk Sutures in Pediatric Neurosurgical Patients. *Child's Nerv. Syst.* **1987**, *3* (6), 375–378.
- (149) Postlethwait, R. W. Long-Term Comparative Study of Nonabsorbable Sutures. *Ann. Surg.* **1970**, *171* (6), 892–898.
- (150) Lam, K. H.; Nijenhuis, A. J.; Bartels, H.; R, P. A.; Jonkman, F. M.; Pennings, A. J.; Nieuwenhuis, P. Reinforced Poly(L-Lactic Acid) Fibres as Suture Material. *J. Appl. Biomater.* **2018**, *6* (3), 191–197.
- (151) Greenwald, D.; Shumway, S.; Albear, P.; Gottlieb, L. Mechanical Comparison of 10 Suture Materials before and after in Vivo Incubation. *J. Surg. Res.* **1994**, No. 56, 372–377.
- (152) Oh, J. E.; Nam, Y. S.; Lee, K. H.; Park, T. G. Conjugation of Drug to Poly(D,L-Lactic-Co-Glycolic Acid) for Controlled Release from Biodegradable Microspheres. *J. Control. Release* **1999**, *57* (3), 269–280.
- (153) Eirik, S.; Bjørn, S.; Gisle, B.; Einar, S. Biocompatibility and Effect on Osteogenesis of Poly(Ortho Ester) Compared to Poly(DL-Lactic Acid). *J. Biomed. Mater. Res.* **1999**, *49* (2), 257–263.
- (154) Weadock, K.; Olson, R. M.; Silver, F. H. Evaluation of Collagen Crosslinking Techniques. *Biomater. Med. Devices. Artif. Organs* **1983**, *11* (4), 293–318.
- (155) Teimouri, A.; Azadi, M.; Emadi, R.; Lari, J.; Chermahini, A. N. Preparation, Characterization, Degradation and Biocompatibility of Different Silk Fibroin Based Composite Scaffolds Prepared by Freeze-Drying Method for Tissue Engineering Application. *Polym. Degrad. Stab.* **2015**, *121*, 18–29.
- (156) Matteo, S.; Antonella, M.; Giuliano, F.; Mario, C. In Vitro Evaluation of the Inflammatory Potential of the Silk Fibroin. *J. Biomed. Mater. Res.* **1999**, *46* (3), 382–389.
- (157) Meinel, L.; Hofmann, S.; Karageorgiou, V.; Kirker-Head, C.; McCool, J.; Gronowicz, G.; Zichner, L.; Langer, R.; Vunjak-Novakovic, G.; Kaplan, D. L. The Inflammatory Responses to Silk Films in Vitro and in Vivo. *Biomaterials* **2005**, *26* (2), 147–155.
- (158) Dal Pra, I.; Freddi, G.; Minic, J.; Chiarini, A.; Armato, U. De Novo Engineering of Reticular Connective Tissue in Vivo by Silk Fibroin Nonwoven Materials. *Biomaterials* **2005**, *26* (14), 1987–1999.
- (159) TSUBOUCHI, K.; IGARASHI, Y.; TAKASU, Y.; YAMADA, H. Sericin Enhances Attachment of Cultured Human Skin Fibroblasts. *Biosci. Biotechnol. Biochem.* **2005**, *69* (2), 403–405.
- (160) Terada, S.; Sasaki, M.; Yanagihara, K.; Yamada, H. Preparation of Silk Protein Sericin as Mitogenic Factor for Better Mammalian Cell Culture. *J. Biosci. Bioeng.* **2005**, *100* (6), 667–671.
- (161) Vassilis, K.; Lorenz, M.; Sandra, H.; Ajay, M.; Vladimir, V.; David, K. Bone Morphogenetic Protein-2 Decorated Silk Fibroin Films Induce Osteogenic Differentiation of Human Bone Marrow Stromal Cells. *J. Biomed. Mater. Res. Part A* **2004**, *71A* (3), 528–537.
- (162) Li, C.; Vepari, C.; Jin, H.-J.; Kim, H. J.; Kaplan, D. L. Electrospun Silk-BMP-2 Scaffolds for Bone Tissue Engineering. *Biomaterials* **2006**, *27*, 3115–3124.
- (163) Lorenz, M.; Sandra, H.; Vassilis, K.; Ludwig, Z.; Robert, L.; David, K.; Gordana, V.-N. Engineering Cartilage-like Tissue Using Human Mesenchymal Stem Cells and Silk Protein Scaffolds. *Biotechnol. Bioeng.* **2004**, *88* (3), 379–391.

- (164) Furuzono T, Kishida A, T. J. Nano-Scaled Hydroxyapatite/Polymer Composite I. Coating of Sintered Hydroxyapatite Particles on Poly(Gamma-Methacryloxypropyl Trimethoxysilane)Grafted Silk Fibroin Fibers through Chemical Bonding. *J Mater Sci Mater Med.* **2004**, *15* (1), 19–23.
- (165) McClain, P. E.; Wiley, E. R. Differential Transitions MRMCKMOXS Scanning Calorimeter of Collagen Rn ' D STABILITY Studies of the Thermal. *J. Biol. Chem.* **1972**, *247*, 692–697.
- (166) Matsunaga, T.; Tomoda, R.; Nakajima, T.; Wake, H. Photoelectrochemical Sterilization of Microbial Cells by Semiconductor Powders. *FEMS Microbiol. Lett.* **1985**, *29* (1-2), 211–214.
- (167) Liu, H.; Fan, H.; Wong, E. J. W.; Toh, S. L.; Goh, J. H. Silk-Based Scaffold for Ligament Tissue Engineering. In *14th Nordic-Baltic Conference on Biomedical Engineering and Medical Physics SE - 10*; Katashev, A., Dekhtyar, Y., Spigulis, J., Eds.; IFMBE Proceedings; Springer Berlin Heidelberg, 2008; Vol. 20, pp 34–37.
- (168) Unger, R. E.; Peters, K.; Wolf, M.; Motta, A.; Migliaresi, C.; Kirkpatrick, C. J. Endothelialization of a Non-Woven Silk Fibroin Net for Use in Tissue Engineering: Growth and Gene Regulation of Human Endothelial Cells. *Biomaterials* **2004**, *25* (21), 5137–5146.
- (169) Liu, S.; Dong, C.; Lu, G.; Lu, Q.; Li, Z.; Kaplan, D. L.; Zhu, H. Bilayered Vascular Grafts Based on Silk Proteins. *Acta Biomater.* **2013**, *9* (July), 8991–9003.
- (170) Farokhi, M.; Mottaghitalab, F.; Fatahi, Y.; Khademhosseini, A.; Kaplan, D. L. Overview of Silk Fibroin Use in Wound Dressings. *Trends Biotechnol.* **2018**.
- (171) Kasoju, N.; Bora, U. Silk Fibroin in Tissue Engineering. *Adv. Healthc. Mater.* **2012**, *1* (4), 393–412.
- (172) Kirker-Head, C.; Karageorgiou, V.; Hofmann, S.; Fajardo, R.; Betz, O.; Merkle, H. P.; Hilbe, M.; von Rechenberg, B.; McCool, J.; Abrahamsen, L.; et al. BMP-Silk Composite Matrices Heal Critically Sized Femoral Defects. *Bone* **2007**, *41*, 247–255.
- (173) Amini, A. A.; Nair, L. S. Injectable Hydrogels for Bone and Cartilage Repair. *Biomed. Mater.* **2012**, *7* (2), 24105.
- (174) Fini, M.; Motta, A.; Torricelli, P.; Giavaresi, G.; Nicoli Aldini, N.; Tschon, M.; Giardino, R.; Migliaresi, C. The Healing of Confined Critical Size Cancellous Defects in the Presence of Silk Fibroin Hydrogel. *Biomaterials* **2005**, *26* (17), 3527–3536.
- (175) Kim, H. J.; Kim, U.-J.; Vunjak-Novakovic, G.; Min, B.-H.; Kaplan, D. L. Influence of Macroporous Protein Scaffolds on Bone Tissue Engineering from Bone Marrow Stem Cells. *Biomaterials* **2005**, *26* (21), 4442–4452.
- (176) WANG, Y.; BLASIOLI, D.; KIM, H.; KAPLAN, D. Cartilage Tissue Engineering with Silk Scaffolds and Human Articular Chondrocytes. *Biomaterials* **2006**, *27* (25), 4434–4442.
- (177) Yang, Y.; Ding, F.; Wu, J.; Hu, W.; Liu, W.; Liu, J.; Gu, X. Development and Evaluation of Silk Fibroin-Based Nerve Grafts Used for Peripheral Nerve Regeneration. *Biomaterials* **2007**, *28* (36), 5526–5535.
- (178) Madduri, S.; Papaloizos, M.; Gander, B. Trophically and Topographically Functionalized Silk Fibroin Nerve Conduits for Guided Peripheral Nerve Regeneration. *Biomaterials* **2010**, *31* (8), 2323–2334.
- (179) Ott, L. M.; Weatherly, R. A.; Detamore, M. S. Overview of Tracheal Tissue Engineering: Clinical Need Drives the Laboratory Approach. *Ann. Biomed. Eng.* **2011**, *39* (8), 2091–2113.
- (180) Nematollahi, Z.; Tafazzoli-Shadpour, M.; Zamanian, A.; Seyedsalehi, A.; Mohammad-Behgam, S.; Ghorbani, F.; Mirahmadi, F. Fabrication of Chitosan Silk-Based Tracheal Scaffold Using Freeze-Casting Method. *Iran. Biomed. J.* **2017**, *21* (4), 228.
- (181) Mandal, B. B.; Grinberg, A.; Gil, E. S.; Panilaitis, B.; Kaplan, D. L. High-Strength Silk Protein Scaffolds for Bone Repair. *Proc. Natl. Acad. Sci.* **2012**, *109* (20), 7699–7704.
- (182) Mandal, B. B.; Kundu, S. C. Cell Proliferation and Migration in Silk Fibroin 3D Scaffolds. *Biomaterials* **2009**, *30* (15), 2956–2965.
- (183) Meinel, L.; Fajardo, R.; Hofmann, S.; Langer, R.; Chen, J.; Snyder, B.; Vunjak-Novakovic, G.; Kaplan, D. Silk Implants for the Healing of Critical Size Bone Defects. *Bone* **2005**, *37* (5), 688–698.
- (184) Assender, H.; Bliznyuk, V.; Porfyakis, K. How Surface Topography Relates to Materials' Properties. *Science (80- )*. **2002**, *297* (5583), 973–976.
- (185) Kasemo, B. Biological Surface Science. *Surf. Sci.* **2002**, *500* (1–3), 656–677.
- (186) Xia, Y.; Whitesides, G. M. Soft Lithography. *Annu. Rev. Mater. Sci.* **1998**, *28* (1), 153–184.
- (187) Tsiolis, K.; Raja, W. K.; Pritchard, E. M.; Panilaitis, B.; Kaplan, D. L.; Omenetto, F. G. Fabrication of Silk Microneedles for Controlled-Release Drug Delivery. *Adv. Funct. Mater.* **2012**, *22* (2), 330–335.
- (188) Hines, D. R.; Siwak, N. P.; Mosher, L. A.; Ghodssi, R. MEMS Lithography and Micromachining Techniques BT - MEMS Materials and Processes Handbook; Ghodssi, R., Lin, P., Eds.; Springer US: Boston, MA, 2011; pp 667–753.
- (189) Shimanovich, U.; Ruggeri, F. S.; De Genst, E.; Adamcik, J.; Barros, T. P.; Porter, D.; Müller, T.; Mezzenga, R.; Dobson, C. M.; Vollrath, F.; et al. Silk Micrococoon for Protein Stabilisation and Molecular

- Encapsulation. *Nat. Commun.* **2017**, *8*, 15902.
- (190) Turunen, S.; Haaparanta, A.-M.; Aänismaa, R.; Kellomäki, M. *Chemical and Topographical Patterning of Hydrogels for Neural Cell Guidance in Vitro*; 2013; Vol. 7.
- (191) Kong, X. D.; Cui, F. Z.; Wang, X. M.; Zhang, M.; Zhang, W. Silk Fibroin Regulated Mineralization of Hydroxyapatite Nanocrystals. *J. Cryst. Growth* **2004**, *270* (1–2), 197–202.
- (192) Kurland, N. E.; Dey, T.; Wang, C.; Kundu, S. C.; Yadavalli, V. K. Silk Protein Lithography as a Route to Fabricate Sericin Microarchitectures. *Adv. Mater.* **2014**, *26* (26), 4431–4437.
- (193) Pal, R. K.; Kurland, N. E.; Wang, C.; Kundu, S. C.; Yadavalli, V. K. Biopatterning of Silk Proteins for Soft Micro-Optics. *ACS Appl. Mater. Interfaces* **2015**, *7* (16), 8809–8816.
- (194) Gattass, R. R.; Mazur, E. Femtosecond Laser Micromachining in Transparent Materials. *Nat. Photonics* **2008**, *2*, 219.
- (195) Marelli, B.; Patel, N.; Duggan, T.; Perotto, G.; Shirman, E.; Li, C.; Kaplan, D. L.; Omenetto, F. G. Programming Function into Mechanical Forms by Directed Assembly of Silk Bulk Materials. *Proc. Natl. Acad. Sci.* **2017**, *114* (3), 451 LP-456.
- (196) Zhuang, X.; Huang, W.; Yang, X.; Han, S.; Li, L.; Yu, J. Biocompatible/Degradable Silk Fibroin:Poly(Vinyl Alcohol)-Blended Dielectric Layer Towards High-Performance Organic Field-Effect Transistor. *Nanoscale Res. Lett.* **2016**, *11* (1), 439.
- (197) Serban, M. A.; Panilaitis, B.; Kaplan, D. L. Adhesives. **2012**, *98* (4), 567–575.
- (198) Chen, Y. Nanofabrication by Electron Beam Lithography and Its Applications: A Review. *Microelectron. Eng.* **2015**, *135*, 57–72.
- (199) Altissimo, M. E-Beam Lithography for Micro-/nanofabrication. *Biomicrofluidics* **2010**, *4* (2), 26503.
- (200) Krsko, P.; Sukhishvili, S.; Mansfield, M.; Clancy, R.; Libera, M. Electron-Beam Surface-Patterned Poly (Ethylene Glycol) Microhydrogels. *Langmuir* **2003**, *19* (14), 5618–5625.
- (201) Hoff, J. D.; Cheng, L.-J.; Meyhöfer, E.; Guo, L. J.; Hunt, A. J. Nanoscale Protein Patterning by Imprint Lithography. *Nano Lett.* **2004**, *4* (5), 853–857.
- (202) Qin, N.; Zhang, S.; Jiang, J.; Corder, S. G.; Qian, Z.; Zhou, Z.; Lee, W.; Liu, K.; Wang, X.; Li, X.; et al. Nanoscale Probing of Electron-Regulated Structural Transitions in Silk Proteins by near-Field IR Imaging and Nano-Spectroscopy. **2016**, *7*, 13079.
- (203) Kim, S.; Marelli, B.; Brenckle, M. A.; Mitropoulos, A. N.; Gil, E.-S.; Tsioris, K.; Tao, H.; Kaplan, D. L.; Omenetto, F. G. All-Water-Based Electron-Beam Lithography Using Silk as a Resist. *Nat Nano* **2014**, *9* (4), 306–310.
- (204) Greve, M. M.; Holst, B. Optimization of an Electron Beam Lithography Instrument for Fast, Large Area Writing at 10 KV Acceleration Voltage. *J. Vac. Sci. Technol. B, Nanotechnol. Microelectron. Mater. Process. Meas. Phenom.* **2013**, *31* (4), 043202.
- (205) Singh, M.; Haverinen, H. M.; Dhagat, P.; Jabbour, G. E. Inkjet Printing—process and Its Applications. *Adv. Mater.* **2010**, *22* (6), 673–685.
- (206) Calvert, P. Inkjet Printing for Materials and Devices. *Chem. Mater.* **2001**, *13* (10), 3299–3305.
- (207) Delaney, J. T.; Smith, P. J.; Schubert, U. S. Inkjet Printing of Proteins. *Soft Matter* **2009**, *5* (24), 4866.
- (208) Boland, T.; Xu, T.; Damon, B.; Cui, X. Application of Inkjet Printing to Tissue Engineering. *Biotechnol. J.* **2006**, *1* (9), 910–917.
- (209) Saunders, R. E.; Derby, B. Inkjet Printing Biomaterials for Tissue Engineering: Bioprinting. *Int. Mater. Rev.* **2014**, *59* (8), 430–448.
- (210) Xu, T.; Jin, J.; Gregory, C.; Hickman, J. J.; Boland, T. Inkjet Printing of Viable Mammalian Cells. *Biomaterials* **2005**, *26* (1), 93–99.
- (211) Saunders, R. E.; Gough, J. E.; Derby, B. Delivery of Human Fibroblast Cells by Piezoelectric Drop-on-Demand Inkjet Printing. *Biomaterials* **2008**, *29* (2), 193–203.
- (212) Nakano, K.; Oyanagi, T.; Fukumoto, H. Photocurable Ink Composition, Ink Cartridge, Inkjet Recording Method and Recorded Matter. Google Patents April 30, 2009.
- (213) Kaiser, E. T.; Kezdy, F. J. Secondary Structures of Proteins and Peptides in Amphiphilic Environments.(A Review). *Proc. Natl. Acad. Sci.* **1983**, *80* (4), 1137–1143.
- (214) Hu, T.; Benedetto, M.; Miaomiao, Y.; Bo, A.; Serdar, O. M.; A., R. J.; L., K. D.; G., O. F. Inkjet Printing of Regenerated Silk Fibroin: From Printable Forms to Printable Functions. *Adv. Mater.* **2015**, *27* (29), 4273–4279.
- (215) Wilson, D.; Valluzzi, R.; Kaplan, D. Conformational Transitions in Model Silk Peptides. *Biophys. J.* **2000**, *78* (5), 2690–2701.
- (216) Jin, H.-J.; Park, J.; Valluzzi, R.; Cebe, P.; Kaplan, D. L. Biomaterial Films of Bombyx Mori Silk Fibroin with Poly(Ethylene Oxide). *Biomacromolecules* **2004**, *5*, 711–717.

- (217) Scranton, A. B.; Bowman, C. N.; Meeting, A. C. S.; Peiffer, R. W.; Engineering, A. C. S. D. of P. M. S. and; Alec B. Scranton, Christopher N. Bowman, R. W. P.; Scranton, A. B.; Bowman, C. N.; Meeting, A. C. S.; Peiffer, R. W.; et al. *Photopolymerization: Fundamentals and Applications*, Volume 673.; ACS symposium series; American Chemical Society, 1997, 1997.
- (218) Miwa, M.; Juodkazis, S.; Kawakami, T.; Matsuo, S.; Misawa, H. Femtosecond Two-Photon Stereo-Lithography. *Appl. Phys. A* **2001**, *73* (5), 561–566.
- (219) Bandelier, P.; Charley, A.-L.; Lagrange, A. Photolithography. In *Lithography*; John Wiley & Sons, Inc., 2013; pp 1–40.
- (220) Pal, R. K.; Kurland, N. E.; Jiang, C.; Kundu, S. C.; Zhang, N.; Yadavalli, V. K. Fabrication of Precise Shape-Defined Particles of Silk Proteins Using Photolithography. *Eur. Polym. J.* **2016**, *85*, 421–430.
- (221) Lee, K.-N.; Shin, D.-S.; Chung, W.-J.; Kim, Y.-K.; Lee, Y.-S. Protein Patterning by Virtual Mask Photolithography Using Micromirror Array. In *2nd Annual International IEEE-EMBS Special Topic Conference on Microtechnologies in Medicine and Biology. Proceedings (Cat. No.02EX578)*; 2002; pp 136–139.
- (222) Decker, C.; Engineers, S. of M. *Ultraviolet Curing Chemistry: Past, Present and Future*; Creative manufacturing engineering program; Society of Manufacturing Engineers, 1987.
- (223) Elisseeff, J.; Anseth, K.; Sims, D.; McIntosh, W.; Randolph, M.; Langer, R. Transdermal Photopolymerization for Minimally Invasive Implantation. *Proc. Natl. Acad. Sci.* **1999**, *96* (6), 3104 LP-3107.
- (224) Hill-West, J. L.; Chowdhury, S. M.; Slepian, M. J.; Hubbell, J. A. Inhibition of Thrombosis and Intimal Thickening by in Situ Photopolymerization of Thin Hydrogel Barriers. *Proc. Natl. Acad. Sci.* **1994**, *91* (13), 5967 LP-5971.
- (225) Wollensak, G.; Wilsch, M.; Spoerl, E.; Seiler, T. Collagen Fiber Diameter in the Rabbit Cornea After Collagen Crosslinking by Riboflavin/UVA. *Cornea* **2004**, *23* (5).
- (226) Wollensak, G.; Spoerl, E.; Seiler, T. Riboflavin/Ultraviolet-A–induced Collagen Crosslinking for the Treatment of Keratoconus. *Am. J. Ophthalmol.* **2003**, *135* (5), 620–627.
- (227) Jeon, E. Y.; Hwang, B. H.; Yang, Y. J.; Kim, B. J.; Choi, B.-H.; Jung, G. Y.; Cha, H. J. Rapidly Light-Activated Surgical Protein Glue Inspired by Mussel Adhesion and Insect Structural Crosslinking. *Biomaterials* **2015**, *67*, 11–19.
- (228) de Gruijl, F. R.; van Kranen, H. J.; Mullenders, L. H. F. UV-Induced DNA Damage, Repair, Mutations and Oncogenic Pathways in Skin Cancer. *J. Photochem. Photobiol. B Biol.* **2001**, *63* (1), 19–27.
- (229) Sinha, R. P.; Häder, D.-P. UV-Induced DNA Damage and Repair: A Review. *Photochem. Photobiol. Sci.* **2002**, *1* (4), 225–236.
- (230) Zhou, D.; Ito, Y. Visible Light-Curable Polymers for Biomedical Applications. *Sci. China Chem.* **2014**, *57* (4), 510–521.
- (231) Jakubiak, J.; Rabek, J. F. Photoinitiators for Visible Light Polymerization. *Polimery* **1999**, *44* (7–8), 447–461.
- (232) Allen, N. S. Photoinitiators for UV and Visible Curing of Coatings: Mechanisms and Properties. *J. Photochem. Photobiol. A Chem.* **1996**, *100* (1–3), 101–107.
- (233) Fouassier, J.-P. *Photoinitiation, Photopolymerization, and Photocuring: Fundamentals and Applications*; Hanser, 1995.
- (234) Quentin, M.; Veronika, K.; P., F. B. Cationic Polymerization: From Photoinitiation to Photocontrol. *Angew. Chemie Int. Ed.* **2017**, *56* (33), 9670–9679.
- (235) Nguyen, K. T.; West, J. L. Photopolymerizable Hydrogels for Tissue Engineering Applications. **2002**, *23* (October 2001), 4307–4314.
- (236) Ifkovits, J. L.; Burdick, J. A. Photopolymerizable and Degradable Biomaterials for Tissue Engineering Applications. *Tissue Eng.* **2007**, *13* (10), 2369–2385.
- (237) Sawhney, A. S.; Pathak, C. P.; Hubbell, J. A. Bioerodible Hydrogels Based on Photopolymerized Poly (Ethylene Glycol)-Co-Poly (. Alpha.-Hydroxy Acid) Diacrylate Macromers. *Macromolecules* **1993**, *26* (4), 581–587.
- (238) Elisseeff, J.; McIntosh, W.; Anseth, K.; Riley, S.; Ragan, P.; Langer, R. Photoencapsulation of Chondrocytes in Poly (Ethylene Oxide)-based Semi-interpenetrating Networks. *J. Biomed. Mater. Res. An Off. J. Soc. Biomater. Japanese Soc. Biomater. Aust. Soc. Biomater. Korean Soc. Biomater.* **2000**, *51* (2), 164–171.
- (239) Kim, I.-S.; Jeong, Y.-I.; Kim, S.-H. Self-Assembled Hydrogel Nanoparticles Composed of Dextran and Poly (Ethylene Glycol) Macromer. *Int. J. Pharm.* **2000**, *205* (1–2), 109–116.
- (240) Muller, B. Photocrosslinked Polymers. Google Patents April 16, 1996.
- (241) Martens, P.; Anseth, K. S. Characterization of Hydrogels Formed from Acrylate Modified Poly (Vinyl

- Alcohol) Macromers. *Polymer (Guildf)*. **2000**, 41 (21), 7715–7722.
- (242) Matsuda, T.; Moghaddam, M. J.; Miwa, H.; Sakurai, K.; Iida, F. Photoinduced Prevention of Tissue Adhesion. *ASAIO J. (American Soc. Artif. Intern. Organs 1992)* **1992**, 38 (3), M154-7.
- (243) Bulpitt, P.; Aeschlimann, D. New Strategy for Chemical Modification of Hyaluronic Acid: Preparation of Functionalized Derivatives and Their Use in the Formation of Novel Biocompatible Hydrogels. *J. Biomed. Mater. Res.* **1999**, 47 (2), 152–169.
- (244) Kim, S.; Chu, C. Synthesis and Characterization of Dextran–methacrylate Hydrogels and Structural Study by SEM. *J. Biomed. Mater. Res. An Off. J. Soc. Biomater. Japanese Soc. Biomater.* **2000**, 49 (4), 517–527.
- (245) Kim, S.-H.; Chu, C.-C. In Vitro Release Behavior of Dextran-Methacrylate Hydrogels Using Doxorubicin and Other Model Compounds. *J. Biomater. Appl.* **2000**, 15 (1), 23–46.
- (246) Bryant, S. J.; Davis-Arehart, K. A.; Luo, N.; Shoemaker, R. K.; Arthur, J. A.; Anseth, K. S. Synthesis and Characterization of Photopolymerized Multifunctional Hydrogels: Water-Soluble Poly (Vinyl Alcohol) and Chondroitin Sulfate Macromers for Chondrocyte Encapsulation. *Macromolecules* **2004**, 37 (18), 6726–6733.
- (247) Schmedlen, R. H.; Masters, K. S.; West, J. L. Photocrosslinkable Polyvinyl Alcohol Hydrogels That Can Be Modified with Cell Adhesion Peptides for Use in Tissue Engineering. *Biomaterials* **2002**, 23 (22), 4325–4332.
- (248) Nuttelman, C. R.; Henry, S. M.; Anseth, K. S. Synthesis and Characterization of Photocrosslinkable, Degradable Poly (Vinyl Alcohol)-Based Tissue Engineering Scaffolds. *Biomaterials* **2002**, 23 (17), 3617–3626.
- (249) Alarcon, E. I.; Poblete, H.; Roh, H. G.; Couture, J. F.; Comer, J.; Kochevar, I. E. Rose Bengal Binding to Collagen and Tissue Photobonding. *ACS Omega* **2017**, 2 (10), 6646–6657.
- (250) Heo, J.; Koh, R. H.; Shim, W.; Kim, H. D.; Yim, H.-G.; Hwang, N. S. Riboflavin-Induced Photo-Crosslinking of Collagen Hydrogel and Its Application in Meniscus Tissue Engineering. *Drug Deliv. Transl. Res.* **2016**, 6 (2), 148–158.
- (251) Barbetta, A.; Massimi, M.; Conti Devirgiliis, L.; Dentini, M. Enzymatic Cross-Linking versus Radical Polymerization in the Preparation of Gelatin PolyHIPEs and Their Performance as Scaffolds in the Culture of Hepatocytes. *Biomacromolecules* **2006**, 7 (11), 3059–3068.
- (252) Yang, L.-J.; Lin, W.-Z.; Yao, T.-J.; Tai, Y.-C. Photo-Patternable Gelatin as Protection Layers in Low-Temperature Surface Micromachinings. *Sensors Actuators A Phys.* **2003**, 103 (1), 284–290.
- (253) Ovsianikov, A.; Deiwick, A.; Van Vlierberghe, S.; Dubruel, P.; Möller, L.; Dräger, G.; Chichkov, B. Laser Fabrication of Three-Dimensional CAD Scaffolds from Photosensitive Gelatin for Applications in Tissue Engineering. *Biomacromolecules* **2011**, 12 (4), 851–858.
- (254) Van Den Bulcke, A. I.; Bogdanov, B.; De Rooze, N.; Schacht, E. H.; Cornelissen, M.; Berghmans, H. Structural and Rheological Properties of Methacrylamide Modified Gelatin Hydrogels. *Biomacromolecules* **2000**, 1 (1), 31–38.
- (255) Brinkman, W. T.; Nagapudi, K.; Thomas, B. S.; Chaikof, E. L. Photo-Cross-Linking of Type I Collagen Gels in the Presence of Smooth Muscle Cells: Mechanical Properties, Cell Viability, and Function. *Biomacromolecules* **2003**, 4 (4), 890–895.
- (256) Baier Leach, J.; Bivens, K. A.; Patrick Jr, C. W.; Schmidt, C. E. Photocrosslinked Hyaluronic Acid Hydrogels: Natural, Biodegradable Tissue Engineering Scaffolds. *Biotechnol. Bioeng.* **2003**, 82 (5), 578–589.
- (257) Park, Y. D.; Tirelli, N.; Hubbell, J. A. Photopolymerized Hyaluronic Acid-Based Hydrogels and Interpenetrating Networks. *Biomaterials* **2003**, 24 (6), 893–900.
- (258) Smeds, K. A.; Pfister-Serres, A.; Hatchell, D. L.; GRINSTAFF, M. W. Synthesis of a Novel Polysaccharide Hydrogel. *J. Macromol. Sci. Appl. Chem.* **1999**, 36 (7–8), 981–989.
- (259) Zhang, Y.; Chu, C. Biodegradable Dextran–polylactide Hydrogel Networks: Their Swelling, Morphology and the Controlled Release of Indomethacin. *J. Biomed. Mater. Res. An Off. J. Soc. Biomater. Japanese Soc. Biomater. Aust. Soc. Biomater. Korean Soc. Biomater.* **2002**, 59 (2), 318–328.
- (260) Wang, W. *Instability, Stabilization, and Formulation of Liquid Protein Pharmaceuticals*; 1999; Vol. 185.
- (261) Jameela, S. R.; Lakshmi, S.; James, N. R.; Jayakrishnan, A. Preparation and Evaluation of Photocrosslinkable Chitosan as a Drug Delivery Matrix. *J. Appl. Polym. Sci.* **2002**, 86 (8), 1873–1877.
- (262) Ono, K.; Ishihara, M.; Ozeki, Y.; Deguchi, H.; Sato, M.; Saito, Y.; Yura, H.; Sato, M.; Kikuchi, M.; Kurita, A. Experimental Evaluation of Photocrosslinkable Chitosan as a Biologic Adhesive with Surgical Applications. *Surgery* **2001**, 130 (5), 844–850.
- (263) Sun, C.; Fang, N.; Wu, D. M.; Zhang, X. Projection Micro-Stereolithography Using Digital Micro-Mirror Dynamic Mask. *Sensors Actuators A Phys.* **2005**, 121 (1), 113–120.
- (264) Selimis, A.; Mironov, V.; Farsari, M. Direct Laser Writing: Principles and Materials for Scaffold 3D Printing.

- Microelectron. Eng.* **2015**, *132*, 83–89.
- (265) Pitts, J. D.; Howell, A. R.; Taboada, R.; Banerjee, I.; Wang, J.; Goodman, S. L.; Campagnola, P. J. New Photoactivators for Multiphoton Excited Three-dimensional Submicron Cross-linking of Proteins: Bovine Serum Albumin and Type 1 Collagen $\alpha$ 1(I). *Photochem. Photobiol.* **2002**, *76* (2), 135–144.
- (266) Kaehr, B.; Allen, R.; Javier, D. J.; Currie, J.; Shear, J. B. Guiding Neuronal Development with in Situ Microfabrication. *Proc. Natl. Acad. Sci. United States Am.* **2004**, *101* (46), 16104–16108.
- (267) Alarcón, E.; Edwards, A. M.; Aspée, A.; Borsarelli, C. D.; Lissi, E. A. Photophysics and Photochemistry of Rose Bengal Bound to Human Serum Albumin. *Photochem. Photobiol. Sci.* **2009**, *8* (7), 933.
- (268) Kurland, N. E.; Dey, T.; Kundu, S. C.; Yadavalli, V. K. Precise Patterning of Silk Microstructures Using Photolithography. *Adv. Mater.* **2013**, *25* (43), 6207–6212.
- (269) Liu, W.; Zhou, Z.; Zhang, S.; Shi, Z.; Tabarini, J.; Lee, W.; Zhang, Y.; Gilbert Corder, S. N.; Li, X.; Dong, F.; et al. Precise Protein Photolithography (P3): High Performance Biopatterning Using Silk Fibroin Light Chain as the Resist. *Adv. Sci.* **2017**, *4* (9), 1700191–n/a.
- (270) Sun, Y.-L.; Li, Q.; Sun, S.-M.; Huang, J.-C.; Zheng, B.-Y.; Chen, Q.-D.; Shao, Z.-Z.; Sun, H.-B. Aqueous Multiphoton Lithography with Multifunctional Silk-Centred Bio-Resists. *Nat. Commun.* **2015**, *6*.
- (271) Dickerson, M. B.; Dennis, P. B.; Tondiglia, V. P.; Nadeau, L. J.; Singh, K. M.; Drummy, L. F.; Partlow, B. P.; Brown, D. P.; Omenetto, F. G.; Kaplan, D. L.; et al. 3D Printing of Regenerated Silk Fibroin and Antibody-Containing Microstructures via Multiphoton Lithography. *ACS Biomater. Sci. Eng.* **2017**, *3* (9), 2064–2075.
- (272) Malinauskas, M.; Farsari, M.; Piskarskas, A. Ultrafast Laser Nanostructuring of Photopolymers : A Decade of Advances. *Phys. Rep.* **2013**, *533* (1), 1–31.
- (273) Whittaker, J. L.; Choudhury, N. R.; Dutta, N. K.; Zannettino, A. Facile and Rapid Ruthenium Mediated Photo-Crosslinking of Bombyx Mori Silk Fibroin. *J. Mater. Chem. B* **2014**, *2* (37), 6259–6270.
- (274) Park, J.; Lee, S.-G.; Marelli, B.; Lee, M.; Kim, T.; Oh, H.-K.; Jeon, H.; Omenetto, F. G.; Kim, S. Eco-Friendly Photolithography Using Water-Developable Pure Silk Fibroin. *RSC Adv.* **2016**, *6* (45), 39330–39334.
- (275) Wang, S. D.; Zhang, K. Q. Electrogelation and Rapid Prototyping of Bombyx Mori Silk Fibroin. *Mater. Lett.* **2016**, *169*, 5–9.
- (276) Maximova, K.; Wang, X.; Balčytis, A.; Fan, L.; Li, J.; Juodkakis, S. Silk Patterns Made by Direct Femtosecond Laser Writing. *Biomicrofluidics* **2016**, *10* (5).
- (277) Zhou, Y.; Liang, K.; Zhao, S.; Zhang, C.; Li, J.; Yang, H.; Liu, X.; Yin, X.; Chen, D.; Xu, W.; et al. Photopolymerized Maleilated Chitosan/Methacrylated Silk Fibroin Micro/Nanocomposite Hydrogels as Potential Scaffolds for Cartilage Tissue Engineering. *Int. J. Biol. Macromol.* **2018**, *108*, 383–390.
- (278) Costantini, M.; Barbetta, A. 6 - Gas Foaming Technologies for 3D Scaffold Engineering BT - Functional 3D Tissue Engineering Scaffolds; Woodhead Publishing, 2018; pp 127–149.
- (279) Li, M.; Wu, Z.; Zhang, C.; Lu, S.; Yan, H.; Huang, D.; Ye, H. Study on Porous Silk Fibroin Materials. II. Preparation and Characteristics of Spongy Porous Silk Fibroin Materials. *J. Appl. Polym. Sci.* **2001**, *79* (12), 2192–2199.
- (280) Lv, Q.; Feng, Q. Preparation of 3-D Regenerated Fibroin Scaffolds with Freeze Drying Method and Freeze Drying/Foaming Technique. *J. Mater. Sci. Mater. Med.* **2006**, *17*, 1349–1356.
- (281) Tamada, Y. New Process to Form a Silk Fibroin Porous 3-D Structure. *Biomacromolecules* **2005**, *6* (6), 3100–3106.
- (282) Cameron, N. R.; Sherrington, D. C. High Internal Phase Emulsions (HIPEs)—structure, Properties and Use in Polymer Preparation. In *Biopolymers liquid crystalline polymers phase emulsion*; Springer, 1996; pp 163–214.
- (283) Barbetta, A.; Carnachan, R. J.; Smith, K. H.; Zhao, C. T.; Cameron, N. R.; Katakly, R.; Hayman, M.; Przyborski, S. A.; Swan, M. Porous Polymers by Emulsion Templating. *Macromol. Symp.* **2005**, *226*, 203–211.
- (284) Silverstein, M. S. PolyHIPEs: Recent Advances in Emulsion-Templated Porous Polymers. *Prog. Polym. Sci.* **2014**, *39* (1), 199–234.
- (285) Holland, C. Silk Rheology Thesis. **2008**.
- (286) Madsen, B.; Vollrath, F. Mechanics and Morphology of Silk Drawn from Anesthetized Spiders. *Naturwissenschaften* **2000**, *87* (3), 148–153.
- (287) Pérez-Rigueiro, J.; Elices, M.; Plaza, G. R.; Real, J. I.; Guinea, G. V. The Influence of Anaesthesia on the Tensile Properties of Spider Silk. *J. Exp. Biol.* **2006**, *209* (2), 320 LP-326.
- (288) Lee, Y.-H.; Lee, H.-Y.; Kim, H. R. Purification and Characterization of Epidermis-Origin Hemolymph Protein in *Galleria Mellonella*. *Comp. Biochem. Physiol. Part A Mol. Integr. Physiol.* **2000**, *125* (1), 95–104.
- (289) Knight, D. P.; Vollrath, F. Changes in Element Composition along the Spinning Duct in a *Nephila* Spider.

- Naturwissenschaften* **2001**, *88*, 179–182.
- (290) Israelachvili, J. The Different Faces of Poly(Ethylene Glycol). *Proc. Natl. Acad. Sci.* **1997**, *94* (16), 8378–8379.
- (291) Janmey, P. A.; Georges, P. C.; Hvidt, S. B. T.-M. in C. B. Basic Rheology for Biologists. In *Cell Mechanics*; Academic Press, 2007; Vol. 83, pp 1–27.
- (292) Storm, C.; Pastore, J. J.; MacKintosh, F. C.; Lubensky, T. C.; Janmey, P. A. Nonlinear Elasticity in Biological Gels. *Nature* **2005**, *435*, 191.
- (293) Michelson, A. A.; Morley, E. W. On the Relative Motion of the Earth and of the Luminiferous Ether. *Sidereal Messenger*, vol. 6, pp. 306-310 **1887**, *6*, 306–310.
- (294) Boulet-Audet, M.; Lefèvre, T.; Buffeteau, T.; Pézolet, M. Attenuated Total Reflection Infrared Spectroscopy: An Efficient Technique to Quantitatively Determine the Orientation and Conformation of Proteins in Single Silk Fibers. *Appl. Spectrosc.* **2008**, *62* (9), 956–962.
- (295) Boulet-Audet, M. Why and How Is Silk Spun? Integrating Rheology with Advanced Spectroscopic Techniques. **2013**, 330.
- (296) Boulet-Audet, M.; Vollrath, F.; Holland, C. Identification and Classification of Silks Using Infrared Spectroscopy. *J. Exp. Biol.* **2015**, *218* (19), 3138–3149.
- (297) Hull, C. W. Apparatus for Production of Three-Dimensional Objects by Stereolithography. Google Patents March 11, 1986.
- (298) Jacobs, P. F. *Stereolithography and Other RP&M Technologies: From Rapid Prototyping to Rapid Tooling*; Society of Manufacturing Engineers, 1995.
- (299) Jacobs, P. F. *Rapid Prototyping & Manufacturing: Fundamentals of Stereolithography*; Society of Manufacturing Engineers, 1992.
- (300) Zhang, X.; Jiang, X. N.; Sun, C. Micro-Stereolithography of Polymeric and Ceramic Microstructures. *Sensors Actuators A Phys.* **1999**, *77* (2), 149–156.
- (301) Shen, Y.-R. The Principles of Nonlinear Optics. *New York, Wiley-Interscience, 1984, 575 p.* **1984**.
- (302) Allen, N. S. *Photopolymerisation and Photoimaging Science and Technology*; Springer, 1989.
- (303) Correa, D. S.; Almeida, J. M. P.; Almeida, G. F. B.; Cardoso, M. R.; Boni, L. De; Mendonça, C. R. Ultrafast Laser Pulses for Structuring Materials at Micro / Nano Scale : From Waveguides to Superhydrophobic Surfaces. **2017**.
- (304) Farsari, S. T. and E. K. and K. T. and J. V. and C. F. and M. K. and M. Pico- and Femtosecond Laser-Induced Crosslinking of Protein Microstructures: Evaluation of Processability and Bioactivity. *Biofabrication* **2011**, *3* (4), 45002.
- (305) Waldner, J. C.; Lahr, S. J.; Edgell, M. H.; Pielak, G. J. Nonideality and Protein Thermal Denaturation. *Biopolymers* **1999**, *49* (1999), 471–479.
- (306) Melchels, F. P. W.; Feijen, J.; Grijpma, D. W. A Review on Stereolithography and Its Applications in Biomedical Engineering. *Biomaterials* **2010**, *31* (24), 6121–6130.
- (307) Lee, K.-S.; Kim, R. H.; Yang, D.-Y.; Park, S. H. Advances in 3D Nano/Microfabrication Using Two-Photon Initiated Polymerization. *Prog. Polym. Sci.* **2008**, *33* (6), 631–681.
- (308) Serbin, J.; Egbert, A.; Ostendorf, A.; Chichkov, B. N.; Houbertz, R.; Domann, G.; Schulz, J.; Cronauer, C.; Fröhlich, L.; Popall, M. Femtosecond Laser-Induced Two-Photon Polymerization of Inorganic–organic Hybrid Materials for Applications in Photonics. *Opt. Lett.* **2003**, *28* (5), 301–303.
- (309) Chichkov, B. N.; Ostendorf, A. Two-Photon Polymerization: A New Approach to Micromachining. *Photonics Spectra* **2006**, *40* (October), 72–79.
- (310) Bártolo, P. J. *Stereolithography: Materials, Processes and Applications*; SpringerLink : Bücher; Springer US, 2011.
- (311) Chrisey, J. Y. and Y. H. and D. B. Laser-Assisted Printing of Alginate Long Tubes and Annular Constructs. *Biofabrication* **2013**, *5* (1), 15002.
- (312) Kaehr, B.; Ertaş, N.; Nielson, R.; Allen, R.; Hill, R. T.; Plenert, M.; Shear, J. B. Direct-Write Fabrication of Functional Protein Matrixes Using a Low-Cost Q-Switched Laser. *Anal. Chem.* **2006**, *78* (9), 3198–3202.
- (313) Sun, Y.-L.; Dong, W.-F.; Niu, L.-G.; Jiang, T.; Liu, D.-X.; Zhang, L.; Wang, Y.-S.; Chen, Q.-D.; Kim, D.-P.; Sun, H.-B. Protein-Based Soft Micro-Optics Fabricated by Femtosecond Laser Direct Writing. *Light Sci. & Appl.* **2014**, *3*, e129.
- (314) Murphy, S. V; Atala, A. 3D Bioprinting of Tissues and Organs. *Nat Biotech* **2014**, *32* (8), 773–785.
- (315) Parker, S. T.; Domachuk, P.; Amsden, J.; Bressner, J.; Lewis, J. A.; Kaplan, D. L.; Omenetto, F. G. Biocompatible Silk Printed Optical Waveguides. *Adv. Mater.* **2009**, *21* (23), 2411–2415.
- (316) Pitts, J. D.; Campagnola, P. J.; Epling, G. A.; Goodman, S. L. Submicron Multiphoton Free-Form Fabrication of Proteins and Polymers: Studies of Reaction Efficiencies and Applications in Sustained Release.



- Macromolecules* **2000**, *33* (5), 1514–1523.
- (317) Su, P.-J.; Tran, Q. A.; Fong, J. J.; Eliceiri, K. W.; Ogle, B. M.; Campagnola, P. J. Mesenchymal Stem Cell Interactions with 3D ECM Modules Fabricated via Multiphoton Excited Photochemistry. *Biomacromolecules* **2012**, *13* (9), 2917–2925.
- (318) Chen, X.; Su, Y.-D.; Ajeti, V.; Chen, S.-J.; Campagnola, P. J. Cell Adhesion on Micro-Structured Fibronectin Gradients Fabricated by Multiphoton Excited Photochemistry. *Cell. Mol. Bioeng.* **2012**, *5* (3), 307–319.
- (319) Basu, S.; Cunningham, L. P.; Pins, G. D.; Bush, K. A.; Taboada, R.; Howell, A. R.; Wang, J.; Campagnola, P. J. Multiphoton Excited Fabrication of Collagen Matrixes Cross-Linked by a Modified Benzophenone Dimer: Bioactivity and Enzymatic Degradation. *Biomacromolecules* **2005**, *6* (3), 1465–1474.
- (320) Basu, S.; Wolgemuth, C. W.; Campagnola, P. J. Measurement of Normal and Anomalous Diffusion of Dyes within Protein Structures Fabricated via Multiphoton Excited Cross-Linking. *Biomacromolecules* **2004**, *5* (6), 2347–2357.
- (321) Basu, S.; Campagnola, P. J. Properties of Crosslinked Protein Matrices for Tissue Engineering Applications Synthesized by Multiphoton Excitation. *J. Biomed. Mater. Res. Part A* **2004**, *71A* (2), 359–368.
- (322) Zhan, X.; Xu, H.; Sun, H. Femtosecond Laser Processing of Microcavity Lasers. *Front. Optoelectron.* **2016**, *9* (3), 420–427.
- (323) MacDonald, P. F. and A. M. and L. P. and C. T. A. B. and W. S. and K. D. and M. P. Two-Photon Ablation with 1278 Nm Laser Radiation. *J. Opt. A Pure Appl. Opt.* **2007**, *9* (6), S19.
- (324) Danilevicius, P.; Rekštyte, S.; Gadonas, R.; Malinauskas, M.; Balciunas, E.; Jarasiene, R.; Baltriukiene, D.; Bukelskiene, V.; Kraniauskas, A.; Sirmenis, R. Micro-Structured Polymer Scaffolds Fabricated by Direct Laser Writing for Tissue Engineering. **2012**, *17*, 81405–81408.
- (325) Applegate, M. B.; Marelli, B.; Kaplan, D. L.; Omenetto, F. G. Determination of Multiphoton Absorption of Silk Fibroin Using the Z-Scan Technique. *Opt. Express* **2013**, *21* (24), 29637–29642.
- (326) Hawkins, C. L.; Davies, M. J. Generation and Propagation of Radical Reactions on Proteins. *Biochim. Biophys. Acta - Bioenerg.* **2001**, *1504*, 196–219.
- (327) Tilley, K. a.; Benjamin, R. E.; Bagorogoza, K. E.; Okot-Kotber, B. M.; Prakash, O.; Kwena, H. Tyrosine Cross-Links: Molecular Basis of Gluten Structure and Function. *J. Agric. Food Chem.* **2001**, *49*, 2627–2632.
- (328) Sundarar Krishnan, A.; Herrero Acero, E.; Coburn, J.; Chwalek, K.; Partlow, B.; Kaplan, D. L. Phenol Red-Silk Tyrosine Cross-Linked Hydrogels. *Acta Biomater.* **2016**, *42*, 102–113.
- (329) Holland, C.; Urbach, J. S.; Blair, D. L. Direct Visualization of Shear Dependent Silk Fibrillogenesis. *Soft Matter* **2012**, *8* (9), 2590–2594.
- (330) Ayub, Z. H.; Hirabayashi, K.; Arai, M. EFFECT OF PH ON SILK FIBROIN GELATION. *Sen'i Gakkaishi* **1992**, *48* (3), 141–144.
- (331) Hu, X.; Shmelev, K.; Sun, L.; Gil, E.-S.; Park, S.-H.; Cebe, P.; Kaplan, D. L. Regulation of Silk Material Structure by Temperature-Controlled Water Vapor Annealing. *Biomacromolecules* **2011**, *12* (5), 1686–1696.
- (332) Askarieh, G.; Hedhammar, M.; Nordling, K.; Saenz, A.; Casals, C.; Rising, A.; Johansson, J.; Knight, S. D. Self-Assembly of Spider Silk Proteins Is Controlled by a PH-Sensitive Relay. *Nature* **2010**, *465* (7295), 236–238.
- (333) Marmion, D. M. *Handbook of US Colorants: Foods, Drugs, Cosmetics, and Medical Devices*; John Wiley & Sons, 1991.
- (334) Doughty, M. J. Rose Bengal Staining as an Assessment of Ocular Surface Damage and Recovery in Dry Eye Disease-A Review. *Contact Lens Anterior Eye* **2013**, *36* (6), 272–280.
- (335) Ginimuge, P. R.; Jyothi, S. D. Methylene Blue: Revisited. *J. Anaesthesiol. Clin. Pharmacol.* **2010**, *26* (4), 517–520.
- (336) Byth, H.-A.; Mchunu, B. I.; Dubery, I. A.; Bornman, L. Assessment of a Simple, Non-Toxic Alamar Blue Cell Survival Assay to Monitor Tomato Cell Viability. *Phytochem. Anal.* **2001**, *12* (5), 340–346.
- (337) Larson, E. M.; Doughman, D. J.; Gregerson, D. S.; Obritsch, W. F. A New, Simple, Nonradioactive, Nontoxic in Vitro Assay to Monitor Corneal Endothelial Cell Viability. *Invest. Ophthalmol. Vis. Sci.* **1997**, *38* (10), 1929–1933.
- (338) Shiloh, M. U.; Ruan, J.; Nathan, C. Evaluation of Bacterial Survival and Phagocyte Function with a Fluorescence-Based Microplate Assay. *Infect. Immun.* **1997**, *65* (8), 3193–3198.
- (339) van Tonder, A.; Joubert, A. M.; Cromarty, A. D. Limitations of the 3-(4,5-Dimethylthiazol-2-Yl)-2,5-Diphenyl-2H-Tetrazolium Bromide (MTT) Assay When Compared to Three Commonly Used Cell Enumeration Assays. *BMC Res. Notes* **2015**, *8*, 47.
- (340) Sylvester, P. W. Optimization of the Tetrazolium Dye (MTT) Colorimetric Assay for Cellular Growth and Viability BT - Drug Design and Discovery: Methods and Protocols; Satyanarayanajois, S. D., Ed.; Humana

- Press: Totowa, NJ, NJ, 2011; pp 157–168.
- (341) Edmondson, J. M.; Armstrong, L. S.; Martinez, A. O. A Rapid and Simple MTT-Based Spectrophotometric Assay for Determining Drug Sensitivity in Monolayer Cultures. *J. tissue Cult. methods* **1988**, *11* (1), 15–17.
- (342) Johnson, D. W.; Sherborne, C.; Didsbury, M. P.; Pateman, C.; Cameron, N. R.; Claeysens, F. Macrostructuring of Emulsion-Templated Porous Polymers by 3D Laser Patterning. *Adv. Mater.* **2013**, *25* (23), 3178–3181.
- (343) Pateman, C. J.; Harding, A. J.; Glen, A.; Taylor, C. S.; Christmas, C. R.; Robinson, P. P.; Rimmer, S.; Boissonade, F. M.; Claeysens, F.; Haycock, J. W. Nerve Guides Manufactured from Photocurable Polymers to Aid Peripheral Nerve Repair. *Biomaterials* **2015**, *49*, 77–89.
- (344) Soeken, T. A.; Zhu, H.; DeMartelaere, S.; Davies, B. W.; Kim, M.; Wang, H.-C.; Aden, J.; Grimm, R.; Alt, C.; Kochevar, I. E.; et al. Sealing of Corneal Lacerations Using Photoactivated Rose Bengal Dye and Amniotic Membrane. *Cornea* **2018**, *37* (2).
- (345) Cherfan, D.; Verter, E. E.; Melki, S.; Gisel, T. E.; Doyle, F. J.; Scarcelli, G.; Yun, S. H.; Redmond, R. W.; Kochevar, I. E. Collagen Cross-Linking Using Rose Bengal and Green Light to Increase Corneal Stiffness. *Invest. Ophthalmol. Vis. Sci.* **2013**, *54* (5), 3426–3433.
- (346) Halliday, D.; Resnick, R.; Walker, J. *Fundamentals of Physics, Chapters 33-37*; John Wiley & Sons, 2010.
- (347) Pope, R. M.; Fry, E. S. Absorption Spectrum (380–700 Nm) of Pure Water. II. Integrating Cavity Measurements. *Appl. Opt.* **1997**, *36* (33), 8710–8723.
- (348) Ludvikova, L.; Fris, P.; Heger, D.; Sebej, P.; Wirz, J.; Klan, P. Photochemistry of Rose Bengal in Water and Acetonitrile: A Comprehensive Kinetic Analysis. *Phys. Chem. Chem. Phys.* **2016**, *18* (24), 16266–16273.
- (349) DSC-Curves-of-Collagen-05-SF-1-and-SF-Collagen-Blend-with-Ratio-of-50-50.
- (350) Savu, I. D.; Savu, S. V.; Sirbu, N. A. Heat Affected Zones in Polymer Laser Marking. *J. Therm. Anal. Calorim.* **2014**, *115* (2), 1427–1437.
- (351) Rabal, H. J.; Braga Jr, R. A. *Dynamic Laser Speckle and Applications*; CRC Press, 2008.
- (352) Sigel, R.; Fytas, G.; Vainos, N.; Pispas, S.; Hadjichristidis, N. Pattern Formation in Homogeneous Polymer Solutions Induced by a Continuous Wave Visible Laser. *Science (80-. )*. **2002**, *297* (July), 66.
- (353) Zhang, P.; Aso, Y.; Yamamoto, K.; Banno, Y.; Wang, Y.; Tsuchida, K.; Kawaguchi, Y.; Fujii, H. Proteome Analysis of Silk Gland Proteins from the Silkworm, Bombyx Mori. *Proteomics* **2006**, *6* (8), 2586–2599.
- (354) Lee, J.-M.; Yu, J.-E.; Koh, Y.-S. Experimental Study on the Effect of Wavelength in the Laser Cleaning of Silver Threads. *J. Cult. Herit.* **2003**, *4*, 157–161.
- (355) Le Harzic, R.; Huot, N.; Audouard, E.; Jonin, C.; Laporte, P.; Valette, S.; Fraczkiewicz, A.; Fortunier, R. Comparison of Heat-Affected Zones Due to Nanosecond and Femtosecond Laser Pulses Using Transmission Electronic Microscopy. *Appl. Phys. Lett.* **2002**, *80* (21), 3886–3888.
- (356) Griffin, B. J. A Comparison of Conventional Everhart-Thornley Style and in-Lens Secondary Electron Detectors—a Further Variable in Scanning Electron Microscopy. *Scanning* **2011**, *33* (3), 162–173.
- (357) Peng, Q.; Shao, H.; Hu, X.; Zhang, Y. Role of Humidity on the Structures and Properties of Regenerated Silk Fibers. *Prog. Nat. Sci. Mater. Int.* **2015**, *25* (5), 430–436.
- (358) Wan, Q.; Abrams, K. J.; Masters, R. C.; Talari, A. C. S.; Rehman, I. U.; Claeysens, F.; Holland, C.; Rodenburg, C. Mapping Nanostructural Variations in Silk by Secondary Electron Hyperspectral Imaging. *Adv. Mater.* **2017**, *29* (47), 1703510.
- (359) Prasong, S.; Yaowalak, S.; Wilaiwan, S. Characteristics of Silk Fiber with and without Sericin Component: A Comparison between Bombyx Mori and Philosamia Ricini Silks. *Pakistan J. Biol. Sci.* **2009**, *12* (11), 872.
- (360) Gabriel, B. L. SEM: A User's Manual for Materials Science. **1985**.
- (361) Yoshioka, T.; Hata, T.; Kojima, K.; Nakazawa, Y.; Kameda, T. Fabrication Scheme for Obtaining Transparent, Flexible, and Water-Insoluble Silk Films from Apparently Dissolved Silk-Gland Fibroin of Bombyx Mori Silkworm. *ACS Biomater. Sci. Eng.* **2017**, *3* (12), 3207–3214.
- (362) Tao, H.; Kainerstorfer, J. M.; Siebert, S. M.; Pritchard, E. M.; Sassaroli, A.; Panilaitis, B. J. B.; Brenckle, M. A.; Amsden, J. J.; Levitt, J.; Fantini, S.; et al. Implantable, Multifunctional, Bioresorbable Optics. *Proc. Natl. Acad. Sci.* **2012**, *109* (48), 19584–19589.
- (363) Zarbin, M. A. Accelerated in Vitro Degradation of Optically Clear Low-Beta Sheet Silk Films by Enzyme-Mediated Pretreatment. *JAMA Ophthalmol.* **2013**, *131* (5), 676.
- (364) Mark, J. E. *Physical Properties of Polymers Handbook*; Springer, 2007; Vol. 1076.
- (365) Ewald, Melanie; Sindlinger, Julia; LeBlanc, Alexander Fabian; Proll, Günther; Gauglitz, G. Reflektometrische Interferenzspektroskopie. **2010**, No. May, 1–4.
- (366) Baimark, Y.; Srihanam, P. Effect of Methanol Treatment on Regenerated Silk Fibroin Microparticles Prepared by the Emulsification-Diffusion Technique. *J. Appl. Sci.* **2009**, *9* (21), 3876–3881.

- (367) Streltsov, A. M.; Borrelli, N. F. Study of Femtosecond-Laser-Written Waveguides in Glasses. *JOSA B* **2002**, *19* (10), 2496–2504.
- (368) Kato, Y.; Uchida, K.; Kawakishi, S. AGGREGATION OF COLLAGEN EXPOSED TO UVA IN THE PRESENCE OF RIBOFLAVIN: A PLAUSIBLE ROLE OF TYROSINE MODIFICATION. *Photochem. Photobiol.* **1994**, *59* (3), 343–349.
- (369) Mita, K.; Ichimura, S.; James, T. C. Highly Repetitive Structure and Its Organization of the Silk Fibroin Gene. *J. Mol. Evol.* **1994**, *38* (6), 583–592.
- (370) Wollensak, G.; Spoerl, E. *Collagen Crosslinking of Human and Porcine Sclera*; 2004; Vol. 30.
- (371) Armstrong, S. J.; Wiberg, M.; Terenghi, G.; Kingham, P. J. ECM Molecules Mediate Both Schwann Cell Proliferation and Activation to Enhance Neurite Outgrowth. *Tissue Eng.* **2007**, *13* (12), 2863–2870.
- (372) Bell, J. H. A.; Haycock, J. W. Next Generation Nerve Guides: Materials, Fabrication, Growth Factors, and Cell Delivery. *Tissue Eng. Part B Rev.* **2011**, *18* (2), 116–128.
- (373) Tojima, T.; Yamane, Y.; Takahashi, M.; Ito, E. Acquisition of Neuronal Proteins during Differentiation of NG108-15 Cells. *Neurosci. Res.* **2000**, *37* (2), 153–161.
- (374) RG, F.; SG, T.; Feenstra, R. P. .; Tseng, S. C. . What Is Actually Stained by Rose Bengal. *Acta Ophthalmol.* **1992**, *110* (7), 984–993.
- (375) Lee, YC; Park, CK; Kim, MS; Kim, J. InVitro Study for Staining and Toxicity of Rb on Bovine Corneal Endothelial Cells. *Cornea*. 1996, pp 376–385.
- (376) Linden, S. M.; Neckers, D. C. Type I and Type II Sensitizers Based on Rose Bengal Onium Salts. *Photochem. Photobiol.* **1988**, *47* (4), 543–550.
- (377) Sebrão, C. C. N.; Junior, A. G. B.; de França, P. H. C.; Ferreira, L. E.; Westphalen, V. P. D. Comparison of the Efficiency of Rose Bengal and Methylene Blue as Photosensitizers in Photodynamic Therapy Techniques Aiming at Enterococcus Faecalis Inactivation. *Photodiagnosis Photodyn. Ther.* **2015**, *12* (3), 355.
- (378) Zhang, S.; Huang, F.; Gates, M.; Holmberg, E. G. Role of Endogenous Schwann Cells in Tissue Repair after Spinal Cord Injury. *Neural Regen. Res.* **2013**, *8* (2), 177–185.
- (379) Manthorpe, M.; Engvall, E.; Ruoslahti, E.; Longo, F. M.; Davis, G. E.; Varon, S. Laminin Promotes Neuritic Regeneration from Cultured Peripheral and Central Neurons. *J. Cell Biol.* **1983**, *97* (6), 1882–1890.
- (380) Tse, C. C. W.; Ng, S. S.; Stringer, J.; MacNeil, S.; Haycock, J. W.; Smith, P. J. Utilising Inkjet Printed Paraffin Wax for Cell Patterning Applications. *Int. J. Bioprinting* **2016**, *2* (0).
- (381) Smith, L. E.; Smallwood, R.; Macneil, S. A Comparison of Imaging Methodologies for 3D Tissue Engineering. *Microsc. Res. Tech.* **2010**, *73* (12), 1123–1133.
- (382) Patil, N.; Truong, V.; Holmberg, M. H.; Stoflet, N. D.; McCoy, M. R.; Dutton, J. R.; Holmberg, E. G.; Parr, A. M. Safety and Efficacy of Rose Bengal Derivatives for Glial Scar Ablation in Chronic Spinal Cord Injury. *J. Neurotrauma* **2018**.
- (383) Van Reempts, J.; Van Deuren, B.; Ashton, D.; Borgers, M. A New Model of Photochemically Induced Acute and Reversible Demyelination in the Peripheral Nervous System. *Experimental Neurology*. 1993, pp 283–290.
- (384) Zhang, S.; Kluge, B.; Huang, F.; Nordstrom, T.; Doolen, S.; Gross, M.; Sarmiere, P.; Holmberg, E. G. Photochemical Scar Ablation in Chronically Contused Spinal Cord of Rat. *J. Neurotrauma* **2007**, *24* (2), 411–420.
- (385) BRAY, D. *Cell Movements From Molecules to Motilit*; Taylor & Francis Group.
- (386) Caliarì, S. R.; Burdick, J. A. A Practical Guide to Hydrogels for Cell Culture. *Nat. Methods* **2016**, *13* (5), 405–414.
- (387) Pang, S.; Fiume, M. Z. Final Report on the Safety Assessment of Ammonium, Potassium, and Sodium Persulfate. *Int. J. Toxicol.* **2001**, *20*, 7–21.
- (388) Song, C.; Wang, L.; Ye, G.; Song, X.; He, Y.; Qiu, X. Residual Ammonium Persulfate in Nanoparticles Has Cytotoxic Effects on Cells through Epithelial-Mesenchymal Transition. *Sci. Rep.* **2017**, *7* (1), 1–12.
- (389) Elvin, C. M.; Vuocolo, T.; Brownlee, A. G.; Sando, L.; Huson, M. G.; Liyou, N. E.; Stockwell, P. R.; Lyons, R. E.; Kim, M.; Edwards, G. A.; et al. A Highly Elastic Tissue Sealant Based on Photopolymerised Gelatin. *Biomaterials* **2010**, *31* (32), 8323–8331.
- (390) Sgambellone, M. A.; David, A.; Garner, R. N.; Dunbar, K. R.; Turro, C. Cellular Toxicity Induced by the Photorelease of a Caged Bioactive Molecule: Design of a Potential Dual-Action Ru (II) Complex. *J. Am. Chem. Soc.* **2013**, *135* (30), 11274–11282.
- (391) Fox, S. I. *Human Physiology 9th Editon*; McGraw-Hill press, New York, USA, 2006.
- (392) Shimanovich, U.; Pinotsi, D.; Shimanovich, K.; Yu, N.; Bolisetty, S.; Adamcik, J.; Mezzenga, R.; Charmet, J.; Vollrath, F.; Gazit, E.; et al. Biophotonics of Native Silk Fibrils. *Macromol. Biosci.* n/a-n/a.

- (393) Kim, S.; Mitropoulos, A. N.; Spitzberg, J. D.; Tao, H.; Kaplan, D. L.; Omenetto, F. G. Silk Inverse Opals. *Nat Phot.* **2012**, *6* (12), 818–823.
- (394) Galeotti, F.; Andicsová, A.; Yunus, S.; Botta, C. *Precise Surface Patterning of Silk Fibroin Films by Breath Figures*; 2012; Vol. 8.
- (395) Amsden, J. J.; Domachuk, P.; Gopinath, A.; White, R. D.; Negro, L. D.; Kaplan, D. L.; Omenetto, F. G. Rapid Nanoimprinting of Silk Fibroin Films for Biophotonic Applications. *Adv. Mater.* **2010**, *22* (15), 1746–1749.
- (396) Ramendra, K. P.; Ahmed, A. F.; Maryanne, M. C.; Subhas, C. K.; Vamsi, K. Y. Photolithographic Micropatterning of Conducting Polymers on Flexible Silk Matrices. *Adv. Mater.* **2015**, *28* (7), 1406–1412.
- (397) Wray LS, Rnjak-Kovacina J, Mandal BB, Schmidt DF, Gil ES, K. D. A Silk-Based Scaffold Platform with Tunable Architecture for Engineering Critically-Sized Tissue Constructs. *Biomaterials* **2012**, *33* (36), 9214–9224.
- (398) Lee, M. P.; Cooper, G. J. T.; Hinkley, T.; Gibson, G. M.; Padgett, M. J.; Cronin, L. Development of a 3D Printer Using Scanning Projection Stereolithography. *Sci. Rep.* **2015**, *5*.
- (399) Pan, Y.; Zhou, C.; Chen, Y. A Fast Mask Projection Stereolithography Process for Fabricating Digital Models in Minutes. *J. Manuf. Sci. Eng.* **2012**, *134* (5), 51011–51019.
- (400) Chia, H. N.; Wu, B. M. Recent Advances in 3D Printing of Biomaterials. *J. Biol. Eng.* **2015**, *9* (1), 4.
- (401) Ikuta, K.; Maruo, S.; Kojima, S. New Micro Stereo Lithography for Freely Movable 3D Micro Structure-Super IH Process with Submicron Resolution. In *Proceedings MEMS 98. IEEE. Eleventh Annual International Workshop on Micro Electro Mechanical Systems. An Investigation of Micro Structures, Sensors, Actuators, Machines and Systems (Cat. No.98CH36176)*; 1998; pp 290–295.
- (402) Pan, Y.; Dagli, C. Dynamic Resolution Control in a Laser Projection-Based Stereolithography System. *Rapid Prototyp. J.* **2017**, *23* (1), 190–200.
- (403) Cronin-Golomb, M.; Murphy, A. R.; Mondia, J. P.; Kaplan, D. L.; Omenetto, F. G. Optically Induced Birefringence and Holography in Silk. *J. Polym. Sci. Part B Polym. Phys.* **2011**, *50* (4), 257–262.
- (404) Jeon, O.; Bouhadir, K. H.; Mansour, J. M.; Alsbberg, E. Photocrosslinked Alginate Hydrogels with Tunable Biodegradation Rates and Mechanical Properties. *Biomaterials* **2009**, *30* (14), 2724–2734.
- (405) Janakiraman, V.; Kienitz, B. L.; Baskaran, H. Lithography Technique for Topographical Micropatterning of Collagen-Glycosaminoglycan Membranes for Tissue Engineering Applications. *J. Med. Device.* **2007**, *1* (3), 233–237.
- (406) Seck, T. M.; Melchels, F. P. W.; Feijen, J.; Grijpma, D. W. Designed Biodegradable Hydrogel Structures Prepared by Stereolithography Using Poly(Ethylene Glycol)/Poly(d,l-Lactide)-Based Resins. *J. Control. Release* **2010**, *148* (1), 34–41.
- (407) Kim, Z. W. and R. A. and B. P. and R. S. and S. G. and K. A Simple and High-Resolution Stereolithography-Based 3D Bioprinting System Using Visible Light Crosslinkable Bioinks. *Biofabrication* **2015**, *7* (4), 45009.
- (408) Lin, H.; Zhang, D.; Alexander, P. G.; Yang, G.; Tan, J.; Cheng, A. W.-M.; Tuan, R. S. Application of Visible Light-Based Projection Stereolithography for Live Cell-Scaffold Fabrication with Designed Architecture. *Biomaterials* **2013**, *34* (2), 331–339.
- (409) Huang, T. Q.; Qu, X.; Liu, J.; Chen, S. 3D Printing of Biomimetic Microstructures for Cancer Cell Migration. *Biomed. Microdevices* **2014**, *16* (1), 127–132.
- (410) Grogan, S. P.; Chung, P. H.; Soman, P.; Chen, P.; Lotz, M. K.; Chen, S.; D’Lima, D. D. Digital Micromirror Device Projection Printing System for Meniscus Tissue Engineering. *Acta Biomater.* **2013**, *9* (7), 7218–7226.
- (411) Partlow, B. P.; Tabatabai, A. P.; Leisk, G. G.; Cebe, P.; Blair, D. L.; Kaplan, D. L. Silk Fibroin Degradation Related to Rheological and Mechanical Properties. *Macromol. Biosci.* **2016**, *16* (5), 666–675.
- (412) Kim, H. H.; Song, D. W.; Kim, M. J.; Ryu, S. J.; Um, I. C.; Ki, C. S.; Park, Y. H. Effect of Silk Fibroin Molecular Weight on Physical Property of Silk Hydrogel. *Polymer (Guildf)*. **2016**, *90* (Supplement C), 26–33.
- (413) Neves-Petersen, M. T.; Gajula, G. P.; Petersen, S. B. UV Light Effects on Proteins : From Photochemistry to Nanomedicine. *Mol. Photochem. - Var. Asp.* **2012**, 125–158.
- (414) Sionkowska, A.; Planecka, A. The Influence of UV Radiation on Silk Fibroin. *Polym. Degrad. Stab.* **2011**, *96* (4), 523–528.
- (415) Armstrong, B. K.; Krickler, A. The Epidemiology of UV Induced Skin Cancer. *J. Photochem. Photobiol. B Biol.* **2001**, *63* (1), 8–18.
- (416) Texas Instruments. *DMD Product Preview Data Sheet*; 2005.
- (417) Ball, G. F. M. *Vitamins: Their Role in the Human Body*; John Wiley & Sons, 2008.
- (418) Wurtman, R. J. The Effects of Light on the Human Body. *Sci. Am.* **1975**, *233* (1), 68–77.
- (419) FDA. *Select Committee on GRAS Substances (SCOGS) Opinion: Riboflavin, Riboflavin-5'-Phosphate*; New Hampshire Avenue Silver Spring, MD, 1979.

- (420) Baldursdóttir, S. G.; Kjøniksen, A.-L.; Karlsen, J.; Nyström, B.; Roots, J.; Tønnesen, H. H. Riboflavin-Photosensitized Changes in Aqueous Solutions of Alginate. *Rheological Studies. Biomacromolecules* **2003**, *4* (2), 429–436.
- (421) White, J. C.; Stoppel, W. L.; Roberts, S. C.; Bhatia, S. R. Addition of Perfluorocarbons to Alginate Hydrogels Significantly Impacts Molecular Transport and Fracture Stress. *J. Biomed. Mater. Res. Part A* **2013**, *101* (2), 438–446.
- (422) Galston, A. W.; Baker, R. S. Studies on the Physiology of Light Action. II. The Photodynamic Action of Riboflavin. *Am. J. Bot.* **1949**, 773–780.
- (423) Periolatto, M.; Ferrero, F.; Vineis, C. Antimicrobial Chitosan Finish of Cotton and Silk Fabrics by UV-Curing with 2-Hydroxy-2-Methylphenylpropane-1-One. *Carbohydr. Polym.* **2012**, *88* (1), 201–205.
- (424) Edwards, A. M.; Silva, E. Effect of Visible Light on Selected Enzymes, Vitamins and Amino Acids. *J. Photochem. Photobiol. B Biol.* **2001**, *63* (1), 126–131.
- (425) Bhatia, J.; Stegink, L. D.; Ziegler, E. E. Riboflavin Enhances Photo-Oxidation of Amino Acids under Simulated Clinical Conditions. *J. Parenter. Enter. Nutr.* **1983**, *7* (3), 277–279.
- (426) Anseth, K. S.; Bowman, C. N.; Brannon-Peppas, L. Mechanical Properties of Hydrogels and Their Experimental Determination. *Biomaterials* **1996**, *17* (17), 1647–1657.
- (427) Shechtman, D.; Blech, I.; Gratias, D.; Cahn, J. W. Metallic Phase with Long-Range Orientational Order and No Translational Symmetry. *Phys. Rev. Lett.* **1984**, *53* (20), 1951–1953.
- (428) Yuan, C.-. Efficient Light Scattering Modeling for Alignment, Metrology, and Resist Exposure in Photolithography. *IEEE Trans. Electron Devices* **1992**, *39* (7), 1588–1598.
- (429) Bragg, P. W. H.; Bragg, W. L. 428 Prof. W. H. Bragg and Mr. W. L. Bragg. [Apr. 7., **1913**, *17*, 428–438.
- (430) Klug, H. P.; Alexander, L. E. X-Ray Diffraction Procedures: For Polycrystalline and Amorphous Materials. *X-Ray Diffr. Proced. Polycryst. Amorph. Mater. 2nd Ed. by Harold P. Klug, Leroy E. Alexander, pp. 992. ISBN 0-471-49369-4. Wiley-VCH, May 1974.* **1974**, 992.
- (431) Humar, M.; Kwok, S. J. J.; Choi, M.; Yetisen, A. K.; Cho, S.; Yun, S. H. Toward Biomaterial-Based Implantable Photonic Devices. *Nanophotonics* **2017**, *6* (2), 414–434.
- (432) Jiang, L.-C.; Zhang, W.-D. A Highly Sensitive Nonenzymatic Glucose Sensor Based on CuO Nanoparticles-Modified Carbon Nanotube Electrode. *Biosens. Bioelectron.* **2010**, *25* (6), 1402–1407.
- (433) Slinger, C.; Cameron, C.; Stanley, M. Computer-Generated Holography as a Generic Display Technology. *Computer (Long. Beach. Calif.)* **2005**, *38* (8), 46–53.
- (434) Lin, D.; Fan, P.; Hasman, E.; Brongersma, M. L. Dielectric Gradient Metasurface Optical Elements. *Science (80-. )* **2014**, *345* (6194), 298 LP-302.
- (435) Omenetto, F. G.; Kaplan, D. L. A New Route for Silk. *Nat Phot.* **2008**, *2* (11), 641–643.
- (436) Cerveny, D. Systems, Methods, and Apparatus for Integrating Scannable Codes in Medical Devices. Google Patents September 18, 2014.
- (437) Czuszynski, K.; Ruminski, J. Interaction with Medical Data Using QR-Codes. In *2014 7th International Conference on Human System Interactions (HSI)*; 2014; pp 182–187.
- (438) Han, S.; Bae, H. J.; Kim, J.; Shin, S.; Choi, S.-E.; Lee, S. H.; Kwon, S.; Park, W. Lithographically Encoded Polymer Microtaggant Using High-Capacity and Error-Correctable QR Code for Anti-Counterfeiting of Drugs. *Adv. Mater.* **2012**, *24* (44), 5924–5929.
- (439) Hara, M. Method for Displaying and Reading Information Code for Commercial Transaction. Google Patents February 14, 2006.
- (440) Partlow, B. P.; Applegate, M. B.; Omenetto, F. G.; Kaplan, D. L. Dityrosine Cross-Linking in Designing Biomaterials. *ACS Biomater. Sci. Eng.* **2016**, *2* (12), 2108–2121.
- (441) Balasubramanian, D.; Du, X.; Zigler, J. S. The Reaction of Singlet Oxygen with Proteins, with Special Reference to Crystallins. *Photochem. Photobiol.* **1990**, *52* (4), 761–768.
- (442) Correia, M.; Neves-Petersen, M. T.; Jeppesen, P. B.; Gregersen, S.; Petersen, S. B. UV-Light Exposure of Insulin: Pharmaceutical Implications upon Covalent Insulin Dityrosine Dimerization and Disulphide Bond Photolysis. *PLoS One* **2012**, *7* (12), e50733.
- (443) Ohgo, K.; Bagusat, F.; Asakura, T.; Scheler, U. Investigation of Structural Transition of Regenerated Silk Fibroin Aqueous Solution by Rheo-NMR Spectroscopy Investigation of Structural Transition of Regenerated Silk Fibroin Aqueous Solution by Rheo-NMR Spectroscopy. *Biomacromolecules* **2008**, No. 3, 4182–4186.
- (444) Boulet-Audet, M.; Terry, A. E.; Vollrath, F.; Holland, C. Silk Protein Aggregation Kinetics Revealed by Rheo-IR. *Acta Biomater.* **2014**, *10* (2), 776–784.
- (445) Kuo, C. K.; Ma, P. X. Ionically Crosslinked Alginate Hydrogels as Scaffolds for Tissue Engineering: Part 1. Structure, Gelation Rate and Mechanical Properties. *Biomaterials* **2001**, *22* (6), 511–521.

- (446) Tse, J. R.; Engler, A. J. Preparation of Hydrogel Substrates with Tunable Mechanical Properties. In *Current Protocols in Cell Biology*; John Wiley & Sons, Inc., 2001.
- (447) Hunter, E. P. L.; Desrosiers, M. F.; Simic, M. G. The Effect of Oxygen, Antioxidants, and Superoxide Radical on Tyrosine Phenoxyl Radical Dimerization. *Free Radic. Biol. Med.* **1989**, *6* (6), 581–585.
- (448) Chaudhury, S.; Holland, C.; Porter, D.; Vollrath, F.; Carr, A. J. Are They Tough Enough? A Comparison of How The Shear Mechanical Properties of Rotator Cuff Repair Patches Match Normal and Torn Rotator Cuff Tendons. *J. Bone & Joint Surgery, Br. Vol.* **2012**, *94-B* (SUPP XVIII), 42 LP-42.
- (449) Chaudhury, S.; Holland, C.; Thompson, M. S.; Vollrath, F.; Carr, A. J. Tensile and Shear Mechanical Properties of Rotator Cuff Repair Patches. *J. Shoulder Elb. Surg.* **2018**, *21* (9), 1168–1176.
- (450) Chaudhury, S.; Holland, C.; Vollrath, F.; Carr, A. J. Comparing Normal and Torn Rotator Cuff Tendons Using Dynamic Shear Analysis. *J. Bone & Joint Surgery, Br. Vol.* **2011**, *93-B* (7), 942 LP-948.
- (451) Holland, C.; Vollrath, F.; Gill, H. S. Horses and Cows Might Teach Us about Human Knees. *Naturwissenschaften* **2014**, *101* (4), 351–354.
- (452) Barnes, J. M.; Przybyla, L.; Weaver, V. M. Tissue Mechanics Regulate Brain Development, Homeostasis and Disease. *J. Cell Sci.* **2017**, *130* (1), 71 LP-82.
- (453) Stansbury, J. W.; Idacavage, M. J. 3D Printing with Polymers: Challenges among Expanding Options and Opportunities. *Dent. Mater.* **2016**, *32* (1), 54–64.
- (454) Shin, D.-S.; Lee, K.-N.; Jang, K.-H.; Kim, J.-K.; Chung, W.-J.; Kim, Y.-K.; Lee, Y.-S. Protein Patterning by Maskless Photolithography on Hydrophilic Polymer-Grafted Surface. *Biosens. Bioelectron.* **2003**, *19* (5), 485–494.
- (455) Hsieh, T. M.; Benjamin Ng, C. W.; Narayanan, K.; Wan, A. C. A.; Ying, J. Y. Three-Dimensional Microstructured Tissue Scaffolds Fabricated by Two-Photon Laser Scanning Photolithography. *Biomaterials* **2010**, *31* (30), 7648–7652.
- (456) Wang, Q.; Chen, Q.; Yang, Y.; Shao, Z. Effect of Various Dissolution Systems on the Molecular Weight of Regenerated Silk Fibroin. *Biomacromolecules* **2012**, *14* (1), 285–289.
- (457) Cho, H. J.; Ki, C. S.; Oh, H.; Lee, K. H.; Um, I. C. Molecular Weight Distribution and Solution Properties of Silk Fibroins with Different Dissolution Conditions. *Int. J. Biol. Macromol.* **2012**, *51* (3), 336–341.
- (458) Rnjak-Kovacina, J.; Wray, L. S.; Burke, K. A.; Torregrosa, T.; Golinski, J. M.; Huang, W.; Kaplan, D. L. Lyophilized Silk Sponges: A Versatile Biomaterial Platform for Soft Tissue Engineering. *ACS Biomater. Sci. Eng.* **2015**, *1* (4), 260–270.
- (459) Gimenes, M. L.; Silva, V. R.; Vieira, M. G. A.; Silva, M. G. C.; Scheer, A. P. High Molecular Sericin from Bombyx Mori Cocoons: Extraction and Recovering by Ultrafiltration. *Int. J. Chem. Eng. Appl.* **2014**, *5* (3), 266–271.
- (460) Aramwit, P.; Siritientong, T.; Srichana, T. Potential Applications of Silk Sericin, a Natural Protein from Textile Industry by-Products. *Waste Manag. Res.* **2011**, *30* (3), 217–224.
- (461) Da Silva, T. L.; Da Silva, A. C.; Ribani, M.; Vieira, M. G. A.; Gimenes, M. L.; Da Silva, M. G. C. Evaluation of Molecular Weight Distribution of Sericin in Solutions Concentrated via Precipitation by Ethanol and Precipitation by Freezing/Thawing. *Chem. Eng. Trans.* **2014**, *38*, 103–108.
- (462) Aramwit, P.; Damrongsakkul, S.; Kanokpanont, S.; Srichana, T. Properties and Antityrosinase Activity of Sericin from Various Extraction Methods. *Biotechnol. Appl. Biochem.* **2010**, *55* (2), 91–98.
- (463) Decker, C.; Elzaouk, B.; Decker, D. Kinetic Study of Ultrafast Photopolymerization Reactions. *J. Macromol. Sci. Part A* **1996**, *33* (2), 173–190.
- (464) Nie, Z.; Kumacheva, E. Patterning Surfaces with Functional Polymers. *Nat Mater* **2008**, *7* (4), 277–290.
- (465) McKendry, R.; Huck, W. T. S.; Weeks, B.; Fiorini, M.; Abell, C.; Rayment, T. Creating Nanoscale Patterns of Dendrimers on Silicon Surfaces with Dip-Pen Nanolithography. *Nano Lett.* **2002**, *2* (7), 713–716.
- (466) Zhang, F.; You, X.; Dou, H.; Liu, Z.; Zuo, B.; Zhang, X. Facile Fabrication of Robust Silk Nanofibril Films via Direct Dissolution of Silk in CaCl<sub>2</sub>–Formic Acid Solution. *ACS Appl. Mater. Interfaces* **2015**, *7* (5), 3352–3361.
- (467) Boulet-Audet, M.; Holland, C.; Gheysens, T.; Vollrath, F. Dry-Spun Silk Produces Native-Like Fibroin Solutions. *Biomacromolecules* **2016**, *17* (10), 3198–3204.
- (468) Numata, K.; Cebe, P.; Kaplan, D. L. Mechanism of Enzymatic Degradation of Beta-Sheet Crystals. *Biomaterials* **2010**, *31* (10), 2926–2933.
- (469) Li, M.; Ogiso, M.; Minoura, N. Enzymatic Degradation Behavior of Porous Silk Fibroin Sheets. *Biomaterials* **2003**, *24* (2), 357–365.
- (470) Horan, R. L.; Antle, K.; Collette, A. L.; Wang, Y.; Huang, J.; Moreau, J. E.; Volloch, V.; Kaplan, D. L.; Altman, G. H. In Vitro Degradation of Silk Fibroin. *Biomaterials* **2005**, *26* (17), 3385–3393.
- (471) Bauer, C. A. Active Centers of Streptomyces Griseus Protease 1, Streptomyces Griseus Protease 3, and

- $\alpha$ -Chymotrypsin: Enzyme-Substrate Interactions. *Biochemistry* **1978**, *17* (2), 375–380.
- (472) Yucel, T.; Lovett, M. L.; Kaplan, D. L. Silk-Based Biomaterials for Sustained Drug Delivery. *J. Control. Release* **2014**, *190*, 381–397.
- (473) Lammel, A. S.; Hu, X.; Park, S.-H.; Kaplan, D. L.; Scheibel, T. R. Controlling Silk Fibroin Particle Features for Drug Delivery. *Biomaterials* **2010**, *31* (16), 4583–4591.
- (474) Wang, H.; Liu, X. Y.; Chuah, Y. J.; Goh, J. C. H.; Li, J. L.; Xu, H. Design and Engineering of Silk Fibroin Scaffolds with Biomimetic Hierarchical Structures. *Chem. Commun.* **2013**, *49* (14), 1431.
- (475) Bellas, E.; Lo, T. J.; Fournier, E. P.; Brown, J. E.; Abbott, R. D.; Gil, E. S.; Marra, K. G.; Rubin, J. P.; Leisk, G. G.; Kaplan, D. L. Injectable Silk Foams for Soft Tissue Regeneration. *Adv. Healthc. Mater.* **2015**, *4* (3), 452–459.
- (476) Zhang, Y.; Fan, W.; Ma, Z.; Wu, C.; Fang, W.; Liu, G.; Xiao, Y. The Effects of Pore Architecture in Silk Fibroin Scaffolds on the Growth and Differentiation of Mesenchymal Stem Cells Expressing BMP7. *Acta Biomater.* **2010**, *6* (8), 3021–3028.
- (477) Hollister, S. J. Porous Scaffold Design for Tissue Engineering. *Nat. Mater.* **2005**, *4* (7), 518.
- (478) Bhungara, Z. Polyhipe Foam Materials as Filtration Media. *Filtr. Sep.* **1995**, *32* (3), 245–251.
- (479) Bandarian, M.; Shojaei, A.; Rashidi, A. M. Thermal, Mechanical and Acoustic Damping Properties of Flexible Open-cell Polyurethane/Multi-walled Carbon Nanotube Foams: Effect of Surface Functionality of Nanotubes. *Polym. Int.* **2011**, *60* (3), 475–482.
- (480) Papadopoulos, A. M. State of the Art in Thermal Insulation Materials and Aims for Future Developments. *Energy Build.* **2005**, *37* (1), 77–86.
- (481) Calmidi, V. V.; Mahajan, R. L. The Effective Thermal Conductivity of High Porosity Fibrous Metal Foams. *J. Heat Transfer* **1999**, *121* (2).
- (482) Busby, W.; Cameron, N. R.; Jahoda, C. A. B. Emulsion-Derived Foams (PolyHIPEs) Containing Poly ( $\epsilon$ -Caprolactone) as Matrixes for Tissue Engineering. *Biomacromolecules* **2001**, *2* (1), 154–164.
- (483) Hughes, J. M.; Budd, P. M.; Tiede, K.; Lewis, J. Polymerized High Internal Phase Emulsion Monoliths for the Chromatographic Separation of Engineered Nanoparticles. *J. Appl. Polym. Sci.* **2015**, *132* (1).
- (484) Paterson, T. E.; Gigliobianco, G.; Sherborne, C.; Green, N. H.; Dugan, J. M.; MacNeil, S.; Reilly, G. C.; Claeysens, F. Porous Microspheres Support Mesenchymal Progenitor Cell Ingrowth and Stimulate Angiogenesis. *APL Bioeng.* **2018**, *2* (2), 26103.
- (485) Owen, R.; Sherborne, C.; Paterson, T.; Green, N. H.; Reilly, G. C.; Claeysens, F. Emulsion Templated Scaffolds with Tunable Mechanical Properties for Bone Tissue Engineering. *J. Mech. Behav. Biomed. Mater.* **2016**, *54*, 159–172.
- (486) Zhang, J.; Rajkhowa, R.; Li, J. L.; Liu, X. Y.; Wang, X. G. Silkworm Cocoon as Natural Material and Structure for Thermal Insulation. *Mater. Des.* **2013**, *49*, 842–849.
- (487) Zhao, L.; Wang, H.; Luo, J.; Cai, C.; Song, G. L.; Tang, G. Y. Fabrication of Silk Fibroin Film with Properties of Thermal Insulation and Temperature Monitoring. *J. Polym. Sci. Part B Polym. Phys.* **2016**, *54* (18), 1846–1852.
- (488) Aldrich, W. E. Thermal Insulation Material Comprising a Mixture of Silk and Synthetic Fiber Staple. Google Patents August 23, 1983.
- (489) Fan, J.; Tsang, H. W. K. Effect of Clothing Thermal Properties on the Thermal Comfort Sensation during Active Sports. *Text. Res. J.* **2008**, *78* (2), 111–118.
- (490) Lemmon, E. W.; Jacobsen, R. T. Viscosity and Thermal Conductivity Equations for Nitrogen, Oxygen, Argon, and Air. *Int. J. Thermophys.* **2004**, *25* (1), 21–69.
- (491) Morikawa, J.; Ryu, M.; Maximova, K.; Balcytis, A.; Seniutinas, G.; Fan, L.; Mizeikis, V.; Li, J.; Wang, X. X. X. X. X.; Zamengo, M.; et al. Silk Fibroin as a Water-Soluble Bio-Resist and Its Thermal Properties. *RSC Adv.* **2016**, *6* (14), 11863–11869.
- (492) Lee, J. W.; Lee, B. W.; Yeon, Y. K.; Lee, O. J.; Park, C. H.; Park, J.; Ko, J.-H. Effect of Crystallinity on Acoustic Behaviors of Biocompatible Silk Studied by Brillouin Spectroscopy. *J. Korean Phys. Soc.* **2017**, *71* (3), 144–149.
- (493) Lovell, P. A.; El-Aasser, M. S.; Lovell, P. *Emulsion Polymerization and Emulsion Polymers*; Wiley New York, 1997.
- (494) Smith, W. V; Ewart, R. H. Kinetics of Emulsion Polymerization. *J. Chem. Phys.* **1948**, *16* (6), 592–599.
- (495) Tadros, T. F. *Emulsion Formation and Stability*; John Wiley & Sons, 2013.
- (496) Mahdi Jafari, S.; He, Y.; Bhandari, B. Nano-Emulsion Production by Sonication and Microfluidization—a Comparison. *Int. J. Food Prop.* **2006**, *9* (3), 475–485.
- (497) Schacht, S.; Huo, Q.; Voigt-Martin, I. G.; Stucky, G. D.; Schüth, F. Oil-Water Interface Templating of Mesoporous Macroscale Structures. *Science* (80-. ). **1996**, *273* (5276), 768–771.

- (498) Rajinder, P. Effect of Droplet Size on the Rheology of Emulsions. *AIChE J.* **2018**, *42* (11), 3181–3190.
- (499) Saito, H.; Shinoda, K. The Stability of W/O Type Emulsions as a Function of Temperature and of the Hydrophilic Chain Length of the Emulsifier. *J. Colloid Interface Sci.* **1970**, *32* (4), 647–651.
- (500) Mukerjee, P.; Mysels, K. J. *Critical Micelle Concentrations of Aqueous Surfactant Systems*; National Standard reference data system, 1971.
- (501) Walstra, P. Principles of Emulsion Formation. *Chem. Eng. Sci.* **1993**, *48* (2), 333–349.
- (502) Bancroft, W. D. The Theory of Emulsification, V. *J. Phys. Chem.* **1913**, *17* (6), 501–519.
- (503) Ruckenstein, E. Microemulsions, Macroemulsions, and the Bancroft Rule. *Langmuir* **1996**, *12* (26), 6351–6353.
- (504) Anton, N.; Benoit, J.-P.; Saulnier, P. Design and Production of Nanoparticles Formulated from Nano-Emulsion Templates—a Review. *J. Control. Release* **2008**, *128* (3), 185–199.
- (505) Bibette, J.; Morse, D. C.; Witten, T. A.; Weitz, D. A. Stability Criteria for Emulsions. *Phys. Rev. Lett.* **1992**, *69* (16), 2439.
- (506) Trallero, J. L.; Sarica, C.; Brill, J. P. A Study of Oil-Water Flow Patterns in Horizontal Pipes. *SPE Prod. Facil.* **1997**, *12* (03), 165–172.
- (507) Nädler, M.; Mewes, D. Flow Induced Emulsification in the Flow of Two Immiscible Liquids in Horizontal Pipes. *Int. J. Multiph. flow* **1997**, *23* (1), 55–68.
- (508) Mazutis, L.; Baret, J.-C.; Treacy, P.; Skhiri, Y.; Araghi, A. F.; Ryckelynck, M.; Taly, V.; Griffiths, A. D. Multi-Step Microfluidic Droplet Processing: Kinetic Analysis of an in Vitro Translated Enzyme. *Lab Chip* **2009**, *9* (20), 2902–2908.
- (509) Okushima, S.; Nisisako, T.; Torii, T.; Higuchi, T. Controlled Production of Monodisperse Double Emulsions by Two-Step Droplet Breakup in Microfluidic Devices. *Langmuir* **2004**, *20* (23), 9905–9908.
- (510) Munson, B. R.; Okiishi, T. H.; Huebsch, W. W.; Rothmayer, A. P. *Fluid Mechanics*; Wiley Singapore, 2013.
- (511) Tadros, T. F. Emulsion Formation, Stability, and Rheology. *Emuls. Form. Stab.* **2013**, 1–76.
- (512) Zifu, L.; Manda, X.; Jianfang, W.; To, N. Pure Protein Scaffolds from Pickering High Internal Phase Emulsion Template. *Macromol. Rapid Commun.* **2012**, *34* (2), 169–174.
- (513) Buchmeiser, M. R. Polymeric Monolithic Materials: Syntheses, Properties, Functionalization and Applications. *Polymer (Guildf)*. **2007**, *48* (8), 2187–2198.
- (514) Gokmen, M. T.; Du Prez, F. E. Porous Polymer Particles—A Comprehensive Guide to Synthesis, Characterization, Functionalization and Applications. *Prog. Polym. Sci.* **2012**, *37* (3), 365–405.
- (515) Schofield, W. C. E.; Bain, C. D.; Badyal, J. P. S. Cyclodextrin-Functionalized Hierarchical Porous Architectures for High-Throughput Capture and Release of Organic Pollutants from Wastewater. *Chem. Mater.* **2012**, *24* (9), 1645–1653.
- (516) Robinson, J. L.; McEnery, M. A. P.; Pearce, H.; Whitely, M. E.; Munoz-Pinto, D. J.; Hahn, M. S.; Li, H.; Sears, N. A.; Cosgriff-Hernandez, E. Osteoinductive PolyHIPE Foams as Injectable Bone Grafts. *Tissue Eng. Part A* **2016**, *22* (5–6), 403–414.
- (517) Bokhari, M. A.; Akay, G.; Zhang, S.; Birch, M. A. The Enhancement of Osteoblast Growth and Differentiation in Vitro on a Peptide Hydrogel—polyHIPE Polymer Hybrid Material. *Biomaterials* **2005**, *26* (25), 5198–5208.
- (518) Christenson, E. M.; Soofi, W.; Holm, J. L.; Cameron, N. R.; Mikos, A. G. Biodegradable Fumarate-Based PolyHIPEs as Tissue Engineering Scaffolds. *Biomacromolecules* **2007**, *8* (12), 3806–3814.
- (519) Barbetta, A.; Dentini, M.; Zannoni, E. M.; De Stefano, M. E. Tailoring the Porosity and Morphology of Gelatin-Methacrylate PolyHIPE Scaffolds for Tissue Engineering Applications. *Langmuir* **2005**, *21* (26), 12333–12341.
- (520) Hubbell, J. A. Biomaterials in Tissue Engineering. *Nat. Biotechnol.* **1995**, *13* (6), 565.
- (521) Nair, L. S.; Laurencin, C. T. Biodegradable Polymers as Biomaterials. *Prog. Polym. Sci.* **2007**, *32* (8–9), 762–798.
- (522) Fu, C.; Shao, Z.; Fritz, V. Animal Silks: Their Structures, Properties and Artificial Production. *Chem. Commun.* **2009**, No. 43, 6515–6529.
- (523) Cameron, N. R. High Internal Phase Emulsion Templating as a Route to Well-Defined Porous Polymers. *Polymer (Guildf)*. **2005**, *46* (5), 1439–1449.
- (524) Box, P. O. Ntp Technical Report on the Toxicology and Carcinogenesis Studies of Ginkgo Biloba Extract in F344 / N Rats and B6C3F1 / N Mice National Toxicology Program. **2013**, No. 90045.
- (525) Gaylord Chemical Company LLC. Dimethyl Sulfoxide (Health and Safety Information). *Gaylord Chem. Co. Bull.* **2014**, *2014* (June), 1–16.
- (526) Record, F.; Displays, D. Human Health Effects : Toxicity Summary : Evidence for Carcinogenicity : Human Toxicity Excerpts : **2015**, *7* (1998), 1–112.



- (527) Lligadas, G.; Ronda, J. C.; Galià, M.; Cádiz, V. Renewable Polymeric Materials from Vegetable Oils: A Perspective. *Mater. Today* **2013**, *16* (9), 337–343.
- (528) Diamante, L. M.; Lan, T. Absolute Viscosities of Vegetable Oils at Different Temperatures and Shear Rate Range of 64.5 to 4835 S<sup>-1</sup>. *J. food Process.* **2014**, *2014*.
- (529) Tsukada, M.; Kato, H.; Freddi, G.; Kasai, N.; Ishikawa, H. Structural Changes and Dyeability of Silk Fibroin Fiber Following Shrinkage in Neutral Salt Solution. *J. Appl. Polym. Sci.* **1994**, *51*, 619–624.
- (530) Fereshteh, Z. 7 - Freeze-Drying Technologies for 3D Scaffold Engineering; Deng, Y., Kuiper, J. B. T.-F. 3D T. E. S., Eds.; Woodhead Publishing, 2018; pp 151–174.
- (531) Murphy, C. M.; Haugh, M. G.; O'Brien, F. J. The Effect of Mean Pore Size on Cell Attachment, Proliferation and Migration in Collagen–glycosaminoglycan Scaffolds for Bone Tissue Engineering. *Biomaterials* **2010**, *31* (3), 461–466.
- (532) Maniglio, D.; Bonani, W.; Migliaresi, C.; Motta, A. Silk Fibroin Porous Scaffolds by N<sub>2</sub>O Foaming. *J. Biomater. Sci. Polym. Ed.* **2018**, *29* (5), 491–506.
- (533) Fay, J. A. Physical Processes in the Spread of Oil on a Water Surface. In *International Oil Spill Conference*; American Petroleum Institute, 1971; Vol. 1971, pp 463–467.
- (534) Eastoe, J.; Dalton, J. S. Dynamic Surface Tension and Adsorption Mechanisms of Surfactants at the Air–water Interface. *Adv. Colloid Interface Sci.* **2000**, *85* (2–3), 103–144.
- (535) Bai, G.; Bee, J. S.; Biddlecombe, J. G.; Chen, Q.; Leach, W. T. Computational Fluid Dynamics (CFD) Insights into Agitation Stress Methods in Biopharmaceutical Development. *Int. J. Pharm.* **2012**, *423* (2), 264–280.
- (536) Chu, L.; Utada, A. S.; Shah, R. K.; Kim, J.; Weitz, D. A. Controllable Monodisperse Multiple Emulsions. *Angew. Chemie* **2007**, *119* (47), 9128–9132.
- (537) Shah, R. K.; Shum, H. C.; Rowat, A. C.; Lee, D.; Agresti, J. J.; Utada, A. S.; Chu, L.-Y.; Kim, J.-W.; Fernandez-Nieves, A.; Martinez, C. J. Designer Emulsions Using Microfluidics. *Mater. Today* **2008**, *11* (4), 18–27.
- (538) Utada, A. S.; Lorenceau, E. L.; Link, D. R.; Kaplan, P. D.; Stone, H. A.; Weitz, D. A. Monodisperse Double Emulsions Generated from a Microcapillary Device. *Science (80- )*. **2005**, *308* (5721), 537–541.
- (539) Goddard, E. D. *Interactions of Surfactants with Polymers and Proteins: 0*; CRC press, 2017.
- (540) Song, J.-H.; Kim, H.-E.; Kim, H.-W. Production of Electrospun Gelatin Nanofiber by Water-Based Co-Solvent Approach. *J. Mater. Sci. Mater. Med.* **2008**, *19* (1), 95–102.
- (541) Migliaresi, C.; Kesenci, K.; Motta, A. Method for the Preparation of Silk Fibron Hydrogels. Google Patents December 30, 2004.
- (542) Yu-yue, C.; Hong, L.; Yu, R.; Hong-wei, W.; Liang-jun, Z. Study On Bombyx Mori Silk Treated by Oxygen Plasma. *J. Zhejiang Univ. A* **2004**, *5* (8), 918–922.
- (543) Perkins, T. K.; Johnston, O. C. A Review of Diffusion and Dispersion in Porous Media. *Soc. Pet. Eng. J.* **1963**, *3* (01), 70–84.
- (544) Gailin, L. A.; Nail, S. L. Freeze Drying: A Practical Overview. *Bioprocess Technol.* **1993**, *18*, 317.
- (545) Keey, R. B. *Drying: Principles and Practice*; Elsevier, 2013; Vol. 13.
- (546) Hentze, H.-P.; Antonietti, M. Porous Polymers and Resins for Biotechnological and Biomedical Applications. *Rev. Mol. Biotechnol.* **2002**, *90* (1), 27–53.
- (547) Wu, D.; Xu, F.; Sun, B.; Fu, R.; He, H.; Matyjaszewski, K. Design and Preparation of Porous Polymers. *Chem. Rev.* **2012**, *112* (7), 3959–4015.
- (548) Mills, N. J.; Zhu, H. X. The High Strain Compression of Closed-Cell Polymer Foams. *J. Mech. Phys. Solids* **1999**, *47* (3), 669–695.
- (549) Schuetz, M. A.; Glicksman, L. R. A Basic Study of Heat Transfer through Foam Insulation. *J. Cell. Plast.* **1984**, *20* (2), 114–121.
- (550) Aravand, M. A.; Semsarzadeh, M. A. Particle Formation by Emulsion Inversion Method: Effect of the Stirring Speed on Inversion and Formation of Spherical Particles. *Macromol. Symp.* **2008**, *274* (1), 141–147.
- (551) Colombié, S.; Gaunand, A.; Lindet, B. Lysozyme Inactivation under Mechanical Stirring: Effect of Physical and Molecular Interfaces. *Enzyme Microb. Technol.* **2001**, *28* (9–10), 820–826.
- (552) McClements, D. J. Critical Review of Techniques and Methodologies for Characterization of Emulsion Stability. *Crit. Rev. Food Sci. Nutr.* **2007**, *47* (7), 611–649.
- (553) Vollrath, F.; Porter, D. Silks as Ancient Models for Modern Polymers. *Polymer (Guildf)*. **2009**, *50* (24), 5623–5632.
- (554) Mo, C.; Holland, C.; Porter, D.; Shao, Z.; Vollrath, F. Concentration State Dependence of the Rheological and Structural Properties of Reconstituted Silk. *Biomacromolecules* **2009**, *10*, 2724–2728.
- (555) Panilaitis, B.; Altman, G. H.; Chen, J.; Jin, H. J.; Karageorgiou, V.; Kaplan, D. L. Macrophage Responses to Silk. *Biomaterials* **2003**, *24*, 3079–3085.

- (556) Dicko, C.; Vollrath, F.; Kenney, J. M. Spider Silk Protein Refolding Is Controlled by Changing PH. *Biomacromolecules* **2004**, *5*, 704–710.
- (557) Bhattacharjee, P. K.; Oberhauser, J. P.; McKinley, G. H.; Leal, L. G.; Sridhar, T. Extensional Rheometry of Entangled Solutions. *Macromolecules* **2002**, *35*, 10131–10148.
- (558) Pulko, I.; Krajnc, P. High Internal Phase Emulsion Templating—a Path to Hierarchically Porous Functional Polymers. *Macromol. Rapid Commun.* **2012**, *33* (20), 1731–1746.
- (559) Li, G.; Liu, H.; Li, T.; Wang, J. Surface Modification and Functionalization of Silk Fibroin Fibers/Fabric toward High Performance Applications. *Mater. Sci. Eng. C* **2012**, *32* (4), 627–636.
- (560) Lee, S.-M.; Pippel, E.; Gösele, U.; Dresbach, C.; Qin, Y.; Chandran, C. V.; Bräuniger, T.; Hause, G.; Knez, M. Greatly Increased Toughness of Infiltrated Spider Silk. *Science (80-. )*. **2009**, *324* (5926), 488–492.
- (561) Arai, T.; Freddi, G.; Colonna, G. M.; Scotti, E.; Boschi, A.; Murakami, R.; Tsukada, M. Absorption of Metal Cations by Modified B. Mori Silk and Preparation of Fabrics with Antimicrobial Activity. *J. Appl. Polym. Sci.* **2001**, *80* (2), 297–303.
- (562) Turner, W. C.; Malloy, J. F. Thermal Insulation Handbook.[Includes Glossary]. **1981**.
- (563) Dowd, D.; Hayduke, N. Insulating Gasket. Google Patents November 27, 2001.
- (564) Martini-Vvedensky, J. E.; Suh, N. P.; Waldman, F. A. Microcellular Closed Cell Foams and Their Method of Manufacture. Google Patents September 25, 1984.
- (565) Lock, P. M.; Webb, D. R. Wound Dressing Materials. Google Patents November 18, 1980.
- (566) Kreuter, J. Nanoparticles and Microparticles for Drug and Vaccine Delivery. *J. Anat.* **1996**, *189* ( Pt 3), 503–505.
- (567) Nazarov, R.; Jin, H.; Kaplan, D. L. Porous 3-D Scaffolds from Regenerated Silk Fibroin.Pdf. **2004**, 718–726.
- (568) Chen, S.; Jiang, Y. The Acoustic Property Study of Polyurethane Foam with Addition of Bamboo Leaves Particles. *Polym. Compos.* **2018**, *39* (4), 1370–1381.
- (569) D., C. J. Further Studies on the Mechanical Properties of Mollusc Shell Material. *J. Zool.* **2018**, *180* (4), 445–453.
- (570) Januszewski, J.; Khokhar, M. I.; Mujumdar, A. S. Thermal Conductivity of Some Porous Materials. **1977**, *4*, 417–423.
- (571) Rood, E. S. Thermal Conductivity of Some Wearing Materials. *Phys. Rev.* **1921**, *18* (5), 356–361.
- (572) Wang, L.; Li, C. Preparation and Physicochemical Properties of a Novel Hydroxyapatite/Chitosan-Silk Fibroin Composite. *Carbohydr. Polym.* **2007**, *68*, 740–745.
- (573) Zhou, Z.; Zhang, S.; Cao, Y.; Marelli, B.; Xia, X.; Tao, T. H. Engineering the Future of Silk Materials through Advanced Manufacturing. *Adv. Mater.* **2018**, *1706983*, 1706983.
- (574) Loh, Q. L.; Choong, C. Three-Dimensional Scaffolds for Tissue Engineering Applications: Role of Porosity and Pore Size. *Tissue Eng. Part B. Rev.* **2013**, *19* (6), 485–502.